

---

---

EXOPLANET TRANSIT SPECTROSCOPY:  
DEVELOPMENT AND APPLICATION OF A GENERIC  
TIME DOMAIN SIMULATOR

---

---

*by*

Subhajit Sarkar

A THESIS SUBMITTED TO CARDIFF UNIVERSITY  
FOR THE DEGREE OF DOCTOR OF PHILOSOPHY

SEPTEMBER 2017

**Author:** Subhajit Sarkar

**Title:** Exoplanet transit spectroscopy:  
development and application of a generic  
time domain simulator

**Date of submission:** September 2017







*'Somewhere, something incredible is waiting to  
be known.'*

---

CARL SAGAN



# DEDICATION

---

---

I dedicate this thesis to my mother, Dipti Sarkar, and to my late father, Sarbani Prasad Sarkar, who fortunately learned of my acceptance on to this programme before his passing. Thank you both for being there on this road less traveled.



# ACKNOWLEDGEMENTS

---

---

I Am very grateful to my primary supervisor, Enzo Pascale, for his guidance and tuition over these years, and to Andreas Papageorgiou, for his patient help in all things computational. I would like to thank also the other members of my supervisory team, Haley Gomez and Emyr MacDonald, for their big picture advice and guidance. Thank you to all my fellow PhD students and to the post-docs, academics and staff in the Physics and Astronomy department at Cardiff University for making my time here so pleasant and stimulating. Thanks to my office mates over the years, Ken Marsh, Tom Rayner, Gwen Williams, Rachael Spowage, Camilo Penalosa and Gustavo Dopcke, and to other members in the Star Formation and Astronomy Instrumentation groups, for the picking of brains and bouncing of ideas. Thanks to colleagues at University College London, Giovanna Tinetti, Ingo Waldmann, Jo Barstow, Giuseppe Morrelo, Tiziano Zingales and others, with whom our group at Cardiff have worked closely on exoplanets research, particularly on the ARIEL mission. Also to colleagues in the ARIEL consortium for giving me the opportunity to be involved in such an interesting and groundbreaking project. Particular thanks to Bart Vandebussche and Yannis Argyriou at KU Leuven for providing results from their stellar variability model. Thanks also to Hannu Parviainen at Oxford, for advice on phase curve simulation. I'd like to also thank my former MSc tutor at UCL, Ian Mason, for setting me on this path and his help and advice over the years. This work was supported by funding from the Science and Technology Facilities Council for which I am very grateful.



# PUBLICATIONS

---

---

## FIRST AUTHOR

Sarkar S., Pascale E., 2015, *ExoSim: a novel simulator of exoplanet spectroscopic observations*, EPSC Abstracts, 10, EPSC2015-187

Sarkar S., Papageorgiou A., Pascale E., 2016, *Exploring the potential of the ExoSim simulator for transit spectroscopy noise estimation*, Proc. SPIE, 9904, 99043R; doi: 10.1117/12.2234216

Sarkar S. et al., 2017, *ARIEL Performance Analysis Report*, ESA / ARIEL Technical Note ARIEL-CRDF-PL-AN-001, Iss 2.2

Sarkar S. et al., 2017, *The effects of stellar variability on transit spectroscopy observations in the ARIEL space mission examined using the ExoSim simulator*, EPSC Abstracts, 11, EPSC2017-447-2

Sarkar S. et al., 2017, *Stellar pulsation and granulation as noise sources in exoplanet transit spectroscopy in the ARIEL space mission*, submitted to MNRAS

Sarkar S., Papageorgiou A., Pascale E., 2017, *ExoSim: elucidating noise on exoplanet transit spectroscopy observations using a generic time domain simulator*, in preparation

## CO-AUTHOR

Pascale E., Sarkar S., 2014, *Detecting Exoplanet Atmospheres Using High Altitude Balloon Telescopes*, EPSC Abstracts, 9, EPSC2014-780

Pascale E. et al., 2015, *EChOSim: The Exoplanet Characterisation Observatory software simulator*, *Exp. Astron.*, 40, 601; doi:10.1007/s10686-015-9471-0

Tinetti G. et al., 2016, *The science of ARIEL (Atmospheric Remote-sensing Infrared Exoplanet Large-survey)*, *Proc. SPIE*, 9904, 99041X; doi: 10.1117/12.2232370

Papageorgiou A., Pascale E., Sarkar S., 2017, *ARIEL Performance Model*, ESA/ARIEL Technical Note ARIEL-CRDF-PL-ML-001, Iss 2.0

Pascale E. et al., 2017, *The EXoplanet Infrared Climate Telescope (EXCITE)*, *EPSC Abstracts*, 11, EPSC2017-729-1

Zingales T. et al., 2017, *The ARIEL Mission Reference Sample*, *EPSC Abstracts*, 11, EPSC2017-638

Zingales T. et al., 2017, *The ARIEL Mission Reference Sample*, submitted to *Exp. Astron.*

Tinetti G. et al., 2017, *A chemical survey of exoplanets with ARIEL*, submitted to *Exp. Astron.*

# ABSTRACT

---

---

**I**N this thesis I describe the development and validation of a generic time domain simulator of exoplanet transit spectroscopy called ExoSim, and apply it to various problems in the field. ExoSim models both the astrophysical scene and the optical system in an end-to-end simulation, outputting a time series of images akin to a real observation. The simulator was validated through a series of tests against predictions, alternate simulations and published data, showing it was accurate to within 5% of most comparisons. ExoSim modeled the Hubble Wide Field Camera 3 IR instrument, finding that scanning mode was superior to staring mode (38% less noise), with no significant excess noise. The results supported uncertainties in published studies for GJ 1214b. ExoSim was used in the ARIEL Phase A study, playing a key role in formulating and verifying an instrument design that was low risk and compatible with the science case of spectroscopically surveying 1000 exoplanets. Spectral jitter noise was found to be a feature of ARIEL observations, but using ExoSim it was shown this could be mitigated in data reduction without design level changes. ExoSim was used to quantify the uncertainties due to stellar variability on the transmission spectrum, finding that noise from pulsations and granulation is not significant in ARIEL observations. For spots, variations of +3.9 to -5.2% in contrast ratio were projected for GJ 1214b and +0.9 to -0.5% for HD209458b in the visual range, but in the mid-IR range variations fall well within the photon noise limit. ExoSim was used to simulate observations of the TRAPPIST-1 system, from which we found that ARIEL could characterise primordial H<sub>2</sub>-He atmospheres on all 7 planets, but that only planets b and h would be candidates for observing high molecular weight atmospheres. Overall, ExoSim was found to be a valuable tool applicable to diverse problems in the field of transit spectroscopy.



# CONTENTS

---

---

<b>Dedication</b>	<b>ix</b>
<b>Acknowledgements</b>	<b>xi</b>
<b>Publications</b>	<b>xiii</b>
<b>Abstract</b>	<b>xv</b>
<b>List of Tables</b>	<b>xxii</b>
<b>List of Figures</b>	<b>xxv</b>
<b>1 Introduction</b>	<b>1</b>
1.1 Transit spectroscopy and exoplanets . . . . .	2
1.1.1 Exoplanets . . . . .	2
1.1.2 Transit spectroscopy . . . . .	9
1.2 Signal and noise in transit spectroscopy . . . . .	16
1.2.1 Light curves . . . . .	16
1.2.2 Signal . . . . .	19
1.2.3 Noise . . . . .	23
1.3 The case for a generic time domain simulator . . . . .	30
1.3.1 Motivation . . . . .	30
1.3.2 Previous simulators . . . . .	32
1.3.3 Requirements . . . . .	34
<b>2 Development and validation of ExoSim</b>	<b>37</b>
2.1 The ExoSim algorithm . . . . .	37
2.1.1 Overview . . . . .	37

2.1.2	Inputs . . . . .	40
2.1.3	Modules . . . . .	41
2.2	Validation . . . . .	56
2.2.1	Validation of focal plane signal and non-jitter noise against analytical predictions . . . . .	56
2.2.2	ExoSim vs ESA Radiometric Model . . . . .	58
2.2.3	Validation of jitter noise model . . . . .	64
2.2.4	Validation of jitter noise spatial sampling method . . . . .	66
2.2.5	Validation of jitter frame rate independence . . . . .	68
2.2.6	ExoSim vs Hubble WFC3 . . . . .	70
2.3	Discussion . . . . .	73
<b>3</b>	<b>Simulating the Hubble Wide Field Camera 3</b>	<b>75</b>
3.1	Background . . . . .	76
3.1.1	Spatial scanning on the WFC3 IR . . . . .	76
3.2	Analysis of scanning mode data . . . . .	81
3.2.1	Measuring the scan rate and variations with exposure . . . . .	81
3.2.2	Forward and backward scans in program 13021 . . . . .	82
3.3	Hubble WFC3 model . . . . .	88
3.3.1	Other WFC3 simulators . . . . .	88
3.3.2	Instrument model . . . . .	89
3.3.3	Hubble pointing jitter power spectrum . . . . .	91
3.4	Simulations . . . . .	93
3.4.1	Goals and case studies . . . . .	93
3.4.2	Spatial scanning model . . . . .	93
3.4.3	Simulated observations . . . . .	94
3.4.4	Data reduction . . . . .	95
3.5	Results . . . . .	96
3.6	Analysis . . . . .	102
3.6.1	Case 1 . . . . .	102
3.6.2	Case 2 . . . . .	104
3.6.3	Case 3 . . . . .	104
3.6.4	Case 4 . . . . .	105
3.7	Discussion . . . . .	105

<b>4</b>	<b>ExoSim and the ARIEL Phase A study</b>	<b>109</b>
4.1	ARIEL . . . . .	109
4.1.1	Science goals . . . . .	110
4.1.2	Payload . . . . .	112
4.1.3	ExoSim in the ARIEL Phase A study . . . . .	113
4.2	Early proposal designs for the ARIEL spectrometer . . . . .	115
4.2.1	HRS vs LRS . . . . .	115
4.2.2	Evaluation of initial designs with ExoSim . . . . .	119
4.3	Pointing jitter and its mitigation . . . . .	135
4.3.1	Pointing jitter mechanism . . . . .	135
4.3.2	Jitter noise mitigation . . . . .	142
4.3.3	Implementing mitigation . . . . .	143
4.3.4	Summary . . . . .	155
4.4	Establishing noise requirements compatible with science case . . . . .	158
4.4.1	Finding $N_{min}$ . . . . .	159
4.4.2	Finding $X$ . . . . .	160
4.4.3	Methodology . . . . .	161
4.4.4	Results . . . . .	165
4.4.5	Mission viability . . . . .	166
4.5	Evaluation of final Phase A design . . . . .	169
4.5.1	Methodology . . . . .	169
4.5.2	Results . . . . .	174
4.5.3	Analysis . . . . .	174
4.5.4	Compliance with requirements . . . . .	179
4.6	Discussion . . . . .	179
<b>5</b>	<b>The impact of stellar variability and activity</b>	<b>183</b>
5.1	Pulsations and granulation . . . . .	184
5.1.1	Methodology . . . . .	185
5.1.2	Results . . . . .	186
5.1.3	Analysis and Discussion . . . . .	190
5.2	Star spots . . . . .	191
5.2.1	Background . . . . .	191
5.2.2	Impact on transit spectroscopy . . . . .	193

5.2.3	Star spot study with ExoSim . . . . .	200
5.2.4	Methodology . . . . .	209
5.2.5	Results . . . . .	214
5.2.6	Analysis . . . . .	227
5.2.7	Discussion . . . . .	233
<b>6</b>	<b>Observing TRAPPIST-1 planets with ARIEL</b>	<b>239</b>
6.1	The TRAPPIST-1 exosystem . . . . .	239
6.1.1	Background . . . . .	239
6.1.2	The feasibility of ARIEL observations . . . . .	243
6.2	Methodology . . . . .	244
6.2.1	Estimating the signal . . . . .	245
6.2.2	Noise simulation . . . . .	246
6.2.3	Data reduction . . . . .	248
6.2.4	SNR and $N_{transits}$ calculation . . . . .	250
6.3	Results . . . . .	254
6.4	Analysis . . . . .	267
6.4.1	Primary transit . . . . .	267
6.4.2	Secondary eclipse . . . . .	271
6.5	Discussion . . . . .	272
<b>7</b>	<b>Conclusions</b>	<b>275</b>
7.1	Goals of the thesis . . . . .	275
7.2	Approach to development and validation . . . . .	276
7.3	Key Findings . . . . .	277
7.3.1	Chapter 3 . . . . .	277
7.3.2	Chapter 4 . . . . .	278
7.3.3	Chapter 5 . . . . .	279
7.3.4	Chapter 6 . . . . .	280
7.4	Limitations . . . . .	280
7.5	Future work . . . . .	283
<b>A</b>	<b>Appendix</b>	<b>287</b>
A.1	Proof for 2-D jitter noise expression . . . . .	287
A.2	Zodiacal light adjustment . . . . .	290

A.3 V2,V3-X,Y transformation . . . . .	293
<b>Bibliography</b>	<b>294</b>



# LIST OF TABLES

---

---

1.1	Molecular and atomic ‘detections’ in exoplanets. . . . .	15
1.2	Random and systematic error sources that can affect transit and eclipse spectroscopy observations. . . . .	27
1.3	Dynamic versus static simulators. . . . .	33
1.4	Proposed simulator contrasted with previous exoplanet simulators. . .	35
2.1	Configuration of the ARIEL model used in ExoSim for comparison with the ESA Radiometric Model. . . . .	61
3.1	Exoplanet transit and eclipse spectroscopy studies performed with the Hubble WFC3 IR instrument and the G141 grism. . . . .	77
3.2	Published and measured scan rates for some WFC3 IR scanning mode studies. . . . .	83
3.3	Jitter rms in x and y directions during scans, and variation on the re-positioning of each scan. . . . .	85
3.4	Summary of case 1 results. . . . .	98
3.5	Summary of case 2 results. . . . .	99
3.6	Summary of case 3 results. . . . .	100
3.7	Summary of case 4 results. . . . .	101
4.1	ARIEL three-tiered observational strategy. . . . .	112
4.2	Comparing estimates of $\sigma_{cr}$ from different methods. . . . .	121
4.3	Configurations of the Low Resolution Spectrometer (LRS) and High Resolution Spectrometer (HRS) designs implemented in ExoSim. . .	123
4.4	Jitter mechanisms and mitigation strategies for each mechanism. . .	143
4.5	ARIEL instrument prescription used in noise requirements test. . . .	162
4.6	Integration times for each target for the noise requirements test. . . .	163

4.7	Summary of $X$ and $N_{min}$ results from ExoSim simulations and ERM inputs for the MRS study. . . . .	168
4.8	ARIEL instrument prescription used for Phase A final noise budget performance analysis. . . . .	170
4.9	Integration times for each target for Phase A final noise budget performance analysis. . . . .	171
4.10	Apertures used for FGS channels. . . . .	172
5.1	Stellar convection noise/signal as ppm. . . . .	190
5.2	Stellar convection noise variance as a percent of photon noise variance.	190
5.3	Measured simulation filling factors, brightness variations and Q factors, for each input spot coverage. . . . .	213
5.4	$\sigma_{spot} / \sigma_{photon}$ for each ARIEL channel. . . . .	227
6.1	TRAPPIST-1 system parameters. . . . .	241
6.2	ARIEL instrument prescription used for TRAPPIST-1 study. . . . .	249
6.3	Scale height and primary transit atmospheric signal at different mean molecular weights for each TRAPPIST-1 planet. . . . .	256
6.4	Median secondary eclipse signal in each channel and median $N_{transits}$ to achieve goal SNR. . . . .	257
6.5	$N_{limit}$ for different TRAPPIST-1 planets, and maximum $\mu$ detectable at each tier. . . . .	266
6.6	$N_{transits}$ to detect primordial $\mu = 2.22$ g/mol atmosphere for different TRAPPIST-1 planets at different tiers. . . . .	266

# LIST OF FIGURES

---

---

1.1	Current known exoplanets: radius vs semimajor axis. . . . .	3
1.2	Current known exoplanets: number vs radius. . . . .	3
1.3	Planet radius vs mass. . . . .	5
1.4	Theoretical scheme for the formation and evolution of different types of exoplanet atmosphere. . . . .	7
1.5	The C/O ratio of a planet may give an insight to its formation location. . . . .	8
1.6	Variations in observed flux due to planet primary transit, secondary eclipse and phase curves. . . . .	10
1.7	Molecular signatures in the 1-16 $\mu\text{m}$ range. . . . .	12
1.8	Light curve shape and duration as a function of impact parameter. . . . .	17
1.9	Geometry of transit spectroscopy. . . . .	20
1.10	The primary transit contrast ratio spectrum caused by wavelength-dependent variations in atmospheric absorption. . . . .	21
1.11	The transmission spectrum of GJ 1214b from Kreidberg et al. (2014a). . . . .	25
2.1	ExoSim modular architecture and information flow. . . . .	39
2.2	Example of an ExoSim Input Configuration File. . . . .	42
2.3	Simulating phase curves. . . . .	45
2.4	Construction of spectrum from PSFs. . . . .	48
2.5	2-D pixel response function. . . . .	49
2.6	Herschel model pointing jitter PSD profiles. . . . .	54
2.7	ExoSim focal plane signal compared to analytical prediction. . . . .	57
2.8	ExoSim non-jitter noise compared to predictions. . . . .	59
2.9	ExoSim and ESA Radiometric Model cross-validation test . . . . .	63
2.10	ExoSim jitter noise compared to predictions. . . . .	65
2.11	Jitter noise vs pixel oversampling rate. . . . .	68

2.12	Verifying that ExoSim jitter noise is frame-rate independent. . . . .	69
2.13	Comparison of focal plane spectrum from ExoSim and Berta et al. (2012). . . . .	71
2.14	Comparison of white light curves from ExoSim and Kreidberg et al. (2014a). . . . .	72
3.1	Comparison of staring mode and spatial scanning mode images. . . . .	78
3.2	Scanning mode induced variations in row counts between exposures. . . . .	80
3.3	Positional offsets (jitter) during scans for program 13021. . . . .	84
3.4	Variation of initial scan position in each visit for program 13021. . . . .	87
3.5	The Hubble Space Telescope and the Wide Field Camera 3 IR instrument. . . . .	90
3.6	Obtaining a power spectral density (PSD) profile for the ExoSim Hubble Space Telescope model. . . . .	92
3.7	Sequence of scanned NDR images from the ExoSim Hubble WFC3 IR model. . . . .	94
3.8	Monte Carlo simulation result example for the baseline WFC3 IR model. . . . .	97
3.9	Histogram of transit depths for the 1.56 $\mu\text{m}$ bin. . . . .	97
3.10	Case 1: uncertainty on primary transit contrast ratio spectrum. . . . .	98
3.11	Case 2: uncertainty on primary transit contrast ratio spectrum. . . . .	99
3.12	Case 3: uncertainty on primary transit contrast ratio spectrum. . . . .	100
3.13	Case 4: uncertainty on primary transit contrast ratio spectrum. . . . .	101
4.1	The ARIEL spacecraft and layout of components. . . . .	114
4.2	Optical pathways in the ARIEL telescope. . . . .	115
4.3	Black body fluxes for a range of likely ARIEL planet targets. . . . .	117
4.4	Spectral features for a variety of molecules likely in ARIEL target planet atmospheres. . . . .	117
4.5	Finding the uncertainty on the contrast ratio using Monte Carlo simulation. . . . .	122
4.6	Aperture masks used in basic data reduction pipeline. . . . .	127
4.7	Noise budgets for HRS and LRS designs for 55 Cancri. . . . .	131
4.8	Noise budgets for HRS and LRS designs for GJ 1214. . . . .	132

4.9	Jitter mechanism. . . . .	137
4.10	RPE and PDE definitions. . . . .	139
4.11	Power spectral density profiles developed for ExoSim simulations using ARIEL pointing requirements. . . . .	140
4.12	Effect of image shift decorrelation on LRS jitter noise when observ- ing 55 Cancri. . . . .	146
4.13	Effect of image shift decorrelation on jitter noise on the final end-of- Phase A AIRS design. . . . .	147
4.14	Importance of flat fielding prior to image shift decorrelation of jitter noise in the final end-of-Phase A AIRS design. . . . .	148
4.15	Comparison of different methods for image shift decorrelation. . . . .	150
4.16	Effect of image shift decorrelation implemented with a fixed non- moving aperture mask. . . . .	151
4.17	Comparison of image shift decorrelation vs aperture-based jitter decorrelation in FGS 1 and FGS 2. . . . .	152
4.18	Blue end widening of the aperture mask. . . . .	153
4.19	Effect of aperture mask widening on spatial jitter. . . . .	154
4.20	The importance of using accurate PSF profiles in the simulation of jitter noise. . . . .	156
4.21	Wavefront-error-abberated PSFs for photometric channels used in ExoSim simulations. . . . .	157
4.22	$N_{min}$ values from ExoSim simulations. . . . .	166
4.23	$X$ values found from ExoSim simulations for each target. . . . .	167
4.24	ARIEL Mission Reference Sample results. . . . .	168
4.25	Finding optimal value for $x$ (blue end widening) in each channel. . . . .	172
4.26	Relative SNR vs aperture radius factor $r$ . . . . .	173
4.27	ARIEL noise budget for OOT observation of HD 219134. . . . .	175
4.28	ARIEL noise budget for OOT observation of HD 209458. . . . .	176
4.29	ARIEL noise budget for OOT observation of GJ 1214. . . . .	177
4.30	$N_{min}$ results from ExoSim final Phase A configuration simulations. . . . .	179
4.31	$X$ results from ExoSim final Phase A configuration simulations. . . . .	180
5.1	KU Leuven pulsation and granulation model. . . . .	185

5.2	Timeline of proportional variations in the signal of GJ 1214 due to stellar convection. . . . .	187
5.3	Stellar convection noise contribution for OOT observation of HD 209458. . . . .	188
5.4	Stellar convection noise contribution for OOT observation of GJ 1214. . . . .	189
5.5	Effects of occulted and unocculted spots on the transit depth. . . . .	195
5.6	SpotSim: the dedicated ExoSim star spot simulator. . . . .	202
5.7	Mean facular area vs mean spot area for the Sun. . . . .	206
5.8	Power law Q factor prediction for different spot coverages. . . . .	207
5.9	Spot temperature contrast vs star temperature. . . . .	208
5.10	Example light curves from SpotSim-ExoSim showing the effects of spots and faculae. . . . .	210
5.11	Monte Carlo simulations for HD 209458b and GJ 1214b with photon noise only. . . . .	216
5.12	Monte Carlo simulations for HD 209458b with spots only, at different spot filling factors. . . . .	217
5.13	Monte Carlo simulations for HD 209458b with spots and faculae, at different spot filling factors. . . . .	218
5.14	HD 209458b: $\sigma_{cr}$ vs wavelength from spots only, spots and faculae and photon noise only. . . . .	219
5.15	HD 209458b: ratio of $\sigma_{spot}$ to $\sigma_{photon}$ vs wavelength. . . . .	220
5.16	HD 209458b: $\sigma_{spot}/\sigma_{photon}$ vs spot filling factor, for each ARIEL channel. . . . .	221
5.17	Monte Carlo simulations for GJ 1214b with spots only, at different spot filling factors. . . . .	222
5.18	Monte Carlo simulations for GJ 1214b with spots and faculae, at different spot filling factors. . . . .	223
5.19	GJ 1214b: $\sigma_{cr}$ vs wavelength from spots only, spots and faculae and photon noise only. . . . .	224
5.20	GJ 1214b: ratio of $\sigma_{spot}$ to $\sigma_{photon}$ vs wavelength. . . . .	225
5.21	GJ 1214b: $\sigma_{spot}/\sigma_{photon}$ vs spot filling factor, for each ARIEL channel. . . . .	226
5.22	Potential issues with correction for unocculted spots. . . . .	237
6.1	TRAPPIST-1 system of seven terrestrial planets. . . . .	240

6.2	ZAMS habitable zone and tidal lock limit. . . . .	242
6.3	Pointing jitter power spectral density profile for TRAPPIST-1. . . . .	247
6.4	Testing for correlated noise in NIRSpec by time averaging. . . . .	251
6.5	ARIEL noise budget for OOT observation of TRAPPIST-1. . . . .	252
6.6	Scale heights for each planet for a $\mu = 28.97$ g/mol atmosphere. . . . .	255
6.7	Median $A_{se}$ for each planet in Ch0 and Ch1. . . . .	257
6.8	Planet b: $N_{transits}$ vs mean molecular mass of atmosphere. . . . .	258
6.9	Planet c: $N_{transits}$ vs mean molecular mass of atmosphere. . . . .	259
6.10	Planet d: $N_{transits}$ vs mean molecular mass of atmosphere. . . . .	260
6.11	Planet e: $N_{transits}$ vs mean molecular mass of atmosphere. . . . .	261
6.12	Planet f: $N_{transits}$ vs mean molecular mass of atmosphere. . . . .	262
6.13	Planet g: $N_{transits}$ vs mean molecular mass of atmosphere. . . . .	263
6.14	Planet h: $N_{transits}$ vs mean molecular mass of atmosphere. . . . .	264
6.15	Median $N_{transits}$ and IQR for limiting channel vs mean molecular mass for each planet. . . . .	265
A.1	ExoSim Zodiacal light model vs Leinert et al. (1998). . . . .	290
A.2	Intensity of zodiacal light as a function of ecliptic latitude from two studies. . . . .	292
A.3	Relative intensity of zodiacal light versus ecliptic latitude. . . . .	292
A.4	IR-FIX aperture in relation to spacecraft U2 and U3 axes. . . . .	293



# CHAPTER 1

## INTRODUCTION

---

---

**E**XOPLANET transit spectroscopy is an observational technique that has been used to obtain the first atmospheric spectra of distant worlds. Thus far, only a small proportion of the thousands of known exoplanets have been studied spectroscopically. The technique, together with its eclipse spectroscopy variant, remains highly challenging due to the tiny atmospheric signals and its time domain nature, making it particularly vulnerable to noise and systematics. Mitigation of noise and detrending of systematics is thus essential where possible. Accurate assessment of the effects of noise and systematics is crucial to the proper representation of the final uncertainties on the reconstructed planet spectrum, the confidence of various model atmosphere fits to the data, and the final scientific conclusions. However it is often difficult to accurately elucidate the effects of complex noise sources, both instrumental and astrophysical, on the final data. This impacts both the understanding of the predicted performance of new instruments, as well as the uncertainties that are assumed in studies from existing instruments. One way to better assess the effects of complex noise at the system level is to use a time domain simulator that can model the astrophysical scene, the optical system and all noise sources including time-correlated noise and time-dependent systematics. Such a simulator could be used to address a wide variety of signal and noise problems within this field such as the effects of stellar variability, the performance of new instruments, the effects of complex instrumental noise sources, and the feasibility of observations. In this introductory chapter, I review the field of exoplanet research and transit spectroscopy. This is then followed by a discussion of signal and noise. The case for a generic transit spectroscopy simulator is then presented.

## 1.1 TRANSIT SPECTROSCOPY AND EXOPLANETS

### 1.1.1 EXOPLANETS

#### 1.1.1.1 THE DIVERSITY OF EXOPLANETS

In the 1990s, the first exoplanets were discovered, beginning with the planets around the pulsar PSR1257 + 12 (Wolszczan & Frail, 1992) using pulsar timing variations, and later the first planet discovered around a main sequence star, the hot Jupiter 51 Pegasi b (Mayor & Queloz, 1995), discovered through radial velocity measurements of the host star. The first detection using the transit photometry technique was the hot Jupiter HD 209458 b around its Sun-like star (Charbonneau et al., 2002). Radial velocity and transit photometry have been the two most prolific methods for discovering exoplanets. Other methods that have led to new discoveries include direct imaging, gravitational microlensing, transit timing and transit duration variations, reflection/emission modulations and relativistic beaming. The Gaia spacecraft is expected to make thousands of discoveries through the astrometric method<sup>1</sup>.

Early discoveries were strongly biased towards gas giants at close distances to the host star, i.e. hot Jupiters, that gave the best signals in both radial velocity and transit photometry. With improved techniques and sensitivity, many new discoveries from ground-based transit and radial velocity surveys, such as WASP and HARPS, and the results from pioneering space-based transit surveys by Corot and Kepler, our picture of the statistical distribution of exoplanets has changed dramatically. Kepler in particular has revolutionized the field with thousands of new discoveries. Today over 3000 planets are confirmed, which appear to follow a smooth size distribution ranging from sub-Earth-sized to super-Jupiters, encroaching on the size of brown dwarfs. Although the data are still biased towards planets at smaller semi-major axes (Figure 1.1), we now know that smaller rocky planets are far more numerous than gas giants (Figure 1.2). This large diversity of planet sizes and masses include so-called 'transitional' planets, super-Earths and mini-Neptunes, not seen in our Solar System. A wide range of bulk densities have also been found from the inflated hot Jupiters to the extremely dense Kepler 10c which is  $17 M_{\oplus}$  in mass, and only  $2 R_{\oplus}$  in radius. There is also a wide range of temperatures and orbital parameters, including many in highly eccentric orbits.

---

<sup>1</sup> By using the astrometric method, Gaia will be most sensitive to detecting long period planets at large separations from the host stars. It will therefore be complimentary to radial velocity and transit surveys which are biased towards detecting shorter period planets.

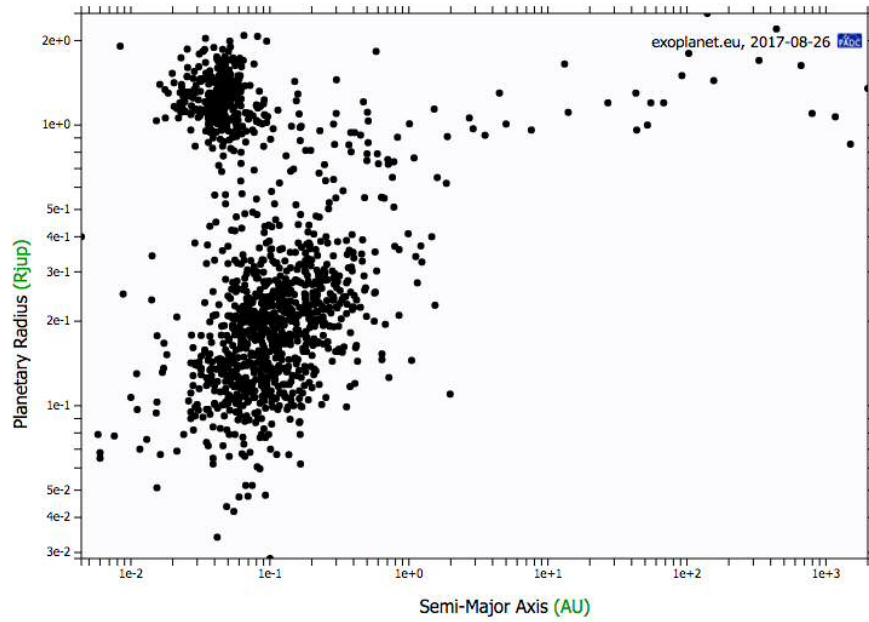


FIGURE 1.1 Current known exoplanets: radius vs semimajor axis, showing bias for planets close to the star. Figure from the 'Extrasolar Planets Encyclopaedia' (<http://exoplanets.eu/>).

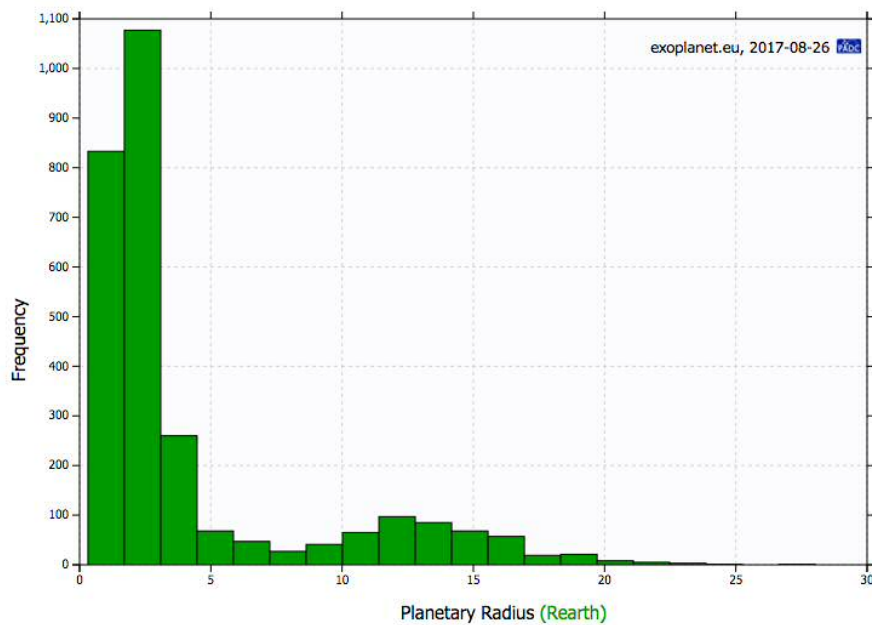


FIGURE 1.2 Current known exoplanets: number vs radius, showing that most exoplanets are Earth- to super-Earth-sized by radius. Figure from the 'Extrasolar Planets Encyclopaedia' (<http://exoplanets.eu/>).

Planets have been found around almost every type of star as well in binary systems. It is estimated that every star in the Milky Way has at least one planetary companion, giving over  $10^{12}$  planets in the Milky Way (Cassan et al., 2012; Batalha N. M., 2014). In the next few years thousands of new discoveries will be made especially from space-based transit photometry, with further results from Kepler in the K2 mission (Crossfield et al., 2016), the Transiting Exoplanet Survey Satellite (TESS) (Ricker et al., 2014) which will focus on all sky transits of bright and nearby stars, PLATO 2.0 (Rauer et al., 2014) that will expand the parameter space with longer period planets out to the habitable zones of G-type stars, and the CHaracterising ExOPlanet Satellite (Cheops) (Fortier et al., 2014) that will perform high precision photometry of mostly known targets. As mentioned above, the Gaia astrometry mission (Perryman et al., 2014) is also projected to discover thousands of new planets. Ground-based transit surveys include the Next Generation Transit Survey (NGTS) (Wheatley et al., 2017b), the Trans-atlantic Exoplanet Survey (TrES) (Alonso et al., 2007), TRAPPIST (Jehin et al., 2011) and MEarth (Irwin J. et al., 2008), and radial velocity surveys such as CARMENES (Quirrenbach et al., 2014) will also contribute many hundreds of new discoveries.

Characterizing, classifying and comprehending this diversity of planets is now a fundamental challenge. Characterising a planet begins with data on its size and mass from such discovery studies. The equilibrium temperature of the planet can also be calculated, and bulk density found for planets that have a combination of radius and mass measurements. Photometric phase curves can be used to produce longitudinal temperature 'maps' of the planet, e.g. for HD 189733b (Knutson et al., 2007). 2-D maps have been produced too from 'eclipse mapping' where the ingress and egress of the planet secondary eclipse are precisely measured, e.g. for HD 189733b (Majeau et al., 2012).

However a more complete characterisation includes probing the atmospheric structure and composition through spectroscopy. The atmospheric temperature will differ from the equilibrium temperature depending on the albedo and greenhouse effect (e.g the 30 K discrepancy between the equilibrium temperature and the atmospheric temperature of the Earth). Bulk density can be revealing in constraining to a first order the interior structure of an exoplanet to particular models (Figure 1.3). However many planets fall in ambiguous regions outside the lines represented by such models, such as highly inflated hot Jupiters and some super-Earths. A key example is the well-studied  $6.55 M_{\oplus}$  super-Earth GJ 1214 b, with a bulk density of  $1.9 \text{ g/mol}$ , which makes it consistent with multiple models including a rocky planet with an outgassed hydrogen-rich atmosphere, a mini-

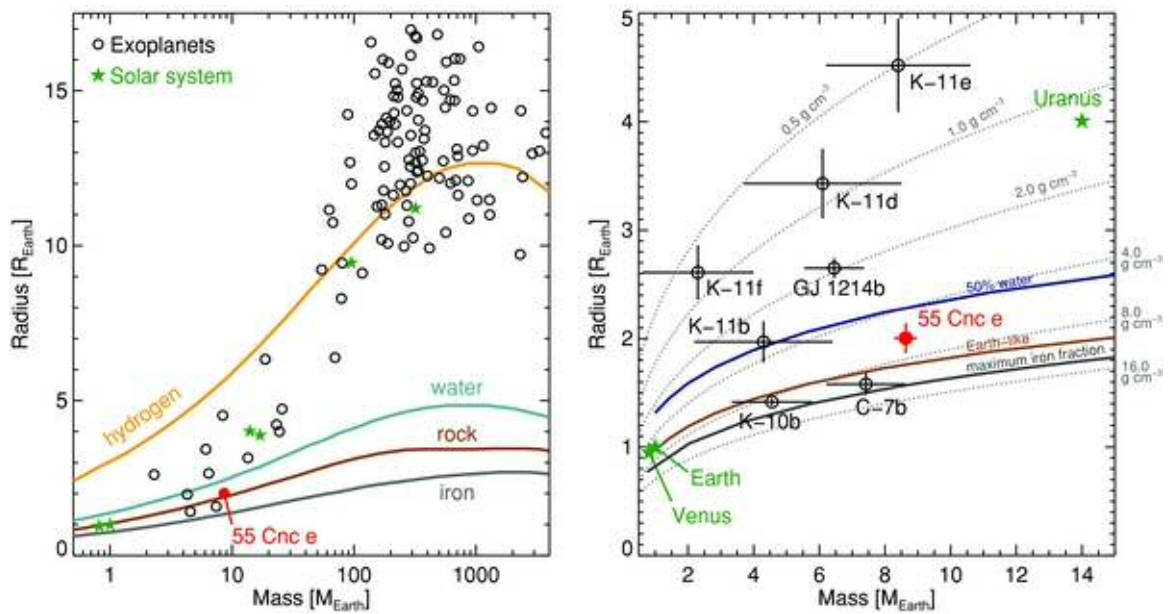


FIGURE 1.3 Planet radius vs mass for exoplanets showing that while some bulk densities constrain likely interior models, others (e.g. that for GJ 1214b) are ambiguous, requiring spectroscopy to break the degeneracy. Figure from Winn et al. (2011)

Neptune, or an ocean planet (Rogers & Seager, 2010).

Spectroscopic observations of exoplanets can break these degeneracies better constraining interior models (Rogers & Seager, 2010), especially in hot planets with less condensation and sequestration (Tinetti et al., 2016). Spectroscopy is also key to constraining the atmospheric composition, chemistry, temperature and vertical thermal structure. The elemental makeup of the planet may be found and compared to the star, providing clues to its formation and migration history.

### 1.1.1.2 FORMATION AND EVOLUTION

In the past decade models of planet formation and evolution have been developed but remain poorly constrained by observations. Planet formation is initiated within the disc of gas and dust surrounding the young active star (solar nebular hypothesis). The disc is composed of rocky materials, volatiles and gas. This circumstellar disc is subject to temperature and pressure gradients, extreme ultraviolet (EUV) radiation from the star and magnetic fields, resulting in physical and chemical variegation within the disc. Many proto-planetary discs have been observed directly (e.g. proplyds) or inferred through the infrared excess of the stellar spectral energy distribution (SED). Possible signatures of planet formation have been seen in such discs e.g. HL Tau (Akiyama et al., 2016).

It is thought that instability and turbulence sets up the initial conditions for planet formation, with formation occurring through one of 2 fundamental mechanisms: core accretion or gravitational instability. A planet with an elemental composition similar to its host star may indicate formation through gravitational instability, whereas core accretion is likely to show metal enhancement relative to the star. Gravitational instability is more favourable for gas giants at in the outer regions of high mass disks. Core accretion is required to explain rocky planets, but also favours gas giant formation in low mass disks.

The disk cools leading to formation of dust grains composed of rocky materials and volatiles. Various ice lines are hypothesised within the disc for volatiles e.g for water, CO<sub>2</sub> and CO, that will affect the local environment of the disc and the efficiency of accretion of grains forming from rocky material and ices. At the water ice line, the density of solid particles in the disk will increase, and cores will form faster, reaching the 10  $M_{\oplus}$  threshold that leads to runaway accumulation of hydrogen and helium forming a gas giant. Gas giants are therefore thought to form beyond this water ice line. The presence of hot Jupiters at orbits well within the ice line, and the fact that almost half of all known exoplanets orbit within 0.1 AU is strongly indicative of 'migration' mechanisms. Migration is thought to affect both small and large planets and could be due to interaction with the disc or between planets.

Smaller planets are thought to form in the inner disk within the ice line, from coagulation of purely rocky grains, followed by rocky planetesimal formation, runaway and oligarchic accretion and violent mergers, producing a few terrestrial planets. Volatiles may be added by late delivery towards the end of accretion, or may occur within the grains if the embryos form a mixture of materials from the inner and outer disc. The transitional planets may be the cores of evaporated gas planets that may or may not have retained the H<sub>2</sub>/He envelope (Super Earths) or gas giants that did not reach Neptune-size (mini-Neptunes).

Rocky planets may form secondary atmospheres from outgassing, modified by stellar and planetary processes. Forget & Leconte (2014) hypothesised various 'transitions' between different atmosphere types, from H<sub>2</sub>/He atmospheres, to volatile-dominated atmospheres (e.g. N<sub>2</sub>/CO<sub>2</sub>), to silicate (or absent) atmospheres, depending on planet mass and temperature (Figure 1.4). They also hypothesize extremely hot rocky planets of liquid silicate and silicate atmospheres, so-called 'lava' planets, of which 55 Cancri e or Corot 7b may be examples. Other unusual planets that have been hypothesised are 'ocean' planets, which are planets forming at the water ice line and then migrating inwards, containing vast amounts

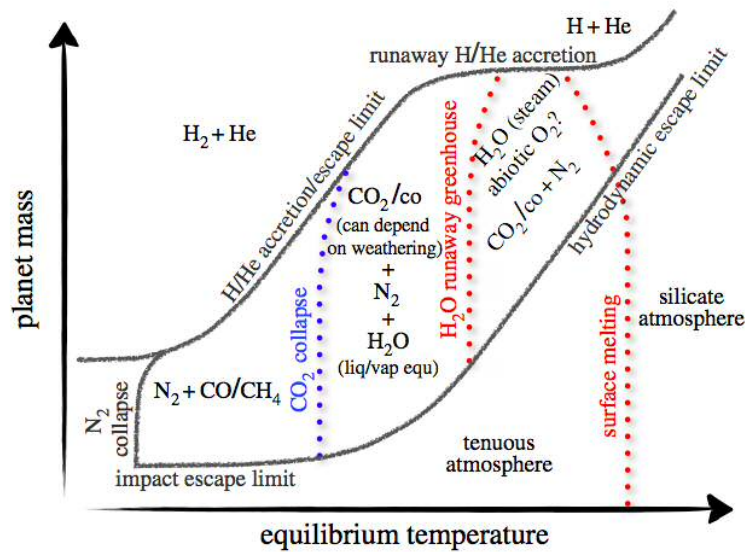


FIGURE 1.4 Theoretical scheme for the formation and evolution of different types of exoplanet atmosphere. Figure from Forget & Leconte (2014).

of water (Leger et al., 2004).

The metallicity of the host star appears to be higher than solar for hot Jupiters, but the trend is weaker for other planet types. Differences between the stellar and planet metallicities may give insight into planet formation mechanisms. The C/O ratio of a planet in particular may give insight into its formation and migration history. Due to the different ice line distances for water, CO<sub>2</sub> and CO, and varying fractions of gas and grains with distance in the disc, the C/O ratio of a planet could reflect its formation location (Figure 1.5).

Spectroscopy can potentially measure the C/O ratio and the planet's metallicity, providing constraints for formation and evolution theories. The chemical composition of the atmosphere will depend on many processes including the C/O ratio. The measurement of the chemical composition will also help to understand chemical processes in the atmosphere and whether they are consistent with thermochemical equilibrium or non-equilibrium processes such as transport-induced quenching or photochemistry. Spectroscopy can also provide information about the presence and types of clouds and Rayleigh scattering<sup>2</sup>.

<sup>2</sup> Clouds will typically result in 'flat' spectra, and Rayleigh scattering can manifest as a 'slope' in the NIR and visual range following its  $1/\lambda^4$  wavelength dependency.

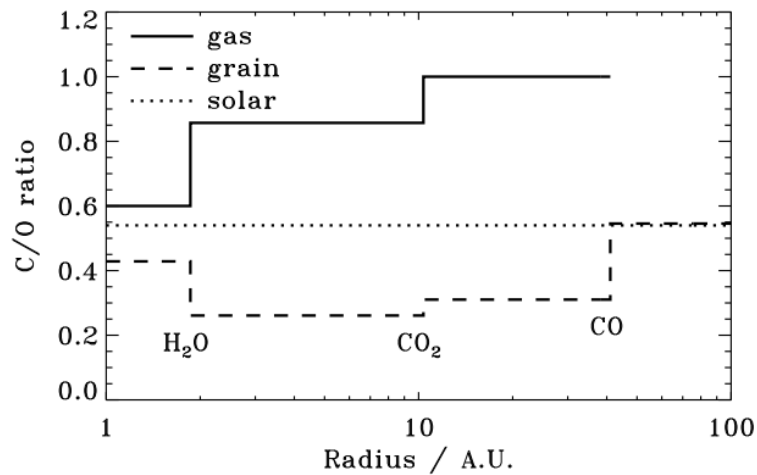


FIGURE 1.5 The C/O ratio of a planet may give an insight to its formation location, due to variation in gas-dust ratio and condensation lines for main molecules. Figure from Oberg et al. (2011) for a disk around a solar-type star.

### 1.1.1.3 HABITABLE PLANETS

Another goal in the field of exoplanets is the identification and characterisation of so-called 'habitable' planets, planets with the potential to host life. To a first order these are rocky planets in the 'habitable zones' of their host stars.

The so called 'habitable zone' around a star delineates the region where liquid water may be able to exist on the surface. It is a function of both the star and the planet, depending as it does on the insolation received by the planet and planetary factors such as albedo and the greenhouse effect that will modify the energy budget affecting the final planet temperature. For dimmer stars, the habitable zone is closer in, and at such distances tidal locking can occur that further influences the zoning, since tidally locked planets will have a higher equilibrium temperature than non-tidally locked planets. Definitions by Kasting et al. (1993) have been most widely adopted. Assuming terrestrial planets with H<sub>2</sub>O, CO<sub>2</sub> and N<sub>2</sub> atmospheres, they established various criteria defining the inner and outer limits of the habitable zone. The conservative zone is delimited by the so-called 'water loss' (inner) and '1st CO<sub>2</sub> condensation' (outer) limits, and the optimistic zone by the 'runaway greenhouse' (inner) and 'maximum greenhouse' (outer) limits. These have been recently revised by Kopparapu (2013).

The Planetary Habitability Laboratory<sup>3</sup> of the University of Puerto Rico at Arecibo, currently lists 13 terrestrial planets in conservative habitable zone, and

<sup>3</sup> <http://phl.upr.edu/>

an additional 39 within optimistic habitable zone. The nearest habitable planet is Proxima Centauri b at 1.3 pc, which unfortunately has not displayed any transits. Recently the TRAPPIST-1 system has yielded 7 transiting terrestrial planets (Gillon et al., 2017) of which four (planets d,e,f and g) are within the optimistic habitable zone of the parent M8 star. Petigura et al. (2013) used extrapolations from Kepler data to predict a frequency of about 0.22 for the frequency of Sun-like stars that have an Earth-sized planet in the habitable zone. For the more ubiquitous M-type stars, Kopparapu (2013) analysing Kepler data has projected the frequency of Earth-sized planets ( $0.5\text{-}1.4 R_{\oplus}$ ) in the conservative habitable zone of M-dwarf stars to be 0.48. Dressing & Charbonneau (2015) more recently project 0.56 Earth-sized planets ( $1\text{-}1.5 R_{\oplus}$ ) per M-dwarf star, and a frequency of 0.16 in the conservative habitable zone. Thus the number of potentially habitable planets is vast. The concept of the habitable zone can be challenged however as it does not take into account life emerging in liquid water from alternate heat sources such as planet internal thermal or tidal energy (as speculated for the subsurface oceans of Europa and other gas-giant moons) at distances well beyond the habitable zone boundary. In addition, many other factors will influence habitability including the space radiation environment, which may be harsh in the habitable zone of highly active M-dwarfs especially for planets lacking a magnetosphere (which may be more likely if the planet is tidally locked due to a relatively low planetary magnetic moment). The huge interest in habitable zone planets stems from the possibility of finding the signatures of life through biomarkers. For the Earth the main ones are  $\text{O}_2$ ,  $\text{O}_3$ ,  $\text{CH}_4$  and  $\text{N}_2\text{O}$  (Kaltenegger, 2011), and spectroscopy is the key technique for being able to realise this goal.

### 1.1.2 TRANSIT SPECTROSCOPY

Transit spectroscopy is an observational technique used to obtaining exoplanet atmosphere spectra. This technique was theorized by Seager & Sasselov (2000) and relies on measuring the transit light curve in primary transit (Figure 1.6) at different wavelengths, recovering the planet-star area ratio  $(R_p/R_s)^2$  at each wavelength. Differences in area ratio with wavelength constitute a 'transmission spectrum' and are attributed to modulation of the stellar photon flux by the atmosphere in terminator region. This can be due to absorption by atomic, ionic or molecular species, or scattering and absorption by hazes, clouds or Rayleigh scattering molecules. The signal and noise in transit spectroscopy are discussed in more detail in the next section.

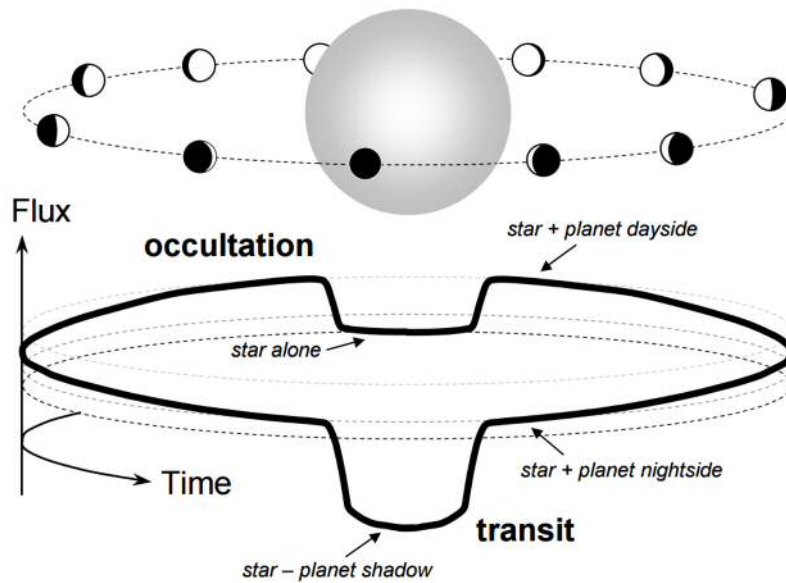


FIGURE 1.6 Variations in observed flux due to planet primary transit, secondary eclipse and phase curves. Figure from Winn (2010). In spectroscopy the transit or eclipse measurement is performed at multiple wavelengths.

Primary transit spectra can provide constraints on upper atmosphere column density, temperature and pressure, allow derivation of the scale height of the atmosphere and thus its mean molecular weight, probe scattering processes such as Rayleigh scattering through the slopes in the continuum, and constrain cloud top depths.

The method was first demonstrated by Charbonneau et al. (2002) who detected sodium in the atmosphere of the hot Jupiter HD 209458b, using the Hubble Space Telescope Imaging Spectrograph (STIS) instrument in the visual range. Using the same target and instrument, Vidal-Madjar et al. (2003) used the technique in the ultraviolet to detect atomic hydrogen absorption in the Lyman- $\alpha$  line<sup>4</sup>. A much stronger detection of sodium was found in the hot Jupiter HD 189733b using ground-based observations (Redfield et al., 2008). Potassium was also predicted in the atmosphere of hot Jupiters and subsequently detected using ground-based observations (Colón et al., 2012). Using the Hubble Advanced Camera for Surveys (ACS), Pont et al. (2008) first detected haze in the atmosphere of the hot Jupiter HD 189733 b. These early studies started to provide the first observation constraints for models of the upper atmospheres of hot Jupiters.

Subsequently studies using the Hubble and Spitzer space telescopes and

<sup>4</sup> The hydrogen is thought to exist in the exosphere caused by evaporation of the planet.

ground-based facilities, probed the near- and mid-infrared wavelength ranges which encompass well-characterised ro-vibrational signatures for neutral molecular species, including those of interest for exoplanet atmospheres such as H<sub>2</sub>O, CH<sub>4</sub>, NH<sub>3</sub>, CO<sub>2</sub>, CO and various hydrocarbons (Figure 1.7). Lower resolution can be also used in the infrared to detect such signals as the features are broader compared to the narrow cores of alkali metals in the visual range that required medium to high resolutions. Early molecular detections made in the infrared included H<sub>2</sub>O (Tinetti et al., 2007; Swain et al., 2008) and CH<sub>4</sub> (Swain et al., 2008) in HD 189733b. The detection of H<sub>2</sub>O in hot Jupiters is prolific: Deming et al. (2013) and Mandell et al. (2013) published the detection of H<sub>2</sub>O in five hot Jupiters using a variety of instruments including the Hubble Wide Field Camera 3 (WFC3). The water content of hot Jupiters has been found to be highly variable with Sing et al. (2016) finding a range of water abundances in a series of 10 hot Jupiter primary transit spectra. They find this is consistent with varying amounts of clouds and hazes rather than levels of water depletion in the disc at the time of formation.

More recently a number of flat infrared transmission spectra have been obtained, e.g. for the super Earth GJ 1214b (Kreidberg et al., 2014a) and the warm Neptune GJ 436 b (Knutson et al., 2014a), many of which have been observed with the Hubble WFC3 infrared (IR) instrument. Flat spectra indicate either high molecular weight atmospheres, with reduced spectral amplitude, or possibly the presence of high altitude clouds or hazes that truncate spectral features.

A similar principle underlies secondary eclipse spectroscopy, where the star occults the planet, resulting in a fall in flux since the planet contribution to flux is removed producing an eclipse light curve (Figure 1.6). The light curve fractional transit depth gives ratio of the planet flux (emission and reflection) to the stellar flux ( $F_p/F_s$ ). When measured over multiple wavelengths, this gives the secondary eclipse spectrum, also known as the dayside emission spectrum. The near- to mid-infrared is the ideal range for secondary eclipse spectra as the planet black body flux peaks in this range giving the optimal values for  $F_p/F_s$ . Spectral features in the secondary eclipse spectrum can appear in absorption or emission, and since different wavelengths contribute to the emission from different levels in the atmosphere it may be possible to probe the vertical thermal structure.

Early secondary eclipse spectra detected H<sub>2</sub>O (Grillmair et al., 2008) using the Spitzer Infrared Spectrograph (IRS), and H<sub>2</sub>O, CO and CO<sub>2</sub> using Hubble NICMOS (Swain et al., 2009b), all in HD 189733b. Hubble NICMOS was also used to detect H<sub>2</sub>O, CH<sub>4</sub> and CO<sub>2</sub> in the secondary eclipse spectra of HD 209458b (Swain et al., 2009a). Temperature inversion was also initially suspected in HD 209458b

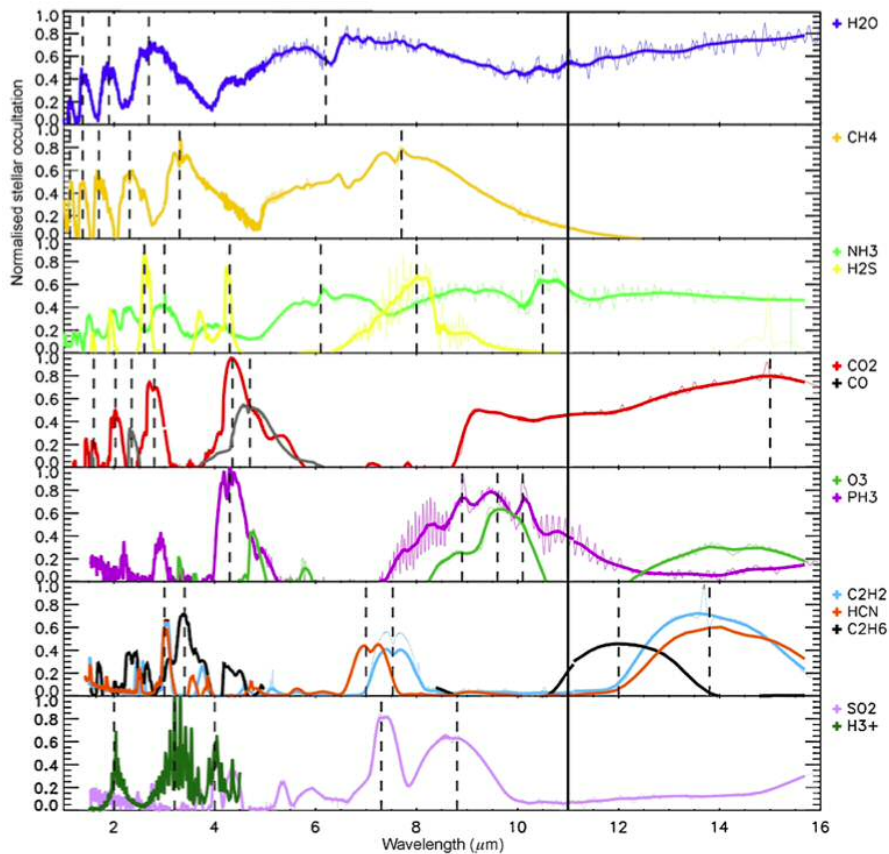


FIGURE 1.7 Molecular signatures in the 1-16  $\mu\text{m}$  range. The near- to mid-infrared wavelength range contains ro-vibrational spectral features for many molecules likely to be present in exoplanet atmospheres and is therefore key for transit spectroscopic characterisation of such atmospheres. Figure from Tinetti et al. (2013).

(Knutson et al., 2008) based on multi-wavelength broad band photometry with Spitzer, but a higher resolution study with Hubble WFC3 IR subsequently did not find evidence of an inversion (Line et al., 2016).

A recent more sophisticated variant, phase-resolved emission spectroscopy (Stevenson et al., 2014) has been performed that obtains the emission spectrum as function of planet phase and can map spatial changes in the temperature-pressure profile. This has the potential for better characterising the day-night variations in atmospheric structure and composition, and weather patterns.

The interpretation of the reconstructed planet spectra, in either primary transit or secondary eclipse, is usually based on comparison with atmospheric models from radiative transfer codes such as TauRex (Waldmann et al., 2015) or NEMESIS (Irwin P. G. J. et al., 2008). This may use a ‘forward model’ frequentist approach where, given assumptions about the atmosphere, a set of predicted

synthetic models are produced and stastically compared to the data. For example in Berta et al. (2012) for GJ 1214b, with its ambiguous bulk density, the spectrum obtained was compared to solar composition, 50 x solar metallicity<sup>5</sup> and water-dominated models. A second approach is to use atmospheric or spectral 'retrievals' where the model parameters are adjusted in a Bayesian framework until a maximum likelihood solution is obtained.

Today the number of planets studied with either spectroscopic or multi-band photometric spectra in transmission or emission remains below 100, a small fraction compared to the thousands of known planets. In addition, the vast majority of these are still hot Jupiters, with a small number of Neptune-sized, Super-Earth and Earth-sized planets. This reflects one of the challenges of transit and eclipse spectroscopy, where the atmospheric signatures being measured (i.e the modulations in the planet-star area ratio or flux ratio spectrum) are about an order of magnitude less than the transit depth itself, and where hot Jupiters provide the best signal-to-noise ratios (SNRs).

The 'Extrasolar Planets Encyclopaedia' database<sup>6</sup> currently lists 36 objects with claimed molecular and atomic detections or species inferred from atmospheric modeling. This list is reproduced in Table 1.1. The most massive 7 objects are all brown dwarfs. Of the remaining 29 planets, all are either sub-Jupiter-, Jupiter- or super-Jupiter-sized, except for the Neptune-sized GJ 436b, the super Earth 55 Cancri e, and the hot Earth-sized planet GJ 1132b.

We can see that the list includes many of the expected molecules seen in Solar System planets such as CO<sub>2</sub>, H<sub>2</sub>O, CH<sub>4</sub> and NH<sub>3</sub>, as well as more exotic species such as TiO and VO, and alkali metals predicted in the atmospheres of hot Jupiters. Not all the species listed are based on the detection of unambiguous spectral features. For example the O<sub>2</sub> on GJ 1132b, a hot (410 K) Earth-sized exoplanet transiting an M-dwarf (Schaefer et al., 2016), is inferred from a model that fits the tenuous atmosphere and assumptions about the surface conditions and atmospheric chemistry.

Indeed detection of spectral species has sometimes been controversial e.g. the 3.25  $\mu\text{m}$  non-LTE<sup>7</sup> CH<sub>4</sub> feature detected in the ground-based emission spectrum of HD 189733b by Swain et al. (2010) challenged due to subsequent non-detection by Mandell et al. (2011). Hansen et al. (2014) looked at 44 planets with broadband emission spectra, mostly obtained using Spitzer, and reassessed the

<sup>5</sup> Approximately equivalent to the ice giants in our solar system.

<sup>6</sup> <http://exoplanets.eu/>

<sup>7</sup> Local thermodynamic equilibrium.

uncertainties. They concluded that these had been underestimated in the original studies and that virtually all molecular detections and inferences about atmospheric structure including inversions were unreliable and were due to astrophysical and instrumental noise rather than molecular signals. More recently, Barstow et al. (2017) performed spectral retrievals on a set of 10 previously studied hot Jupiters finding little evidence for the presence of molecular absorbers other than H<sub>2</sub>O.

In a sense, while transit photometry has emerged from the early bias towards hot-Jupiters and now reveals the predominance of smaller planets, transit spectroscopy still remains in an era dominated by hot Jupiters. Among the many planets studied, certain planets have been studied in particular detail in multiple studies, such the hot Jupiters HD 209458b, HD 189733b and WASP 12b, and the super Earth GJ 1214b (an example of the 'M-dwarf advantage').

As well as the low amplitudes of the atmospheric signals and vulnerability to noise and systematics which we discuss in the next section, limitations to ground-based transit spectroscopy include the narrow wavelength bands available for infrared observations from the ground, which give space-based observatories the advantage for broad wavelength coverage. Ground-based observations also are also vulnerable to telluric contamination, added noise from atmospheric scintillation, and noise from instrument emission at longer wavelengths.

Many space-based instruments on Hubble and Spitzer have been used to obtain both transmission and emission spectra, but the wavelength ranges of individual instruments are very limited (e.g. 1.1-1.7  $\mu\text{m}$  on the Hubble WFC3 IR instrument with the G141 grism), or consist of a few photometric points (e.g. Spitzer MIPS, IRS and IRAC). Broadband coverage is desirable to break degeneracies between overlapping spectral bands from different species, between temperature structure and molecular signals in emission spectra, and to aid cloud diagnostics.

Observations from different instruments at different times are sometimes combined to produce spectra covering a wider wavelength range. However there may be inaccuracies due to instrument calibration and the effects of stellar variability between different observations when stitching together results from different instruments and studies this way. The upcoming James Webb Space Telescope (JWST) promises to provide the first continuous wavelength coverage from 0.6-28  $\mu\text{m}$  (Beichman et al., 2014) using a combination of instruments all capable of transit spectroscopy: NIRSpec (0.7-5  $\mu\text{m}$ ), NIRISS (0.6-2.5  $\mu\text{m}$ ), NIRCам (0.7-5  $\mu\text{m}$ ) and MIRI (5-28  $\mu\text{m}$ ). A dedicated transit spectroscopy space-based observatory, the Atmospheric Remote Sensing Infrared Exoplanet Large Survey (ARIEL), has

TABLE 1.1 Molecular and atomic ‘detections’ in exoplanets, as listed on the ‘Extrasolar Planets Encyclopaedia’ (<http://exoplanets.eu/>). Not all of these are true detections of spectral features, but may be inferred from modeling.

Name	Mass ( $M_J$ )	Radius ( $R_J$ )	Semi-major axis (AU)	Discovery year	Species
GJ 1132 b	0.0051	0.103	0.015	2015	O <sub>2</sub> , H <sub>2</sub> , N <sub>2</sub> , CO <sub>2</sub>
55 Cnc e	0.0263	0.178	0.016	2004	H <sub>2</sub> O, HCN
GJ 436 b	0.07	0.380	0.029	2004	CH <sub>4</sub> , H, CO <sub>2</sub> , CO, H <sub>2</sub> O
WASP-49 b	0.378	1.115	0.038	2011	Na
WASP-52 b	0.46	1.270	0.027	2011	Na
51 Peg b	0.47	1.900	0.052	1995	CO, H <sub>2</sub> O
WASP-31 b	0.478	1.537	0.047	2010	K
WASP-17 b	0.486	1.991	0.052	2009	O I, Na, C, K
HAT-P-1 b	0.525	1.319	0.056	2006	H <sub>2</sub> O, O I, K, C
WASP-80 b	0.554	0.952	0.035	2013	CH <sub>4</sub> , CO, Na, K, H <sub>2</sub> O, He, H
XO-2N b	0.62	0.973	0.037	2007	Na, K
HD 209458 b	0.69	1.380	0.047	1999	O <sub>2</sub> , VO, H <sub>2</sub> O, O I, CO <sub>2</sub> , Mg, CH <sub>4</sub> , NH <sub>3</sub> , Na, CO, K, H, H <sub>2</sub> , C, HCN, TiO
WASP-98 b	0.83	1.100	0.036	2013	TiO, VO
XO-1 b	0.9	1.184	0.049	2006	O I, C
HD 179949 b	0.92	1.050	0.045	2000	CO, H <sub>2</sub> O
WASP-19 b	1.114	1.395	0.016	2009	O I, C
HD 189733 b	1.142	1.138	0.031	2005	H <sub>2</sub> O, O I, CO <sub>2</sub> , CH <sub>4</sub> , CO, Na, H, C
WASP-121 b	1.184	1.865	0.025	2015	TiO, H <sub>2</sub> O, VO
WASP-12 b	1.404	1.736	0.023	2008	TiO, VO, H <sub>2</sub> O, O I, CO <sub>2</sub> , CH <sub>4</sub> , CO, H <sub>2</sub> , HCN, C
WASP-43 b	2.052	1.036	0.015	2011	CH <sub>4</sub> , NH <sub>3</sub> , C, CO, CO <sub>2</sub> , H <sub>2</sub> O, O I
HD 80606 b	3.94	0.921	0.449	2001	K
GJ 504 b	4	0.960	43.5	2013	CH <sub>4</sub>
tau Boo b	5.84	1.060	0.046	1996	H <sub>2</sub> O
HR 8799 b	7	1.200	68	2008	CH <sub>4</sub> , H <sub>2</sub> O, CO
beta Pic b	7	1.650	13.18	2008	H
ROXs 42B b	9	2.500	140	2013	H <sub>2</sub> O, CO, K
51 Eri b	9.1	1.110	14	2015	CH <sub>4</sub> , H <sub>2</sub> O
GU Psc b	11	1.350	2000	2014	CH <sub>4</sub>
Ross 458 (AB) c	11.3	1.070	1168	2010	CH <sub>4</sub> , H <sub>2</sub> O, H <sub>2</sub> , K
2M 2236+4751 b	12.5		230	2016	H <sub>2</sub> O, CO
WISE 0458+6434 b	13	1.009	5	2011	CH <sub>4</sub> , H <sub>2</sub> O
1RXS 1609 b	14	1.700	330	2008	H <sub>2</sub> O, CO, K
kappa And b	14	1.200	55	2013	H <sub>2</sub> O
WISE 1217+16 A b	22	0.960	7.6	2012	CH <sub>4</sub> , H <sub>2</sub> O, H <sub>2</sub>
GJ 570 D	42.5	0.855	1500	2000	NH <sub>3</sub>
GJ 758 b	45		44.8	2009	CH <sub>4</sub>

recently been proposed (Tinetti et al., 2016) that would perform the first large transit spectroscopy survey of exoplanets. Both these telescopes will greatly expand the database of atmospheric spectra addressing the big questions about the formation, evolution and diversity of exoplanets.

Although a more intuitive method, direct imaging for obtaining the reflection-emission spectra of exoplanets has thus far been restricted to larger, hotter planets in young systems at wide separations from the host star e.g, the multiple planet system of HR 8799 system (Marois et al., 2008). Such planets are atypical of Solar System planets or most exoplanets discovered. Direct imaging relies on suppression of the host star light using high-contrast imaging coronagraphs or nulling interferometry, and requires mitigation of wavefront distortions and suppression of residual speckles. A small number of directly imaged spectra have been obtained such as the featureless spectrum of HR 8799b (Bowler et al., 2010). Whereas the proportion of planets that can potentially be studied by transit spectroscopy is limited by the transit probability of planets<sup>8</sup> and also the frequency of transits, such factors are not an issue for direct imaging, although direct imaging will work best for face-on systems. Thus direct imaging may be the way forward for planets with long periods where the frequency of observations in the transit method will be low. An Earth-like planet in the habitable zone of a Sun-like star would be such a planet, however current direct imaging systems cannot achieve the required contrast of  $10^{-10}$ . A space-based telescope will probably be required to achieve this since ground-based telescopes are ultimately limited by residual errors from the mitigation of atmospheric turbulence via adaptive optics. WFIRST (Content et al., 2013), a 2.4-m telescope is a future space telescope planned for launch in the mid 2020s that will have a coronagraph that will be able to image Jupiter-, Neptune- and, possibly, super-Earth-sized planets around nearby stars.

## 1.2 SIGNAL AND NOISE IN TRANSIT SPECTROSCOPY

### 1.2.1 LIGHT CURVES

Transit and eclipse spectroscopy rely on high precision light curve measurements at multiple wavelengths as the exoplanet transits or is eclipsed by the star. Each light curve will have a characteristic transit depth, duration ( $T_{14}$ ) and ingress and egress periods ( $T_1 - T_2$  and  $T_3 - T_4$ ) (Figure 1.8)

<sup>8</sup>  $\sim R_s/a$ , where  $R_s$  is the stellar radius and  $a$  is the semi-major axis.

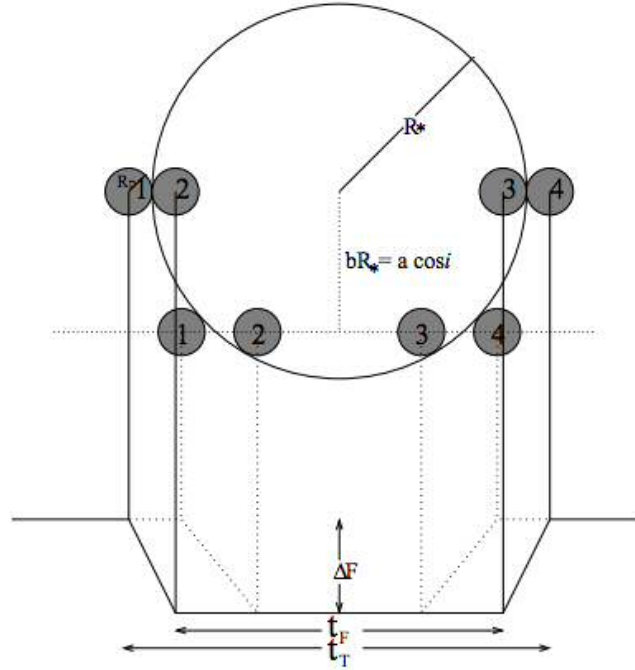


FIGURE 1.8 Light curve shape and duration as a function of impact parameter. The light curve can be considered in terms of regions defined by the contacts between the planet and star,  $T_1, T_2, T_3$  and  $T_4$  as shown. The light curve for a higher impact parameter,  $b$ , results in a shorter transit duration ( $T_{14}$ ) and longer ingress and egress times (dotted line), compared to the lower impact parameter (solid line). Figure from Seager & Mallén-Ornelas (2003).

In primary transit, in the absence of limb darkening, the transit depth divided by the out-of-transit (OOT) flux gives the ratio of the planet area<sup>9</sup> to the star area, i.e. the square of the radius ratio,  $(R_p/R_s)^2$ . The length of the transit (from first to last contact),  $L_t$ , is a function of increasing star and/or planet radius and decreasing impact parameter,  $b$ :  $L_t = 2\sqrt{(R_s + R_p)^2 - b^2}$ .  $b$  is a function of the inclination,  $i$ , and the semi-major axis,  $a$ :  $b = a \cos i / R_s$  (assuming a circular orbit).

The length of the ingress and egress decreases (and steepness increases) with decreasing  $R_p$ , increasing  $R_s$  and decreasing  $b$  (Figure 1.8). The transit duration,  $T_{14}$  is given by (Seager & Mallén-Ornelas, 2003):

$$T_{14} = \frac{PR_s}{\pi a} \sqrt{\left(1 + \frac{R_p}{R_s}\right)^2 - b^2} \quad (1.1)$$

where  $P$  is the period.

Thus not only the radius ratio can be recovered from the light curve but

<sup>9</sup> Assuming the entire planet area transits or is occulted.

also system parameters such as  $a/R_s$ ,  $i$  and  $P$ . The inclination allows the mass to be constrained from  $M_p \sin i$  (where  $M_p$  is the planet mass) which is obtained from radial velocity measurements.

In the presence of stellar limb-darkening the light curve will be modified with a more curved trough, since the star brightness is no longer uniform. With limb darkening, the ratio of the maximum transit depth to the OOT flux may be different to the actual area ratio causing this, and the shapes of the ingress and egress regions will be modified. Fitting a model light curve (normalized to the out-of-transit flux) that includes the effects of limb-darkening such as that by Mandel & Agol (2002), allows to the recovery of the matching radius ratio and system parameters.

In transit spectroscopy studies, the white light curve (which will have a higher SNR than the individual spectral light curves) is often used to find system parameters ( $a/R_s$ ,  $i$ ,  $P$  and the time of central transit), which are then fixed for the spectroscopic light curve fits, leaving  $R_p/R_s$ , the OOT flux and possibly limb darkening coefficients as free parameters.

In the absence of atmospheric absorption, the area and radius ratios in primary transit should be constant values with wavelength, although this can be complicated by the presence of star spots (as discussed in Chapter 5).

In eclipse spectroscopy the same principles apply except that limb-darkening is not a significant issue and the model light curves should be normalized to the mid-transit flux which gives the stellar flux level free of the planet emission and reflection contribution. The eclipse depth to out of eclipse flux ratio gives the ratio of the planet flux (in reflection and emission and at near full phase)  $F_p$  to the combined flux of the star and planet,  $F_s + F_p$ . Since  $F_p \ll F_s$ , this flux ratio is  $\approx F_p/F_s$ .  $F_p/F_s$  will have a wavelength dependency even in absence of any spectral features.

In this thesis, the term 'contrast ratio' will be used to describe the ratio of the observed change in flux in transit to the OOT observed flux. In secondary eclipse the contrast ratio is  $F_p(\lambda)/F_s(\lambda)$ . In primary transit the contrast ratio is  $R_p^2(\lambda)/R_s^2$  assuming no limb darkening. If limb darkening is considered, I will still use 'contrast ratio' to refer to the recovered area ratios, or the input area ratios used in simulations.

The final data product of a transit spectroscopy observation is a contrast ratio spectrum. Each point in the spectrum is the recovered fractional transit depth in a given wavelength bin (or photometric channel), with an associated experimental uncertainty (usually depicted as an error bar).

Unwanted signals can interfere with this light curve such as those from the effects of stellar variability and activity, or instrumental systematics. One of the challenges of this time domain technique is to accurately account for these effects.

### 1.2.2 SIGNAL

The signal-to-noise ratio (SNR) in transit or eclipse spectroscopy informs us of the ability to discern the presence of a variation in the contrast ratio spectrum. Such a variation may be a spectral feature due to absorption or emission, or a slope in the continuum due to scattering processes. Such variations alone may imply the presence of an atmosphere.

The 'signal' in this case is this variation (rather than the absolute value of the contrast ratio at any wavelength). I refer to this as an amplitude in the contrast ratio spectrum. This might be for example the amplitude of a specific spectral feature. The 'noise' is then the uncertainty on the measurement of that variation or amplitude.

#### 1.2.2.1 PRIMARY TRANSIT

In primary transit the contrast ratio spectrum gives the 'transmission spectrum' in absorption, of the planet's terminator region.

The baseline contrast ratio at any wavelength will be  $(R_p/R_s)^2$  due to the planet alone<sup>10</sup>, but an additional wavelength-dependent contribution comes from from the atmosphere. Per Tinetti et al. (2013), this additional contribution,  $A_{pt}(\lambda)$ , at any wavelength  $\lambda$  is given by:

$$A_{pt}(\lambda) = \frac{2 \int_0^{z_{max}} (R_p + z)(1 - e^{-\tau(z,\lambda)}) dz}{R_s^2} \quad (1.2)$$

where  $z$  is the altitude above  $R_p$  and  $\tau$  is the optical depth. The latter is given by:

$$\tau(z, \lambda) = \sum_i \tau_i(z, \lambda) \quad (1.3)$$

where  $i$  is an absorbing species.  $\tau_i(z, \lambda)$  is given by:

$$\tau_i(z, \lambda) = 2 \int_0^{l(z)} \rho(z') \chi_i(z') \sigma_i(\lambda, T) dl \quad (1.4)$$

<sup>10</sup> For gas giants the planet radius may be defined as the 1-10 bar pressure level.

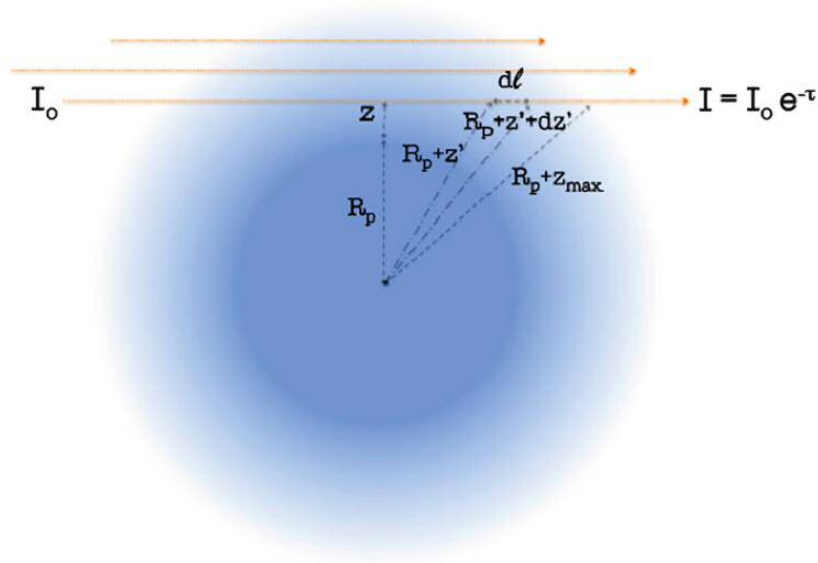


FIGURE 1.9 Geometry of transit spectroscopy. Figure from Tinetti et al. (2013).

where  $l$  is the path taken by stellar photons at the height  $z$ ,  $\rho$  is the column density,  $\chi_i$  is the mixing ratio,  $\sigma_i$  is the absorption coefficient,  $T$  is the temperature,  $z'$  is the value of  $z$  for the length element  $dl$ , and  $l(z) = \sqrt{(R_p + z_{max})^2 - (R_p + z)^2}$  (Figure 1.9).

Per Berta et al. (2012), the atmospheric contribution with wavelength can be simplified to:

$$A_{pt}(\lambda) \approx n_H(\lambda) \frac{2(R_p H)}{R_s^2} \quad (1.5)$$

where  $n_H(\lambda)$  varies with the opacities involved and can range from 1-10 depending on the strength of features and  $H$  is the planet atmospheric pressure scale height.  $H$  is given by:

$$H = \frac{kT_p}{\mu g} \quad (1.6)$$

where  $k$  is Boltzman's constant,  $T_p$  is the planet mean atmospheric temperature,  $\mu$  is the mean molecular mass and  $g$  is the surface gravity.

Figure 1.10 illustrates how the atmospheric contribution results in an additional contribution to the transit depth that varies with wavelength, while the planet contribution is constant. This gives the variations in the contrast ratio spectrum that might indicate a spectral feature. These variations in the transit depth are at least an order of magnitude lower than the transit depth itself, making transit spectroscopy that much more challenging than obtaining a single photometric

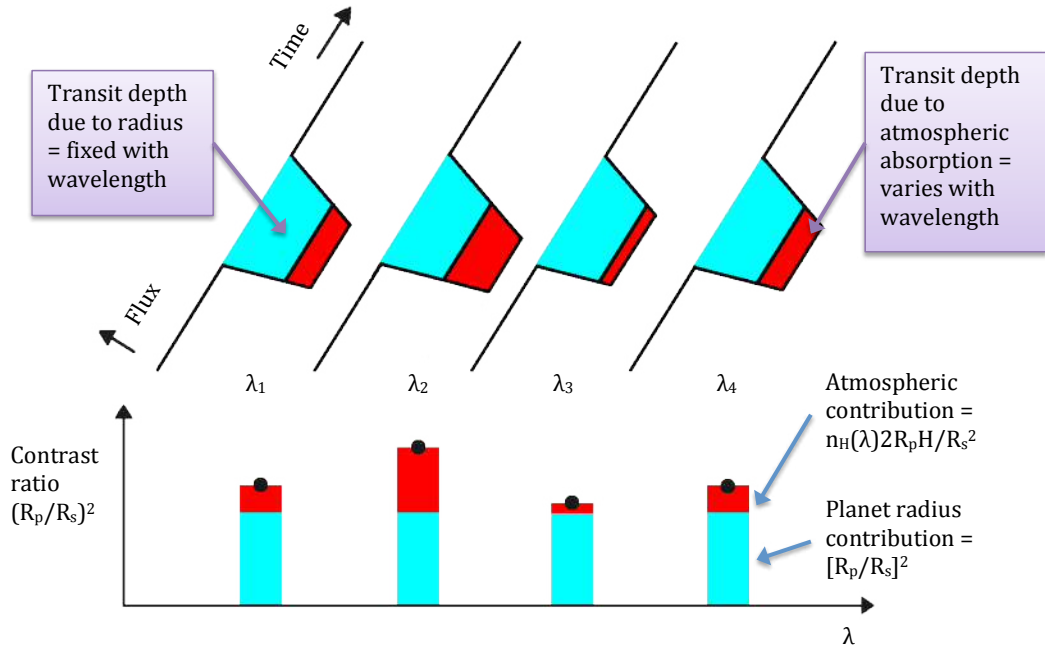


FIGURE 1.10 The primary transit contrast ratio spectrum caused by wavelength-dependent variations in atmospheric absorption. The contrast ratio at any wavelength is the combination of a planet component that is fixed and the atmospheric component that can vary.

transit measurement.

A further approximation (Tinetti et al., 2013) gives a nominal measure of a potential atmospheric signal,  $A_{pt}$ , by assuming the atmosphere causes complete absorption of star light over 5 scale heights:

$$A_{pt} \approx \frac{2(R_p 5H)}{R_s^2} \quad (1.7)$$

This gives an estimate of the maximum variation or amplitude in the contrast ratio spectrum due to a spectral feature during transit.

The transit atmospheric signal therefore increases with larger scale height, which in turn increases with higher mean planetary atmospheric temperature, lower planet gravity and lower mean molecular weight. The atmospheric signal also improves with larger  $R_p$  (increasing the inner and outer radii of the atmospheric annulus) and lower  $R_s$ . Using Equation 1.7 we obtain a value for  $A_{pt}$  for the hot Jupiter HD 209458b of  $7.70 \times 10^{-4}$  (770 parts per million [ppm]) for a  $H_2$ -He atmosphere with  $\mu$  of 2.22 g/mol. This is considered a strong signal.

For the Earth around the Sun,  $A_{pt}$  becomes  $1.11 \times 10^{-6}$  (1.1 ppm) assuming  $\mu$  of 28.97 g/mol, which is clearly much weaker. This shows the enormous difference in atmospheric signals between a hot Jupiter with a 'primordial' H<sub>2</sub>-He atmosphere, and a temperate terrestrial-sized planet with a high molecular weight secondary atmosphere. If we move the Earth into the habitable zone of the M-dwarf star Proxima Centauri,  $A_{pt}$  improves to  $5.65 \times 10^{-5}$  (56.5 ppm). For super-Earths, especially hotter ones, the signal will be higher still around an M-dwarf. This demonstrates the so-called 'M-dwarf advantage', where both transit and radial velocity signals are higher around smaller stars. Compared to larger stars, the transit probability for the habitable zone also increases, as well as the frequency of transits, permitting the combination of many observations to improve SNR.

#### 1.2.2.2 SECONDARY ECLIPSE

In secondary eclipse, the contrast ratio spectrum gives the emission and reflection spectrum of the planet 'dayside',  $(F_p/F_s)(\lambda)$ . There will be a wavelength-dependency to this spectrum even in the absence of any atmospheric absorption. Spectral features in absorption or emission are discerned as variations or amplitudes from this baseline. Thus a nominal atmospheric signal can be considered where there is complete absorption of the planet flux at a particular wavelength, resulting in an amplitude,  $A_{se}(\lambda)$ , which would be equal to  $(F_p/F_s)(\lambda)$ .

The planet flux will consist of a thermal emission component (strongest in the infrared) and a reflected component (strongest in the visual wavelength range).  $A_{se}(\lambda)$  can be estimated as:

$$A_{se}(\lambda) = \frac{B_\lambda(T_p)}{B_\lambda(T_s)} \left( \frac{R_p}{R_s} \right)^2 + \rho \left( \frac{R_p}{a} \right)^2 \quad (1.8)$$

where the first term on the RHS is the planet emission and the second term is the reflected component, both at full phase.  $B_\lambda(T_p)$  is the Planck function for the planet,  $B_\lambda(T_s)$  is the Planck function for the star,  $\rho$  is the geometric albedo and  $a$  is the semi-major axis.

This shows that higher planet temperatures and larger planet radii, with lower stellar temperatures and radii will produce stronger secondary eclipse signals. Assuming an albedo of 0.3, for HD 209458b this gives a signal at 2  $\mu\text{m}$  of  $1.96 \times 10^{-4}$  (196 ppm). However for the Earth around the Sun, we obtain a signal of just  $5.44 \times 10^{-10}$ .

### 1.2.3 NOISE

#### 1.2.3.1 SNR

The uncertainty on the contrast ratio in any spectral bin can be approximated by:

$$\sigma_{cr} = \sqrt{2} \frac{\sigma_{oot}}{S_{oot}} \quad (1.9)$$

where  $S_{oot}$  is the total OOT observed flux in a period equal to the transit duration, and  $\sigma_{oot}$  is the noise on this flux. This formula assumes an equal amount of time observed in- and out-of-transit.

In the formalism by Rauer et al. (2011) (their Equation 16)<sup>11</sup> the SNR for a primary transit atmospheric signal,  $A_{pt}$ , is given by

$$SNR_{A_{pt}} = SNR_{oot} \frac{A_{pt}}{\sqrt{2}} \quad (1.10)$$

where  $SNR_{oot}$  is the SNR of the out-of-transit stellar signal,  $S_{oot}$ . This is the same as saying:

$$SNR_{A_{pt}} = \frac{A_{pt}}{\sqrt{2} \sigma_{oot} / S_{oot}} \quad (1.11)$$

In other words the noise on  $A_{pt}$  is:

$$\sigma_{A_{pt}} = \sqrt{2} \frac{\sigma_{oot}}{S_{oot}} \quad (1.12)$$

This approximation again assumes an equal amount of observing time in and out-of-transit, and returns a result equal to  $\sigma_{cr}$  above.

Similarly in secondary eclipse per Rauer et al. (2011) (their Equation 3):

$$SNR_{A_{se}} = SNR_{oot} \frac{A_{se}}{\sqrt{2}} \quad (1.13)$$

This is the same as saying:

$$SNR_{A_{se}} = \frac{F_p / F_s \sigma_{oot}}{\sqrt{2} S_{oot}} \quad (1.14)$$

So the noise on  $A_{se}$  is:

$$\sigma_{A_{se}} = \sqrt{2} \frac{\sigma_{oot}}{S_{oot}} \quad (1.15)$$

<sup>11</sup> I have changed some of names of the variables used in that paper for consistency.

Note that in primary transit the above noise estimate assumes that the atmospheric component acts as an independent signal modulating the stellar light curve. In reality, as shown in Figure 1.10, it is additional component to the transit caused by the planet radius. This means that in practice, detecting an amplitude such as  $A_{pt}$  due to a spectral feature requires measuring the *difference* between the contrast ratios in at least 2 spectral bins. Thus the SNR here could be described as a contrast-to-noise ratio (CNR). Since each bin will have its own independent uncertainty, the uncertainty on  $A_{pt}$  should be higher than (upto  $\times\sqrt{2}$ ) the estimate given above. This also applies to the secondary eclipse amplitude estimate. It appears more common in the literature to just consider the noise on the amplitude of a feature to be that in the individual spectral bin than for the difference with some continuum value, e.g. Rauer et al. (2011) as above, the ‘individual bin method’ of Tessenyi et al. (2013), and the method used for SNR calculations in the ESA Radiometric Model (Puig et al., 2015; Zingales et al., 2017). However Belu et al. (2011) (their Equation 2) calculates SNRs for spectral features where the noise is  $\sqrt{4}$ x the quadrature sum of individual noises. This appears to be taking into account the extra  $\sqrt{2}$  for the uncertainty on the difference between two spectral bins ( $\sqrt{2} \times \sqrt{2}\sigma_{oot}/S_{oot}$ ). Thus the exact definition of ‘SNR’ and how it is calculated may vary somewhat between different authors. If the amplitude due to the atmospheric signal,  $A_{pt}$ , due to a spectral feature, is measured as the difference between the contrast ratio in a spectral bin with noise on the contrast ratio of  $\sqrt{2}\sigma_{oot}/S_{oot}$  and a well-constrained continuum, the latter may have a much smaller uncertainty, and  $\sigma_{A_{pt}}$  will approach  $\sqrt{2}\sigma_{oot}/S_{oot}$  as in the above equations. This may be implied in Rauer et al. (2011) who state that the SNR calculated is ‘conservative compared with the continuum flux region’. These types of calculation are used for feasibility studies, e.g. the ARIEL Mission Reference Sample (Zingales et al., 2017).

In such feasibility studies, a goal SNR for detection of a spectral feature needs to be defined. Rauer et al. (2011) and Tessenyi et al. (2013) have used threshold SNRs of 3 for example. If  $N$  independent transit observations are combined the noise should fall by  $\sqrt{N}$ , so that if the if  $SNR_1$  is the SNR achieved in 1 transit then the number of transits to achieve the threshold SNR,  $SNR_{goal}$ , is given by:

$$N_{transits} = \left( \frac{SNR_{goal}}{SNR_1} \right)^2 \quad (1.16)$$

I adopt this approach in Chapter 6 to assess the feasibility of observing the Earth-sized TRAPPIST-1 planets with the ARIEL spacecraft.

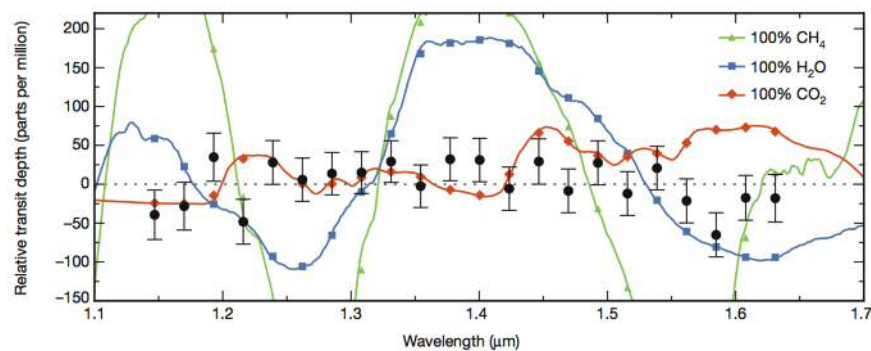


FIGURE 1.11 The transmission spectrum of GJ 1214b from Kreidberg et al. (2014a). Data points have 1 sigma error bars shown. The different forward models are compared with the data through the  $\chi^2$  statistic. The models shown are all rejected at high confidence, and the data is most consistent with a flat spectrum indicating clouds. The size of the error bars is crucial to the rejection of the various models. Figure from Kreidberg et al. (2014a).

### 1.2.3.2 RANDOM AND SYSTEMATIC ERRORS

The final result of a transit spectroscopy study is a transmission spectrum giving the planet-star area ratio (or some derivative such as the radius ratio or relative transit depth), e.g. Figure 1.11, or an emission spectrum of the planet-star flux ratio with wavelength in the case of secondary eclipse spectroscopy. The figure shows the importance of the error bars in the final spectrum, which directly affect the rejection or acceptance of the various hypothetical models. Accurate assessment of the final uncertainty is thus crucial for correct scientific conclusions to be reached.

Transit and eclipse spectroscopic observations are particularly vulnerable to noise due to a) the tiny atmospheric signals as described above, b) the division of the photometric transit into multiple spectral bins reducing the SNR per light curve compared to the white light curve, and c) the time domain nature of the observation, such that it is particularly sensitive to time-correlated noise. In addition, the observations are vulnerable to unwanted signals distorting the light curve such as time-dependent instrument systematics. Photometric stability is required over period of the order of hours at a level below the expected contrast ratio modulations (on the order of 10s to 100s ppm). The final data points on the contrast ratio spectrum, and the final uncertainties on those points will be subject to the ensemble effects of multiple sources of random and systematic errors.

A random error results in random noise, a statistical fluctuation that affects the precision of the measurement. Random error sources can occur within the

instrument or external to the instrument. A systematic error is usually considered to be an instrumental effect that biases the measurement (which can occur in a time-dependent manner) from the true value and affects therefore the accuracy of the measurement. The final uncertainty on the measured value is the range of values in which the true value is asserted to lie, and so should incorporate both the effect of random and systematic errors (that have not been corrected).

Random noise sources can be divided into uncorrelated (or 'white noise') and correlated noise, depending on their temporal behaviour. In the former case we assume zero values for the off-diagonal elements in the covariance matrix. This leads to simpler equations for  $\chi^2$ , maximum likelihood estimation and error propagation formulae. Random noise can arise from many different sources, each with its own characteristics. In the context of errors affecting transit spectroscopy observations, these can be divided into astrophysical (and/or atmospheric) and instrumental sources.

Astrophysical uncorrelated noise sources include the photon noise from the source which is a fundamental physical limit and obeys Poisson statistics ('shot noise') so that its standard deviation is the square root of the signal. The fractional photon noise (photon noise/signal) therefore falls with higher signals and longer integration times. Additionally there is shot noise contribution from the diffuse sky background. In space, this is principally the Solar System zodiacal dust. Astrophysical correlated noise includes stellar variations from granulations and pulsation, which are discussed more in Chapter 5. For ground-based telescopes there is in addition correlated noise from atmospheric scintillation due to turbulence.

Instrumental uncorrelated noise sources include read out noise (uncertainty in the conversion of charge in the on-chip amplifier to analogue voltage), reset noise<sup>12</sup> (due to random thermal motion of electric charge which results in a variation in charge when resetting the detector capacitor prior to readout), shot noise from dark current (thermally generated electrons in the detector) and shot noise from the thermal emission of the telescope common optics and the optical elements in the instrument (dichroics, mirrors and dispersive elements). Instrumental correlated noise sources include pointing jitter interacting with the detector non-uniformity.

Examples of systematics include include time-dependent PSF changes due to thermal breathing affecting the telescope focus, and time-dependent detector charge offsets due to persistence in infrared detectors, both of which are seen in the Hubble WFC3 IR instrument. To maximise accuracy and precision of the final

---

<sup>12</sup> Also known as "kTC noise" since it depends on temperature and sense node capacitance.

TABLE 1.2 Random and systematic error sources that can affect transit and eclipse spectroscopy observations.

Uncorrelated	Correlated	Systematic
Source photon noise	Pointing jitter (spectral, spatial)	Detector persistence
Dark current	Atmospheric scintillation	Crosstalk
Emission from optics	Electronics 1/f noise	Detector non-linearity
Zodiacal light	Stellar variability	Detector non-uniformity
Sky background		Geometric distortions
Read out noise		
kTC noise		

contrast ratio spectrum, random and systematic errors need to be mitigated where possible or otherwise accounted for fully in the final uncertainty. Mitigation occurs either at the hardware level, through design and effective calibration, or the level of observational strategy and data reduction methods.

Random noise can be mitigated depending on the noise source, e.g. reducing photon noise by longer integration times, cooling detectors to reduce dark current noise, or removing kTC noise in post-processing using correlated double sampling (CDS). Correlated random noise can in some situations be monitored and reduced through decorrelation. This would include scintillation noise decorrelation by monitoring other stars, and by adaptive optics, or decorrelation of pointing jitter.

Systematics if detected can be detrended from the data. Examples of such corrections include modeling the systematic, such as the parametric model for the time-dependent Hubble WFC3 IR persistence ‘ramp’ which distorts the light curve (Berta et al., 2012). Alternatively comparison data can be used to detrend the systematic, such as the ‘divide-white’ method for the WFC3 IR ramp (Berta et al., 2012; Kreidberg et al., 2014a). More advanced methods such as Gaussian processes or principal components analysis can be applied to isolate the systematics or instrument state values. An error may result however from the systematic correction itself, e.g. after detrending the WFC3 IR ‘ramp’ systematic, Berta et al. (2012) add an error inflation factor of 1.22 to account for increased photometric uncertainty from the correction. Table 1.2 gives a list of some major types of noise and systematics that can be an issue in transit and eclipse spectroscopy.

### 1.2.3.3 UNCORRELATED NOISE

This is also known as ‘white’ noise, and has a flat power spectrum, with autocorrelation which is the Dirac delta function (infinite at separation zero, and zero everywhere else). Characteristics of white noise include that the standard error of the mean of a set of  $N$  data points is given by:

$$\sigma_N = \frac{\sigma}{\sqrt{N}} \quad (1.17)$$

where  $\sigma$  is the standard deviation of data (taken to be the uncertainty on the individual data points).

When fitting a model to data (e.g. a planet transit model to the data light curve) the aim is to minimize the  $\chi^2$  statistic (or maximise the likelihood). For uncorrelated noise:

$$\chi^2 = \sum_i \frac{(d_i - m_i)^2}{\sigma_i^2} \quad (1.18)$$

where  $d_i$  is the data,  $m_i$  the model, and  $\sigma_i$  is the uncertainty on the data. In a Bayesian model fitting framework such as Markov Chain Monte Carlo (MCMC), where the maximum likelihood estimate for the model parameters (e.g. the transit depth) is found through a random walk, a joint posterior distribution is obtained from which the uncertainty on any single parameter can be found through marginalisation (obtaining the width of the 1 sigma Bayesian credible region). This is often used to obtain the final experimental uncertainty on the transit depth. Sometimes a factor is applied to the noise term,  $\sigma_i$ , as a free parameter, adjusting the uncertainty on the individual data points to achieve a reduced  $\chi^2$  of unity.

### 1.2.3.4 CORRELATED NOISE

In correlated noise, each data point has some ‘memory’ of the previous data, the autocorrelation function is non-zero, and the power spectrum of the time series is not flat. ‘Red’ noise is a commonly used term to describe correlated noise but technically refers only to noise with a  $1/f^2$  power spectrum (also known as ‘brown’ noise). ‘Pink’ noise has a  $1/f$  power spectrum. The exact power spectrum of the noise may however be complex, without the specific behaviour of red or pink noise. As photon noise is ‘beaten down’ by integrating for longer periods, correlated noise sources may become a greater proportion of the total noise. Correlated noise must be properly accounted for, or if possible removed through decorrelation if the process that generates it is known and can somehow be monitored (e.g.

pointing jitter).

With correlated noise, the calculation of the standard error of the mean of  $N$  data points must now include covariance terms. From Pont et al. (2006):

$$\sigma_N = \sqrt{\frac{\sum_{i,j} C_{ij}}{N^2}} = \sqrt{\frac{\sigma^2}{N} + \frac{\sum_{i \neq j} C_{ij}}{N^2}} \quad (1.19)$$

where  $C_{ij}$  are the covariance coefficients between the  $i$ th and  $j$ th measurements,  $i$  and  $j$  indices cover the measurements taken during the transit, and  $\sigma$  is the standard deviation of data (the diagonal terms in  $C$  are assumed to all equal  $\sigma^2$ ). This shows that the standard error on the mean will be underestimated if the off-diagonal covariance terms are not included.

When fitting a parametric model through  $\chi^2$  minimisation,  $\chi^2$  is now defined more generally (assuming a linear model) as:

$$\chi^2 = (d - Ax)^T C^{-1} (d - Ax) \quad (1.20)$$

where  $d$  is the data vector,  $A$  is a matrix of linear equations,  $x$  is the model parameter vector and  $C$  is the covariance matrix. This collapses to the more common version of  $\chi^2$  if the off-diagonal terms in  $C$  are zero.

When maximising the likelihood function in an MCMC model fit in the presence of correlated noise, the uncertainties represented by the size of the Bayesian credible region will be underestimated if this more generalised version of  $\chi^2$  is not used. However obtaining the exact covariance matrix is not easy or straightforward. A number of methods have been suggested in the literature to deal with correlated noise.

In 'time-averaging' (Winn et al., 2008) the residuals of a light curve fit, are binned into  $M$  bins of  $N$  points. If the standard deviation of the unbinned residuals is  $\sigma$ , the error on the binned residuals,  $\sigma_{binned}$ , assuming white noise is:

$$\sigma_{binned} = \frac{\sigma}{\sqrt{N}} \sqrt{\frac{M}{M-1}} \quad (1.21)$$

A correction factor,  $\beta$ , is found which is the proportion by which the actual noise is higher than the predicted noise at a designated bin size. This factor is then applied to inflate the uncertainties either on the  $\chi^2$  term going into an MCMC fitting routine, or on the final uncertainties after MCMC.

A second method is the residual permutation Monte Carlo method, sometimes called the ‘prayer bead’ method (Gillon et al., 2007). Here, after finding the best fit model to the light curve, the uncertainty on the fitted parameter is obtained by obtaining the residuals, shifting these by a certain number of points, applying the shifted residuals to the model, and performing a new fit. This is repeated at different shifts, obtaining a distribution of transit depths and other parameters. In the presence of correlated noise the variance of this distribution will be higher than that obtained assuming uncorrelated noise, and the proportional change is used to apply an inflating factor to the final uncertainties.

Some methods attempt to estimate the covariance matrix,  $C$ , for the likelihood function, or otherwise take the correlations directly into account. These include sophisticated methods such as wavelet-based likelihood (Carter & Winn, 2009) where the likelihood function is calculated in a wavelet basis where the correlation between the wavelet coefficients is negligible (Cubillos et al., 2017), and Gaussian processes (Gibson et al., 2012) where a functional form of  $C$  is used. There is no consensus on which methods are best, though soundness of methods that inflate the uncertainties has been challenged by Cubillos et al. (2017).

## 1.3 THE CASE FOR A GENERIC TIME DOMAIN SIMULATOR

### 1.3.1 MOTIVATION

We have seen the importance of accurately capturing the ensemble uncertainty on the contrast ratio spectrum, and how this can be underestimated in the presence of correlated noise. Accurate representation of the error bars on the spectrum is important to reach the correct scientific conclusions.

When predicting performance of a future instrument or indeed an existing instrument for a given observation, modeling as accurately as possible all major sources of noise, including those that have complex behaviour in the time-domain, will lead to the most accurate assessment. The result of greatest interest is ultimately how these sources of noise and systematics will combine to affect the accuracy and precision of the final reconstructed contrast ratio spectrum.

To do this to the highest level of accuracy, a simulator needs to model the observation in an end-to-end manner, and must include models of the astrophysical scene (including the the modulation of the stellar spectrum during transit or

eclipse) and the optical system (telescope, instrument, detector) outputting a time series of images akin to a real observation. Like a real observation, these images will then need to be processed through a realistic data reduction pipeline to obtain the reconstructed contrast ratio spectrum. The simulator also needs to model the time domain, so that the impact of time-correlated noise and systematics can be captured. By mimicking the real observation all the way through to the construction of the emergent planet spectrum, the final uncertainties arising from the ensemble of error sources can be measured at level of the spectrum itself, ultimately the most important result. There is currently a paucity of transit spectroscopy simulation tools that can produce such a high fidelity time domain 'end-to-end' simulation.

Additionally, if such a simulator could be made 'generic', not hard-coded for any particular instrument, its versatility would be greatly enhanced, opening it up to address numerous and varied signal and noise issues in transit spectroscopy, and making it potentially applicable to many different instruments. There is currently no truly generic simulation tool available for end-to-end transit spectroscopy studies.

Simulation tools are usually considered 'prospective' in that they are used to predict feasibility or performance for future instruments, perhaps not yet built, often as part of the study and development phase. Whilst this is a key role it is also rather limited. A generic simulator however could also be applied to *existing* instruments such as the Hubble Space Telescope in a 'retrospective' manner opening up further applications. For example, by modeling the existing instrument and its noise sources, simulated observations can be used to replicate published observations. These can be repeated 100s or 1000s of times as a Monte Carlo simulation unlike the real observation, and the distribution of recovered transit depths compared to error bars on published data. Given the debate on whether errors are correctly accounted for, such simulations give an additional dimension to explore the validity of published data or the concerns over novel observing modes.

By simulating the time domain in small evolving steps (a numerical simulation) such a tool can be used to predict the effects of complex noise sources that cannot be accurately represented through analytic models (in contrast to simple noise sources such as the source photon noise). These will include correlated noise with complex time domain behaviour and multiple contributory factors. Examples of complex instrumental noise sources pertinent to transit spectroscopy observations are spacecraft pointing jitter and spatial scanning over a non-uniform detector (spatial scanning being used for many transit spectra studies on the Hubble WFC3 IR). Examples of complex astrophysical noise include the effects of stellar

granulations and pulsations on the light curve, and the effects of star spots, which have thus far been very difficult to quantify at the level of the final spectrum. We have seen how correlated noise sources and systematics can adversely affect the accuracy and precision of a transit spectroscopy observation and how they can be hard to quantify. Therefore such a generic time domain simulator can provide an additional facility to test the impact of such sources directly on the spectrum. By combining simulated observations with a data reduction pipeline incorporating noise mitigation methods such as decorrelation or detrending, the efficacy of such methods can be tested. If mitigation cannot be performed or is only partially successful, the simulation can tell us how much the noise source impacts and the added contribution to the final uncertainty.

The generic nature of the simulator can facilitate diverse functionality, such as simulation of ground- or space-based observatories, different observing modes, and variants of transit spectroscopy such as phase-curve spectroscopy.

Therefore fundamental to the uniqueness and versatility of such a novel simulator are its generic nature and its time domain simulation capability.

### 1.3.2 PREVIOUS SIMULATORS

Simple performance modeling tools, static or radiometric models, have been used to assess signal and noise in transit spectroscopy observations. These do not simulate the time domain directly but rely on static calculations and analytical expressions. An example is the ESA Radiometric Model (Puig et al., 2015) developed originally for the proposed Exoplanet Characterisation Observatory (EChO) mission. Radiometric models whilst fast and requiring no complex data reduction, may fail to capture accurately noise sources with complex time domain behaviour. Table 1.3 compares and contrasts the advantages and disadvantages of a dynamic time domain simulator of transit spectroscopy compared to a static model.

Previous time domain simulators for transit spectroscopy have been dedicated for particular missions and thus were not generic. This limited their applications and versatility. EChOSim (Pascale et al., 2015) was a time domain simulator developed for the EChO mission led by our group at Cardiff University. EChO would have performed a transit spectroscopy survey over near and mid infrared wavelengths from space. However EChOSim was limited in its capacity to be used for other instruments with EChO-specific features hard-coded into its algorithm. It also lacked versatility to applications beyond simply performing noise performance testing for EChO. Although EChOSim produced time series images, it did

TABLE 1.3 Dynamic versus static simulators.

Feature	Dynamic	Static
Uncorrelated noise	Simulates well	Simulates well
Correlated noise	Simulates well	Simulates poorly
Systematics	Simulates well	Simulates poorly
Transit light curve	Can simulate	Cannot simulate
Stellar variability	Can simulate	Cannot simulate
Jitter noise	Models from basic mechanism	Analytical expression
Spectral reconstruction	Can perform from data	Cannot perform from data
Noise mitigation	Can test and develop	Cannot test and develop
Data reduction	Can test and develop	Cannot test and develop
Speed	Slower	Faster
Output	Time series images needing further processing	Processed signal and noise per bin
Survey simulation	Better for single object studies	Better for assessing long list of objects

not simulate correlated noise in a numerical manner using small time steps, but still used simple models, e.g. an analytical expression for jitter noise was applied to each image, rather than generating the noise from basic mechanisms in the time domain. In addition jitter noise was only simulated in the spatial direction and not the spectral direction. The complexity, accuracy and versatility of the simulation was thus limited.

On considering developing a second generation simulator, while learning from the experience gained in EChOSim, it is important for a new simulator to be coded de novo with a view to improved accuracy, generic capability, versatility to different tasks, full time domain simulation of noise sources using discrete time steps, ease of upgrades and possible interfacing with external models. This would greatly expand on EChOSim's capabilities, addressing not only the performance of a specific instrument but additional applications within the general field of exoplanet transit spectroscopy.

The JWST consortium have described a simulator (Batalha N. E. et al., 2015) that models both in- and out-of-transit spectra, and includes multiple noise sources including zodiacal and stray light, flat field errors, Poisson and read noise. It is not clear from the description that the simulator models the time domain in a numerical manner, and if this is not the case, it would not be able to capture very complex time-dependent behaviour. The simulator is also clearly not generic and coupled

closely to the specific instrument.

A Hubble WFC3 IR simulator has been described, Wayne, (Varley et al., 2015) which performs a numerical transit spectroscopy simulation. Wayne incorporates a high level of detail in its WFC3 IR instrument model, but is clearly dedicated for a single instrument on a single observatory and thus has a limited range of usage. It is clearly not a generic simulator, making its versatility or adaptability for other instruments or tasks non-optimal.

Pand-exo (Batalha N. E. et al., 2017) is another WFC3 IR simulator introduced as an open-access community tool to assess SNRs for transit and eclipse spectroscopy, and is based on Pandeia, an exposure time calculator for JWST. Pand-Exo estimates in- and out-of-transit fluxes to obtain noise on the transit depth, but does not simulate the light curve in a numerical step-wise approach, and cannot therefore capture time domain effects such as stellar noise, pointing jitter or drift. It is therefore neither generic nor a time domain simulator.

A number of other simulators relevant to exoplanet transit photometry or spectroscopy missions are listed in Table 1.4. The list can be divided into photometric versus spectroscopic simulators and dynamic (taken to mean the simulation generates a time series of data) versus static models. The capabilities of the proposed generic time domain simulator are contrasted with each of these in turn.

### 1.3.3 REQUIREMENTS

To be a truly unique contribution to the field, the generic time domain simulator is required to have the following capabilities.

- 1) Applicable to any instrument capable of transit spectroscopy.
- 2) Able to capture complex time domain effects from correlated noise sources and systematics with such as pointing jitter and stellar variability.
- 3) Able to mimic the complete end-to-end a real observation to a high level of accuracy.
- 4) Able to switch between different instrument configurations in simple manner.
- 5) Have a modular structure that is easily upgradeable and able to interact with external models, e.g of models of stellar variability or temporal thermal variations.
- 6) Run fast enough to perform Monte Carlo simulations to directly obtain the distribution of the transit depths on the final spectrum as a way of quantifying the ensemble uncertainty from all noise sources, both correlated and uncorrelated, and systematics.

TABLE 1.4 Proposed simulator contrasted with previous exoplanet simulators.

Simulator (Mission)	Reference	Static or dynamic	Description	Comparison with proposed simulator
E TEM (Kepler)	Bryson et al., 2010	Dynamic	Kepler end-to-end simulator; simulates transit photometry	Photometric not spectroscopic
PlatoSim (PLATO)	Marcos-Arenal et al., 2014	Dynamic	PLATO 2.0 simulator; does not appear to simulate transit	Photometric not spectroscopic; no transit simulation?
IRACSIM (Spitzer)	Ingalls et al., 2016	Dynamic	Spitzer IRAC transit simulator	Photometric not spectroscopic
Wayne (HST)	Varley et al., 2017	Dynamic	Highly detailed model of WFC3; simulates transit spectroscopy in time domain	Not generic, less versatile, limited validation
JWST simulator (JWST)	Batalha N.E. et al., 2015	? Static	Dedicated JWST simulator; models in- and out-of-transit spectrum	Not generic; unclear if time domain is simulated in discrete steps
aXeSim (HST)	Kummel et al., 2007	Static	WFC3 simulator; does not simulate transit	Static, no simulation of light curves
PandExo (JWST)	Batalha N.E. et al., 2017	Static	WFC3 simulator; simulates noise in transit spectroscopy	Static, no simulation of light curves, limited noise model
ESA Radiometric model (EChO, ARIEL)	Puig et al., 2015	Static	Obtains SNR for transit spectroscopy; used for target list assessments	Static, not generic

- 7) Capable of outputting realistic spectral images so that data reduction pipelines, noise mitigation and decorrelation strategies can be tested.
- 8) Extensively validated to prove accuracy of its predictions.
- 9) Able to model transit spectroscopy variants such as eclipse spectroscopy, phase curve photometry and phase curve spectroscopy, as well as transit photometry.
- 10) Applicable to ground-based, space-based and balloon-borne instruments.
- 11) Applicable to both proposed new instruments and existing instruments to allow prospective and retrospective analysis.
- 12) Versatile enough to address questions of general interest to the exoplanet community (such as the effects of stellar variations, the detectability of Earth-like planets, the diagnostics of clouds and hazes, 2-D thermal mapping of planets, etc.).
- 13) Able to cross-validate other simulators and compare results.
- 14) Capable of being released as a community tool.

*ExoSim* was therefore developed as such a generic time domain transit spectroscopy simulator. *ExoSim* is the most versatile and validated end-to-end

simulator of transit spectroscopy currently developed. In this thesis, I describe the ExoSim algorithm and its validation, and then apply it to solve specific signal and noise problems in transit spectroscopy including the contribution of noise from stellar variability, the detectability of Earth-like planets, a controversy about instrumental noise affecting existing results, and the design of a transformative space mission in transit spectroscopy. In doing so, I will also demonstrate ExoSim's unique level of versatility by applying it to different instruments, both existing and proposed, to retrospective as well as prospective analysis, and to the elucidation of complex noise sources, both instrumental and astrophysical.

## CHAPTER 2

# DEVELOPMENT AND VALIDATION OF EXOSIM

---

---

**E**XOSIM is a highly versatile generic time domain simulator of transit spectroscopy observations. It incorporates both astrophysical and instrument models, and simulates signal modulations and noise in the time domain using a step-wise numerical method. It outputs a time series of spectral images akin to a real observation which then requires data reduction. ExoSim is designed to be generic and versatile. In Chapter 1 it was stated that one requirement for ExoSim was that it should be extensively validated to test the accuracy of its simulation. In this chapter, I describe the ExoSim algorithm, followed by the results of validation testing. ExoSim was tested against simple model predictions and alternate simulations, and also against real data from the Hubble Wide Field Camera 3 infrared instrument<sup>1</sup>.

### 2.1 THE EXOSIM ALGORITHM

#### 2.1.1 OVERVIEW

ExoSim simulates a complete time domain transit spectroscopic or photometric observation, including the astrophysical scene with planet primary transit or secondary eclipse, modulation of the signal through the telescope, instrument and detector, and addition of multiple noise sources and time-dependent systematics. Multiple instrument channels can be simulated. It outputs a time series of

---

<sup>1</sup> Material from this chapter is presented in Sarkar et al. (2016), Sarkar et al. (2017b) and Zingales et al. (2017).

images akin to a real observation, which then requires a data reduction pipeline to extract the required signal and noise information or to reconstruct the planet spectrum through fitting of model light curves. ExoSim simulates low to medium resolution spectrometers, using gratings, grisms or prisms, typically used for infrared transit spectroscopy, but cannot currently simulate integral field or Fourier transform spectrometers. ExoSim adopts a modular structure (Figure 2.1) that allows for upgrades in future versions and broadly represents the flow of information through the simulated system. It also utilizes as much as possible community maintained software.

As stated in Chapter 1, development of ExoSim followed the experience gained in EChOSim. The modular nomenclature is similar and limited short lengths of code are re-used from EChOSim (Pascale et al., 2015) namely for the generation of zodiacal light, the Planck function and calculation of transit duration ( $T_{14}$ ). Although the module names are similar, the code for individual modules in ExoSim is written de novo with new structure and functionality, and the overall functional architecture is different. In contrast to EChOSim, to make the new simulator truly generic, no hard-coded elements (specific to a fixed instrument or target) are written into the modules, classes or libraries, which thus act as a generic shell. A single hard-coded element, the Input Configuration File (*ICF*), written in XML, holds the specific instrumental and observational parameters<sup>2</sup> (Figure 2.2). By switching or editing this file, the simulation can be changed to a completely different instrument design, target or observational mode. Unlike in EChOSim, planet and star parameters are automatically selected by accessing the Open Exoplanet Catalogue (OEC) (Rein, 2012) database using the Exodata package (Varley, 2016)<sup>3</sup>. Unlike in EChOSim, in the astrophysical scene, phase curve simulations can be performed as well as primary and secondary transits. ExoSim utilizes the Python package PyTransit (Parviainen, 2015) to generate light curves. Unlike EChOSim, ExoSim's *Instrument* module simulates the focal plane array more realistically in 2-dimensions using a 2-D intra-pixel response function, inter-pixel quantum efficiency (QE) variations, and wavelength-dependent QE variations. The final focal plane spectra are generated from 2-D wavelength-dependent point spread functions (PSFs) (unlike 1-D functions used in EChOSim). This is linked to a novel pointing jitter model that captures the jitter noise in both the spectral direction (i.e. in parallel to the spectral trace) and the spatial direction (i.e. perpendicular to the

---

<sup>2</sup> Original coding for the XML file and parsing of parameters performed by E. Pascale and A. Papageorgiou.

<sup>3</sup> Implemented by E. Pascale.

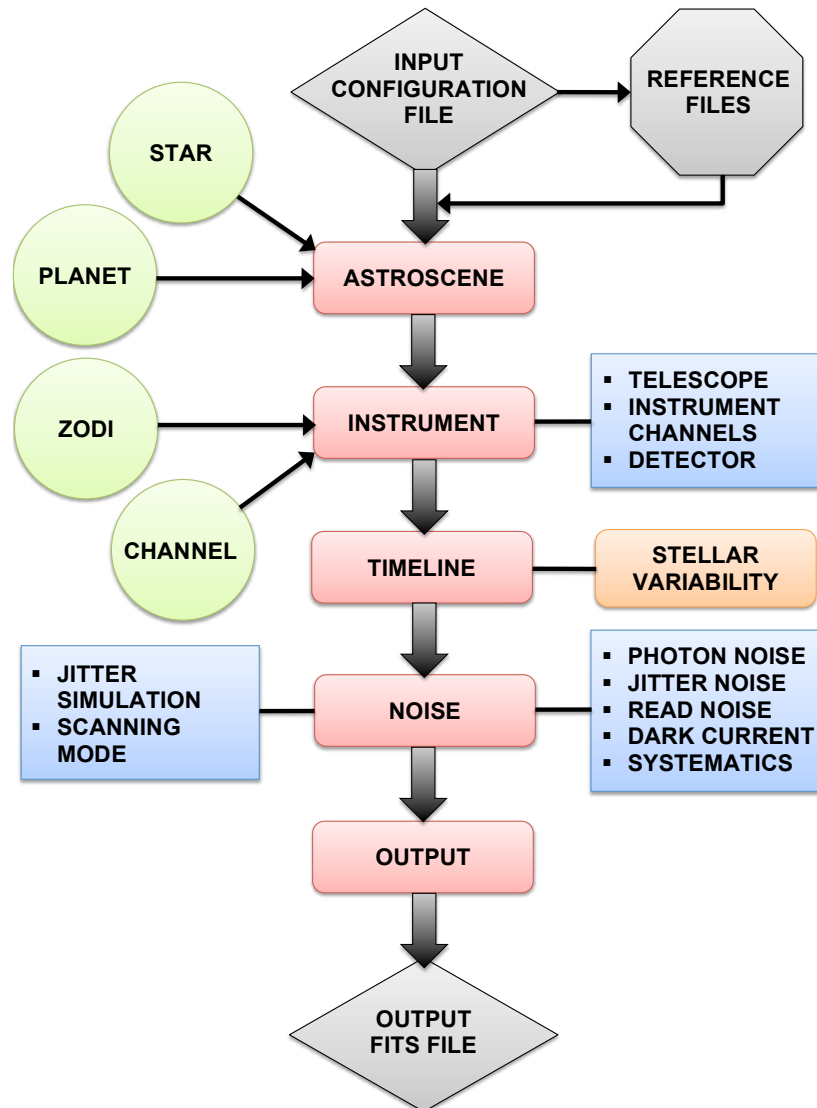


FIGURE 2.1 ExoSim modular architecture and information flow. The shell of the algorithm is completely generic. The only hard-coded element is the exchangeable Input Configuration File (*ICF*). This sets the simulation parameters and calls on instrument specific reference files. Key object classes are shown in green. Modules shown in red can be upgraded. Stellar variability can also be simulated using models of star spots and stellar convection modifying the light curve (see Chapter 5).

spectral trace), rather than just spatial jitter as in EChOSim, and uses a numerical method rather than an analytic approximation as in EChOSim. Jitter effects within the exposure time (causing broadening of the PSF) can now also be captured. Non-standard PSFs from optical simulation software or real instruments can also be used. Unlike EChOSim, ExoSim can simulate different dispersive elements (grism, grating or prism), and simulates photometer channels as well as spectrometer channels. Observational modes are more realistic and sophisticated than in EChOSim, with the timeline including realistic duty cycles with and the simulation of multiple NDRs per exposure. In contrast to EChOSim, ExoSim makes use of small time steps (shorter than the integration time) and a simulation frame rate that sets this, to produce high resolution time domain simulations. This can be used for the modulation of the signal within the integration time, e.g. by pointing jitter, but can also be utilized for other complex time-dependent processes. Spatial scanning mode, as used in the Hubble Wide Field Camera 3 infrared (WFC3 IR) instrument, can now be simulated as well as the usual staring mode. ExoSim is also able to interface in the *Timeline* module with external models providing time domain modulations (e.g. due to stellar variations). Overall, compared to EChOSim, ExoSim is generically structured with a more accurate time domain simulation, has greatly increased functionality and versatility, and has been more extensively validated.

### 2.1.2 INPUTS

ExoSim inputs consist of the *ICF* (Figure 2.2) and a set of reference files that define instrumental parameters. Reference files define the wavelength dependency of each optical surface's emission and transmission, the detector QE, and the wavelength solution of the dispersion element. Reference files are needed also for the spacecraft pointing jitter power spectrum, as well a 2-D grid for inter-pixel QE variations. Changing this input file allows ExoSim to switch between highly different instrument models, as well as change the target planet, and parameters defining the simulated observation mode (e.g exposure time, proportion of time in- and out-of-transit, number of NDRs, duty cycle, etc.). The contrast ratio spectrum must be provided as an input file<sup>4</sup>. For primary transit the input contrast ratio spectrum gives  $(R_p/R_s)^2(\lambda)$ , where  $R_p(\lambda)$  is assumed to be the sum of the both the planet radius and the additional 'height' due to atmospheric absorption. For secondary eclipse the input spectrum gives  $(F_p/F_s)(\lambda)$ .

<sup>4</sup> These can be generated from external radiative transfer codes.

An input stellar spectrum is required and ExoSim can select the best matching PHOENIX stellar spectrum model (matched to the host star parameters) (Allard et al., 2012) from a library<sup>5</sup>, or can use a black body approximation. Different noise sources can be switched on or off in the *ICF* allowing simulations to be run with particular noise sources in isolation. This can be used to discern the contribution of different noise sources in the overall noise budget, or to investigate the effects of particular noise source on the final spectrum. The root mean square deviation (rms) of the pointing jitter can be adjusted in the *ICF*. Jitter can be simulated in just the spectral direction or spatial direction, to investigate the effects of each in isolation, or combined. Spatial scanning versus staring mode can also be selected. The telescope aperture and optical surfaces are defined in the *ICF* as are the parameters for each instrument channel (e.g plate scale and f-number) as well as the characteristics of its detector (e.g. pixel size, dark current and read noise). Figure 2.2 shows an example of an *ICF* for the Hubble WFC3 IR instrument, with the purpose of each section identified.

### 2.1.3 MODULES

#### 2.1.3.1 ASTROSCENE

The signal processing algorithm begins in the *Astrosce* module. Here the exosystem data is loaded from the OEC via ExoData, using the planet name specified in the *ICF*. The *Star* object class is instantiated for the host star in the selected exosystem, with the stellar parameters populated from OEC exosystem data. This is used to select the matching stellar spectrum which serves as the initial signal in the algorithm giving surface flux  $F_{\star}(\lambda)$  in units of  $\text{W}/\text{m}^2/\mu\text{m}$ . From this, the observed flux of the star at the telescope,  $F_{tel}(\lambda)$ , is obtained:

$$F_{tel}(\lambda) = F_{\star}(\lambda) \left( \frac{R_s}{D} \right)^2 \quad (2.1)$$

where  $R_s$  is the stellar radius and  $D$  is the distance of the system.

The *Planet* class is then instantiated and the exosystem data is used to populate the planet parameters.  $T_{14}$  is then calculated. Light curves are generated in the planet class, but are called from the *Timeline* module later in the algorithm. These light curves are used to modulate the stellar signal in the time domain.

<sup>5</sup> Unless otherwise stated, the PHOENIX models used in this thesis are all BT-Settl CIFIST2011\_2015 models.

```

<root>
  <common>
    <logbinres val="1000" units="" comment="Resoving power for common spectral binnin. A linear binning wavelength integral is estimated
    as wl_min/R"/>
    <wl_min val="0.0" units="micron" comment="Shortest wavelength in simularion used for binning input spectra"/>
    <wl_max val="2.2" units="micron" comment="Shortest wavelength in simularion used for binning input spectra"/>
    <ExoSimOutputPath val="~/ExoSimOutput/Hubble" comment="output directory to store Sims" />
    <ConfigPath val = "__path__" />
  </common>

  <aocs>
    <PointingModel val="__path__/_data/instrument/hubble_pointing_model_psd.csv" comment="Jitter PSD in units of deg**2/Hz" />
    <pointing_rms val="4.0e-5" units="deg" comment="RMS of desired jitter. Omit this keyword to use the normalisation of the PSD" />
    <pointing_scan_throw val="19.2" units="arcsec" comment="Positive value enables scan-mode simulation. The value defines the throw of
    the scan, in arcsec. The period of the scan is defined by the exposure time. 10.98 for 88.1/1/1/1 set up, 18.48 for
    152.4/1/1/126" />
  </aocs>

  <astrosceene>
    <transit_is_primary val = "True"/>
    <planet val = 'gj1214b' />
    <planetCR val="__path__/_data/planetary/transmission/0400K_gj1214.dat" comment="planet/star contrast ratio"/>
    <OpenExoplanetCatalogue val = "__path__/_data/open_exoplanet_catalogue/systems/" comment="Path to openexoplanet catalogue. Null
    string downloads from URL."/>
    <StarSEDPath val_all="~/mnt/blast/data0/stellar_spectra/seed" val="__path__/_data/star" />
    <StarLimbDarkening val="__path__/_data/star/lcd_coeffs.dat" comment="Path to Model Limb Darkening coefficients table"/>
    <NTransits val="1" units="" />
  </astrosceene>

  <noise>
    <EnableSpatialJitter val="True" />
    <EnableSpectralJitter val="True" />
    <EnableShotNoise val="False" />
    <EnableReadoutNoise val="False" />
  </noise>

  <timeline>
    <exposure_time val="160.0" units="s" comment="time for one exposure containg set of NDRs" />
    <multiaccum val="13" units="" comment="number of NDRs per exposure" />
    <frame_rate val="2" units="1/s" comment="frame rate in SPS" />
    <nGD val="1." units="" comment="duration of reset event in units of 1/frame_rate" />
    <nNDR0 val="1." units="" comment="Integration time of first NDR in units of 1/frame_rate" />
    <nNST val = '138' units="" comment="Time lapse between last NDR and reset in units of 1/frame_rate" />
    <before_transit val="0.5" units="" comment="fraction of T14 for pre-transit observation" />
    <after_transit val="0.5" units="" comment="fraction of T14 for post-transit observation" />
  </timeline>

  <common_optics>
    <optical_surface type="mirror" transmission="__path__/_data/hubble/wfc3_ir_primary.csv" emissivity="__path__/_data/instrument/
    mirror_emissivity.csv" val="150" units="K" comment="M2"/>
    <optical_surface type="mirror" transmission="__path__/_data/hubble/wfc3_ir_secondary.csv" emissivity="__path__/_data/instrument/
    mirror_emissivity.csv" val="150" units="K" comment="M2"/>
    <TelescopeEffectiveDiameter val="2.4" units="m" />
  </common_optics>

  <channel name="WFC3IR" comment="WFC3IR">
    <optical_surface type="dichroic" transmission="__path__/_data/hubble/wfc3_ir_pom.csv" val="100" units="K" comment="D0"/>
    <optical_surface type="dichroic" transmission="__path__/_data/hubble/wfc3_ir_csm.csv" val="100" units="K" comment="D0"/>
    <optical_surface type="dichroic" transmission="__path__/_data/hubble/wfc3_ir_fold.csv" val="100" units="K" comment="D0"/>
    <optical_surface type="dichroic" transmission="__path__/_data/hubble/wfc3_ir_mir1.csv" val="100" units="K" comment="D0"/>
    <optical_surface type="dichroic" transmission="__path__/_data/hubble/wfc3_ir_mir2.csv" val="100" units="K" comment="D0"/>
    <optical_surface type="dichroic" transmission="__path__/_data/hubble/wfc3_ir_mask.csv" val="100" units="K" comment="D0"/>
    <optical_surface type="dichroic" transmission="__path__/_data/hubble/wfc3_ir_rcp.csv" val="100" units="K" comment="D0"/>
    <optical_surface type="dichroic" transmission="__path__/_data/hubble/wfc3_ir_g141.csv" val="100" units="K" comment="D0"/>
    <optical_surface type="dichroic" transmission="__path__/_data/hubble/wfc3_ir_win.csv" val="100" units="K" comment="D0"/>
    <optical_surface type="dichroic" transmission="__path__/_data/hubble/wfc3_ir_corr.csv" val="100" units="K" comment="D0"/>
    <slit_width val="11" units="" comment="Size of slit image in units of detector pixels"/>
    <ld val="0.9, 0.00025, 10" units="" comment="Wavelength solution (q, m, x_ref): wl = q + m(x - x_ref) where x is th pixel
    coordinate in units of micron"/>
    <array_geometry val="128, 256" units="" comment="pixel count"/>
    <wfno val="31.1" units="" transmission="The working f/#" />
    <osf val="3" units="" comment="Oversample each detector pixel by this amount. Need to be changed" />
    <qe val="__path__/_data/hubble/wfc3_ir_qe.csv" comment="" />
    <qe_rms_matrix_file val = "None" comment="[Default 'None'] Path to CSV file containing matrix of QE of pixels."/>
    <plate_scale val="3.61e-05" units="deg" />
    <detector_pixel>
      <pixel_size val="10" units="micron" />
      <Idc val="0.040" units="1/s" comment="Detector dark current"/>
      <sigma_ro val="14.7" units="" comment="Detector redout noise in e-rms"/>
      <pixel_diffusion_length val="0.0" units="micron" />
    </detector_pixel>
  </channel>

</root>

```

FIGURE 2.2 Example of an ExoSim Input Configuration File. The instrument simulated here is the Hubble WFC3 IR instrument. Sections shown have the control the following: a) file path and wavelength range, b) pointing system c) astrophysical scene and observational parameters, d) noise switches, e) timeline parameters, f) telescope, g) instrument, h) detector.

The planet parameters required for light curve generation are obtained from the exosystem data (period,  $a/R_s$ , inclination and eccentricity) and fed directly into PyTransit, which generates light curves using the model of Mandel and Agol (Mandel & Agol, 2002). Also required for light curve generation is the timegrid of the observation (and the central transit time), which is generated in the *Timeline* module. Together with the orbital parameters these are used to produce the  $z$  grid (the grid of positional offsets where  $z$  is the distance from the centre of the stellar disc to the centre of the planet disc in units of  $R_s$ ).

The reference contrast ratio spectrum, rebinned to the channel wavelength solution with one wavelength per pixel column, is also an input for the light curves. The square root of the contrast ratio at each wavelength gives the size ratio,  $p$ , for each light curve, used to generate the transit depth. Thus  $p$  equals  $R_p/R_s$  in primary transit and  $\sqrt{F_p/F_s}$  in secondary eclipse. Finally quadratic limb darkening coefficients can be added as inputs for each light curve. If selected, these are automatically chosen for each wavelength based on the star type<sup>6</sup>.

Secondary eclipse light curves are generated in the same way as primary transit curves with the modification that the light curves are normalized to give unity at the mid-transit point, not in the out-of-transit portion as for the primary transit light curves, and do not incorporate limb-darkening.

Phase curves can also be simulated in ExoSim by modifying either the primary or secondary eclipse light curves. For phase curve simulation, values for the maximum planet-star flux ratios (per wavelength) in both emission and reflection need to be provided, as well as any phase offset of the planet 'hot spot'. Currently ExoSim can only simulate the phase cycle in two halves, each requiring a separate simulation, the first modifying the primary transit light curve, and the second modifying the secondary eclipse light curve. The principle of phase curve simulation is described here.

A phase curve is produced from the planet flux as it varies with orbital phase angle,  $\Phi$ . The planet flux at the telescope,  $F_p(\lambda, \Phi)$ , consists of 2 components:  $F_e(\lambda, \Phi)$ , the emission component, and  $F_r(\lambda, \Phi)$ , the reflected component. The reflected component at full phase (i.e. at opposition with phase angle  $\Phi = 0$ ),  $F_{r,max}(\lambda)$  equals  $F_s(\lambda)\rho(\lambda)(R_p/a)^2$ , where  $F_s(\lambda)$  is the stellar flux,  $\rho(\lambda)$  is the albedo,  $R_p$  is the planetary radius and  $a$  is the semi-major axis. The phase function of the reflected light may be affected by variations in albedo with phase (e.g. varying cloud coverage or surface features), but to a first approximation we

<sup>6</sup> Coefficients were calculated by G. Morello of University College London using ATLAS and PHOENIX stellar models and autoselection in ExoSim was coded by A. Papageorgiou.

can use a function of the cosine of the phase angle. At any phase angle:

$$\begin{aligned} F_r(\lambda, \Phi) &= F_s(\lambda) \rho(\lambda) \left( \frac{R_p}{a} \right)^2 \left( \frac{\cos(\Phi) + 1}{2} \right) \\ &= F_{r,max}(\lambda) \left( \frac{\cos(\Phi) + 1}{2} \right) \end{aligned} \quad (2.2)$$

where  $\Phi$  is zero at opposition, and increases in an anti-clockwise direction. For the emitted component,  $F_e(\lambda)$ , the variation with phase can be more complex, since it will depend on the distribution of temperature over the planet. This potentially depends on multiple factors including planet rotation, tidal locking, and the atmospheric circulation. A simple phase function however can be constructed assuming the following. We can assume a maximum value of  $F_e(\lambda)$  for the 'dayside',  $F_{e,max}(\lambda)$ , which can be approximated by  $(R_p/D)^2 B_\lambda(T_p)$ , where  $T_p$  is the maximum dayside temperature,  $B_\lambda(T_p)$  is the Planck function for the planet, and  $D$  is the distance to the planet. A simple phase function for  $F_e(\lambda)$  can be constructed assuming that the minimum or 'night side' flux will be some fraction  $\alpha$  of the maximum flux, and that the difference between the minimum and maximum values of  $F_e(\lambda)$  modulates with  $(\cos(\Phi) + 1)/2$ . Furthermore, an offset  $\Theta$  can be added to the phase angle to simulate offset 'hotspots' due to atmospheric circulation as seen for example in the temperature map of HD 189733b (Knutson et al., 2007)<sup>7</sup>. Therefore:

$$\begin{aligned} F_e(\lambda, \Phi) &= \left( \frac{R_p}{D} \right)^2 B_\lambda(T_p) \left[ \alpha + (1 - \alpha) \left( \frac{\cos(\Phi + \Theta) + 1}{2} \right) \right] \\ &= F_{e,max}(\lambda) \left[ \alpha + (1 - \alpha) \left( \frac{\cos(\Phi + \Theta) + 1}{2} \right) \right] \end{aligned} \quad (2.3)$$

These varying fluxes with phase are illustrated in Figure 2.3. This figure shows that the total light curve at all phases is constructed from the addition of three components:  $F_s$ , the stellar flux which is assumed to be constant with phase except during the primary transit, and  $F_e$  and  $F_r$  from the planet, which modulate with phase as described above and are both reduced to zero during the secondary eclipse.

In ExoSim, we can simulate the full phase cycle in two halves. For  $\pi/2 < \Phi < 3\pi/2$ , the primary transit light curve,  $LC_p(\lambda, \Phi)$ , is modified. If we normalise the above expressions for  $F_e$  and  $F_r$  to stellar flux  $F_s$ , the sum of both components

<sup>7</sup> This will offset both the maximum and the minimum of the flux.

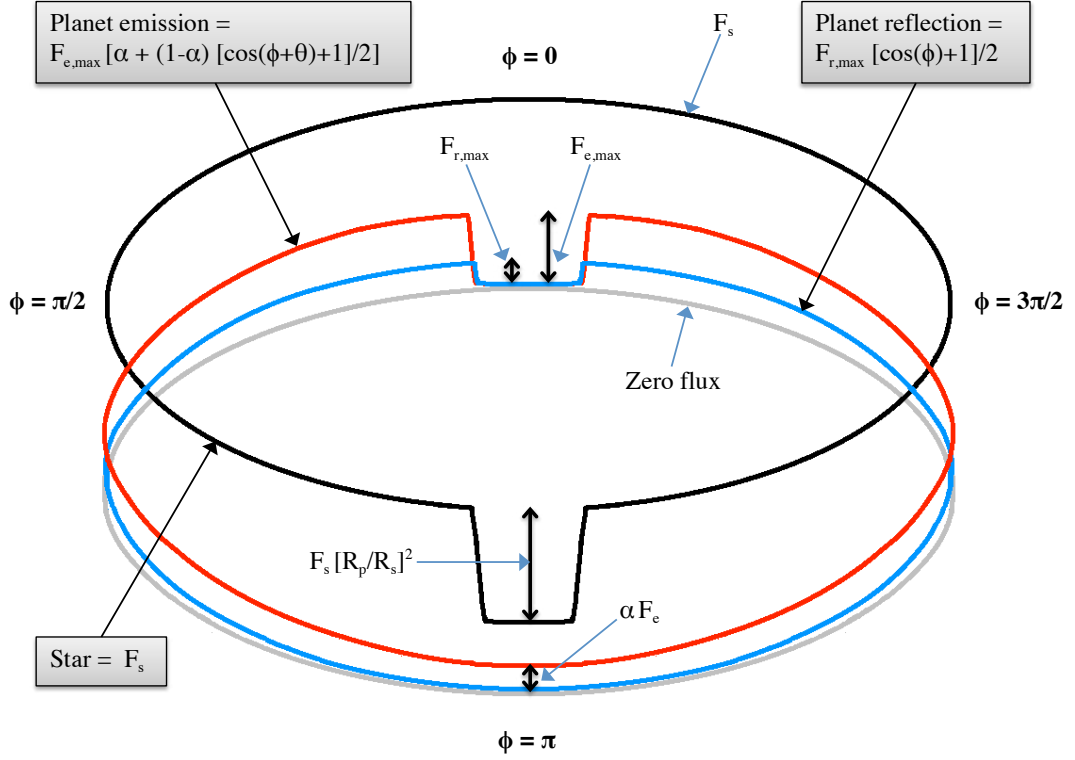


FIGURE 2.3 Simulating phase curves. Phase curves arise from variations in the planet emitted and reflected observed fluxes with orbital phase, on top of the stellar flux. Possible phase functions for simulation of the phase curves are shown; the emission phase function allows for a minimum night-side emission and an offset for the maximum and minimum. Primary transit is shown at  $\Phi = \pi$ , and secondary eclipse at  $\Phi = 0$ .

gives a phase curve,  $LC_\phi(\lambda, \Phi)$ :

$$LC_\phi(\lambda, \Phi) = \rho(\lambda) \left( \frac{R_p}{a} \right)^2 \left( \frac{\cos(\Phi) + 1}{2} \right) + \frac{F_{e,max}(\lambda)}{F_s(\lambda)} \left[ \alpha + (1 - \alpha) \left( \frac{\cos(\Phi + \Theta) + 1}{2} \right) \right] \quad (2.4)$$

The primary transit light curve is then modified as follows:

$$LC'_p(\lambda, \Phi) = LC_p(\lambda, \Phi) + LC_\phi(\lambda, \Phi) \quad (2.5)$$

This is simply the primary transit light curve (which is normalised to the stellar

flux), with the planet emission and reflection added (after division by the stellar flux). For  $3\pi/2 < \Phi < \pi/2$ , the secondary eclipse light curve,  $LC_s(\lambda)$ , is modified as follows:

$$LC'_s(\lambda, \Phi) = 1 + \left[ \frac{LC_s(\lambda, \Phi) - 1}{\frac{F_{e,max}(\lambda)}{F_s(\lambda)} + \rho(\lambda) \left(\frac{R_p}{a}\right)^2} \right] LC_\phi(\lambda, \Phi) \quad (2.6)$$

This equation uses the secondary eclipse light curve shape and timing for the eclipse, but effectively replaces the transit depth from the normal input contrast ratio spectrum with one resulting from the amplitudes of the reflected and emitted phase curves<sup>8</sup>. In effect two additional contrast ratio spectra are needed for phase curve simulation, one defining  $F_{e,max}(\lambda)$  and one defining  $F_{r,max}(\lambda)$ .

### 2.1.3.2 INSTRUMENT

The next module in the ExoSim informational flow is *Instrument*. In this module the telescope, instrument channels and detector are simulated and modulate the signal. The input to the module is  $F_{tel}(\lambda)$ , and the main output is a 2-D focal plane array per channel containing photoelectron counts per second from the stellar spectrum,  $C'_{star}(x, y)$ .

The modulation of the stellar spectrum begins by factoring in the primary mirror area,  $A_{tel}$ , and then attenuation in series by the transmission of each telescope optical surface, to give the wavelength-dependent spectral power in  $W/\mu m$ ,  $L_{ch}(\lambda)$ , entering each instrument channel:

$$L_{ch}(\lambda) = F_{tel}(\lambda) A_{tel} \prod_i v_{tel_i}(\lambda) \quad (2.7)$$

where  $v_{tel_i}(\lambda)$  is the transmission in the  $i$ th optical element of the telescope.

For each instrument channel, a *Channel* class object is instantiated. The *Channel* object stores channel-specific parameters from the *ICF*, the focal plane array output from *Instrument*, channel-specific light curves and the final image time series.

For each channel, the detector focal plane array is initially represented as an empty 2-D array matching the pixel dimensions of the detector. This array is then oversampled by a factor  $f$  (which must be an odd number to permit a single pixel to map to the centre of the original whole pixel, and is set by default to 3). This

<sup>8</sup> I appreciate the help of H. Parviainen in deriving Equation 2.6.

gives a 2-D sub-pixel array (i.e. with  $f^2$  sub-pixels per whole pixel) representing the focal plane,  $C_{null}(x, y)$ , with zero count per sub-pixel  $(x, y)$ . This oversampling is designed to ensure Nyquist sampling of the PSF and spectrum.

$L_{ch}(\lambda)$  is rebinned to the channel-specific wavelength solution of each sub-pixel column,  $x$ , to give  $L_{ch}(x)$ , multiplied by the transmission of each channel optical element, and converted to a photoelectron count per second per sub-pixel column  $C_{col}(x)$ :

$$C_{col}(x) = L_{ch}(x) \prod_i \nu_{ch_i}(x) \delta\lambda(x) QE(x) \left( \frac{hc}{\lambda(x)} \right)^{-1} \quad (2.8)$$

where  $\nu_{ch_i}(x)$  is the transmission of the  $i$ th optical element of the channel,  $\delta\lambda(x)$  is the wavelength pitch of each sub-pixel,  $QE(x)$  is the wavelength-dependent QE,  $\lambda(x)$  is the wavelength solution, and  $h$  and  $c$  are Planck's constant and the speed of light, respectively.

The convolution with the PSF is then simulated. For each sub-pixel column, a 2-D monochromatic PSF is generated according to its associated wavelength,  $\lambda(x)$ , and the channel f-number, using either an Airy function (Figure 2.4 top) or a Gaussian approximation. Alternatively user-defined PSFs can be used; if these are provided at a few wavelengths, the intermediate PSFs can be interpolated in ExoSim to produce a PSF stack covering all sub-pixel columns (Figure 2.4, bottom). Each PSF is returned as a 2-D array of sub-pixels with a normalized volume of unity:  $PSF(x_{psf}, y_{psf})$ , where  $x_{psf}$  and  $y_{psf}$  are the sub-pixel coordinates centred on the middle of the PSF array. On the sub-pixel array, the row  $y_{centre}$  is the row on which the spectral trace is centred. Future versions can incorporate traces that occur at an angle to the x axis or with more complex trace solutions. Each 2-D PSF array corresponding to a sub-pixel column  $x_0$ ,  $PSF_{x_0}(x - x_0, y - y_{centre})^9$ , is multiplied by the count on that sub-pixel column,  $C_{col}(x_0)$ , which thus redistributes the spectral energy over the volume of the PSF. Each modified PSF is then added to  $C_{null}(x, y)$  centred on its sub-pixel position  $(x_0, y_{centre})$ . This co-adding of PSFs generates the convolved stellar spectrum (Figure 2.4, right):

$$C_{star}(x, y) = C_{null}(x, y) + \sum_{x_0} C_{col}(x_0) PSF(x - x_0, y - y_{centre}) \quad (2.9)$$

The planet-star contrast ratio spectrum,  $CR(\lambda)$ , will also be subject to convolution with the PSF to bring its resolution in line with that of the instrument.

<sup>9</sup>  $x_{psf} = x - x_0, y_{psf} = y - y_{centre}$

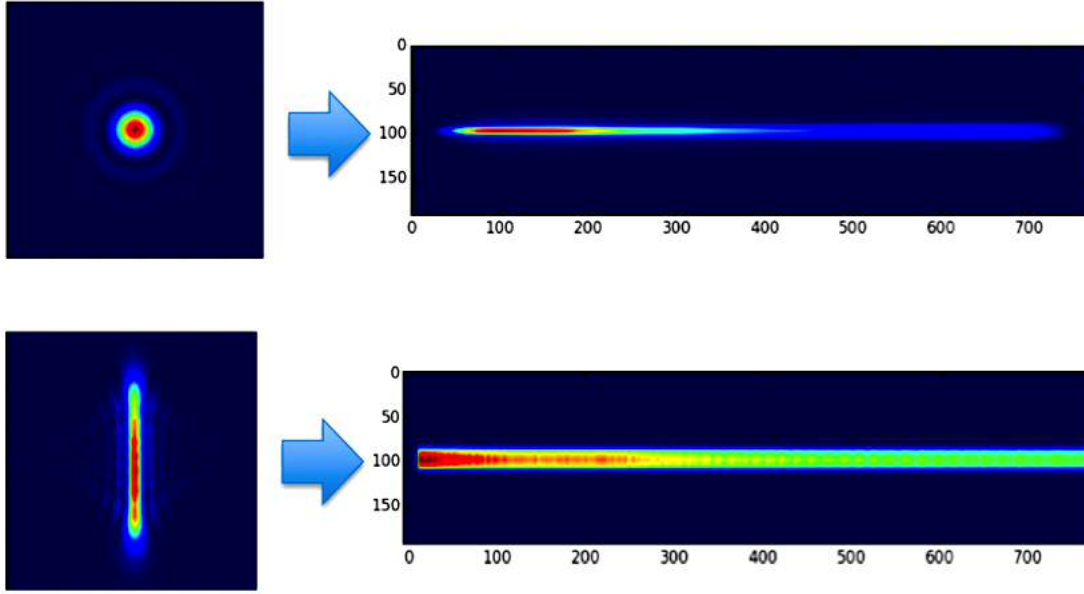


FIGURE 2.4 Exosim normally constructs spectra from model 2-D Airy functions (e.g. top left) or 2-D Gaussians. ExoSim can also use user-defined PSFs (e.g. bottom left) which may be asymmetric or aberrated; with a few samples at different wavelengths, the intervening PSFs are constructed by interpolation. The PSFs are coadded to the focal plane array to produce spectra (right, top and bottom). These spectra were produced for a 0.5m telescope design with an  $R=254$  f/18.5 grating spectrometer. Axes show pixel positions. PSFs are magnified in comparison to the spectra shown.

This is performed by rebinning the contrast ratio spectrum to the wavelength grid of the sub-pixels to give  $CR(x_0)$  and multiplying by a 1-D PSF profile normalized to unity area,  $PSF_x(x - x_0)$ . These 1-D images are then coadded over the spectral dimension to give a convolved 1-D spectrum:

$$CR'(x) = \sum_{x_0} CR(x_0)PSF_{x_0}(x - x_0) \quad (2.10)$$

This spectrum is then used later for generating the light curves.

Finally in preparation for the downstream 2-D pointing jitter simulation, the focal plane array is convolved with a 2-D pixel response function. The resulting convolved focal plane array therefore gives the count over a pixel-sized area centred on any sub-pixel location  $(x, y)$ :

$$C'_{star}(x, y) = \iint C_{star}(x_0, y_0)PRF(x - x_0, y - y_0) dx_0 dy_0 \quad (2.11)$$

where  $PRF$  is the pixel response function. The  $PRF$  can be a 'top hat' function which gives no intra-pixel variation in responsivity. I take the 1-D pixel response

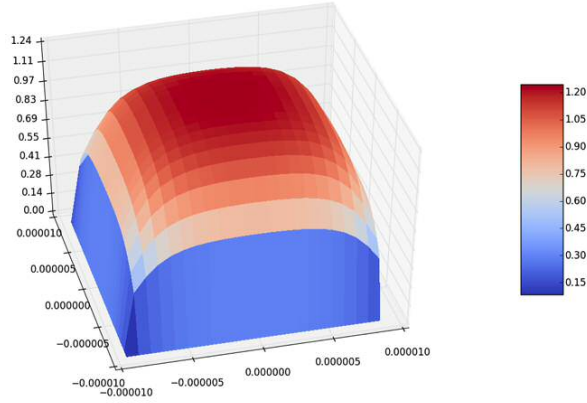


FIGURE 2.5 2-D pixel response function used in ExoSim to simulate intra-pixel variation in responsivity. x and y axes show distance in units of m; z axis shows the responsivity after normalizing the volume to unity.

function from EChOSim (Pascale et al., 2015), that models a gradual fall in responsivity with distance from the centre of the pixel (a ‘bowler hat’ function), and generalise it to 2-D:

$$PRF(x_{prf}, y_{prf}) = \arctan\left(\frac{\tanh(0.5\Delta_{pix} - L_x)}{2d_l}\right) - \arctan\left(\frac{\tanh(-0.5\Delta_{pix} - L_x)}{2d_l}\right) \\ \arctan\left(\frac{\tanh(0.5\Delta_{pix} - L_y)}{2d_l}\right) - \arctan\left(\frac{\tanh(-0.5\Delta_{pix} - L_y)}{2d_l}\right) \quad (2.12)$$

where  $\Delta_{pix}$  is the whole pixel length,  $x_{prf}$  and  $y_{prf}$  are sub-pixel coordinates centred in the middle of the sub-pixel position  $(x_0, y_0)$ <sup>10</sup>,  $L_x$  is the distance from the centre of the pixel<sup>11</sup> and  $d_l$  is the diffusion length, which characterizes the fall off at the pixel edge. A  $d_l$  of  $1.7 \mu\text{m}$  gives a pixel response function as shown in Figure 2.5. If  $d_l$  approaches zero, it will approach the ‘top hat’ function. The  $PRF$  volume is normalized to unity prior to convolution with the focal plane array. It is possible also to add an ‘inter-pixel distance’ to account for the gap between pixels in the array.

The zodiacal light spectral brightness in  $\text{W}/\text{m}^2/\mu\text{m}/\text{sr}$  is modeled using the formula:

$$I_{zodi}(\lambda) = 3.5 \times 10^{-14} B_\lambda(5500\text{K}) + 3.58 \times 10^{-8} B_\lambda(270\text{K}) \quad (2.13)$$

<sup>10</sup>  $x_{prf} = x - x_0, y_{prf} = y - y_0$

<sup>11</sup>  $L_x = x_{prf} \Delta_{subpix}$  and  $L_y = y_{prf} \Delta_{subpix}$ , where  $\Delta_{subpix}$  is the length of a sub-pixel

where  $B_\lambda(5500K)$  is the Planck function for the scattered light component and  $B_\lambda(270K)$  is the Planck function for the thermal emission component of the interplanetary dust cloud. This formula was borrowed from the EChOSim code and is based on a model from Pascale et al. (2015). The formula approximately matches the zodiacal light measurement from the South Ecliptic Pole in Leinert et al. (1998). For targets very near to the ecliptic, a correction factor can be considered to account for increased dust density. This is discussed further in the Appendix. This spectrum is modulated by passing it through telescope and instrument transmissions. For a given instrument channel:

$$I'_{zodi}(\lambda) = I_{zodi}(\lambda) \prod_i v_{tel_i}(\lambda) \prod_j v_{ch_j}(\lambda) \quad (2.14)$$

where  $v_{tel_i}(\lambda)$  is the transmission of the  $i$ th optical element in the telescope, and  $v_{ch_j}(\lambda)$  is the transmission of the  $j$ th optical element in the specific instrument channel.

Telescope and instrument thermal emissions are also simulated. The spectral brightness of each optical element is calculated from the emissivity,  $\epsilon(\lambda)$  in the optical element file, multiplied by its Planck function  $B_\lambda(T)$ , with the exception of the final optical element in the chain, the spectral brightness from each element is modulated by the transmission of all downstream elements. For the telescope this means the modulated intensity arriving at the instrument channel is:

$$I_{emm}(\lambda) = \sum_{i=1}^{N-1} \left( \epsilon_i B_\lambda(T_i) \prod_{k=i+1}^N v_{tel_k}(\lambda) \right) + \epsilon_N B_\lambda(T_N) \quad (2.15)$$

where  $N$  is the number of optical elements in the telescope and  $\epsilon_i$  and  $T_i$  are the emissivity and temperature of the  $i$ th element respectively. For each channel the final modulated intensity is:

$$I'_{emm}(\lambda) = I_{emm}(\lambda) \prod_{j=1}^M v_{ch_j} + \sum_{j=1}^{M-1} \left( \epsilon_j B(\lambda, T_j) \prod_{k=j+1}^M v_{ch_k}(\lambda) \right) + \epsilon_M B(\lambda, T_M) \quad (2.16)$$

where  $M$  is the number of optical elements in the channel and  $\epsilon_j$  and  $T_j$  are the emissivity and temperature of the  $j$ th element respectively within the channel.

The spectrum of both these diffuse sources is then rebinned to the whole pixel array wavelength solution  $\lambda(X)^{12}$  and converted to a photoelectron count

<sup>12</sup>  $X$  and  $Y$  refer to whole pixel positions while  $x$  and  $y$  refer to sub-pixel positions, where  $x = fX - (f - 1)/2$  and  $y = fY - (f - 1)/2$

per second per whole pixel ( $X$ ).

$$C_{zodi}(X) = I'_{zodi}(X) A_{pix} \Omega_{pix} \delta\lambda(X) QE(X) \left( \frac{hc}{\lambda(X)} \right)^{-1} \quad (2.17)$$

$$C_{emm}(X) = I'_{emm}(X) A_{pix} \Omega_{pix} \delta\lambda(X) QE(X) \left( \frac{hc}{\lambda(X)} \right)^{-1} \quad (2.18)$$

where  $A_{pix}$  is the area of a pixel,  $\Omega_{pix}$  is the solid angle subtended at the pixel and  $\delta\lambda(X)$  is the wavelength span per whole pixel<sup>13</sup>.

Next convolution with the spectrometer slit image is simulated. The slit image width is represented by a boxcar function,  $b(X)$ , of height unity and width  $l$ , where  $l$  is the slit image width in pixel units, so that the spectrum on any whole pixel,  $X$  is:

$$C'_{zodi}(X) = (C_{zodi} * b)(X) \quad (2.19)$$

and

$$C'_{emm}(X) = (C_{emm} * b)(X) \quad (2.20)$$

$$\text{where } b(X) = \begin{cases} 1 & -l/2 < X < l/2 \\ 0 & \text{otherwise} \end{cases}$$

These are then repeated in the spatial direction to produce 2-D arrays of the size of the whole pixel grid such that:

$$C'_{zodi}(X, Y) = C'_{zodi}(X) \quad (2.21)$$

and

$$C'_{emm}(X, Y) = C'_{emm}(X) \quad (2.22)$$

These zodi and emission count rates, as well as the count rates resulting from the detector dark current, are not added to the focal plane array in *Instrument*, but added later in the *Noise* module once individual subexposures have been generated with whole pixel counts. This to avoid the diffuse sources and dark current being modulated by the transit light curve.

Photometric channels are simulated with the following modifications<sup>14</sup>:

- 1) The 2-D PSFs generated from the wavelength solution for each sub-pixel column are coadded on the same point on the focal plane.
- 2) The zodiacal and emission count rate spectra are not convolved with the slit, but

<sup>13</sup> The diffuse source equations are the consequence of conservation of entendue.

<sup>14</sup> These modifications were implemented by A. Papageorgiou.

instead are summed and the summed count rate applied to all whole pixels in the array.

3) The central wavelength of the photometric channel is used to select a single contrast ratio value to apply to all pixel columns when generating light curves (and a single set of limb darkening coefficients corresponding to that wavelength), i.e. the same light curve is applied to all pixel columns.

### 2.1.3.3 TIMELINE

The *Timeline* module simulates for each channel, the correct timing and sequencing of the observation, including exposures, subexposures and overheads, and obtains the planet transit light curves. An exposure can be divided into several subexposures and non-destructive reads. Each non-destructive read (NDR) is the cumulative sum of all preceding subexposures in that exposure. The end time of the  $i$ th subexposure is also the end time of the  $i$ th NDR.

Each exposure is allocated its overheads: detector ground and reset times, and the time for the zeroth subexposure,  $NDR_0$  (usually subtracted in data reduction), with the remaining time divided equally among the rest of the subexposures.

The exact final duration of each element in the exposure cycle is restricted by the selected simulation frame rate which sets the time resolution of the simulation: each element must be an integer number of frames. The total amount of time to observe in- and out-of-transit is defined in the *ICF*.

Light curves are generated at this point by calling the *Planet* class, the number of light curves matching the number of whole pixel columns in the channel each with its own wavelength,  $\lambda(X)$  (with the exception for the photometric channels described above where the same central wavelength is used for all light curves), giving a 2-D light curve array,  $LC(X, t)$ . The time sequence of subexposures is used as the timegrid input for Pytransit to calculate the  $z$  parameter for the transit light curves.

### 2.1.3.4 NOISE

In the *Noise* module, the final sequence of NDR images is generated containing noise. If jitter noise is selected in the *ICF* then the following algorithm is followed:

1) A timeline of random jitter offsets is generated independently for each axis (spatial and spectral) on the focal plane. This is performed by a function which requires a model power spectral density (PSD) profile for the spacecraft pointing jitter in

each axis. Note for 'white noise' jitter, this will be a flat PSD, however in reality the PSD is more complex and results in time-correlated jitter offsets. Spacecraft specific PSDs were developed and used for studies on the Hubble Space Telescope and the ARIEL space telescope, and are detailed in Chapters 3 and 4. A default model PSD for ExoSim was generated using 2-D pointing data from the Herschel spacecraft. Recorded variations in right ascension and declination were converted into angular x and y detector axis variations, giving jitter timelines in x ('yaw') and y ('pitch'). Each timeline was real Fourier transformed. The squared modulus was doubled and divided by the frequency gradient to obtain the power spectral density profile (PSD) for each axis. These are shown in Figure 2.6. Since the PSD is not flat, it produces a correlated jitter timeline. To generate a random jitter timeline for each axis from the PSD, the following method is used. The PSD is firstly resampled to ensure the correct number of points in the final timeline is generated, and to ensure Nyquist sampling of the jitter regardless of the selected simulation frame rate. The PSD is then converted to an amplitude power spectrum by reversing the operation described above. The dynamic nature of the power spectrum due to noise is partially modeled through generating a random variation for each simulation, where the amplitude power spectrum is given a random Gaussian offset at each frequency. However we cannot at this time modulate the PSD continuously during the simulation. Random phase angles per frequency are generated from a uniform distribution and then combined with the amplitude spectrum to generate a spectrum of complex numbers which are then inverse real Fourier transformed to produce a jitter offset timeline. The jitter timeline consists therefore of small time steps, where the rate of steps  $\geq$  the Nyquist sampling rate, and is  $\geq$  the simulation frame rate. The rms of the jitter timeline is set by the area of the PSD as per Parseval's theorem, however the rms can be adjusted by scaling the jitter amplitudes in the final jitter offset timeline.

2) The jitter offset timelines for each axis are then imported into the *Noise* module and converted from units of angle to units of sub-pixels (using the plate scale). To Nyquist sample the jitter spatially, the jitter rms can be considered a spatial distance that must be sampled at least twice, thus the resolution of the sub-pixel grid needs to adjust to accommodate this. An oversampling factor,  $f'$ , applied to the whole pixel, is therefore needed for this, where  $f' = 3/rms$  and the rms is in units of whole pixels. Since the jitter rms at this stage in the code is actually now in units of sub-pixels, the sub-pixels will need to be oversampled by  $f'' = 3/rms$ , where the rms is in units of sub-pixels. This results in the same final oversample factor,  $f'$ , since  $f' = f \cdot f''$ . The convolved focal plane array from the *Instrument*

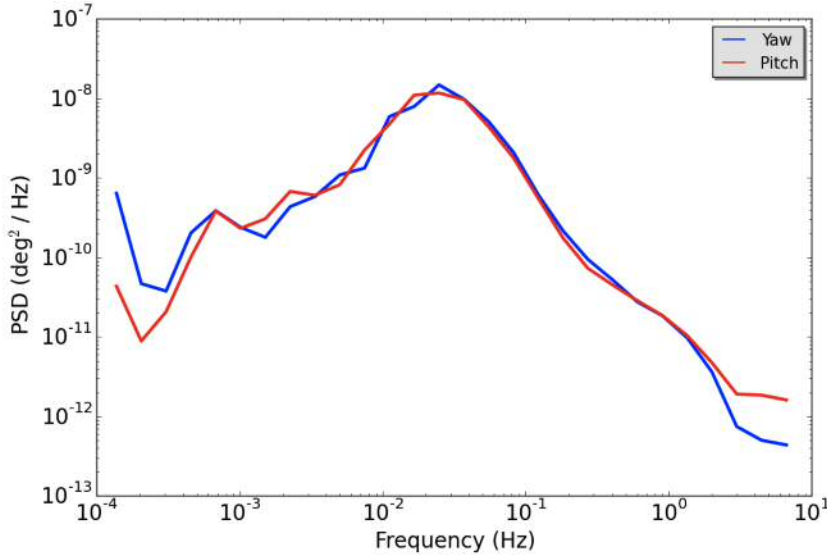


FIGURE 2.6 Model pointing jitter PSD profiles for both axes derived from Herschel spacecraft pointing data. The ‘yaw’ PSD is used for generating x axis jitter and the ‘pitch’ PSD used for generating y axis jitter. Both axis PSDs have similar jitter timeline rms deviations: 93 mas for the ‘yaw’ PSD, and 90 mas for the ‘pitch’ PSD. This gives a bi-axial rms of 129 mas.

module,  $C'_{star}(x, y)$  is therefore further oversampled by the factor  $f''$  (rounded to the nearest odd number). The final grid,  $C''_{star}(x', y')$ <sup>15</sup> is thus oversampled from the original whole pixel grid by a factor  $f'$ , where  $f' = f \cdot f''$ .

3) The code then loops through each jitter time step or ‘subframe’, with different sub-pixel offsets,  $\delta x'$  and  $\delta y'$  at each step<sup>16</sup>. At each step, the photoelectron count per second on each whole pixel  $(X, Y)$ , is found by sampling the convolved sub-pixel grid at positions corresponding to the middle of each whole pixel shifted by the sub-pixel offsets:

$$C_{star}(X, Y) = C''_{star}(f'X - \delta x', f'Y - \delta y') \quad (2.23)$$

where the offsets,  $\delta x'$  and  $\delta y'$  are initially set to  $(f' - 1)/2$ , the non-jittered positions.  $f'$  must be an odd number so that a single sub-pixel maps exactly to the centre of each whole pixel. With each step therefore, the grid shifts to a new set of

<sup>15</sup> where  $x' = f''x - (f'' - 1)/2$  and  $y' = f''y - (f'' - 1)/2$

<sup>16</sup> The original code for this jitter ‘subframe’ routine was written by myself in Python, but later converted into a C version by E. Pascale for added speed. This is the only portion of ExoSim written in C.

sub-pixel positions. This is equivalent to the image moving in the reverse direction.

4) The whole pixel count on each jitter subframe is multiplied by its time period,  $\delta t$ , and then summed per subexposure. The count in photoelectrons on a subexposure consisting of  $i$  subframes is given by:

$$P_{star}(X, Y) = \sum_i^n C''_{star}(f'X - \delta x'_i, f'Y - \delta y'_i)\delta t_i \quad (2.24)$$

$\delta t$  is in practice constant for all subframes, so that the integration time for the subexposure,  $\Delta t_{sub}$ , is given by  $n\delta t$ , where  $n$  is the number of jitter subframes in the subexposure. This thereby captures the effects of jitter within the integration period of a subexposure (which tends to broaden the PSF).

5) If jitter in only one axis is selected (e.g. to isolate spectral or spatial jitter noise), the other axis offsets are not applied in the jitter code. If jitter noise is not selected at all, no offsets are applied apart from the initial offset  $(f' - 1)/2$ . If spatial scanning is selected a sawtooth drift is applied to the spatial direction on top of the jitter timelines, the amplitude of which can be set in the *ICF*.

The 2-D light curve array from *Timeline* is now represented as  $LC(X, \hat{t})$ , where  $\hat{t}$  is a time-dependent index of each subexposure (but not the absolute time value at that index, i.e.  $\hat{t} = [0, 1, 2, \dots, N_{sub} - 1]$ ), where  $N_{sub}$  is the total number of subexposures. The array cube of subexposures, represented by  $P_{star}(X, Y, \hat{t})$ , is then multiplied by the light curve array<sup>17</sup> followed by addition of backgrounds so that the count on any subexposure at time-dependent index  $\hat{t}$  is given by:

$$P_{sub}(X, Y, \hat{t}) = P_{star}(X, Y, \hat{t})LC(X, \hat{t}) + C'_{zodi}(X, Y)\Delta t_{sub}(\hat{t}) + C'_{emm}(X, Y)\Delta t_{sub}(\hat{t}) \quad (2.25)$$

Next QE variations are added to the baseline QE already implemented, to simulate inter-pixel non-uniformity, by multiplying all subexposures by a 2-D array,  $QE_{var}(X, Y)$  factoring these variations (e.g. a 5% rms variation). This is followed by addition of the dark current contribution,  $I_{dc}$ . At this point Poisson noise is generated on the counts on each subexposure, with a random variation added to each pixel,  $\eta_p(X, Y, \hat{t})$ . Thus each subexposure is modified to:

$$P'_{sub}(X, Y, \hat{t}) = P_{sub}(X, Y, \hat{t})QE_{var}(X, Y) + I_{dc}\Delta t_{sub}(\hat{t}) + \eta_p(X, Y, \hat{t}) \quad (2.26)$$

<sup>17</sup> This step can be bypassed if simulation of only the OOT signal and noise is required.

Next the subexposures are converted into NDRs. If there are  $N_{ndr}$  NDRs per exposure and  $N_{exp}$  exposures, then for the  $j$ th NDR [ $j=0,1,2,\dots,N_{ndr}-1$ ] on the  $i$ th exposure [ $i=0,1,2,\dots,N_{exp}-1$ ],  $\hat{T} = iN_{ndr} + j$ , where  $\hat{T}$  is the time-dependent index of each NDR. The final count on each NDR is given by the summation of all preceding subexposures:

$$P_{ndr}(X, Y, \hat{T}) = P_{ndr}(X, Y, iN_{ndr} + j) = \sum_{\hat{t}=iN_{ndr}}^{iN_{ndr}+j} P'_{sub}(X, Y, \hat{t}) \quad (2.27)$$

Finally read out noise is added to each NDR, by adding a random Gaussian variation to each pixel in each NDR,  $\eta_r(X, Y, \hat{T})$ , with standard deviation equal to the read noise in the *ICF*. This gives the final array of NDRs

$$P'_{ndr}(X, Y, \hat{T}) = P_{ndr}(X, Y, \hat{T}) + \eta_r(X, Y, \hat{T}) \quad (2.28)$$

The index  $\hat{T}$  mapped to the specific time values,  $T$ , for each NDR gives the final image array as  $P'_{ndr}(X, Y, T)$ , containing each NDR with its signal and noise.

### 2.1.3.5 OUTPUT

The terminal module in the ExoSim information flow is *Output* which packages the final NDR array into FITS files, with a separate file for each channel. Extensions are included, containing simulation parameters and other information to assist data reduction. Data reduction is not packaged in ExoSim, and so must be applied by the user to process the images, extract signal and noise information, fit light curves and reconstruct the spectrum, as for a real observation.

## 2.2 VALIDATION

ExoSim was validated in a series of tests against predictions from analytical expressions and simple models, independent simulations, and against published real data from the Hubble WFC3.

### 2.2.1 VALIDATION OF FOCAL PLANE SIGNAL AND NON-JITTER NOISE AGAINST ANALYTICAL PREDICTIONS

ExoSim simulations were performed for an out-of-transit (OOT) observation (the transit light curve not applied in the simulation) of the star 55 Cancri. A

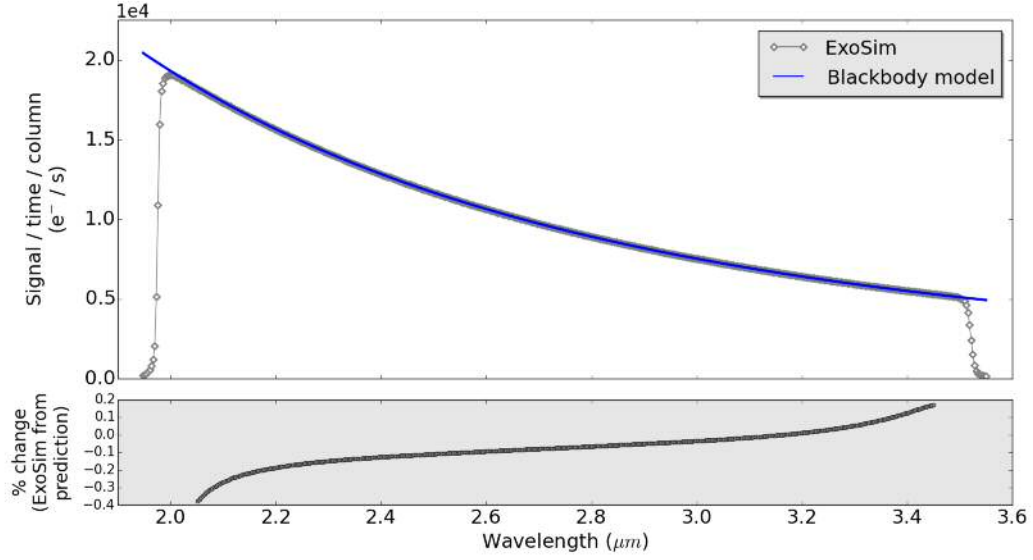


FIGURE 2.7 ExoSim focal plane signal per unit time per pixel column compared to an analytical prediction, where the x axis shows the wavelength on a pixel column. Subplot shows percent difference of ExoSim from prediction over the wavelength range 2.05-3.45  $\mu\text{m}$ .

black body spectrum was used for the star with  $T_{star} = 5196$  K. The optical system was simulated with a 0.5 m primary mirror and an R=254, f/18.5 grating spectrometer channel covering wavelengths 2.0-3.5  $\mu\text{m}$ . The noiseless focal plane signal from the *Instrument* module, in  $e^- / \text{s}$  per pixel column  $X$  (where  $X$  is a function of  $\lambda$ ) was compared to an analytical prediction:

$$C_{col}(X) = \pi B_{\lambda(x)}(T_{star}) \left( \frac{R_s}{D} \right)^2 \nu(X) QE(X) \delta\lambda(X) \frac{\lambda(X)}{hc} \quad (2.29)$$

where  $B_{\lambda(x)}(T_{star})$  is the Planck function of the star,  $\nu(X)$  is the optical transmission,  $\delta\lambda$  is the wavelength range over a pixel column width, and  $h$  and  $c$  are Planck's constant and the speed of light, respectively. The counts from the ExoSim focal plane are compared to the prediction in Figure 2.7. A small region of artefact occurs at the edges of the focal plane as the PSFs are coadded which results in fall of the signal. Ignoring this region, I find that over the wavelength range 2.05-3.45  $\mu\text{m}$ , the variation from the predicted value is always less than 0.4%.

Next the noise variance per unit time in units of  $e^- / \text{s}$  on the integrated pixel column signal,  $C_{col}(X)$ , from different isolated noise sources was compared to analytical predictions for photon noise from the star, dark current noise and read

out noise (using correlated double sampling or CDS<sup>18</sup>), based on the following formulae:

$$\sigma_{star}^2(X) = C_{col}(X) \quad (2.30)$$

$$\sigma_{dc}^2(X) = N_{pix}I_{dc} \quad (2.31)$$

$$\sigma_{rn_{cds}}^2(X) = 2N_{pix}\sigma_{rn_{pix}}^2 \quad (2.32)$$

$$\sigma_{total}^2(X) = \sigma_{star}^2(X) + \sigma_{dc}^2(X) + \sigma_{rn}^2(X) \quad (2.33)$$

where  $N_{pix}$  is the number of pixels in the column, in this case 64,  $I_{dc}$  is the dark current on a pixel (in this case  $20 \text{ e}^-/\text{s}$ ),  $\sigma_{star}$  is the source photon noise,  $\sigma_{dc}$  is the dark current shot noise,  $\sigma_{rn_{pix}}$  is the read noise for a single pixel read (in this case  $20 \text{ e}^-$ ) and  $\sigma_{rn_{cds}}$  is the read noise after CDS. Each of these values is then divided by the CDS integration time of 10 seconds.

In Figure 2.8 we see that although ExoSim shows stochastic variations, the average noise from ExoSim falls close to the analytical predictions in all cases. For photon noise, excluding the edge region, we obtain a mean percentage difference of -0.1%. For dark current noise and read noise the mean differences are -0.3% and -0.4% respectively. The total noise mean difference was -0.4% showing that these noise sources are adding in quadrature as independent sources. Therefore, excluding the edge regions the mean difference from predictions is always within 0.4%.

## 2.2.2 EXOSIM VS ESA RADIOMETRIC MODEL

ExoSim results were compared to those from a radiometric model independently developed by the European Space Agency (ESA) which has been used for both the EChO and ARIEL phase A studies (Puig et al., 2015). ExoSim was adopted as the detailed end-to-end simulator for the ARIEL mission (see Chapter 4). This comparison test was performed as part of the ARIEL phase A study to cross-validate each simulator.

The ESA Radiometric Model (ERM) generates a static signal and noise simulation using both a stellar target and instrument model. Unlike ExoSim it does not simulate the transit itself. The noise is calculated as an exact value and not generated in a stochastic manner as in ExoSim. Like ExoSim it uses model stellar spectra adjusted for stellar size and distance, instrument transmissions and a fixed

<sup>18</sup> The CDS exposure is the final NDR minus  $\text{NDR}_0$ .

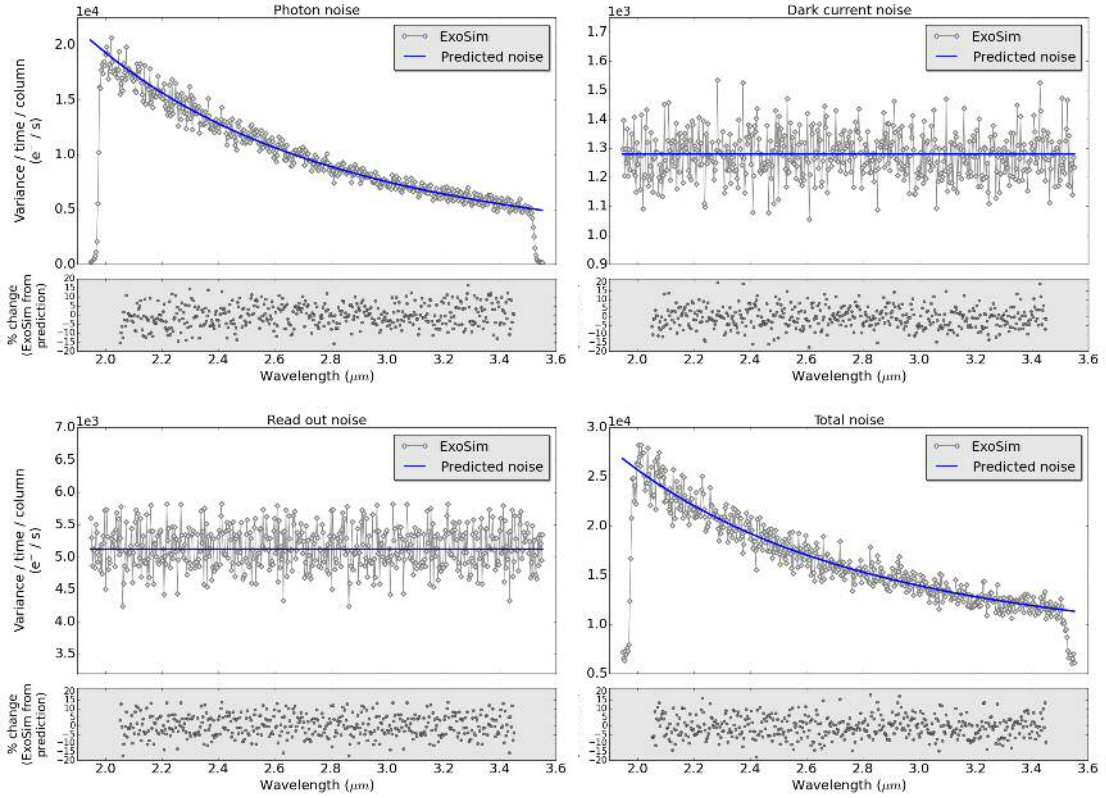


FIGURE 2.8 ExoSim noise variance per unit time per pixel column compared to predictions for non-jitter noise sources. Top left: photon noise from the star. Top right: dark current shot noise. Bottom left: CDS read out noise. Bottom right: total noise. The x axis shows the wavelength on the pixel column. Subplots show percent difference of ExoSim from the prediction over the wavelength range 2.05-3.45  $\mu\text{m}$ .

quantum efficiency (but no variations). It bins the signal and noise into spectral-resolving-element-sized bins (R-binning). The ERM models the total noise variance<sup>19</sup> per unit time on any spectral element as:

$$\frac{\sigma^2}{t}(\lambda) = N_0(\lambda) + XN_0(\lambda) + N_{min}(\lambda) \quad (2.34)$$

where  $N_0$  is the signal (in  $e^-/s$ ) in the bin and represents the source photon noise variance per unit time,  $X$  is a factor that accounts for instrumental noise sources that are proportional to the signal, and  $N_{min}$  is an instrumental noise floor (in  $e^-/s$ ) that is not proportional to the signal.

$X$  is assumed not to have a wavelength dependency, and will encompass read noise and jitter noise. As shown in Chapter 4, we find through using ExoSim

<sup>19</sup> I use the term ‘noise variance’ in this thesis to indicate this variance is being used as measure of the noise, however it is actually the variance of the signal.

that both read noise and jitter noise are actually wavelength-dependent. Since the ERM does not model  $X$  with a wavelength dependency, it was decided to set  $X$  to 0 and to also exclude jitter and read noise from the ExoSim simulations to permit a valid comparison.

$N_{min}$  will include noise from dark current, zodiacal light and instrument emission (though the latter two are not significant compared to the dark current as shown in chapter 4). An aperture mask is assumed to be applied in data reduction on each image around the spectrum prior to extraction (to minimize background and instrumental noise). The width of this mask in the spatial direction is assumed to extend between the first Airy minima on either side of the spectrum, i.e.  $2.44 f\lambda$  in width (where  $f$  is the channel f-number and  $\lambda$  is the wavelength). Only instrumental noise within the aperture is included in  $N_{min}$ . Assuming that only dark current contributes,  $N_{min}$  in  $e^-/s$  per spectral bin can be expressed as:

$$N_{min}(\lambda) = \frac{2.44f\lambda^2}{mR\Delta_{pix}^2} I_{dc} \quad (2.35)$$

where  $I_{dc}$  is the dark current per pixel,  $m$  is the reciprocal linear dispersion of the spectrum in  $\mu\text{m}$  wavelength per  $\mu\text{m}$  distance,  $R$  is the spectral resolving power and  $\Delta_{pix}$  is the pixel pitch. This equation was used in the ERM to generate  $N_{min}(\lambda)$  for this comparison study.

For this test the stars 55 Cancri and GJ 1214 were simulated in each simulator. 55 Cancri is a G8 star with multiple orbiting planets including the hot super-Earth 55 Cancri e, and is one of the brightest targets for the ARIEL mission at K mag 4.015. GJ 1214 is an M4.5 dwarf and host to the well-studied super-Earth GJ 1214b ( $6.55 M_{\oplus}$ ). At K mag 8.78 it represents one of the dimmest targets for ARIEL. The same model PHOENIX spectra were used for each star in each simulator.

The test was performed at an early stage in the ARIEL design study with a candidate grating spectrometer design consisting of 2 infra red channels, Ch0 (1.9-3.9  $\mu\text{m}$ ) binned to  $R=100$ , and Ch1 (3.9-7.8  $\mu\text{m}$ ) binned to  $R=30$ , and a telescope aperture area of  $0.636 \text{ m}^2$ . Other key features of the design are given in Table 2.1.

Only photon noise and dark current noise were simulated in ExoSim, and no inter- or intra-pixel QE variations were applied to allow a valid comparison with the ERM.

Exosim exposure times (after CDS) in both channels for 55 Cancri and GJ 1214 were 0.66 s (95.6% duty cycle) and 40.13 s (99.9% duty cycle) respectively. 500 exposures taken for 55 Cancri and 156 exposures for GJ 1214. For the purposes of this test the integration time was not a critical factor since it is divided out later

TABLE 2.1 Configuration of the ARIEL model used in ExoSim for comparison with the ESA Radiometric Model. Units of reciprocal linear dispersion are  $\mu\text{m}$  of wavelength per  $\mu\text{m}$  of distance.

Parameter	Ch0	Ch1
Wavelength coverage ( $\mu\text{m}$ )	1.95-3.9	3.9-7.8
R (instrument)	98	29
f-number	20.5	10.3
Reciprocal linear dispersion ( $\mu\text{m}/\mu\text{m}$ )	$4.896 \times 10^{-4}$	$3.2883 \times 10^{-3}$
Optical efficiency	0.44	0.44
Quantum efficiency	0.55	0.55
Pixel size ( $\mu\text{m}$ )	18	18
Pixel scale ( $^{\circ}$ /pixel)	5.5833	11.1666
Dark current ( $\text{e}^-/\text{s}$ )	32	120

to obtain counts per unit time. In this test we used an early iteration of ExoSim which outputted a completely noiseless time series of images alongside images with noise<sup>20</sup>.

The ExoSim data reduction pipeline used here was an early variant of the basic pipeline used for ARIEL performance testing in Chapter 4 and elsewhere in this thesis, and is described in more detail in Chapter 4. The pipeline consisted of background subtraction, CDS<sup>21</sup>, a wavelength-dependent aperture mask (applied after dividing into sub-pixels in the spatial direction) centred on the spectrum of width  $2.44 f\lambda$ , i.e. to the first Airy minimum (omitted for the noiseless time series as explained below), integration of the pixel counts per column, and finally binning into spectral resolving element-sized bins. Later versions of the pipeline used a method that performs R-binning across a pixelised spectrum by dividing the whole pixel counts into sub-pixels for finer bin sizes, but here I used interpolation of the signal and noise variance to a sub-pixel-sized grid to achieve this. Flat fielding was not performed in this case since QE variations were omitted.

The noise-containing time series were used to find the noise variance per unit time per spectral bin. The noiseless time series were used to find the signal per unit time per bin.

For each star, 50 ExoSim realizations were performed and processed, from which the average noise variance per unit time per spectral bin was found. The

<sup>20</sup> Due to production of large file sizes, the simultaneous production of noiseless and noise-containing time series was later removed.

<sup>21</sup> This was strictly speaking not necessary in the absence of read noise, but was left in as it was part of the developed pipeline and would have no impact on the results.

noise-free signal did not vary between realizations.

For the noise comparison, I calculate that the aperture masking of the ExoSim images, will cut out approximately 6.8% of the total energy of an Airy disc and thus its associated source noise. To permit a valid comparison, an aperture correction factor of 0.932 was multiplied into to the ERM photon noise variance per bin to account for aperture masking.

For the signal comparison, I omitted aperture masking of the ExoSim noiseless exposures when finding the signal so that a direct comparison with the ERM signal could be made without applying any aperture correction factor.

There is good agreement between ExoSim and the ERM (Figure (2.9)). For 55 Cancri case, the mean difference of ExoSim from the ERM is +1.1% for the signal and +1.0 % for the averaged noise variance. The mean difference of the ERM from ExoSim is -1.1% for the signal and -1.0% for the noise variance. Overall wavelength bins, the ExoSim signal is always within 2% of the ERM, and the ERM signal is within 2% of ExoSim. The ExoSim averaged noise variance is always within 6% of the ERM, and the ERM noise variance is always within 5% of ExoSim. In 94% of the bins, the ERM noise variance is within the standard deviation of the ExoSim noise variance.

For the dimmer target, GJ 1214, the signals are again well-matched, the mean deviation of the ExoSim signal from the ERM being -0.1%, and the mean deviation of the ERM from ExoSim being +0.2%. The ExoSim signal is always within 4% of the ERM over all bins and the ERM signal is always within 4% of ExoSim. In GJ 1214, the instrument noise (basically the dark current noise) is now significant, manifesting as the flattened region at the longer wavelength ends of both channels. Both simulators, which model dark current independently, produce equivalent results. The average ExoSim noise variance has a mean difference of -1.3% from the ERM, and the ERM noise variance has a mean difference of +1.4% from ExoSim. The ExoSim noise variance is within 5% of the ERM over all bins, and the ERM noise variance is within 6% of ExoSim over all bins. Furthermore ERM noise variance is within the standard deviation of the ExoSim noise variance in all bins.

These results cross-validate the signal and noise models of each simulator. This test was an important result for the ARIEL Phase A study as it validated the use of the ERM (against the more thoroughly validated ExoSim) in simulating the ARIEL Mission Reference Sample (Zingales et al., 2017) and testing whether the mission survey goals could be achieved in the available observing time.

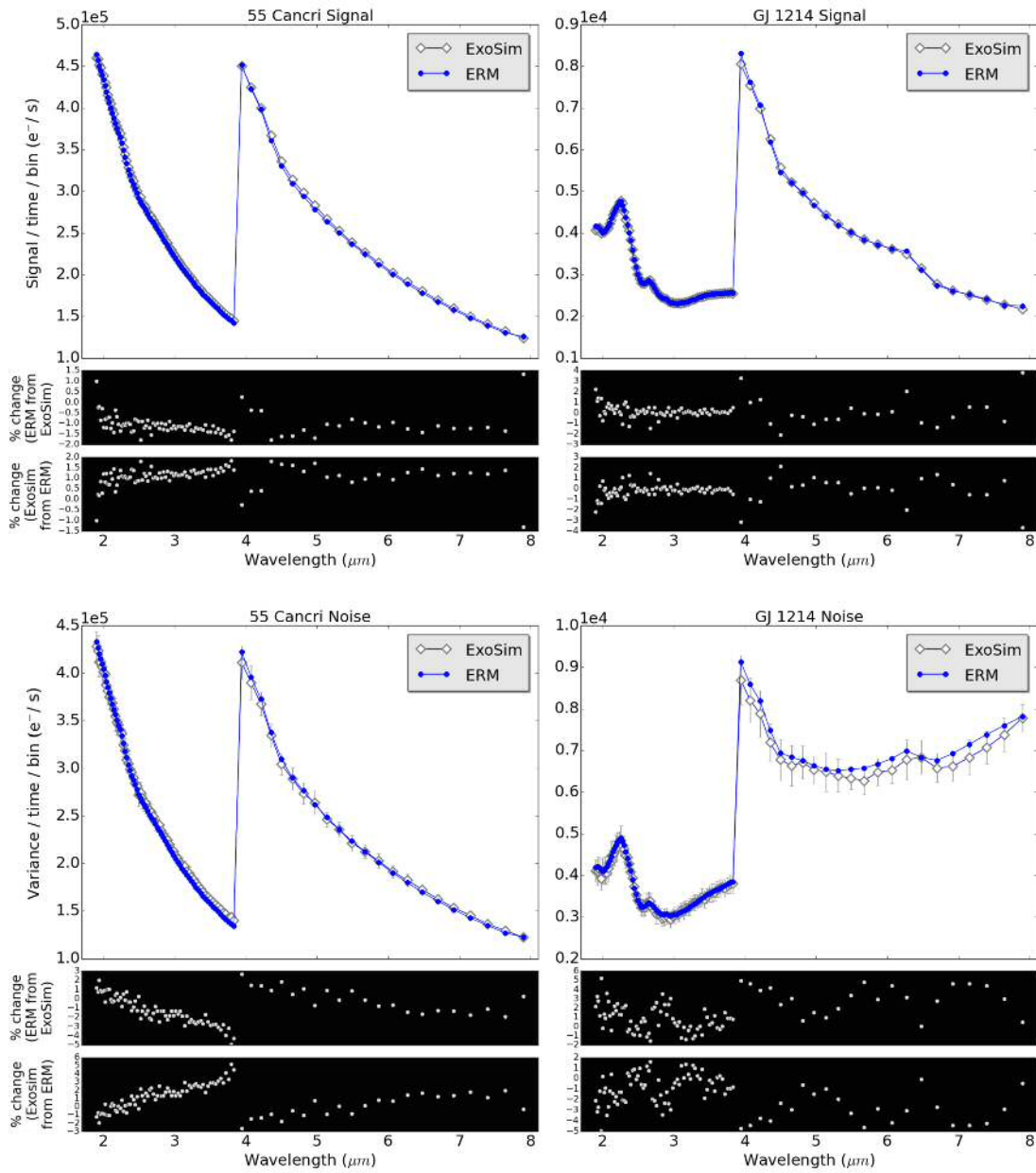


FIGURE 2.9 ExoSim and ESA Radiometric Model cross-validation test. Charts show signal per unit time (top) or noise variance per unit time (bottom) in spectral-resolution-element-sized bins ( $R=100$  for  $1.9\text{--}3.9\ \mu\text{m}$ ,  $R=30$  for  $3.9\text{--}7.8\ \mu\text{m}$ ) for the stars 55 Cancri (left), and GJ 1214 (right). The ExoSim noise results show the average noise variance per unit time for 50 realizations with the standard deviation shown as error bars. Subplots show the percent difference of ExoSim from the ERM and the percent difference of the ERM from ExoSim.

### 2.2.3 VALIDATION OF JITTER NOISE MODEL

The baseline mechanism of the jitter code, i.e. the conversion of signal position variation to photometric variation was tested for validity as follows. Firstly, for the purposes of this test, the ExoSim simulation was simplified to produce a single monochromatic beam using a 2-D Gaussian model. The beam was centred over a known pixel, designated with coordinates (0,0). The beam had a full-width-at-half-maximum (FWHM) of 2.27 pixels, and was normalized to produce a peak photoelectron count of unity on the central pixel. Intra- and inter-pixel variations were disabled. For each axis on the focal plane, an independent white noise jitter timeline was generated with the same standard deviation,  $rms_{jit}$ . The jitter code was run for 1000 jitter time steps, shifting the position of the beam over the pixel grid at each step. The counts on pixels (0,0), (1,1), (2,2) and (3,3), at progressively further distances from the centre of the jitter, were collected for each jitter time step, and the standard deviation of these counts gave the pixel noise  $\sigma_{(a,a)}$  where  $(a, a)$  is the pixel coordinate. The test was repeated at  $rms_{jit}$  of 0.1, 0.2, 0.3, 0.5 and 1.0 pixels.

These results were compared to an analytical expression based on a second order Taylor expansion, that was derived for the expected variation of the count of an equivalent 2-D Gaussian function. The derivation is given in the Appendix.

$$\sigma_{(a,a)} \approx \left[ \exp(-a^2/2s^2) \left( 4rms_{jit}^4 \left[ \frac{a^2 - s^2}{s^4} \right]^2 + rms_{jit}^2 \left[ \frac{2a^2}{s^4} \right] \right) \right]^{1/2} \quad (2.36)$$

where  $\sigma_{(a,a)}$  is the standard deviation of the count predicted at position  $(a, a)$ , and  $s$  is the standard deviation of the 2-D Gaussian ( $s \approx \text{FWHM}/2.355$ ). This expression will be most accurate for small values of  $rms_{jit}$ . The predicted values of  $\sigma_{(a,a)}$  for a 2-D Gaussian matching the ExoSim beam were calculated and compared to the noise measured using ExoSim. The comparison is shown in Figure 2.11, top.

There is good agreement in the absolute counts, ExoSim being within  $2.5 \times 10^{-2}$  counts of the prediction upto  $a = 3$ . In terms of percent deviation from the prediction, ExoSim and the prediction are in good agreement at low values of  $rms_{jit}$  and  $a < 3$ . For example if  $rms_{jit}$  is 0.1 pixels, ExoSim is within 4% of the prediction for  $a < 3$ . However the percent deviation worsens with larger values of  $rms_{jit}$  as may be expected due to the Taylor approximation, and are worst at  $a = 3$ . The greatest difference is 133% at  $rms_{jit}$  of 0.3 pixels and  $a = 3$ .

To assess validity of ExoSim at higher values of  $rms_{jit}$ , I supplemented this

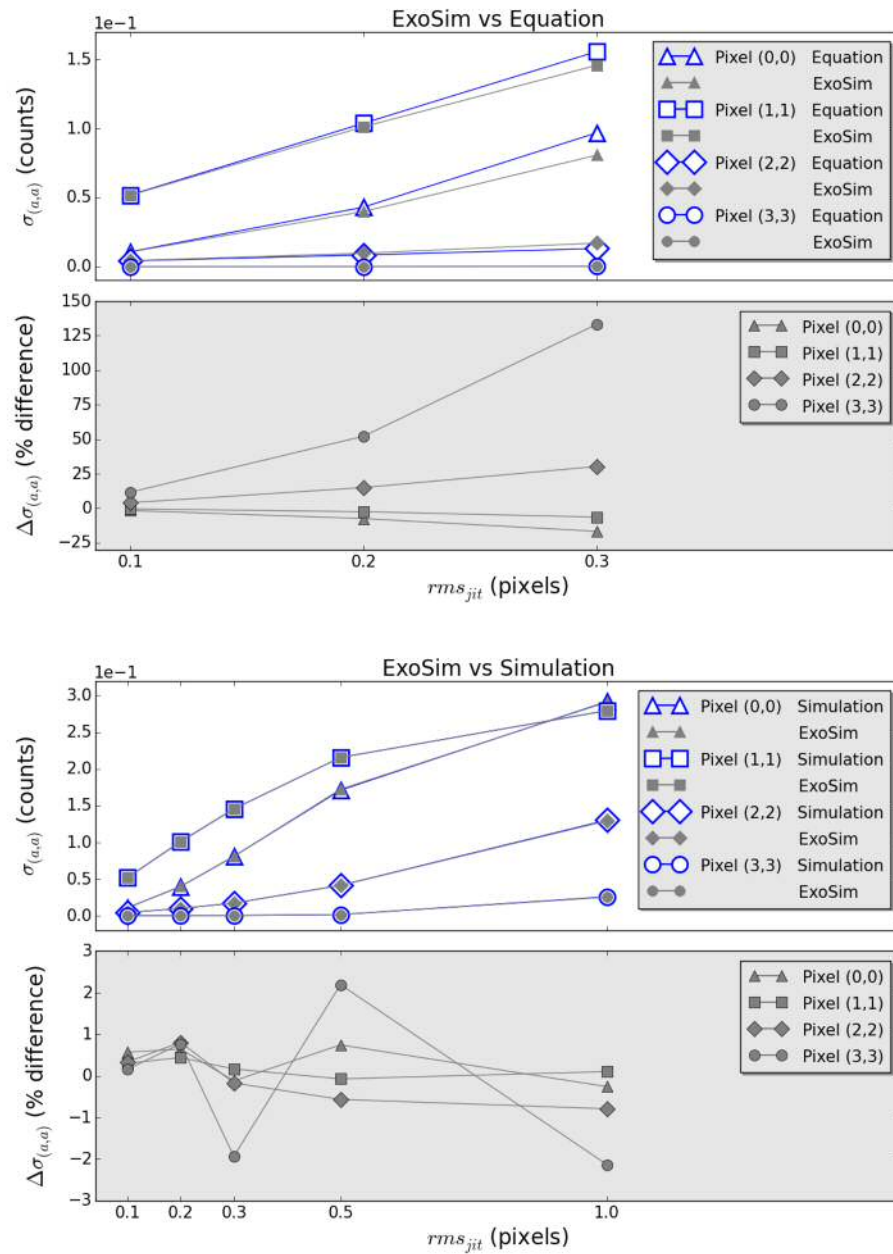


FIGURE 2.10 ExoSim jitter noise compared to predictions for pixel positions shown. Top: ExoSim compared to Equation 2.36. Bottom: Exosim compared to independent simulation. Subplots show percentage difference of ExoSim from the prediction.

analysis by conducting a simple computer simulation of a 2-D Gaussian, matched in size to the ExoSim beam. This function was sampled repeatedly around central points corresponding to pixels  $(a, a)$  [ $a=0,1,2,3$ ]. The local region of the 2-D Gaussian was sampled  $10^6$  times around each point with a random normal distribution of standard deviation  $rms_{jit}$  in each axis. The resulting standard deviation in the count,  $\sigma_{(a,a)}$  at each point  $(a, a)$  was compared with the results from ExoSim as shown in Figure 2.11, bottom.

With this independent simulation we obtain a good agreement upto the higher values of  $a$  and  $rms_{jit}$ , ExoSim always being within 3% of the independent simulation. These results verify the accuracy of the baseline mechanism used in ExoSim's pointing simulation. Additional tests were performed verifying that the pointing jitter is adequately captured using the spatial oversampling method used, and that the jitter noise is independent of the frame rate of the simulation.

#### 2.2.4 VALIDATION OF JITTER NOISE SPATIAL SAMPLING METHOD

Here I check the assumption that the jitter noise is fully sampled by using an oversampling factor of  $f' = 3/rms_{jit}$  in the jitter algorithm, where  $rms_{jit}$  is the standard deviation of the jitter offsets in each axis in units of pixel length.

I vary  $f'$  directly in the code and measure the resulting jitter noise,  $\sigma_{jit}$ , at each value, while keeping the rms of the jitter in each axis,  $rms_{jit}$ , constant. For this test ExoSim uses a model of the Hubble WFC3 IR instrument, which is described in more detail in Chapter 3. This model can be operated in either the usual staring mode or 'spatial scanning' mode. For this test, staring mode was used, and GJ 1214 chosen as a stellar target, observed OOT with jitter noise only activated. Each observation consisted of 144, 88 s exposures, with a simulation frame rate of 2 Hz. Multiaccum<sup>22</sup> was set at 2, with the second subexposure lasting 86.5 s, giving a CDS exposure time ( $NDR_1-NDR_0$ ) of also 86.5 s. This exposure time is realistic for scanning mode but not staring mode (as it would cause detector saturation), however for the purposes of this test it was useful to have a long integration time, so that the jitter-induced variations within the CDS exposure time, as well as the count variations between exposures, could be determined. Inter-pixel QE variations of 3% rms and wavelength-dependent variations of 0.5% rms are included, but no significant intra-pixel variations (more details given in Chapter 3). Residual uncertainties in QE of 0.5% rms are left in which are not flat-fielded.

There were 2595 jitter subframes within each CDS exposure. In this study,

<sup>22</sup> Multiaccum refers to the number of subexposures or NDRs selected per exposure.

I measure this 'intra-exposure' jitter noise as a photometric count rate variation within the 2nd subexposure of each simulation, though in reality it will be 'unresolved', manifesting as smearing of the PSF on the final exposure, being the result of jitter frequencies higher than the cadence of the observation. This is discussed further in Chapter 4.

A model of the Hubble pointing jitter PSD was used (see Chapter 3 for its development) with overall  $rms_{jit}$  in each axis of 2.6 mas, and bi-axial  $rms_{jit}$  of 3.7 mas, which produces correlated non-white jitter timelines. The goal  $f'$  is given by  $3P/rms_{jit}$  where  $P$  is the plate scale in  $^{\circ}/\text{pixel}$ , and  $rms_{jit}$  is in degrees. For the WFC3 model with a plate scale of  $3.61 \times 10^{-5} \text{ }^{\circ}/\text{pixel}$ , the goal value of  $f'$  is 150.

The data were processed with a pipeline (described further in Chapter 3) consisting of flat fielding, background subtraction, CDS, masking with a 31 pixel high rectangular aperture centred on the spectrum, extraction of the spectrum per CDS frame by simple column integration, and finally binning into 5 pixel wide bins.

Figure 2.11 shows the results for 2 selected wavelength bins centred at 1.088 and 1.673  $\mu\text{m}$ . The findings show that as  $f'$  is initially increased so more and more jitter noise is captured upto a peak value at around  $f' = 21$  (14% of the goal  $f'$ ) for noise within the exposure, and  $f' = 27$  (18% of the goal  $f'$ ) for noise between exposures. The noise then falls with increased sampling (more noticeable for jitter noise within the exposure) eventually reaching a steady state, which likely represents the 'true' level of noise. The peak may be due to digitization noise. Steady state is definitely attained by the predicted goal  $f'$  of 150, which indicates the  $f'$  calculation used in ExoSim will indeed capture the noise fully as required for both jitter noise within the exposure time and jitter noise between exposures.

One issue that arises from this however, is that running the simulation with an  $f'$  of 150 (or more) places major demands on computer memory and severely slows down the simulation. For Monte Carlo simulations in particular this would be major problem. This effect will be worst for instruments with small rms pointing jitter such as Hubble. Figure 2.11 however shows that near-steady state values are obtained at much lower values of  $f'$  than the goal. For example at  $f' = 51$  (about 1/3 of the goal value) the noise values for jitter noise within the exposure are all within 5% of that at  $f' = 153$ , and within 1% for jitter noise between exposures.

Thus we can run simulation at 1/3 of the goal  $f'$  value, if needed, and should still obtain good accuracy on the simulated jitter noise. We make use of this finding in Chapter 3 where we perform Monte Carlo simulations using this Hubble model.

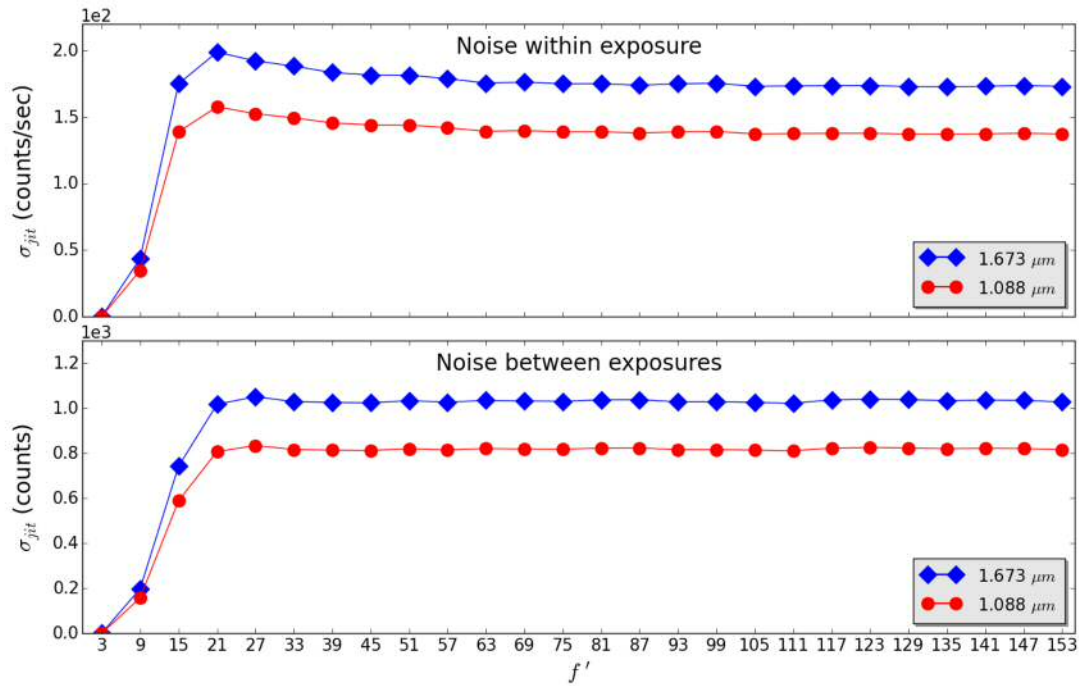


FIGURE 2.11 Jitter noise,  $\sigma_{jit}$ , vs pixel oversampling rate,  $f'$ . Top: Noise within CDS exposure (variation in count rate between jitter subframes within the 2nd subexposure of each simulation). Bottom: Noise between CDS exposures (variation in count between exposures).

### 2.2.5 VALIDATION OF JITTER FRAME RATE INDEPENDENCE

The final test performed on the jitter code was to ensure that the jitter noise generated was independent of the simulation frame rate. Again, the Hubble WFC IR model was used with the simulated GJ 1214 target observed out-of-transit with jitter noise only and with multiaccum set to 2. The test was repeated using two different CDS exposure times: 86.5 s (with 144 exposures), and 10 s (with 250 exposures). The Herschel jitter PSD model (with bi-axial  $rms_{jit}$  of 129 mas) was used rather than the Hubble PSD, so as to provide larger jitter for testing purposes.

In each case, the simulation frame rate was varied from 2 to 80 Hz. 100 simulations were performed at each frame rate in order to obtain an average noise,  $\sigma_{jit}$ . The same data reduction process as above was used, and the average noise within the CDS exposure time (the variation in count rate between jitter subframes within the 2nd subexposure of each simulation) and the average noise between CDS exposures were found for 5 pixel-wide bins at each frame rate.

Over the frame rates examined (Figure 2.12) we find that the average noise

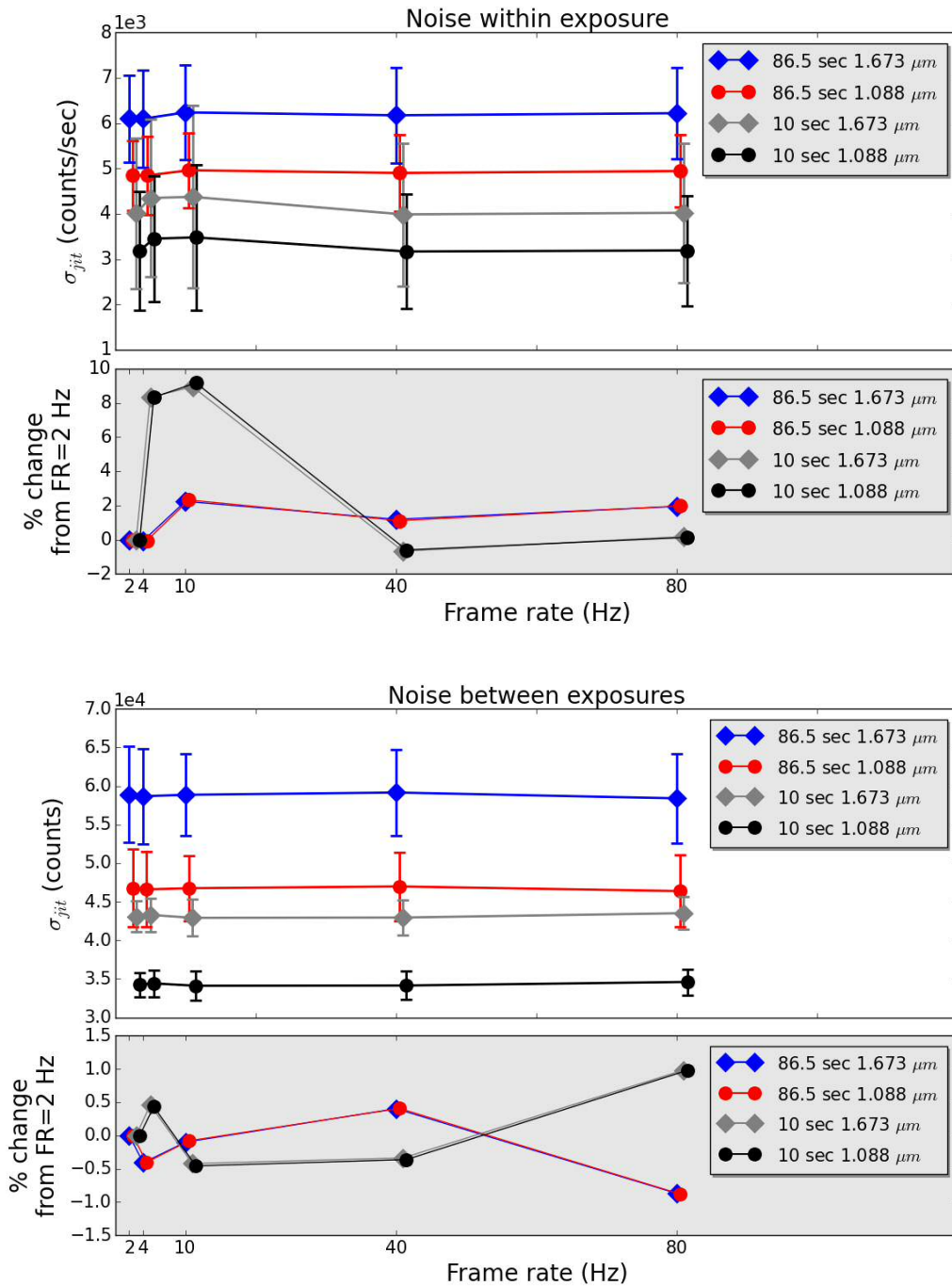


FIGURE 2.12 Verifying that ExoSim jitter noise is frame-rate independent. y axis shows average noise,  $\sigma_{jit}$ , obtained from 100 simulations for 5 pixel wide bins at 1.637 and 1.088  $\mu\text{m}$  with error bars showing the standard deviation in each case. x axis shows simulation frame rate. Points are offset slightly for clarity. Top: Noise within CDS exposure (variation in count rate between jitter subframes within the 2nd subexposure of each simulation). Bottom: Noise between CDS exposures (variation in count between exposures). Repeated for CDS exposure times of 86.5 s and 10 s. Subplots show percentage difference compared to the noise at frame rate = 2 Hz.

within an exposure is always within 9% of the value at frame rate = 2 Hz. The average noise between exposures is within 1% of the value at frame rate = 2 Hz. The variations between frame rates are small compared to the absolute noise at each frame rate, indicating that the jitter noise is largely independent of the frame rate used. This is true for both short (10 s) and long (86.5 s) exposures.

### 2.2.6 EXOSIM VS HUBBLE WFC3

ExoSim results using the model of the Hubble WFC3 IR instrument simulating a primary spectroscopic transit of the super-Earth, GJ 1214b, were compared to results from two transit spectroscopy studies with WFC3 IR that observed GJ 1214b, Berta et al. (2012) (hereafter B12) observing in staring mode, and Kreidberg et al. (2014a) (hereafter K14) observing in spatial scanning mode. GJ 1214 was simulated with a PHOENIX model spectrum ( $T=3000$  K,  $\log g=5.0$ ,  $[\text{Fe}/\text{H}]=0$ ) and all remaining stellar and planet parameters obtained via the OEC.

Firstly the OOT focal plane spectrum, in  $e^-/s$  per pixel column, from ExoSim was compared to that published in B12 (Figure 2.13). Over the range 1.10-1.67  $\mu\text{m}$  we find that the ExoSim spectrum is sometimes higher and sometimes lower than the B12 spectrum, averaging 2% lower, with a peak-to-peak variation of +8 to -11%. Considering that a model is being compared to the real star and instrument, the spectrum is remarkably similar. Integrated over all pixel columns, the total photoelectron count is  $2.665 \times 10^6 e^-/s$  for ExoSim, compared to  $2.707 \times 10^6 e^-/s$  for B12, a 1.6% difference.

Next ExoSim was compared to results from K14. For this, 20 ExoSim simulations were performed with observational parameters closely matched to those used in K14: spatial scanning at  $12''/s$ , 90 s exposures<sup>23</sup>, 160 s cadence and 12 subexposures per exposure. The characteristic 'ramp' systematic due to detector persistence, and gaps in data due to Earth occultation were not simulated. ExoSim utilized the same linear wavelength-dependent limb-darkening coefficients obtained in K14<sup>24</sup>, with the average (0.2674) used outside the published wavelength range. A flat planet transmission spectrum (consistent with known results for this planet) was used, with a planet-star radius ratio of 0.11619, i.e.  $(R_p/R_s)^2 = 0.0135$ .

<sup>23</sup> Compared to 88.1 s in K14. A frame of 2 was used in these tests which limited the values of the exposures time to the nearest 0.5 seconds, hence 90 seconds was the closest to the 'real' exposure time. It is unlikely this 2% difference will significantly affect the comparison. The low frame rate was due to using the same simulation set up as in Chapter 3 where it helps to optimize speed for Monte Carlo simulations.

<sup>24</sup> These were the limb-darkening coefficients obtained after using the 'divide-white' systematic correction method to eliminate the 'ramp'.

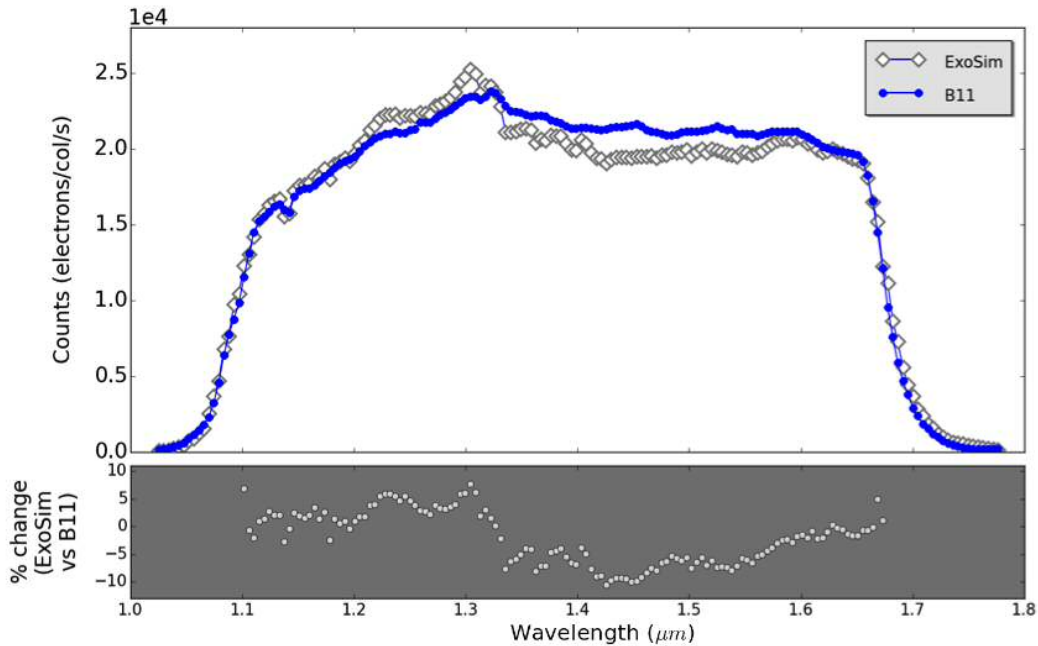


FIGURE 2.13 Comparison of focal plane spectrum from ExoSim and B12 showing photoelectron counts per pixel column per second. Subplot shows percent deviation of ExoSim from B12, over the wavelength range 1.10-1.67 microns. The B12 spectrum was resampled from the original paper using WebPlotDigitizer (Rohatgi, 2017).

Details of the data reduction pipeline used are given in Chapter 3.

I first compare the absolute photoelectron counts in the ‘white light’ curves, i.e. the full array photoelectron counts per exposure (Figure 2.14, top). I find that the average OOT photoelectron count from ExoSim to be  $2.35 \times 10^8 e^-$ , compared to  $2.34 \times 10^8 e^-$  from orbits 2 and 4 in K14. ExoSim is thus within 0.5% of the K14 value. This is within the reported 1% peak-to-peak stellar variability for the parent star in the visual range (Berta et al., 2011). However whilst this is supportive of ExoSim replicating the real star counts closely, some of this agreement is probably fortuitous; minor changes in the simulation such as choosing a slightly different temperature for the PHOENIX spectrum or adopting different values from the literature for  $R_s$  or distance, will cause the absolute value to go up or down; in addition as noted, the ExoSim integration time is 2% longer than in K14, so the simulation may be slightly underestimating the stellar flux compared to the real star. In addition the systematic correction by K14 could possibly have affected the absolute photoelectron counts shown. Taking these caveats into account ExoSim is probably still replicating the true count to within a few percent, which is a good

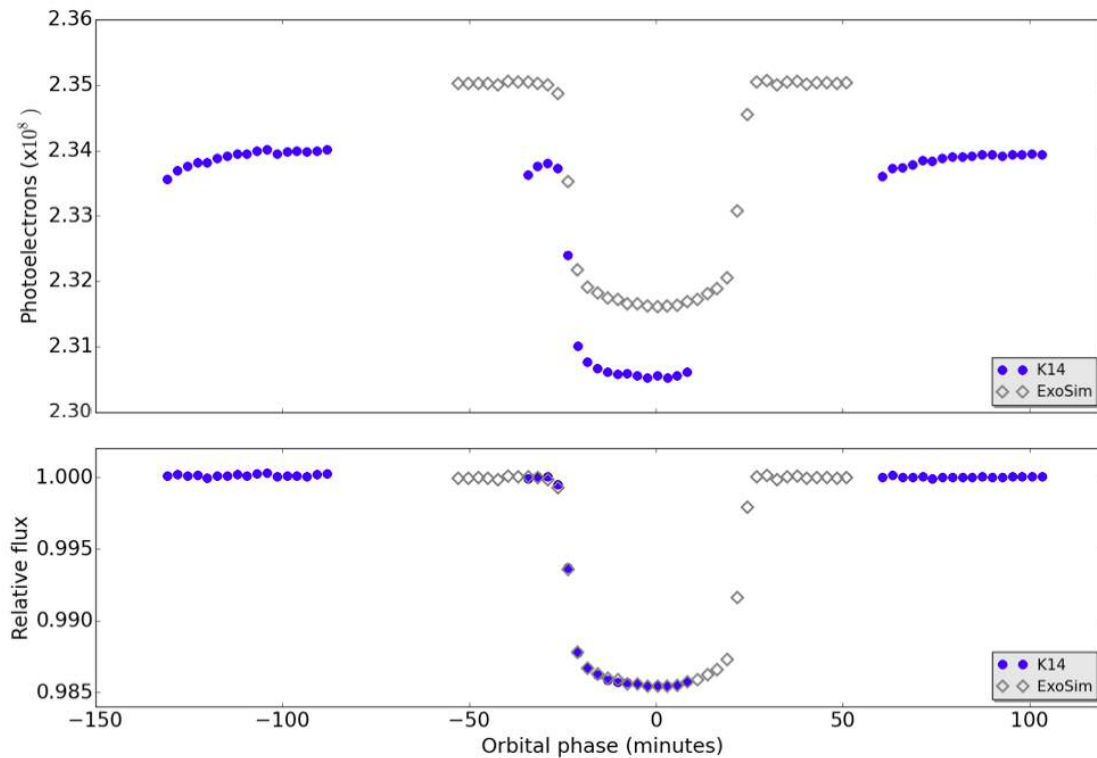


FIGURE 2.14 Comparison of white light curves from ExoSim and K14. Shown are the results from one of 20 ExoSim realizations. K14 data obtained by resampling published graph with WebPlotDigitizer (Rohatgi, 2017). Top: absolute photoelectron counts. Bottom: normalized light curves (with systematic correction in K14). Only orbits 2-4 are shown from K14.

result for absolute counts. However a better comparison may be to compare the normalised light curves.

Therefore, I compared the white light curves from ExoSim normalised to OOT signal, with the example from K14 where in addition to OOT normalisation, the 'ramp' systematic was detrended (Figure 2.14, bottom). The photometric noise on the residuals matches closely: 70 ppm reported in K14, and  $68 \pm 7$  ppm from ExoSim<sup>25</sup>. Comparing the K14 transit curve to one of the 20 ExoSim simulations shown in Figure 2.14 (bottom), visually there is a remarkable similarity in the transit profiles.

To further evaluate the similarity of the transit light curves, the 17 data points from K14 orbit 3 (the partially transiting portion of the normalised white light curve) were compared to the 17 time-matched data points in each of the 20

<sup>25</sup> Standard deviation of all residuals after a curve fitting each white light curve with a Mandel-Agol model with fixed linear limb darkening coefficient of 0.2674 (the average value from K14).

ExoSim simulations, using the 2 sample Kolmorov-Smirnoff (K-S) test. The 2 sample K-S test is used to test the null hypothesis that the two samples come from the same distribution. The test was performed for each of the 20 ExoSim simulations. An average K-S statistic was obtained of  $0.16 \pm 0.04$ , and an average p-value of  $0.9 \pm 0.1$ . Assuming a significance level of 5% ( $\alpha = 0.05$ ) for rejection of the null hypothesis, these results fail to reject the null hypothesis that the two distributions are different, and are thus supportive of the similarity between the ExoSim and K14 light curves.

We have therefore found a number of metrics in good agreement between ExoSim and the real data from these two studies. This gives us additional confidence in the accuracy of the complete end-to-end ExoSim simulation.

## 2.3 DISCUSSION

In this chapter, the ExoSim algorithm was presented together with the results of validation testing. ExoSim was designed to meet the requirements set out at the end of Chapter 1. These include ensuring that it is completely generic which is key to expanding its versatility, beyond that of previous simulators. The requirements also stated ExoSim must be validated extensively. I have shown several validation tests of the ExoSim signal and noise model, from focused evaluation of the fundamental noise mechanisms to comparing the end-to-end simulation of a light curve with a real world example. ExoSim's novel 2-D pointing jitter algorithm has also been tested and appears robust and consistent with predictions. ExoSim therefore stands out from other simulators in its validation testing. This not only adds confidence to using ExoSim, but also allows ExoSim to validate other simulators (e.g. the ESA Radiometric Model). In summary we can say ExoSim is accurate to within 5% in most tests using variety of comparisons with simple models, alternate simulators and real data.

---

ExoSim's capabilities are tested and applied in the next four chapters of this thesis. The simulator is applied to different instruments and used to solve a range of different problems within transit spectroscopy. Firstly, in Chapter 3, ExoSim is used to elucidate a complex form of instrumental noise on the Hubble WFC3 IR instrument which is thought may arise due to spatial scanning across the pixel array. Then in Chapter 4, ExoSim is utilized within the Phase A design

study for the proposed ARIEL mission, where it served as the mission's end-to-end simulator. In Chapter 5, ExoSim is applied to simulations of astrophysical noise, addressing the problem of stellar variability and activity on the accuracy of transit spectroscopic observations in the context of the ARIEL mission. Finally in Chapter 6, ExoSim is applied to the feasibility of characterising terrestrial planets in the context of the ARIEL mission and the newly discovered TRAPPIST 1 planets. Full transit Monte Carlo simulations are used in Chapters 3 and 5, and out-of-transit mode simulations are used in Chapters 4, 5 and 6.

## CHAPTER 3

# SIMULATING THE HUBBLE WIDE FIELD CAMERA 3

---

**O**BSERVATIONS using ‘spatial scanning’ mode have been performed with the Hubble Wide Field Camera 3 infrared instrument (WFC3 IR) for numerous exoplanet transit and eclipse spectroscopy studies. Scanning the image allows for an increased integration time per exposure compared to ‘staring’ mode, increasing the duty cycle, and permitting observation of brighter targets since pixel saturation is delayed. However it may introduce an additional error in the measurements, possibly increasing the final uncertainty on the reconstructed planet spectrum. One study suggested scanning mode was inferior to the usual staring mode in terms of noise and consistency. Various authors have noted possible signatures of additional noise. Despite this, scanning mode has been utilised extensively in recent exoplanet transit spectroscopy studies using WFC3. In this chapter, as an initial test of the generic simulator, the Hubble WFC3 IR instrument is modeled within ExoSim, and scanning mode observations simulated. Using a Monte Carlo approach the uncertainties on the final transmission spectrum are obtained for the case of GJ 1214b in both scanning and staring mode, and compared. This study demonstrates ExoSim’s capability in elucidating the contribution of a complex instrumental noise source directly on the spectrum and in modeling a real existing instrument. The study may either add confidence in the results from existing scanning mode observations or may call into question the published uncertainties<sup>1</sup>.

---

<sup>1</sup> Material from this chapter is presented in Sarkar et al. (2017b).

## 3.1 BACKGROUND

The Hubble Space Telescope (HST) has been extensively used for exoplanet transit and eclipse spectroscopy starting with Charbonneau et al. (2002) obtaining the first detection of an atmospheric species with the STIS instrument. Today the lead instrument for transit spectroscopy on Hubble is the Wide Field Camera 3 infrared instrument (WFC3 IR) used mostly with the G141 grism, which covers the wavelength range from 1.1 to 1.7 microns at  $R \approx 130^2$ . This instrument was installed in 2009 on HST servicing mission 4, and has been used for many exoplanet spectroscopy studies listed in Table 3.1. These include both transmission and emission spectroscopy studies such as the ‘deep field’ study of GJ 1214b (Kreidberg et al., 2014a), as well as phase-resolved emission spectroscopy (Stevenson et al., 2014).

WFC3 has 2 channels: ultra-violet and visual (UVIS) and infrared (IR) (Dressel, 2017) with the IR channel being the one so far used for transit spectroscopy studies. Both channels were designed to perform slitless spectroscopy. The UVIS channel has the G280 grism ( $R = 70$ , wavelength range 190-450 nm), whereas the IR channel has 2 grisms: G102 ( $R = 210$ , 800-1150 nm) and G141 ( $R = 130$ , 1075-1700 nm). This latter grism is the one most used for exoplanet studies though one study has used both the G102 grism and the G141 grism (Kreidberg et al., 2015).

### 3.1.1 SPATIAL SCANNING ON THE WFC3 IR

Since 2012, ‘spatial scanning’ mode has been used for exoplanet transit spectroscopy studies using WFC3 IR in addition to the usual ‘staring’ mode. In the latter, the spectrum remains static on the detector (within the limits of the baseline pointing jitter). In scanning mode, the spacecraft is moved (‘nodded’) in the spatial direction during the exposure so that the spectrum sweeps out a rectangular region over a large number of pixels (Figure 3.1). This allows for a longer overall exposures since the flux is spread over many pixels preventing saturation, resulting in an increase in the duty cycle. Therefore for the same total observing time, more photons will be obtained in scanning mode compared to staring mode. This mode is also be useful for observing brighter targets to avoid saturation.

However scanning mode does introduce the potential for additional correlated noise and systematics. This is because of the increased potential for spatio-temporal variation in the detector pixels sampling the image with each exposure.

---

<sup>2</sup> [http://www.stsci.edu/hst/wfc3/analysis/grism\\_obs/wfc3-grism-resources.html](http://www.stsci.edu/hst/wfc3/analysis/grism_obs/wfc3-grism-resources.html)

TABLE 3.1 Exoplanet transit and eclipse spectroscopy studies performed with the Hubble WFC3 IR instrument and the G141 grism.

Study	Exoplanet	Type	Transmission or Emission	Observing mode	Spectrum detail
Berta et al., 2012	GJ 1214b	Super-Earth	Transmission	Staring	Featureless
Gibson et al., 2012	HD 189733b	Hot Jupiter	Transmission	Staring	Haze dominates into NIR
Mandell et al., 2013	WASP-12b	Hot Jupiter	Transmission	Staring	Weak water feature; flat spectrum almost as likely
	WASP-17b	Hot Jupiter	Transmission	Staring	Water detected
	WASP-19b	Hot Jupiter	Transmission	Staring	Weak water feature; flat spectrum almost as likely
Deming et al., 2013	HD 209458b	Hot Jupiter	Transmission	Scanning	Weak water feature; suggests grey opacity
	XO-1b	Hot Jupiter	Transmission	Scanning	Weak water feature
Line et al., 2013	HAT-P-12b	Warm sub-Saturn	Transmission	Staring	Featureless
Swain et al., 2013a	WASP-12b	Hot Jupiter	Transmission & Emission	Staring	Pure H <sub>2</sub> favoured by BIC; no evidence of inversion; TiO/VO detected
Wakeford et al., 2013	HAT-P-1b	Hot Jupiter	Transmission	Scanning	Water detected
Wilkins et al., 2014	CoRoT-2b	Hot Jupiter	Emission	Staring	Featureless
Knutson et al., 2014a	GJ 436b	Warm Neptune	Transmission	Scanning	Featureless
Knutson et al., 2014b	HD 97658b	Super-Earth	Transmission	Scanning	Featureless
Ehrenreich et al., 2014	GJ 3470b	Warm Uranus	Transmission	Staring	Featureless
Ranjan et al., 2014	TrES-2b	Hot Jupiter	Transmission	Staring	Featureless
	TrES-4b	Hot Jupiter	Transmission	Staring	Featureless
	CoRoT-1b	Hot Jupiter	Transmission	Staring	Featureless
	TrES-3b	Hot Jupiter	Emission	Staring	Most consistent with low metallicity atmosphere
	WASP-4b	Hot Jupiter	Transmission & Emission	Staring	Most consistent with carbon-rich atmosphere
Fraine et al., 2014	HAT-P-11b	Warm Neptune			Water detected
McCullough et al., 2014	HD 189773b	Hot Jupiter	Transmission	Scanning	Water detected
Crouzet et al., 2014	HD 189773b	Hot Jupiter	Emission	Scanning	Marginal evidence for water; no inversion
Kreidberg et al., 2014a	GJ 1214b	Super-Earth	Transmission	Scanning	Featureless
Kreidberg et al., 2014b	WASP-43b	Hot Jupiter	Transmission & Emission	Scanning	Water in both transmission and emission; no inversion
Stevenson et al., 2014	WASP-43b	Hot Jupiter	Emission (phase-resolved)	Scanning	Water detected; no inversion; large day-night differences in thermal structure; Bond albedo of 0.18
Kreidberg et al., 2015	WASP-12b	Hot Jupiter	Transmission	Scanning (also used G102 grism)	Water detected; C/O=0.5
Sing et al., 2015	WASP-31b	Hot Jupiter	Transmission	Scanning	Featureless
Line et al., 2016	HD 209458b	Hot Jupiter	Emission	Scanning	Water detected; no inversion; C/O <1
Evans et al., 2016	WASP-121b	Hot Jupiter	Transmission	Scanning	Water detected; TiO/VO absorbers?
Wakeford et al., 2017	HAT-P-26b	Warm Neptune	Transmission	Scanning	Prominent water feature; likely primordial atmosphere

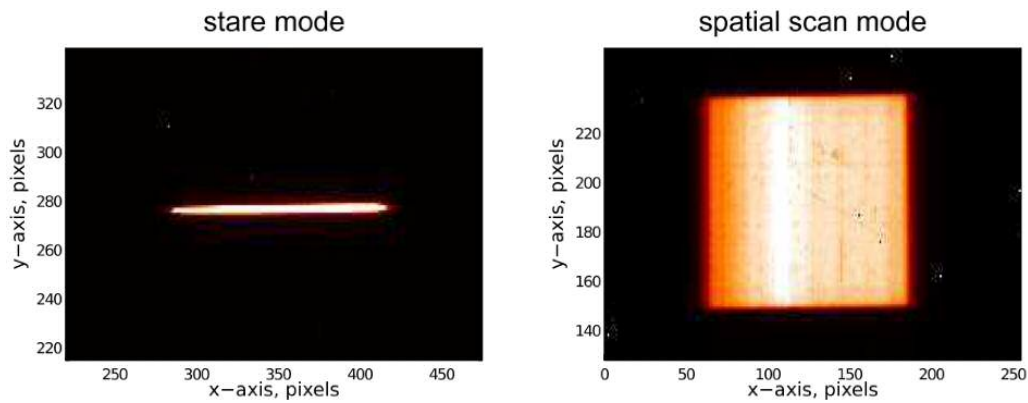


FIGURE 3.1 Comparison of staring mode (left) and spatial scanning mode (right) images for WFC3 IR observations of GJ 1214b. Figure from Swain et al. (2013b).

Spatial scans start at a designated position on the pixel array, and proceed in the y axis or ‘spatial’ direction, i.e. perpendicular to the spectral trace. There is however actually a small tilt of  $0.5^\circ$  with respect to the x-axis for the G141 spectrum. Non-destructive reads may be taken during the scan. After the scan is complete, the spacecraft will reposition to start the scan again from the same original position. A single scan constitutes an exposure.

Repositioning errors after each scan and scan rate variations during the scan mean that the scan may not proceed over exactly the same detector area with each exposure. Different pixels or different parts of pixels may be sampling the same spectral region in each exposure. Depending on the degree of inter- and intra-pixel responsivity variation, this could possibly introduce noise in excess of that for a ‘staring mode’ observation. Scan rate variations between exposures could also change the exact counts returned by each pixel adding to the noise.

In some studies after a ‘forward scan’, a ‘backward scan’ is carried out in the opposite direction, before repeating the forward scan. This further increases the duty cycle, but could potentially add to the noise especially if forward and backward scans are combined, or if there is a systematic difference due to scan direction.

A number of studies have raised concerns over scanning mode noise and systematics. Swain et al. (2013b) compared data on GJ 1214b observations taken in staring and scanning mode. These were obtained from the data sets used for Berta et al. (2012) (staring) and Kreidberg et al. (2014a) (scanning). They concluded that scanning mode was inferior with higher excess noise ( $2 \times$  photon noise limit) than in staring mode ( $1.3 \times$  photon noise limit), with non-Gaussian errors and correlated noise that was inconsistent between visits, compared to consistent Gaussian,

uncorrelated noise in staring mode. They attributed the inferior quality to spatio-temporal variability in the detector performance.

In the original tests of spatial scanning mode, McCullough & MacKenty (2012) noted brightness variations along the scan trail (photometric ‘flicker’) at the 3% level. This was due to Fine Guidance System (FGS) feedback resulting in jitter in the scanning direction. They found that jitter due to FGS feedback in scanning mode was equivalent to that in staring mode which they quote as  $\sim 3.5$  mas in each orthogonal axis. FGS control is used for scans upto  $1''/\text{s}$ , with higher scan rates achieved using the gyro system (without FGS). Under pure gyro control the FGS feedback jitter and flicker did not occur but gyro control is known to result in unpredictable drifts of the order of  $0.001''/\text{s}$ .

Tsiaras et al. (2016b) noted that spatial scanning will sample slightly different wavelength dispersions in the  $y$  axis due to geometric distortion introduced from the  $24^\circ$  tilt of the detector about its  $x$  axis. For a scan length of 350 pixels they found a difference from the bottom to the top of the scan of  $0.014 \mu\text{m}$  at  $\sim 1.6 \mu\text{m}$  pixel column. Without correction, this effect could introduce errors in the final reconstructed spectrum. Corrections for this dispersion effect have been used, e.g. the row by row interpolation method of Kreidberg et al. (2014a).

Deming et al. (2013) used spatial scanning mode for primary transit spectroscopy observations of HD 209458b and XO-1b, quoting a level of precision close to the photon noise limit. They did however note variations in count between exposures of  $\pm 1\%$  per row due to scanning rate variations (Figure 3.2), but concluded these did not contribute significant extra noise as they were occurring perpendicular to the spectrum. In Knutson et al. (2014a), the counts in each row were divided by the total flux in that row to correct for the uneven scan rate. Deming et al. (2013) also noted variations in the 1-D spectral position *between* exposures of up to  $\pm 1$  pixel column (much higher than the  $\pm 0.02$  columns in staring mode), and developed a method that they used to correct for these shifts.

Knutson et al. (2014b) obtaining scanning mode spectra of the super-Earth HD 97658b using both forward and backward scans, noted a small flux offset in the light curves between the two directions. This was removed by dividing each time series (forward and backward) by its median flux value. Kreidberg et al. (2014a) also note a flux offset between forward and reverse scans and fit these as separate data sets. This systematic difference is thought to be either due to scanning over slightly different positions in the array in forward and reverse scans, or the ‘up-stream/down-stream effect’. In the latter, if scanning in the same direction as the readout the effective integration time is greater than if scanning in the opposite

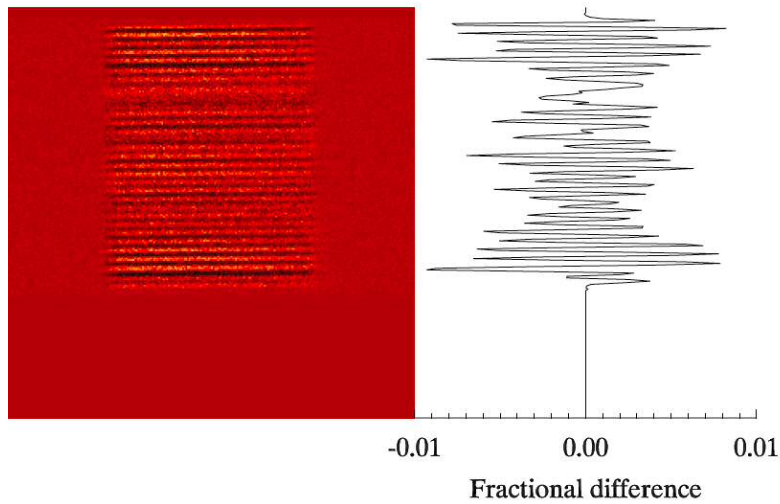


FIGURE 3.2 Scanning mode induced variations in row counts between exposures. Left: difference image between two consecutive scans of HD 209458b. Right: Fractional fluctuations in count per row. Figure from Deming et al. (2013).

direction.

As Table 3.1 shows, many transit spectroscopy studies have been performed with WFC3 in scanning mode. Being a source of correlated noise, it would be important to account for any increased uncertainty arising from this as discussed in Chapter 1. Some of these studies, e.g. Deming et al. (2013), exclude significant correlated noise, while others attempt to account for it, e.g. Knutson et al. (2014b), who find significant correlated noise component using the residual permutation Monte Carlo method. Some studies, e.g. Kreidberg et al. (2014a), do not comment on correlated noise.

The latter study in particular relies heavily on the precision of its final error bars to draw its conclusions that support a cloudy atmosphere for GJ 1214b and exclude a cloud-free water-dominated atmosphere (the main competing hypothesis, consistent with a ‘water world’). If the scanning mode introduced correlated noise on a scale indicated by the conclusions of Swain et al. (2013b) that was unaccounted for, these final error bars could be much higher and could potentially call into question these conclusions.

As an initial test of the applicability of the generic simulator, the issue of scanning mode noise in WFC3 was selected as a topic of investigation. This would test the utility of ExoSim in determining the contribution of a source of complex instrumental noise, and whether it makes a significant impact on the uncertainties on the final spectrum.

In order to simulate such observations a number of pre-requisites are needed. Firstly, to understand how to realistically simulate the Hubble scan in ExoSim, in terms of rate and position variations, I perform an analysis of scanning mode variations from several WFC studies. Next I develop an instrument model of the Hubble WFC3. Finally I develop a custom pointing jitter PSD for Hubble.

For the ExoSim simulations, I will adopt a full transit Monte Carlo approach, focusing on the case of Kreidberg et al. (2014a), simulating an observation closely matched to that study. I will attempt to elucidate any significant additional noise contribution due to scanning mode. Although the main goal will be to test ExoSim's capability in elucidating this noise, depending on how well the simulation matches the real observation, the results may be used to support or challenge the errors in the published study. I will also perform simulated observations in 'staring mode' as a comparison to see if one mode is indeed 'superior' to the other as suggested by Swain et al. (2013b). I will use the staring mode study of GJ 1214b using WFC3 by Berta et al. (2012) as the model for these simulations. As well as a baseline study using the WFC3 model, I will make adjustments to the model parameters to test what factors might influence scanning mode noise in general.

## 3.2 ANALYSIS OF SCANNING MODE DATA

Original data from a number of exoplanet scanning mode studies with WFC3 was obtained via the publicly accessible ESA Hubble Archive<sup>3</sup>. These studies are listed in Table 3.2, and encompass a wide range of different scan rates, from 0.05 "/s to 1.4 "/s.

### 3.2.1 MEASURING THE SCAN RATE AND VARIATIONS WITH EXPOSURE

For each study I obtained the .jit files for the complete observation, containing the position information of the guide star. The files contain data at a cadence of 3 seconds tracking the coordinates of the guide star in spacecraft V2 and V3 axes during the scan. I transformed the coordinates from V2 and V3 to detector x (spectral direction) and y (spatial/scanning direction) axes. For this transformation I use the field position of IR-FIX aperture reference pixel in the V2 and V3 coordinate system and the angle of the aperture with respect to the V3 axis (44.6677°) as

---

<sup>3</sup> <http://archives.esac.esa.int/ehst/>

given in the WFC3 aperture file<sup>4</sup>. The details of the transformation are given in the Appendix.

For each scan (i.e. each exposure), the scan rate (i.e. the y drift rate) was measured by fitting a straight line using the least squares method to the y position versus time and finding the absolute value of the gradient. When fitting, the first and last points of the sequence were excluded since they were visually inconsistent with the slope of the most other points. The same method was applied, fitting a line to the x positions versus time (again excluding first and last points), to obtain the absolute x direction drift rate.

In 4/7 cases (Table 3.2) the reported scan rate is basically identical to the measured value by this method. For Wakeford et al. (2013), Sing et al. (2015) and Fraine et al. (2014) there appears to be a small discrepancy between the published scan rate and my measurement. The standard deviation on the measured scan rates is tiny, indicating that the scan rates are highly consistent between exposures, a reassuring finding, although this does not mean that small scan rate variations are not occurring during the scan.

The measured x drift rates (Table 3.2) are very small, the highest being 0.0039 "/s for Knutson et al. (2014b). For Kreidberg et al. (2014a) in an 88 s exposure, the x drift rate of 0.00033 "/s is equivalent to only  $\sim 0.2$  pixels<sup>5</sup>, indicating this may not be significant. In the same time, the scan rate (y drift rate) covers  $\sim 81$  pixels. Note that the ratio between the x and y drift rates appears very constant across all the studies at about 0.28%, except for Wakeford et al. (2013), which is also the only one where the standard deviation is high compared to the mean x drift. This may be due to either an actual systematic in all the scans causing the same angular deviation of the scan direction from the y axis across all the studies, or a result of the limits of the accuracy of my transformation method. Given the consistency across all the studies, the latter may be more likely. Either way, the x drift within the scan does not appear a significant factor and thus it not critical to include in the ExoSim simulation.

### 3.2.2 FORWARD AND BACKWARD SCANS IN PROGRAM 13021

The data for program 13021 (Kreidberg et al., 2014a) was examined further. By subtracting the x and y line fits, the drift caused during the scan was removed, leaving the underlying pointing jitter timelines in x and y directions, recorded as

<sup>4</sup> <http://www.stsci.edu/hst/observatory/apertures/wfc3.html>

<sup>5</sup> WFC3 IR pixel scale = 0.13 "

TABLE 3.2 Published and measured scan rates for some WFC3 scanning mode studies; (f)=forward scans, (b)=backward scans.

Study	Program	Object	Scan rate (published) (''/s)	Scan rate (measured) (''/s)	x drift rate (measured) (''/s)	x drift rate/scan rate	Number of scans
Deming et al., 2013	12181	HD 209458b	0.9	0.90000 ± 0.00008	0.0026 ± 0.0001	0.00283	125
Deming et al., 2013	12181	XO-1b	0.05	0.05000 ± 0.00004	0.00014 ± 0.00003	0.00271	128
Wakeford et al., 2013	12473	HAT-P-1b	0.1391	0.15001 ± 0.00004	0.00005 ± 0.00003	0.00033	111
Knutson et al., 2014b	13501	HD 97658b	1.4	1.400 ± 0.001	0.0039 ± 0.0003	0.00278	205 (f) 157 (b)
Sing et al., 2015	12473	WASP- 31b	0.0195	0.018998 ± 0.000007	0.00005 ± 0.000004	0.00277	74
Kreidberg et al., 2014a <sup>a</sup>	13021	GJ 1214b	0.12	0.12003 ± 0.00006	0.00033 ± 0.00001	0.00279	608 <sup>b</sup> (f) 252 (b)
Fraine et al., 2014	12449	HAT-P- 11b	0.3981	0.36996 ± 0.00006	0.00106 ± 0.00006	0.00286	183

<sup>a</sup> 12 visits (excluded data from 4<sup>th</sup> and 12<sup>th</sup> August 2013 for reasons given in cited paper).

<sup>b</sup> Of which 273 (7 visits) were 'long' scans of 103 s. and 335 (5 visits) were 'short' scans of 88 s.

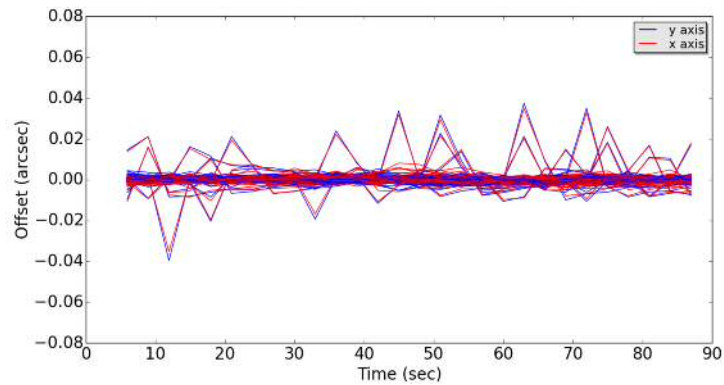
'offsets' in arcsec from the line fit.

In Kreidberg et al. (2014a) 3 types of scan were used. For the first 5 visits, 88 s exposure ('short') forward scans were used. For the remaining visits, 103 s exposure ('long') forward scans were combined with 103 s exposure backward scans. The scan rates in all cases was 12 ''/s, which I verified in Table 3.2.

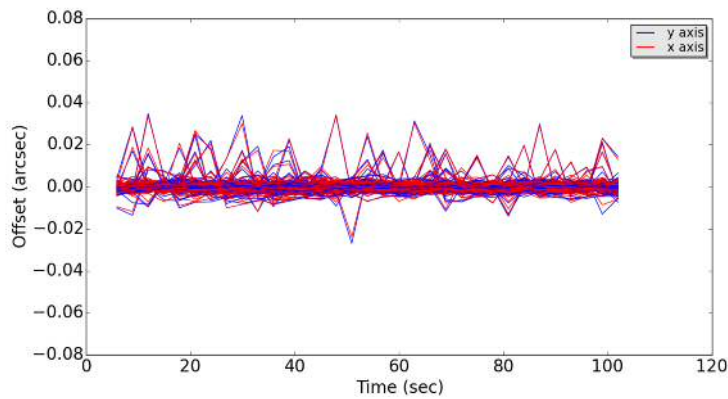
Figure 3.3 shows the offset timelines for sets composed from the three scan types, with x axis offsets in red, and y axis offsets in blue. The jitter rms values,  $rms_{jit}$  from all the timelines combined for a given direction and scan type, are given in Table 3.3.

In most cases the jitter rms is between about 1.5-2.0 mas, of the same order, if slightly lower, that pointing jitter of the Hubble of 3.5 mas per axis reported in McCullough & MacKenty (2012), and very close to the pointing precision for HST from Fruchter et al. (2009) of 2-5 mas, giving  $\sim 1.4-3.5$  mas per axis<sup>6</sup>. This would indicate that no additional jitter is caused by the scan once drift has been subtracted,

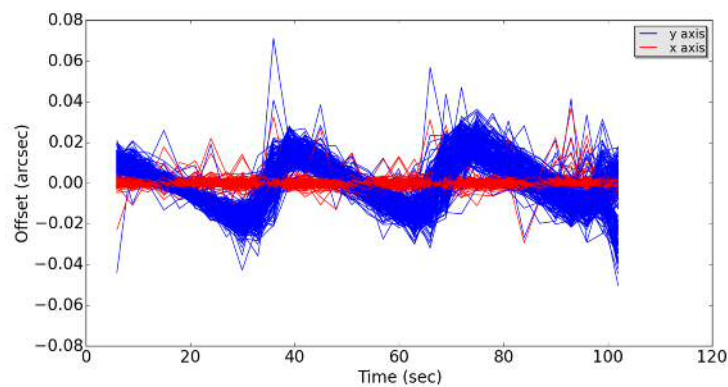
<sup>6</sup> The methods employed in obtaining the rms values in these studies are not well detailed in the reports. The values stated in Fruchter et al. (2009) are consistent with those documented in previous studies such as Gilliland (2005) where the V2 and V3 axis rms data is obtained directly from the jitter files where the rms is recorded automatically over fixed time periods. Fruchter et al. (2009) also state that the rms can be confirmed by reference to the FGS jitter files (which contain the guide star V2 and V3 position data) as used in this study. There is no indication in these reports that the rms was obtained after sigma-clipping or through histogram fits. The value reported in McCullough & MacKenty (2012) was based on an unpublished report by A. Bradley, where the jitter was measured using the FGS and was found to be the same as in staring mode, however further details of how these results were obtained are not given.



(A) Forward scans - 'short'



(B) Forward scans - 'long'



(C) Backward scans

FIGURE 3.3 Positional offsets (jitter) during scans for the program 13021 (Kreidberg et al., 2014a) data set. Red lines show offset timelines in the x (spectral) axis direction. Blue lines show offset timelines in the y (spatial) axis. Rms of offsets is mostly consistent with previously cited variations due Hubble pointing jitter, except for backward scans that have an additional sawtooth like variation in the spatial direction - this sawtooth is absent in forward scans.

TABLE 3.3 Jitter rms in x and y directions during scans (once scan drift is removed),  $rms_{jit}$ , and variation on the re-positioning of each scan shown as the standard deviation of the initial x and y positions of the guide star,  $\sigma_{init}$ .

	Forward scan ('short')		Forward scan ('long')		Backward scan	
	x	y	x	y	x	y
$rms_{jit}$ (mas)	1.58	1.53	2.09	2.00	2.01	11.47
$\sigma_{init}$ (mas)	$1.55 \pm 0.50$	$6.04 \pm 3.05$ $(4.52 \pm 0.42)^a$	$1.36 \pm 0.39$	$3.25 \pm 0.38$	$1.82 \pm 0.94$	$5.77 \pm 1.88$ $(5.05 \pm 0.77)^b$

<sup>a</sup> Excluding visit with 40 mas drift.

<sup>b</sup> Excluding visit with single anomalous position.

which is consistent with the conclusions of McCullough & MacKenty (2012). For simulation purposes in ExoSim, this means that the scan can be simulated by simply adding the baseline Hubble pointing jitter in both axes to a sawtooth profile (with gradient equal to the scan rate) in the spatial direction.

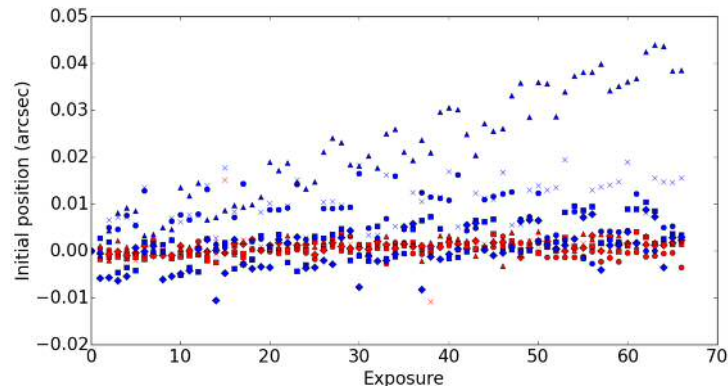
However the notable exceptions are the backward scans which have a sawtooth-like envelope with a peak-to-peak variation of about 20 mas and a period of about 33 seconds. Presumably this is caused by some artefact of the FGS or gyro system, or a spacecraft vibrational mode, that manifests only during the backward scan. It is not clear from the literature that this feature of reverse scanning has been noted before, although McCullough & MacKenty (2012) state that during 'rewind' (i.e. returning to the starting position after a completion of a forward scan) the scan rate is 'not at a constant rate like the actual scans'. Since the periodicity is based on positional data and not photoelectron counts, the effect is not attributable to the 'up-stream/down-stream effect' as discussed in Knutson et al. (2014b), but this finding may also contribute to the flux difference noted between forward and backwards scans in that study (although the scan rate was much higher).

The 20 mas excursion in the backward scan is still small compared to the angular size of the WFC3 IR pixel which is 130 mas, and given that intra-pixel responsivity of the WFC3 IR pixels is considered to be very uniform (Pavlovsky et al., 2011) the impact of this variation may be small in terms of 'jitter noise'. However the excursion will manifest in the scanning direction and could lead to worse scan rate variations than in forward scans and thus potentially worse photometric variations. The backward scan therefore needs to be used with some caution to take any correlated noise into account. The impact of this finding on the Kreidberg et al. (2014a) results is not clear, as the final spectrum is the weighted average

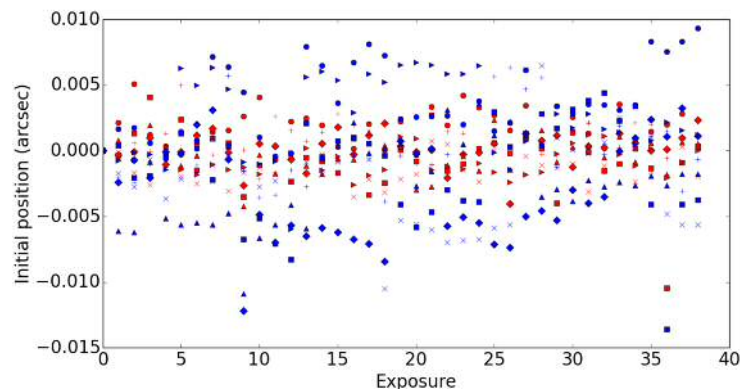
over all (12) epochs, and the reverse scans appear to have been fitted as independent data sets to the forward scans. From the information given it is not clear if the light curve fits from the reverse scans had more uncertainty than the forward scans. Certainly an ExoSim simulation would be a good way to assess the impact of this effect, however for this initial study simulating such a periodicity would require an additional layer of variation on top of the baseline jitter and the scan sawtooth. It was therefore decided to reserve this for a future investigation, and focus presently on the effect of the standard forward scan.

Finally I examined the degree of variation in the initial x and y positions of the guide star (after removing the first point in the sequence, but not subtracting the line fit), between scans in the same visit, for each type of scan. This can give a measure of how much the scan position 'drifts' between different exposures. If this variation is high, then different pixels may scan the same spectral range in different exposures, contributing some additional noise. Figure 3.4 shows the initial x and y positions of each exposure in relation to that of the first exposure in the visit, for each of the three types of scan. A trend is seen in some of the short forward scans upto  $\sim 40$  mas drift in one visit, but the 'long' forward scans and backward scans do not have any obvious trends.

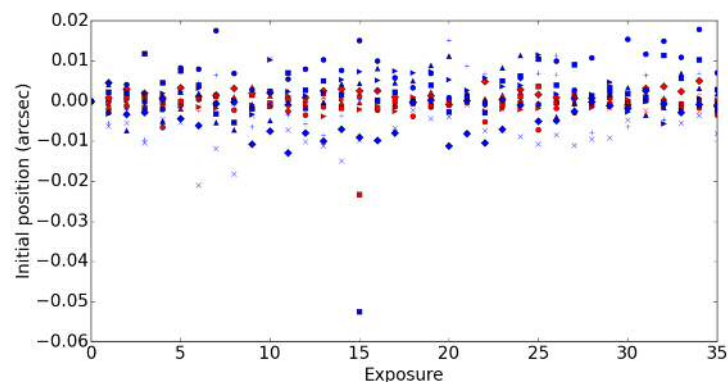
The standard deviation of the initial scan positions in both x and y directions is obtained for each visit and then averaged over all visits for a particular scan type, to give the average standard deviation,  $\sigma_{init}$ , for a particular scan type in either x or y directions (Table 3.2). Mostly, the  $\sigma_{init}$  values are of the order of the known Hubble pointing precision, but are higher for the initial y position than the x position, probably reflecting an added error due to 'rewind' of the scan. However the 'short' forward scans have a slightly higher  $\sigma_{init}$  of 6.04 mas. If the visit causing the 40 mas drift is considered an outlier and removed, then  $\sigma_{init}$  falls to 4.52 mas. It is not clear why only the 'short' forward scans have this added drift compared to the other scans. The backward scans also produce a higher  $\sigma_{init}$  of the initial y position of 5.77 mas. There is a single anomalous position in one visit (visible as the blue outlier in Figure 3.4 C) that causes that visit to have a standard deviation of 10.04 mas. If that visit is removed, the average standard deviation,  $\sigma_{init}$ , falls to 5.05 mas. These variations are still very small compared to the size of the pixel. Even 10.04 mas corresponds to only  $\sim 8\%$  of the pixel width. Since the variations in general are of the order of the Hubble pointing jitter, for the ExoSim simulation I decided to apply no further variations on top of the baseline jitter to the initial positioning of each scan.



(A) Forward scans - 'short'



(B) Forward scans - 'long'



(C) Backward scans

FIGURE 3.4 Variation of initial scan position in each visit for the program 13021 (Kreidberg et al., 2014a) data set. Initial x and y positions for each scan (exposure) are shown relative to the first scan in the visit. Blue symbols show the initial y position in each scan/exposure and red symbols show the initial x position. Each visit is represented with different symbols. For 'short' forward scans there are 5 visits and for 'long' forward and backward scans there are 7 visits.

### 3.3 HUBBLE WFC3 MODEL

To produce an ExoSim model of WFC3 IR, an input configuration file (*ICF*) needs to be developed, together with associated reference files for telescope and instrument transmissions and emissions. Firstly however I briefly review previous WFC3 simulators and how suited they might be to the task of elucidating scanning mode noise.

#### 3.3.1 OTHER WFC3 SIMULATORS

WAYNE (Varley et al., 2015), mentioned in Chapter 2, is a dynamic simulator dedicated to the Hubble WFC3 that models the instrument in great detail including most instrumental systematics. It can model scanning mode, but does not use a correlated jitter timeline based on the spacecraft PSD like ExoSim, and thus models uncorrelated Gaussian jitter. Apart from the original arXiv paper, no results have to-date been published using WAYNE, and thus its applicability to specific problems in transit spectroscopy observations has not been tested. In particular, no results from WAYNE have been published addressing the issue of excess noise from scanning mode.

aXeSim (Kummel et al., 2007) was developed as a static simulator for WFC3, prior to its installation, originally for the simulation of slitless spectroscopy. Its primary purpose was for planning proposed observations, and uses the aXe<sup>7</sup> spectral extraction software to analyse the simulated data. aXeSim has been applied to other spacecraft, namely Euclid and JWST. Notably aXeSim does not have the capability to simulate transit spectroscopy being designed in an era when this was not considered a priority for WFC3. It also does not simulate scanning mode.

Pand-Exo was also mentioned in Chapter 2, and, though dedicated to the WFC3 obtaining estimates of SNR for planet transits, it is a static simulator that does not simulate jitter or scanning mode, and thus cannot be used to address questions of the source of excess instrumental noise.

Other simulators available for the Hubble include the 'exposure time calculators' (ETC)<sup>8</sup> and the TinyTim PSF calculator (Krist et al., 2011). These are mentioned for completeness but neither is designed to simulate full observations or scanning mode noise.

The ETC was developed for all main Hubble instruments: ACS, COS, STIS

---

<sup>7</sup> <http://axe-info.stsci.edu/>

<sup>8</sup> <http://www.stsci.edu/hst/wfc3/tools/etcs/>

and WFC3, each having a separate input page, and includes instrument specific transmission factors, and is comprised of a number of packages written in Python including PySynphot. PySynphot is the synthetic photometry calculating engine common to all the instruments. It calculates SNR for a given exposure time or the exposure time for a given SNR. It can be used for preparation of observing proposals to STSc and was developed independently of aXeSim.

TinyTim is a point spread function modelling tool for HST run via a web interface. Inputs include the instrument camera, the detector chip, filter and input spectral type. An image with the modelled PSF is produced, which can be used for image simulation, observation planning or investigating how the PSF varies under different conditions.

### 3.3.2 INSTRUMENT MODEL

The Hubble WFC3 IR instrument was modeled in ExoSim with a specific *ICF*. A primary mirror diameter of 2.4 m was used with transmissions and emissions for each optical element, including the primary and secondary mirrors and the elements shown in Figure 3.5, bottom. The wavelength-dependent transmissions were obtained from publicly available *synphot* files (Diaz, 2012), which included a transmission ‘correction file’ and a wavelength-dependent quantum efficiency file. The emission of the the mirrors was estimated based on an emissivity of 0.03 for aluminium at a temperature of 150 K, but since no emissivity information was available for the other optical elements in the instrument, it was decided to not to include the emission from these in the simulation.

The f-number for the WFC3 IR instrument is given as 11 in Dressel (2017), however that document also gives model PSF FWHM values which deviate somewhat from the expected Airy function FWHM of  $1.028 f\lambda$ . Fitting a polynomial to these published values we find the relation:  $\text{FWHM} = 3.0795 \lambda^2 - 3.6016 \lambda + 15.509$  (where  $\lambda$  is the wavelength). I adjust the code to allow for this relation, so that the FWHM of the Airy disks produced at each wavelength matches the published model FWHM.

A pixel pitch of 18  $\mu\text{m}$  is used with a 128 x 256 array (which was sufficient to include the entire spectrum and scan for this study), and approximates the 256 x 256 subarray mode of the instrument used in Kreidberg et al. (2014a).

For inter-pixel QE variations, I use a 3% standard deviation, based on a sampling of the publically available F105W and F110W LP flat files<sup>9</sup> in the region of

<sup>9</sup> [http://www.stsci.edu/hst/wfc3/analysis/ir\\_flats](http://www.stsci.edu/hst/wfc3/analysis/ir_flats)

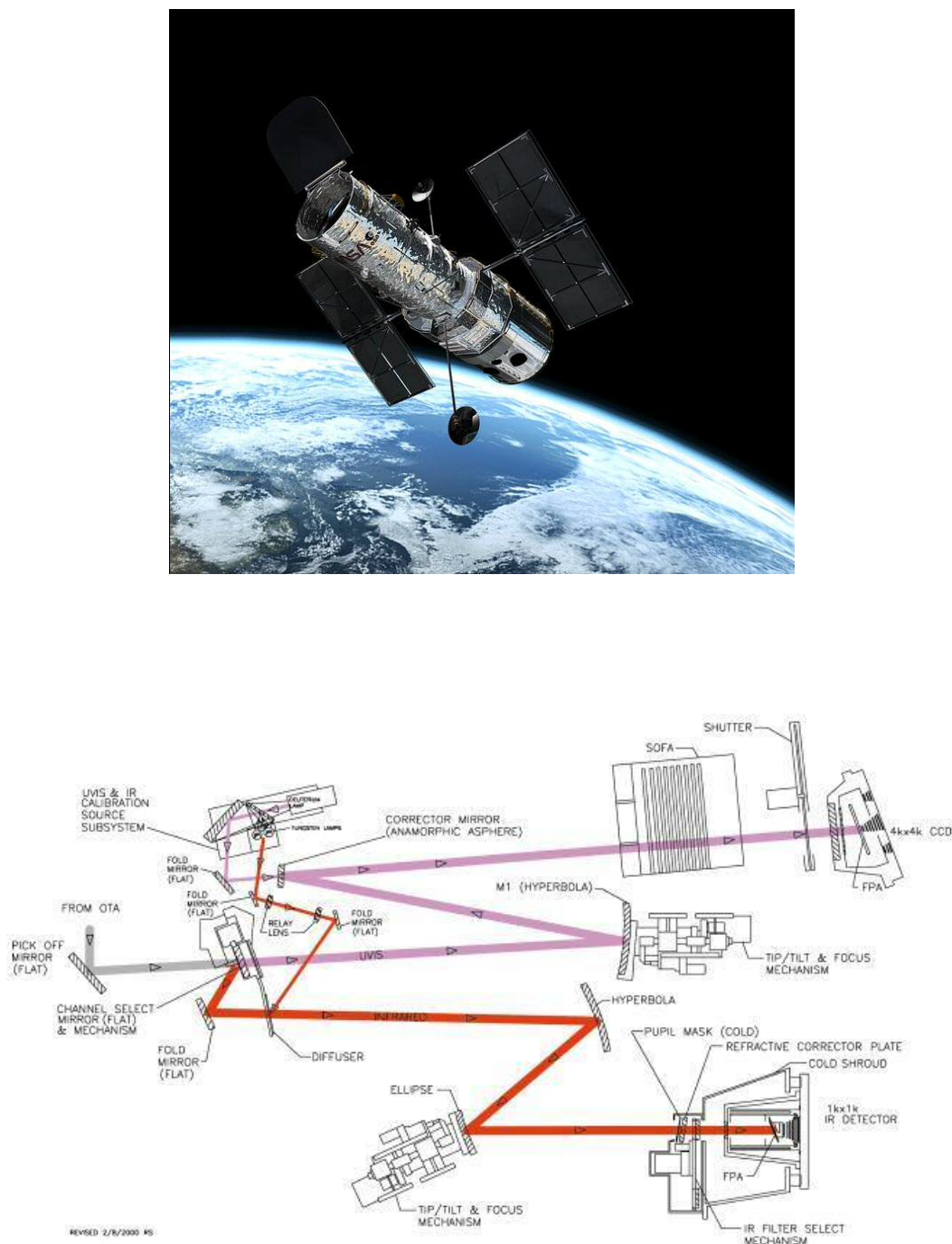


FIGURE 3.5 The Hubble Space Telescope (top) and the Wide Field Camera 3 instrument (bottom) have been a key facility in the advancement of exoplanet transit spectroscopy. The diagram shows the full WFC3 instrument including both UVIS (mauve light path) and IR (red light path) channels. Since it is the IR channel which is used for transit spectroscopy studies, only its elements are modeled in ExoSim. Top figure from <https://www.spacetelescope.org/about/> (credit: NASA/ESA). Bottom figure from [http://www.stsci.edu/hst/wfc3/design/at\\_a\\_glance/](http://www.stsci.edu/hst/wfc3/design/at_a_glance/) (credit: NASA/STScI).

the 256 x 256 subarray. These QE variations are then flat-fielded in data reduction, together with the much smaller wavelength-dependent variations: 0.5% standard deviation between 1.1 and 1.65  $\mu\text{m}$ . Residual uncertainties were left as variations of 0.5% standard deviation (Pirzkal et al., 2011). For the intra-pixel response, the pixel diffusion length was chosen as zero, based on lack of detection of any intra-pixel sensitivity variation by Pavlovsky et al. (2011). Other instrument parameters were obtained or derived from the WFC3 data (Deustua, 2016) and instrument (Dressel, 2017) handbooks. These included a linear dispersion of 0.00025  $\mu\text{m}/\mu\text{m}$ , plate scale of 0.13  $''/\text{pixel}$ , dark current of 0.048  $\text{e}^-/\text{s}$ , and a read noise of 14.7  $\text{e}^-$  per pixel.

In the current model I have not taken into account the small variations in the wavelength solution with row, or the slight tilt of the spectral trace away from the x-axis. In addition in this study I have not included the well-known photometric 'ramp' systematic based on detector persistence.

### 3.3.3 HUBBLE POINTING JITTER POWER SPECTRUM

For pointing jitter, a model PSD for Hubble was produced from publically available pointing data time series. I used data from the following studies: program 12498: Hubble Ultra Deep Field (2012), program 12181: Wasp 18 (2012) and program 13021: GJ 1214 (2012-13). For each time series, I transformed the pointing information of the guide star from spacecraft V2 and V3 axes into detector x (spectral) and y (spatial) axes as described in the Appendix. Note that these data were obtained in 'staring' mode, so no scan or drift was removed as in subsection 3.2.1.

Following the method described in Chapter 2 for producing the Herschel model PSD involving the real Fourier transform, each time series was used to generate a corresponding PSD profile. From these a small number of median PSDs with inter-quartile ranges (IQRs) were produced for PSDs on the same frequency grid (Figure 3.6 A). The medians with IQRs used as weights, were then used to fit separate polynomials to 5 regions of the data (Figure 3.6 B). These fits were cropped at the edges (Figure 3.6 C), and a linear interpolation performed over the remaining points and gaps to give the final model PSD (Figure 3.6 D). The Hubble PSD has a similar general shape to that of Herschel, with a mid-frequency peak, but produces a much lower level of jitter. This model PSD produces a timeline with a jitter rms of 2.6 mas per axis over bandwidth ( $10^{-3}$ -10 Hz), or 3.7 mas over both axes. This is consistent with previously cited Hubble jitter of 2-5 mas (Fruchter et al., 2009), indicating that the method used here appears valid.

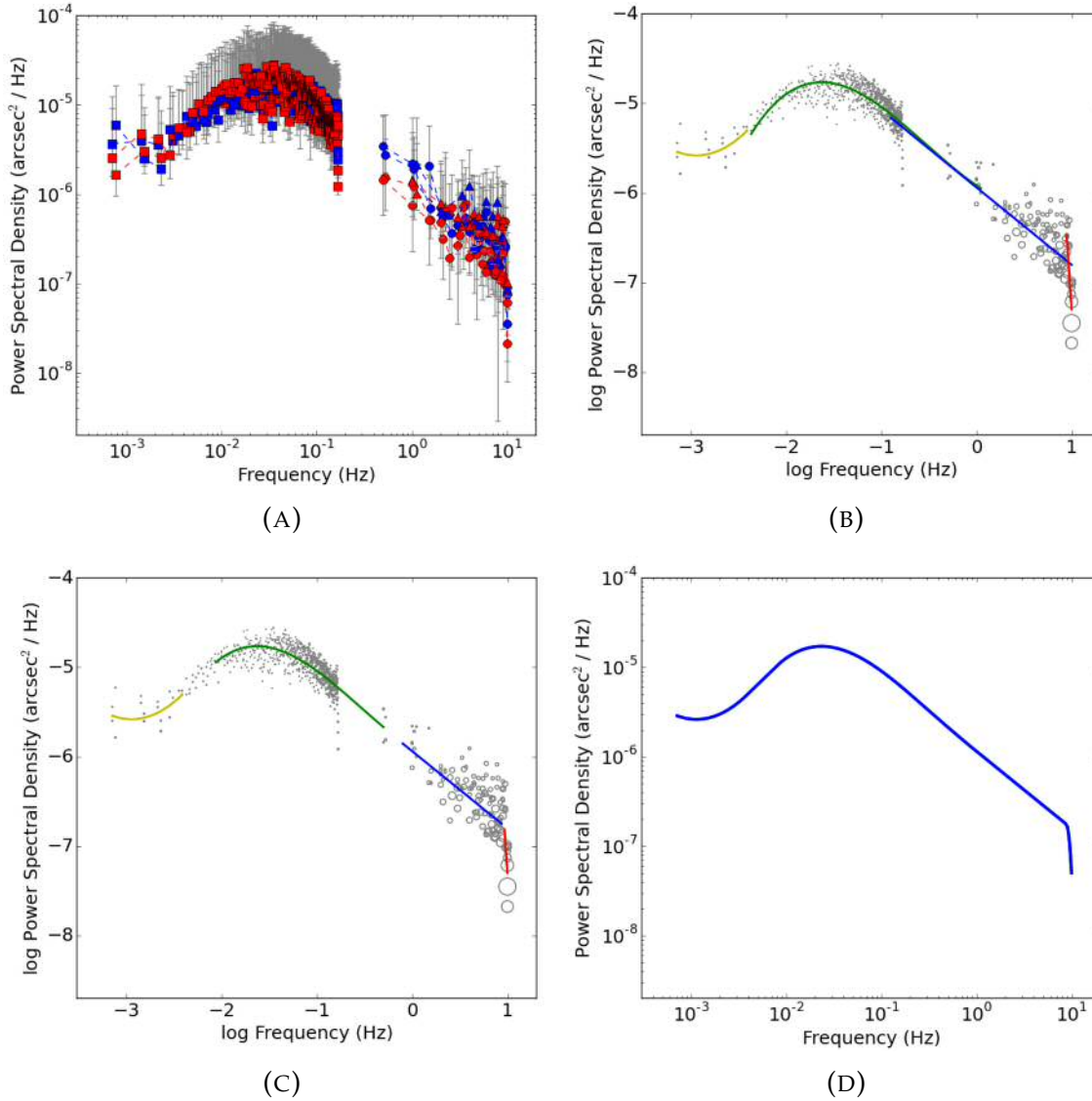


FIGURE 3.6 Obtaining a power spectral density (PSD) profile for the ExoSim Hubble Space Telescope model. A: Median PSDs with grey error bars showing the interquartile ranges (IQRs): red = y jitter, blue = x jitter, squares = program 12498 (Hubble Ultra Deep Field), circles = program 12181 (Wasp 18), triangles = program 13021 (GJ 1214). B: 4 regions are fitted with polynomials: yellow (2nd degree), green (3rd degree), blue (1st degree), red (1st degree). The sizes of the circles are proportional to the weights, where the weight is 1/IQR for each data point. C: The fitted lines are cropped and a linear interpolation performed across these points and gaps to give final PSD. D: Final resultant model PSD for one axis.

## 3.4 SIMULATIONS

### 3.4.1 GOALS AND CASE STUDIES

The goals of this study are to find the noise attributable to the scan, and compare the noise obtained from scanning and staring modes. The metric used is the uncertainty on the contrast ratio,  $\sigma_{cr}$ , in the final reconstructed primary transit spectrum. Full primary transit spectroscopy simulations of the target exoplanet, GJ 1214b, will be performed in both ‘scanning’ mode, modeled along the lines of Kreidberg et al. (2014a) (hereafter K14), and ‘staring’ mode. Two ‘staring’ mode controls are used. In the first, staring mode A, the same exposure time is used as for scanning mode, to allow detection of any added noise purely due to scanning and isolated from other factors. However, since in reality staring mode observations involve much shorter exposure times, a second control, staring mode B, modeled along the lines of Berta et al. (2012) (hereafter B12), is used that has a more ‘realistic’ shorter exposure time. The latter allows for an overall comparison with scanning mode in terms of which may be superior to use. The simulations will be performed with all noise activated and then repeated with only jitter noise activated. The jitter noise only simulations remove all other noise effects, isolating the photometric variations due to movement of the image alone (jitter and scan). 500 realizations will be performed for each simulation, allowing noise to vary randomly between realizations (a Monte Carlo simulation). 4 cases will be examined. *Case 1* is the baseline case of the WFC3 IR with 2.6 mas rms jitter in each axis. However to explore how the noise might be affected under different instrument parameters, three additional cases were examined with modifications to the baseline model. *Case 2* is case 1 with increased intra-pixel variation (by using a pixel diffusion length of 1.7  $\mu\text{m}$  rather than zero in the ‘bowler hat’ pixel response function described in Chapter 2). *Case 3* is case 2 plus a broader PSF (using an f-number of 31.1 that samples the FWHM with 2 pixels at 1  $\mu\text{m}$ ). *Case 4* is case 3 plus increased pointing jitter of 129 mas bi-axial rms by using the model Herschel PSD.

### 3.4.2 SPATIAL SCANNING MODEL

Scanning mode is modeled by superimposing a sawtooth profile to the jitter timeline in the spatial direction. The amplitude of the sawtooth is defined in units of arcsec in the *ICF*. Dividing this by the time for a complete exposure cycle gives the scan rate. The jitter timeline in x and y directions is thus superimposed on

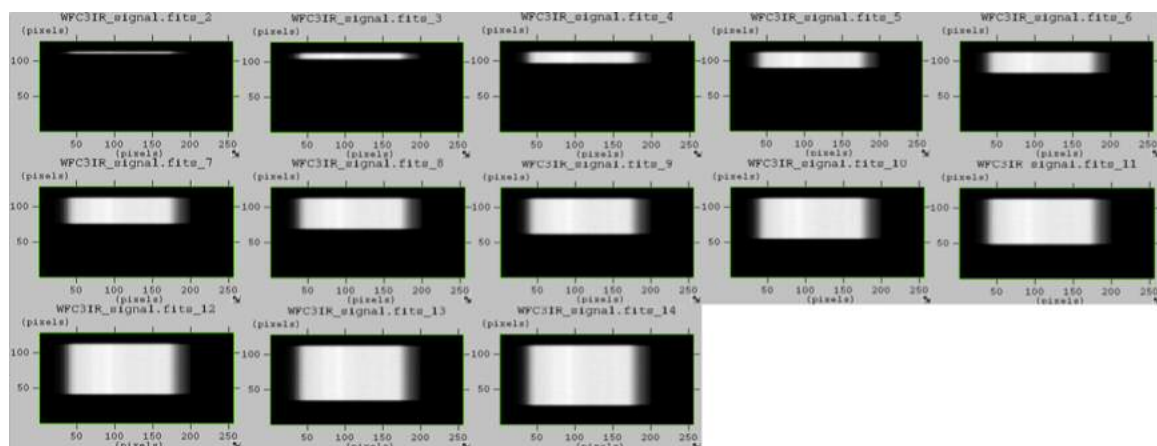


FIGURE 3.7 A sequence of multiaccum=13 NDR images making up an exposure from the ExoSim Hubble WFC3 IR model ‘observing’ GJ 1214b, showing the progressive scan with each NDR.

the scan, which proceeds in the y or ‘spatial’ direction, with the y jitter causing scan rate variations within the scan; this is an adequate simulation of the scan and associated jitter as assessed from subsection 3.2.2. Only forward scanning is simulated. Figure 3.7 shows an example of scanned set of NDRs making up a single exposure using ExoSim.

### 3.4.3 SIMULATED OBSERVATIONS

The super-Earth GJ 1214b was simulated in primary transit. For the spectral energy distribution of the host M-dwarf star I used a PHOENIX stellar model ( $T=3000$  K,  $\log g=5.0$ ,  $[\text{Fe}/\text{H}]=0$ ). Existing studies for the planet indicate a flat transmission spectrum. I therefore adopt a flat contrast ratio of 0.0135 at all wavelengths. This contrast ratio approximates that found from observations. A linear limb darkening coefficient of 0.27 was used for all light curves (close to the average value of the coefficients obtained for spectroscopic light curves in K14 after using the ‘divide white’ systematic correction method). Observations were simulated in scanning mode with a scan rate of  $12''/\text{sec}$ , with 13 NDRs per exposure (the first NDR having an integration time of 0.5 second). The effective integration time for an exposure was 90 seconds (after subtraction of the first NDR), and a total cycle time of 160 seconds was used (56% duty cycle). These observational parameters were designed to match to those for the ‘short’ forward scan exposures in K14. As mentioned in Chapter 2, I elected to use a simulation frame rate of 2 Hz to optimize speed for Monte Carlo simulations, however this limited the values of

the exposures time to the nearest 0.5 seconds. As a result the exposures are 2% longer than in the real study (90 s compared to 88.1 s in K14). To permit faster simulations, the pixel oversampling factor,  $f'$ , was limited to 1/3 of the goal value calculated for the rms of the jitter; as shown in Subsection 2.2.4 this is an acceptable modification that still captures the jitter noise accurately. Unlike K14, these simulations do not include the gaps due to Earth occultation, and the total observing time used is equal to two transit times (with an equal amount of out-of-transit time before and after the transit). For the control, staring mode A, the same simulation parameters were used with just the scan omitted. For staring mode B, the same total observing time was used, but 7 NDRs per exposure were used (the first NDR again having 0.5 seconds) giving an effective integration time (after subtraction of the first NDR) for each exposure of 6 seconds, and a total cycle time of 25 seconds (24% duty cycle). These parameters are based on those in B12 which had an effective integration time of 5.971 s. For each observing mode and each of the 4 case studies, a Monte Carlo simulation consisting of 500 realizations was performed. This is performed initially with all noise sources (photon noise from the source, jitter, dark current, zodiacal foreground, emission, and readout noise) activated and then repeated with jitter noise only.

#### 3.4.4 DATA REDUCTION

The data reduction pipeline broadly mimics that used in K14. Each of the 500 realizations for each Monte Carlo simulation scenario is processed separately to obtain the primary transit spectrum as follows.

Each NDR is flat-fielded, and then the difference between adjacent NDRs taken to give the set of *subexposures* per exposure. Each subexposure is then processed separately as follows. A 31 pixel-wide box is centred on the maximum signal in the subexposure and the median of the background pixels (outside this box) found and subtracted from all pixels. The box is then cropped and the 1-D spectrum extracted from this by integration of the column counts<sup>10</sup>. The spectra from all the subexposures are then summed to give the 1-D spectrum for each exposure. This is then binned into 5 pixel wide columns (to give  $R \approx 70$ ), and 22 spectral bins between 1.155-1.628  $\mu\text{m}$  are then selected for further analysis. The signal time series (light curves) over all exposures is then extracted for each bin. Model Mandel-Agol light curves, with linear limb darkening coefficients, are then

<sup>10</sup> K14 uses optimal extraction for this step.

fitted to each spectral data light curve using a downhill simplex algorithm<sup>11</sup>, minimising  $\chi^2$ , using the standard deviation of the out-of-transit portion of each light curve as the uncertainty on the data. The limb darkening coefficient is fixed at 0.27 for all light curves, with the out-of-transit flux and the transit depth left as free parameters in the fit. The fractional transit depth, or contrast ratio  $(R_p/R_s)^2$ , at each wavelength is obtained and thus the primary transit spectrum for that realization.

Finally the standard deviation of the distribution of all 500 transit depths in each wavelength bin is found, giving the uncertainty on the contrast ratio,  $\sigma_{cr}(\lambda)$  at any wavelength, for the case simulated. This is equivalent to the  $1\sigma$  error bar on the transit depth for a single transit.

### 3.5 RESULTS

Figure 3.8 shows an example of a Monte Carlo simulation result. The case shown is that of the baseline WFC3 model (case 1), all noise sources activated in scanning mode. Each wavelength has a distribution of transit depths, as shown in the example in Figure 3.9. The error bars in Figure 3.8 show the standard deviation of the transit depths at each wavelength constituting the uncertainty on the contrast ratio.

Figures 3.10 - 3.13, show the uncertainty on the contrast ratio,  $\sigma_{cr}$ , in ppm versus wavelength for each observing mode, with all noise activated and with just jitter noise activated, for each case study.

Tables 3.4 - 3.7 summarize the results showing the average value of  $\sigma_{cr}$  over all wavelength bins under the different observing modes and different noise conditions for each case. The results of two-sample Kolmogorov-Smirnov tests comparing the scanning mode data to each of the two controls are also shown.

---

<sup>11</sup> using the function `scipy.optimize.fmin`

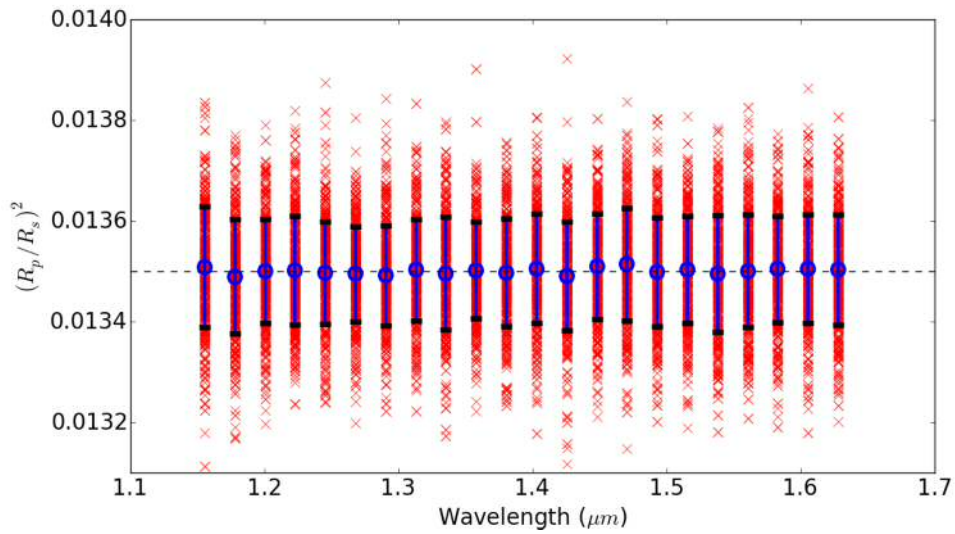


FIGURE 3.8 Monte Carlo simulation result example for the baseline WFC3 IR model (case 1) with all noise activated in scanning mode, with 500 realizations. Red crosses: recovered fractional transit depths (contrast ratios). Blue circles with error bars: mean and standard deviation of each distribution in a wavelength bin. Dashed line: input contrast ratio.

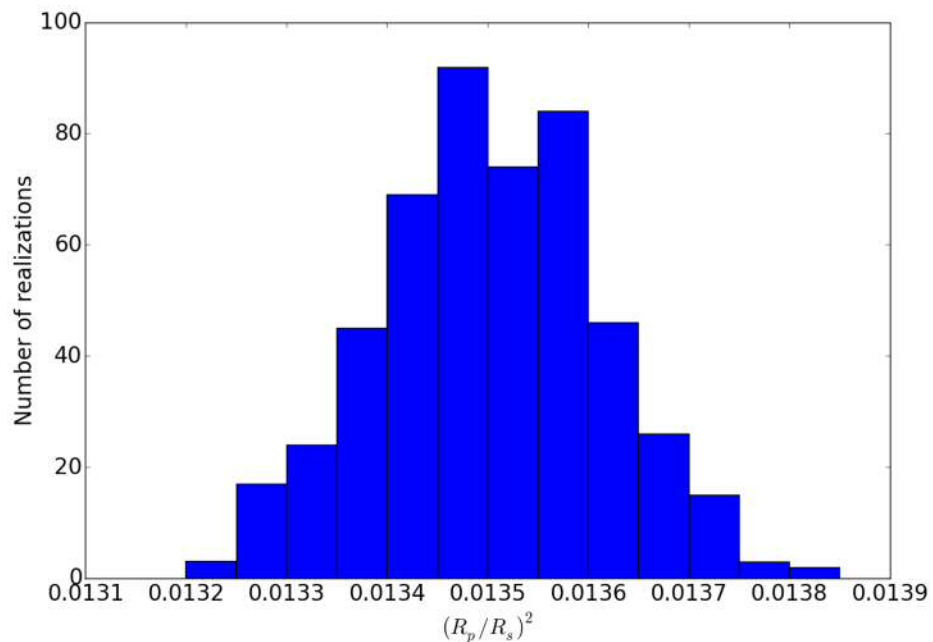


FIGURE 3.9 Histogram of transit depths for the 1.56  $\mu\text{m}$  bin for the baseline WFC3 IR model (case 1) with all noise sources activated in scanning mode.

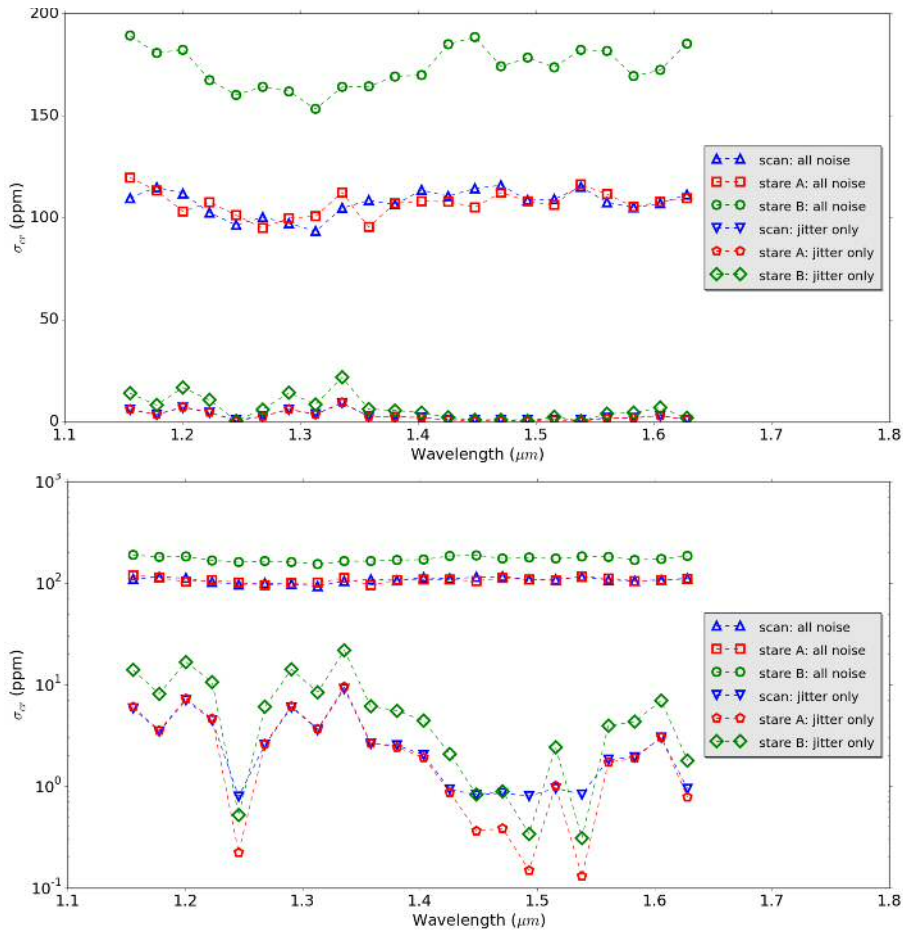


FIGURE 3.10 Case 1: uncertainty on primary transit contrast ratio spectrum,  $\sigma_{cr}(\lambda)$ , under different conditions: scanning mode, staring mode A, staring mode B, with all noise and jitter noise only. Top: normal scale on y axis. Bottom: log scale on y axis.

Noise simulated	Average $\sigma_{cr}$ per spectral bin (ppm)		K-S statistic	p-value
All noise	<i>Scanning mode</i>	<i>Staring mode A</i>	0.23	$5.6 \times 10^{-1}$
	$107.40 \pm 6.18$	$106.93 \pm 6.03$		
	<i>Scanning mode</i>	<i>Staring mode B</i>	1.0	$7.0 \times 10^{-11}$
	$107.40 \pm 6.18$	$173.49 \pm 9.78$		
Jitter noise only	<i>Scanning mode</i>	<i>Staring mode A</i>	0.27	$3.3 \times 10^{-1}$
	$2.86 \pm 2.26$	$2.77 \pm 2.50$		
	<i>Scanning mode</i>	<i>Staring mode B</i>	0.41	$3.6 \times 10^{-2}$
	$2.86 \pm 2.26$	$6.38 \pm 5.74$		

TABLE 3.4 Summary of case 1 results giving average  $\sigma_{cr}$  for each observing mode and noise condition. Also shown are the results of the 2 sample K-S test. A p value of  $< 0.05$  (shown in red) rejects the null hypothesis with  $> 95\%$  confidence.

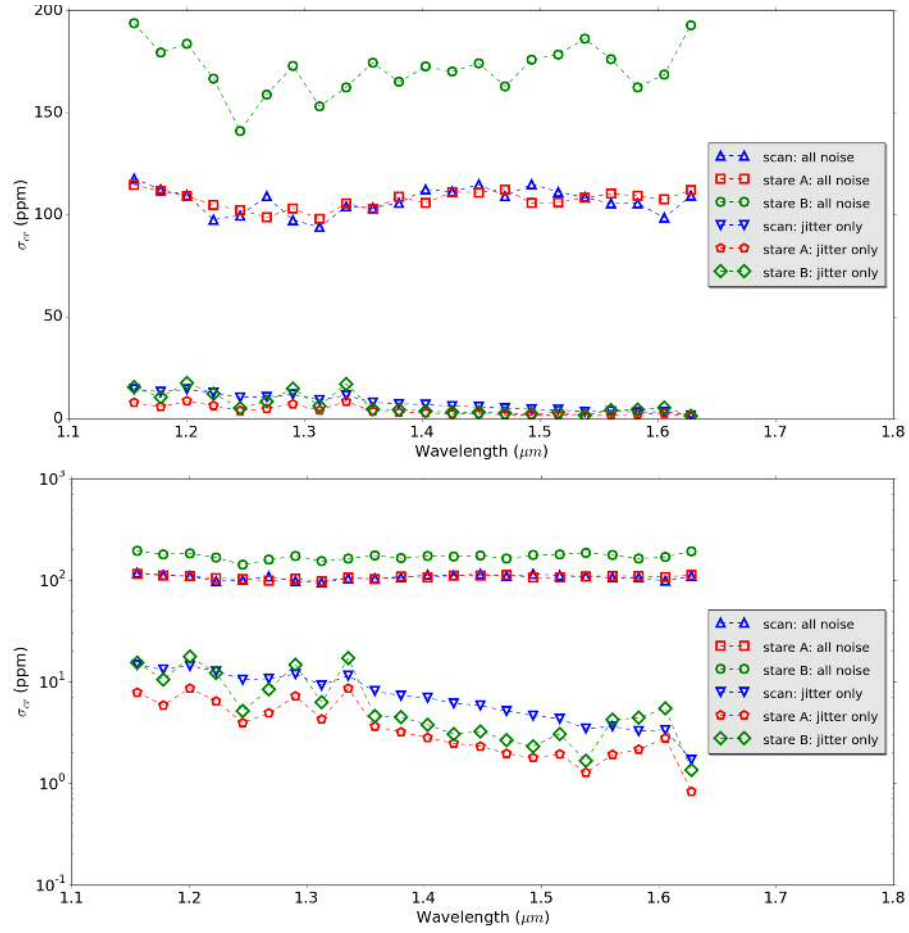


FIGURE 3.11 Case 2: uncertainty on primary transit contrast ratio spectrum,  $\sigma_{cr}(\lambda)$ , under different conditions: scanning mode, staring mode A, staring mode B, with all noise and jitter noise only. Top: normal scale on y axis. Bottom: log scale on y axis.

Noise simulated	Average $\sigma_{cr}$ per spectral bin (ppm)		K-S statistic	p-value
All noise	<i>Scanning mode</i>	<i>Staring mode A</i>	0.14	$9.8 \times 10^{-1}$
	$106.83 \pm 6.26$	$107.16 \pm 4.30$		
	<i>Scanning mode</i>	<i>Staring mode B</i>	1.0	$7.0 \times 10^{-11}$
	$106.83 \pm 6.26$	$171.44 \pm 12.10$		
Jitter noise only	<i>Scanning mode</i>	<i>Staring mode A</i>	0.50	$4.8 \times 10^{-3}$
	$7.82 \pm 3.93$	$3.93 \pm 2.38$		
	<i>Scanning mode</i>	<i>Staring mode B</i>	0.27	$3.3 \times 10^{-1}$
	$7.82 \pm 3.93$	$6.88 \pm 5.10$		

TABLE 3.5 Summary of case 2 results giving average  $\sigma_{cr}$  for each observing mode and noise condition. Also shown are the results of the 2 sample K-S test. A p value of  $< 0.05$  (shown in red) rejects the null hypothesis with  $> 95\%$  confidence.

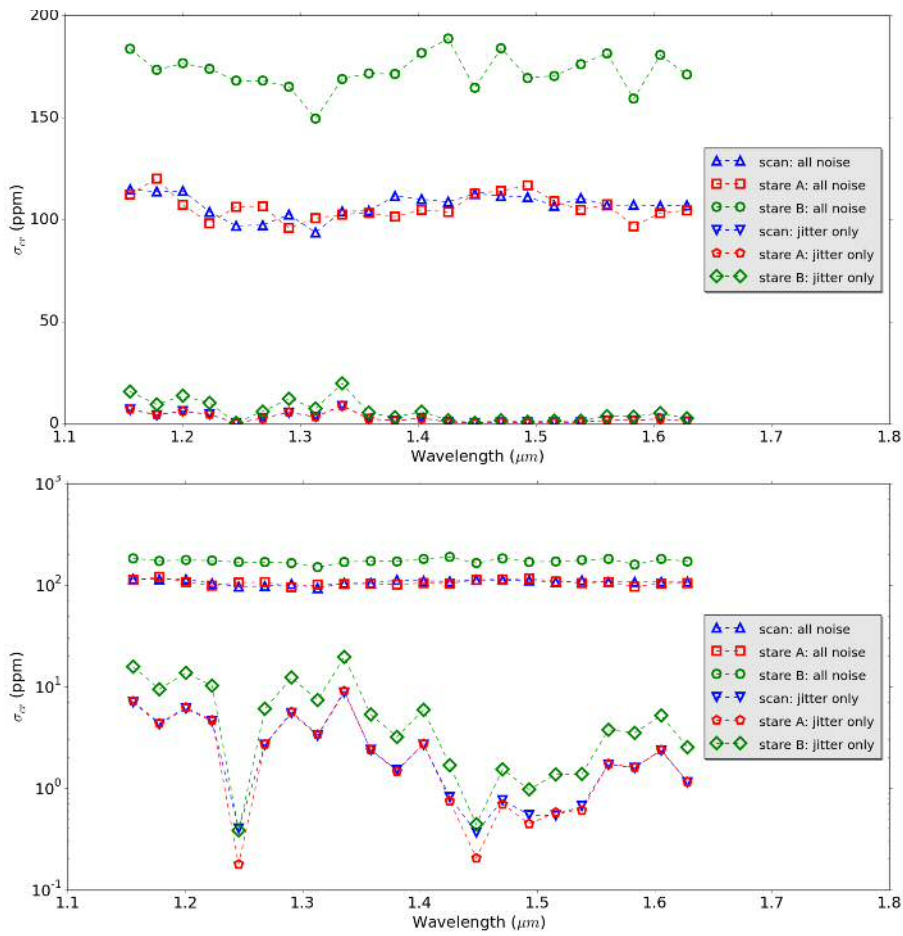


FIGURE 3.12 Case 3: uncertainty on primary transit contrast ratio spectrum,  $\sigma_{cr}(\lambda)$ , under different conditions: scanning mode, staring mode A, staring mode B, with all noise and jitter noise only. Top: normal scale on y axis. Bottom: log scale on y axis.

Noise simulated	Average $\sigma_{cr}$ per spectral bin (ppm)		K-S statistic	p-value
All noise	<i>Scanning mode</i>	<i>Staring mode A</i>	0.32	$1.7 \times 10^{-1}$
	$107.11 \pm 5.60$	$106.03 \pm 6.09$		
	<i>Scanning mode</i>	<i>Staring mode B</i>	1.0	$7.0 \times 10^{-11}$
	$107.11 \pm 5.60$	$172.62 \pm 8.75$		
Jitter noise only	<i>Scanning mode</i>	<i>Staring mode A</i>	0.09	$1.0 \times 10^0$
	$2.72 \pm 2.33$	$2.74 \pm 2.43$		
	<i>Scanning mode</i>	<i>Staring mode B</i>	0.32	$1.7 \times 10^{-1}$
	$2.72 \pm 2.33$	$5.98 \pm 5.27$		

TABLE 3.6 Summary of case 3 results giving average  $\sigma_{cr}$  for each observing mode and noise condition. Also shown are the results of the 2 sample K-S test. A p value of  $< 0.05$  (shown in red) rejects the null hypothesis with  $> 95\%$  confidence.

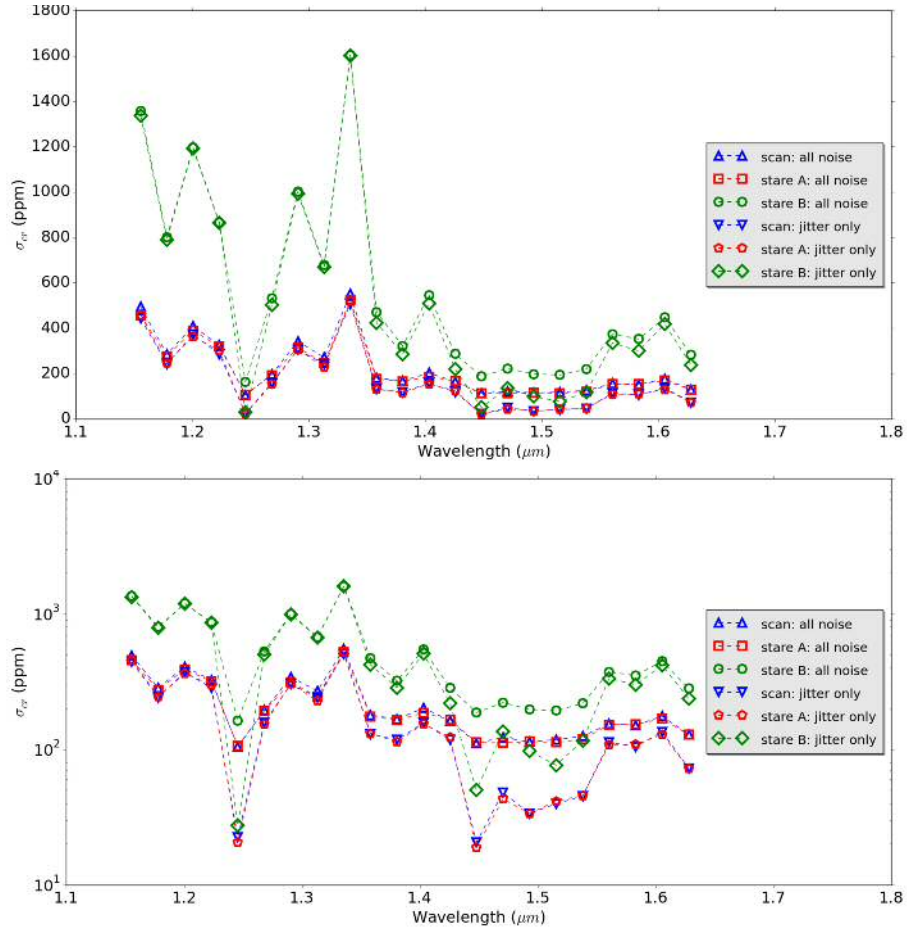


FIGURE 3.13 Case 4: uncertainty on primary transit contrast ratio spectrum,  $\sigma_{cr}(\lambda)$ , under different conditions: scanning mode, staring mode A, staring mode B, with all noise and jitter noise only. Top: normal scale on y axis. Bottom: log scale on y axis.

Noise simulated	Average $\sigma_{cr}$ per spectral bin (ppm)		K-S statistic	p-value
All noise	<i>Scanning mode</i>	<i>Staring mode A</i>	0.09	$1.0 \times 10^0$
	$221.90 \pm 125.39$	$212.73 \pm 116.24$		
	<i>Scanning mode</i>	<i>Staring mode B</i>	0.55	$1.6 \times 10^{-3}$
	$221.90 \pm 125.39$	$558.36 \pm 404.26$		
Jitter noise only	<i>Scanning mode</i>	<i>Staring mode A</i>	0.09	$1.0 \times 10^0$
	$168.37 \pm 135.61$	$168.74 \pm 138.79$		
	<i>Scanning mode</i>	<i>Staring mode B</i>	0.41	$3.6 \times 10^{-2}$
	$168.37 \pm 135.61$	$507.57 \pm 436.96$		

TABLE 3.7 Summary of case 4 results giving average  $\sigma_{cr}$  for each observing mode and noise condition. Also shown are the results of the 2 sample K-S test. A p value of  $< 0.05$  (shown in red) rejects the null hypothesis with  $> 95\%$  confidence.

## 3.6 ANALYSIS

### 3.6.1 CASE 1

The 2-sample Kolmogorov-Smirnov test was used to assess the degree of difference between the noise pattern obtained with scanning mode compared to each of the two staring mode controls. The values of  $\sigma_{cr}(\lambda)$  with wavelength obtained in scanning mode and the corresponding values in the staring mode control constitute the two samples in each case. The null hypothesis for the test is that the two samples come from the same distribution.

In case 1, the baseline case, we see from Figure 3.10 and Table 3.4 that the uncertainty or ‘noise’ on the contrast ratio,  $\sigma_{cr}$ , from jitter noise only is a tiny proportion of from all noise sources, averaging 2.7% in scanning mode, 2.6% in staring mode A and 3.7% in staring mode B.

When comparing scanning mode to staring mode A, with either all noise sources activated or just jitter noise, the average  $\sigma_{cr}$  is about the same in both modes:  $\sim 107$  ppm all noise, and  $\sim 3$  ppm for jitter noise (rounded to the nearest integer). In addition, the K-S test cannot reject the null hypothesis (p-value  $> 0.05$ ) and therefore finds no significant difference between the two sets of data. Since the only difference between scanning mode and staring mode A is the scan effect, this indicates that scanning by itself does not impose any significant additional noise in the Hubble WFC3 IR system under these conditions.

When scanning mode is compared to the more ‘realistic’ staring mode B, we find that the latter produced a much higher value of  $\sigma_{cr}$  than scanning mode in both the all noise case (average of 173 ppm compared to 107 ppm) and the jitter noise only case (average of 6 ppm compared to 3 ppm). The K-S test returns p-values  $< 0.05$  in both these cases, indicating that the null hypothesis is rejected in both cases at  $> 95\%$  confidence, and that therefore the noise in staring mode B is significantly higher than in scanning mode.

This big difference is likely due to the shorter integration time in staring mode B compared to scanning mode. This can increase the fractional photon noise relative to scanning mode due to the lower duty cycle in staring mode B. The jitter noise increase may also be due to the shorter integration time, since less of the high frequencies in the jitter power spectrum fold into the integration time to manifesting as PSF smear (unresolved jitter), and instead contribute to the photometric variation between exposures (resolved jitter).

Therefore I find that rather than introducing any significant extra noise,

scanning mode significantly reduces overall noise and jitter noise in WFC3 IR observations compared to the (realistic) staring mode control, at least under these conditions.

The uncertainties obtained on the contrast ratio are also consistent with published findings. The spectral bin sizes used here are the same as in K14 and B12 allowing a direct comparison with the error bars in the final spectra in those studies. Some accounting for total observing time is however needed.

K14 quote final  $1\sigma$  uncertainties on the published spectrum of 26-33 ppm, obtained from 12 transits (12 visits). To account for the reduced noise from combining multiple transits, we can divide the average 'all noise' value of  $\sigma_{cr}$  in scanning mode by  $\sqrt{12}$ . This gives 31 ppm, which is in the range of the uncertainties in K14. The average uncertainty over all bins in K14 is actually 28 ppm after using the 'divide white' systematic correction or 28.82 ppm after using the 'model ramp' correction. This small difference with the ExoSim value of 31 ppm could possibly be accounted for by slightly reduced fractional photon noise arising from 48 exposures per transit in K14 observation compared to 41 exposures in ExoSim (see Figure 2.14 in Chapter 2). Also some of the K14 transits use the longer exposure time of 103 s ('long' forward and backward scans), which will have an improved duty cycle, and could also contribute to this difference.

We can also compare the staring mode B 'all noise' uncertainties with those from B12. For B12, I calculate an average uncertainty of 215 ppm on the contrast ratio over all bins, derived from the errors given on the size ratio  $R_p/R_s$  in the paper. In this study, staring mode B returns an average 'all noise' value for  $\sigma_{cr}$  of 173 ppm. This is therefore 25% lower than in B12. Some of this difference may be due to the fact that the quoted errors in the paper (obtained using the 'divide out' method to remove the ramp systematic) appear to use only 48 exposures per visit for the curve fitting, giving a total of 144 exposures over the 3 visits. In contrast this simulation produces 262 exposures in one 'visit'. If we assume that to a first order the uncertainty on the contrast ratio is proportional to the total fractional photon noise and that this falls with the square root of the number of exposures, then rescaling the ExoSim error to account for the lower number of exposures in B12, we get 234 ppm, about 9% higher than in B12, but of the same order, indicating this could explain at least some of the discrepancy.

Although the calculation of the error is arrived at very differently in both K14 and B12 compared to the method used here, the fact we arrive at similar values to the published results, is encouraging and would tend to validate the method used here.

### 3.6.2 CASE 2

In case 2, I added intra-pixel variation by changing the diffusion length of the pixel response function to  $1.7 \mu\text{m}$ , causing an appreciable fall in responsivity with distance from the pixel centre. The results for all noise sources combined (Figure 3.11, Table 3.5), are similar in magnitude to those in case 1, with the K-S test again finding no significant difference between scanning mode and staring mode A, both with average  $\sigma_{cr}$  of 107 ppm, and finding that scanning mode B is significantly noisier than staring mode (p-value  $< 0.05$ ), with a much higher average  $\sigma_{cr}$  of 171 ppm.

However for jitter noise in isolation, the results differ from case 1. Now we find that scanning *does* contribute a significant level of additional noise compared to staring, with average  $\sigma_{cr}$  of 8 ppm (rounded to the nearest integer) in scanning mode compared to 4 ppm in staring mode A. The uncertainties across all wavelengths are also significantly different by the K-S test. Thus the intra-pixel variation has resulted in double average  $\sigma_{cr}$  in scanning compared to the effect of baseline jitter alone, although since jitter noise is still a very small percent of the total noise, when added into the mix of all noise sources, this does not result in a significant difference in the overall uncertainty on the contrast ratio.

The  $\sigma_{cr}$  from jitter noise in staring mode B is similar to that in case 1 though very slightly higher (7 ppm). The average scanning mode  $\sigma_{cr}$  has now risen to its level, slightly exceeding it. Scanning mode  $\sigma_{cr}(\lambda)$  appears higher than staring mode B over most of the wavelength range, but the difference does not reach significance by the K-S test.

### 3.6.3 CASE 3

In case 3, the PSF was increased in width by approximately  $3\times$  while keeping the same intra-pixel variations from case 2. The increase in scanning mode jitter-related  $\sigma_{cr}$  is now reversed, the magnitudes and pattern of  $\sigma_{cr}$  returning to something similar to that of case 1 (Figure 3.12 Table 3.6). The broader PSF therefore appears to counter extra noise from intra-pixel non-uniformity and mitigates the effect of the added scanning mode noise in case 2.

The proportion of  $\sigma_{cr}$  attributable to jitter noise compared to that from all noise sources is similar to case 1, and as in case 1 there is no significant difference with staring mode A in the overall noise or isolated jitter noise cases. Staring mode B remains much more noisy than scanning mode, with all noise sources activated,

the average  $\sigma_{cr}$  being 173 ppm compared to 107 ppm in scanning mode.

The broadening of the PSF has also mitigated the jitter noise in staring mode B somewhat, so that while the average  $\sigma_{cr}$  with jitter only is twice that in scanning mode, it does not reach the significance criteria by the K-S test (p-value > 0.05).

### 3.6.4 CASE 4

Finally when we add the much higher level of pointing jitter going from 3.7 to 129 mas bi-axial rms, as might be expected, the jitter noise-related  $\sigma_{cr}$  is greatly increased, and the proportion of  $\sigma_{cr}$  attributable to jitter noise compared to all noise sources is now much higher, averaging 76% and 79% for scanning mode and staring mode A respectively, and 91% for staring mode B (Figure 3.13 and Table 3.7).

Notably, this jitter has not been processed through a decorrelation pipeline, and under these conditions the jitter noise has become the dominant form of noise. Again the K-S test does not detect significant difference between the noise in scanning mode and staring mode A either at the level of all noise or considering jitter in isolation. Thus the scan itself does not appear to add any significance additional noise over the large baseline jitter effect.

The average  $\sigma_{cr}$  in staring mode B is again much higher than than in scanning mode: 2.5 x higher for 'all noise' and 2.3 x for 'jitter noise only', both being significant differences on the K-S test, again showing the much higher sensitivity to jitter noise with the shorter integration time.

## 3.7 DISCUSSION

In this chapter I showed how ExoSim can be used in a 'retrospective' application by modeling an existing instrument, the Hubble WFC IR, and elucidating the contribution of a complex noise source, to help address controversies about the overall noise on the planet spectrum. Here I examined the noise metric that ultimately matters most,  $\sigma_{cr}$ , the uncertainty on the final contrast ratio spectrum itself, directly measured using a Monte Carlo simulation approach.

Overall, in contrast to Swain et al. (2013b), I find from these tests that scanning mode on the WFC3 IR mode appears 'superior' to staring mode in terms of overall noise on the contrast ratio spectrum, resulting in a 38% decrease in average  $\sigma_{cr}$  for the K14- and B12-equivalent simulations of GJ 1214b. The backward scans of K14 were found to have an additional amplitude in the scan direction compared

to forward scans, which were not simulated in this test. This could result in more scanning mode noise than was detected here, but is unlikely to overcome the large difference in overall noise compared to (realistic) staring mode. Also I did not simulate the slight tilt of the spectrum or the effect of small changes in the wavelength solution with row. Again these could result in increased scan noise perhaps detectable in the 'jitter noise only' simulations, but would be unlikely to change this conclusion.

The overall  $\sigma_{cr}$  found in scanning mode simulations is consistent with the error bars in K14, and is thus supportive of that study and its findings that GJ 1214b's spectrum is most consistent with a cloudy atmosphere. However a caveat would be that this simulation did not take into account the 'ramp' systematic and its correction in data reduction, and thus the impact of this on the final error. There was also omission of Earth occultation gaps in the light curves. A more robust verification of K14 could involve a similar Monte Carlo simulation including these effects. Also we have seen that studies in scanning mode use a wide range of scan rates, some of which were verified by my analysis and other were not. It is possible that at higher scan rates, especially if using the gyros rather than FGS, the pattern of noise may differ. A further study could analyse pointing data from additional WFC3 exoplanet scanning mode studies, such as those in Table 3.2, in the same way as the K14 data were analysed, to see if there are different patterns in x and y jitter that may impact on overall noise. Simulations could be performed of these studies in the same way as performed here for K14, and the  $\sigma_{cr}$  results compared to published data, to help verify or question the final conclusions of each study.

I performed a limited analysis of the parameters that modify scanning mode noise, by looking at the three additional case studies. In all cases scanning mode performed better in overall noise than staring mode, which may be largely attributable to its better duty cycle reducing fractional photon noise. However scanning mode also 'protects' from the effects of jitter noise by allowing longer integration times, so that more jitter frequencies are absorbed into the integration time and less manifest causing photometric variation between exposures. The shorter exposure (realistic) scanning mode B was more sensitive to jitter noise as a result. Only case 2, with the intra-pixel variations introduced, showed a definite indication of significant additional noise attributable from the scanning effect alone, and this was reversed by broadening of the PSF in case 3. The high level of pointing precision of Hubble means that even without any jitter decorrelation the jitter noise-related impact on  $\sigma_{cr}$  was only of the order of 2-3% of the overall value. When the Herschel PSD was used instead, jitter noise became the dominant noise

source in all observing modes, thus under such pointing jitter, mitigation strategies such as jitter decorrelation would be essential. We therefore have seen the effect of some factors that influence jitter noise; in the next chapter, in the context of the ARIEL mission I explore the contributory factors to jitter noise in more detail.

This study indicates that scanning mode on WFC3 IR does not appear to be detrimental in terms of noise. This may be aided not only by the high level of pointing stability enjoyed by Hubble but also a fairly uniform intra-pixel response function. Not all spacecraft will have such good pointing stability or pixel non-uniformity, and under such alternate conditions, the impact of scanning could be more significant. ExoSim could be configured for the James Webb Space Telescope and its suite of instruments which will be performing transit spectroscopy of exoplanets. One immediate application could be to similarly assess the potential for spatial scanning noise.



## CHAPTER 4

# EXOSIM AND THE ARIEL PHASE A STUDY

---

---

**A**RIEL is a proposed space telescope that has the goal of performing the first ever large scale spectroscopic survey of exoplanets using the technique of transit spectroscopy. ExoSim was used as the dedicated end-to-end simulator for the mission which had been selected as an ESA M4 candidate mission. In this chapter, I describe the application of ExoSim to the ARIEL Phase A study. The goal was to use ExoSim to simulate the performance of various iterations of the ARIEL instrument design, finding system level solutions that lead to a low cost, low risk instrument compatible with the science goals of the mission. ExoSim was used to select between different candidate designs, and played a crucial role in discovering and mitigating pointing jitter noise. ExoSim was used to find noise requirements compatible with the science case, and finally test the performance of the stabilised end-of-phase design<sup>1</sup>.

### 4.1 ARIEL

ARIEL (the Atmospheric Remote Sensing Infrared Exoplanet Large Survey) is a proposed space telescope dedicated to performing the first ever exoplanet atmospheric characterisation survey using the techniques of transit and eclipse spectroscopy. ARIEL has a 0.9-m class primary mirror and will produce instantaneous and well-calibrated exoplanet spectra over a broad wavelength range (0.5-7.8  $\mu\text{m}$ ). ARIEL was successfully proposed as a European Space Agency (ESA) M4 (medium

---

<sup>1</sup> Material from this chapter is presented in Sarkar et al. (2017a).

class mission) candidate in June 2015 (ARIEL Consortium, 2015)<sup>2</sup>, and has recently completed its Phase A design stage, prior to the final selection decision by ESA in the latter half of 2017. It is one of three missions competing for the M4 slot. If selected, ARIEL will have a planned launch in 2026, operating in a large amplitude L2 orbit, a location that offers the maximum field of regard and thermal stability. It will have a nominal operational lifetime of 3.5-4 years.

### 4.1.1 SCIENCE GOALS

The highest level science goal of the ARIEL mission is to conduct the first ever spectroscopic survey of exoplanets. Such a survey hopes to address the huge diversity of exoplanets, proposing frameworks for planet classification, and aiming to find answers to fundamental questions of planet formation, migration and evolution.

A target list of about 1000 exoplanets, ranging from rocky planets through transitional planets to gas giants, will be selected. The target list, also known as the Mission Reference Sample (MRS), will be designed to cover a wide range of sizes, temperatures, stellar metallicities and stellar spectral classes (F to M). Other considerations are to include a wide range of densities and orbital parameters. The target list will be updated based on anticipated results from upcoming space missions such as PLATO and TESS, as well as ground-based surveys such as NGTS.

ARIEL will focus on warm planets (> 400K) orbiting stars brighter than K mag 9.5. Such planets are less likely to have cold traps and condensation in their atmospheres for key species such as H<sub>2</sub>O, NH<sub>3</sub>, CH<sub>4</sub>, SiO, CO<sub>2</sub>, CO and, if the temperature is high enough, TiO, VO and CrH (ARIEL Consortium, 2017)<sup>3</sup>. This means that atmospheric measurements will offer a direct insight into the bulk and elemental composition of the planet interior, constraining interior models and permitting measurement of the elemental composition which can constrain the chemical history of the planet and provide evidence for migration. Although ARIEL is not aimed at studying rocky temperate planets, I explore the possibility of this in Chapter 5 with simulated observations of the TRAPPIST-1 planets.

The broad and instantaneous coverage over a wide wavelength range avoids having to combine spectral observations from different instruments taken at different times, which may suffer from calibration differences, stellar variations

---

<sup>2</sup> ARIEL Proposal Document: <http://sci.esa.int/science-e/www/object/doc.cfm?fobjectid=56561>. All ARIEL Phase A study documents are available at <https://ariel-spacemission.eu/>

<sup>3</sup> ARIEL Yellow Book: <https://ariel-spacemission.files.wordpress.com/2017/05/sci-2017-2-ariel.pdf>

or changes in planet conditions. This broad coverage is also useful for breaking degeneracies in model atmospheric fits due to overlapping spectral features between different species. As per Barstow et al. (2015a) such broad coverage also aids breaking the degeneracy between chemical abundances and temperature structure in eclipse spectra and is useful for probing cloud properties.

The global strategy will be to observe the target list in 3 rounds or 'tiers', each progressively more selective (ARIEL Consortium, 2017). The features of the three-tiered approach are summarized in Table 4.1.

'Tier 1' is the 'reconnaissance survey', with low-resolution observations designed to assess the complete sample of around 1000 planets, projected to take about 30% of the mission observing time. The lower resolution of this tier gives higher signal-to-noise ratios (SNRs) with the goal of obtaining coarse planet spectra in about one transit. This tier can answer statistical questions such as what fraction of small planets have atmospheres, how many have clouds or a primordial H<sub>2</sub>/He atmosphere, and the range of albedos and bulk temperatures, but may have insufficient resolution for detecting most spectral features. Barstow et al. (2017) showed that the slope of the spectrum in the NIR-visual range can be used for cloud diagnostics such as height and optical depth. Tier 1 also permits the further selection of those planets which may have the potential for more detailed characterisation in the other tiers.

'Tier 2' or the 'deep survey', will be at a higher (but not maximum) resolution and is projected to take up about 60% of the observing time. It aims, within a smaller sample, to detect the main atmospheric components, chemical abundances of trace gases and the elemental composition. In secondary eclipse, the vertical thermal structure can also be probed. Selected planets may be studied with phase curve spectroscopy, probing the day-to-night variations in atmospheric composition and structure.

'Tier 3', known as the 'benchmark survey', is projected to take about 10% of the observing time. A small number of planets will be selected for the highest resolution studies, requiring many transits to achieve the goal SNR. This tier will conduct detailed analysis of the atmosphere and its spatial and temporal variability, gaining deeper insight into the 'weather' of these planets, including variability of cloud coverage or patterns in global circulation.

Transit and eclipse spectroscopy have thus far only characterised a tiny proportion of the known sample of exoplanets. ARIEL has the potential to perform transformative science in this field, producing the largest ever catalogue of exoplanet atmospheres (Tinetti et al., 2016).

TABLE 4.1 ARIEL three-tiered observational strategy. Information obtained from ARIEL Yellow Book (ARIEL Consortium, 2017) and Zingales et al. (2017).

Tier	Mission fraction	Goal SNR	Resolution	Science goals
1 ('Survey')	~30%	$\geq 7$	10 spectral elements	<ul style="list-style-type: none"> <li>fraction of planets with clouds or retain H<sub>2</sub>/He</li> <li>constraining/removing degeneracies in interpretation of mass-radius diagrams</li> <li>classification schemes</li> <li>albedo, temperature and energy balance</li> </ul>
2 ('Deep')	~60%	$\geq 7$	R=10/50/15 (NIRSpec/Ch0/Ch1)	<ul style="list-style-type: none"> <li>main atmospheric component for small planets</li> <li>chemical abundances of trace gases</li> <li>atmosphere thermal structure</li> <li>cloud characterization</li> <li>elemental composition</li> </ul>
3 ('Benchmark')	~10%	$\geq 7$	Full resolving power R=10-20/100/30 (NIRSpec/Ch0/Ch1)	<ul style="list-style-type: none"> <li>detailed planet chemistry and dynamics</li> <li>weather, spatial and temporal variability</li> <li>elemental composition</li> </ul>

### 4.1.2 PAYLOAD

The ARIEL spacecraft and instrument design evolved during the Phase A study, the main features of the 'final' stabilised design at the end of Phase A are presented here. The ARIEL spacecraft has modular design (Figure 4.1) with a payload module (PLM) and a service module (SVM) (Eccleston, 2017)<sup>4</sup>. The SVM consists of the warm payload units. These include the Fine Guidance System (FGS), warm front end electronics, the instrument control unit incorporating the warm front end electronics for the main spectrometer and an active cooler system. The PLM consists of an optical bench for the telescope and instruments, the telescope system and common optics, the main spectrometer known as the ARIEL Infrared Spectrometer or AIRS, the FGS (which incorporates a low resolution Near Infrared Spectrometer or NIRSpec) and thermal hardware. The AIRS detectors will be actively cooled to < 42 K with the rest of the PLM cooled passively to < 55 K.

<sup>4</sup> ARIEL Payload Design Description: [https://arielspacemission.files.wordpress.com/2017/05/ariel-ral-pl-dd-001\\_ariel-payload-design-description\\_iss-2-01.pdf](https://arielspacemission.files.wordpress.com/2017/05/ariel-ral-pl-dd-001_ariel-payload-design-description_iss-2-01.pdf)

**Telescope** The ARIEL telescope will have a 1.1 x 0.7 m off-axis primary mirror in a Cassegrain design with a collecting area of 0.64 m<sup>2</sup> and diffraction limited at 3 μm. A series of additional mirrors and dichroics direct the beam into the instrument channels (Figure 4.2). A re-focusing mechanism is included behind the M2 mirror. The dispersive elements within all the spectrometer channels are prism-based.

**Instruments** There are two main instruments, AIRS and the FGS, each consisting of multiple channels. AIRS consists of 2 channels: Channel 0 (Ch0) covering 1.95-3.9 μm at R~100, and Channel 1 (Ch1) covering 3.9-7.8 μm at R~30. The FGS consists of 3 visual range narrow-band photometric channels (two of which are used also for closed-loop feedback on the Attitude and Orbit Control System) and NIRSpec covering 1.25-1.9 μm at R~10-20<sup>5</sup>.

### 4.1.3 EXOSIM IN THE ARIEL PHASE A STUDY

ARIEL underwent a Phase A study between Jan 2016 and Feb 2017, during which ExoSim was used as the dedicated end-to-end simulator for the mission. ExoSim was utilized to find system level solutions for noise issues wherever possible in data reduction and analysis. The overall aim was to obtain a design that was minimized in cost, complexity and risk but still able to fulfill the mission's science objectives. Specific uses of ExoSim in Phase A were as follows:

- 1) Selection between the proposal instrument (a 'high resolution' spectrometer) and a lower resolution alternate design, both of which would be compatible with the science case.
- 2) Validation of the ESA Radiometric Model<sup>6</sup>, essential in testing the ARIEL Mission Reference Sample, and thus viability of the science case.
- 3) Discovery of high pointing spectral jitter noise in ARIEL observations, followed by exploration of the mechanism and dependencies of jitter noise, formulation and implementation of mitigation strategies, and demonstration that data reduction methods including decorrelation techniques, could control this noise without major redesign to a more expensive spacecraft attitude control system.
- 4) Establishing noise requirements compatible with a viable science using a matured but not final design.

<sup>5</sup> This is the goal R for the instrument, however the stabilised design at the end of Phase A design has a higher instrumental R power of 30-66 (Table 4.8).

<sup>6</sup> Described in Chapter 2.

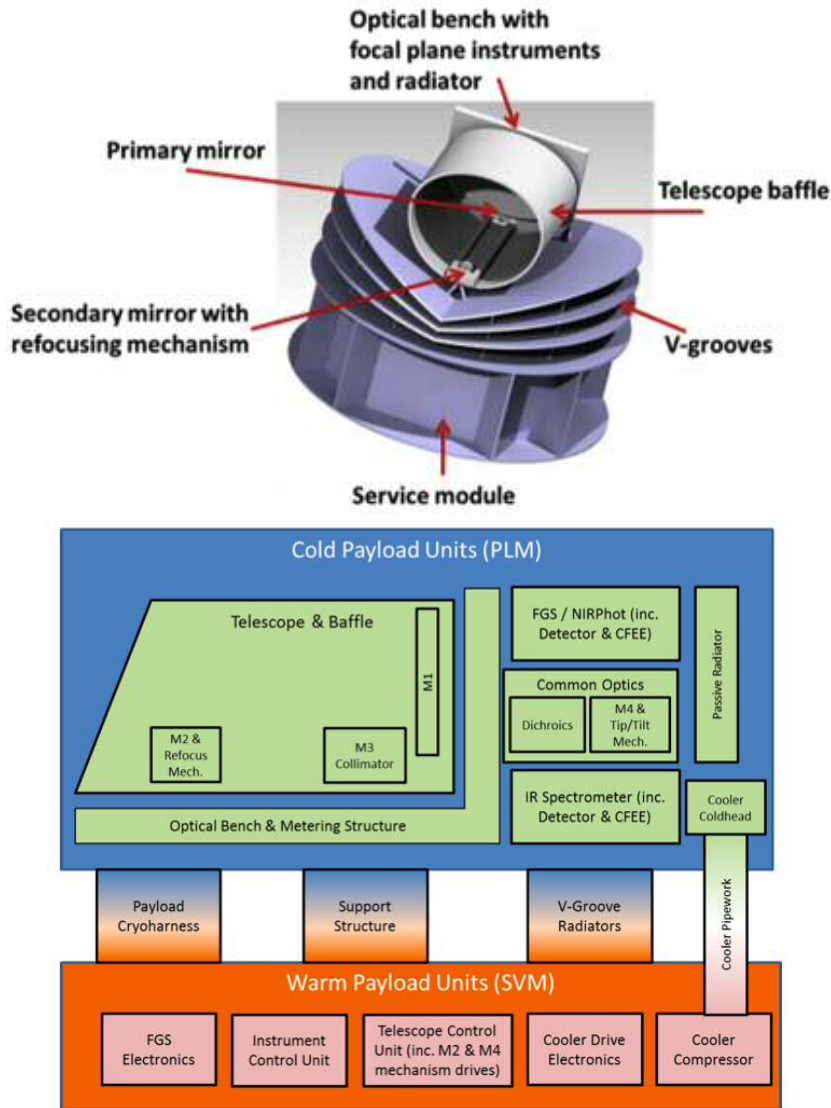


FIGURE 4.1 The ARIEL spacecraft and layout of components. Top: CAD diagram of current ARIEL concept. Bottom: baseline payload architecture. Figures from ARIEL Payload Design Description (Eccleston, 2017).

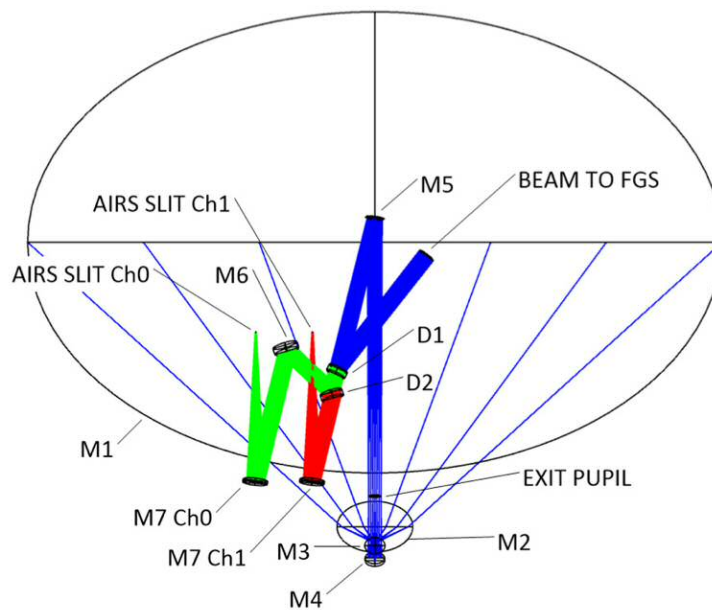


FIGURE 4.2 Optical pathways in the ARIEL telescope. Figure from ARIEL Yellow Book (ARIEL Consortium, 2017).

5) Testing the 'final' stabilised end of Phase A design, assessing its noise performance characteristics, and ensuring it remained compatible with the mission science case.

To process the ExoSim output, a basic data reduction pipeline was also developed as part of this study, which itself underwent modifications during the course of Phase A. These Phase A studies are now described in more detail.

## 4.2 EARLY PROPOSAL DESIGNS FOR THE ARIEL SPECTROMETER

### 4.2.1 HRS vs LRS

#### 4.2.1.1 ORIGINAL 'HIGH RESOLUTION' SPECTROMETER

The initial proposal design (ARIEL Consortium, 2015) for the main infrared spectrometer consisted of a grating design covering 1.95-7.8  $\mu\text{m}$  and 2 photometric bands 0.55-0.7  $\mu\text{m}$  and 0.8-1.0  $\mu\text{m}$  provided by FGS, coupled to passively cooled Mercury-Cadmium-Telluride (MCT) detectors. The spectrometer was divided into 2 bands: Ch0 covering 1.95-3.9  $\mu\text{m}$  at  $R=200$ , and Ch1 covering 3.9-7.8  $\mu\text{m}$  at  $R=100$ .

The justification for choosing this wavelength range and resolution was as follows:

1) The peaks of the black body fluxes for the range of temperatures expected for the ARIEL planet sample (400 - 2000 K) occur in the 1-8  $\mu\text{m}$  range, which gives the best secondary eclipse signal ( $F_p/F_s$ ) for these planets (Figure 4.3). A broad coverage allows the probing of different layers of the atmosphere to build up a temperature-pressure profile.

2) The 1.95-7.8  $\mu\text{m}$  range contains ro-vibrational bands for key molecular species expected in exoplanet atmospheres. These include  $\text{H}_2\text{O}$ ,  $\text{CO}_2$ ,  $\text{NH}_3$ ,  $\text{CO}$  and  $\text{CH}_4$ , all major constituents in the Solar System (Figure 4.4). The range also contains signatures of more exotic species such as  $\text{VO}$ ,  $\text{TiO}$ ,  $\text{H}_2\text{S}$  and  $\text{HCN}$ . The features in this wavelength range are also generally stronger than at shorter wavelengths, and in addition the spectroscopic profiles for molecules at  $< 2 \mu\text{m}$  are not as well characterized especially at higher temperatures (Tinetti et al., 2013). Finally, since most molecules have at several spectral features in this range, degeneracies between different molecules can be broken, as well as degeneracies between molecular abundances and the vertical thermal structure in emission spectra.

3) According to Tinetti et al. (2013), for an unambiguous identification of a given spectral feature, the spectral resolving power should ideally be sufficient to separate two adjacent J-components of the molecular band. For example for the water band at 2.69  $\mu\text{m}$ , such an analysis predicts an R power of 130, and for the band at 6.27 an R of 55. This reasoning drives having a 'high resolution' design with instrument  $R \approx 200$  in Ch0 and  $R \approx 100$  in Ch1.

Although not providing spectroscopic information, the two visual photometric channels were deemed useful for the following scientific reasons:

1) The reflected component of the reflection-emission spectrum of the planet will peak in the visual-NIR with the black body peak of the star. Constraining its magnitude in this region can help to constrain the albedo of the planet, and thus the energy budget.

2) Stellar variability is greatest in the visual range. Thus these channels can monitor variations in flux and these can be used to apply corrections on the transit depth (see Chapter 5).

3) The slope of the the continuum in this region is deflected to higher transit depths by Rayleigh scattering. The effect on intensity varies as  $1/\lambda^4$ , and thus the scattering is more marked in the visual than in the IR. Characterising the slope can help to constrain the likely scattering molecules. Clouds can also affect the slope at these wavelengths.

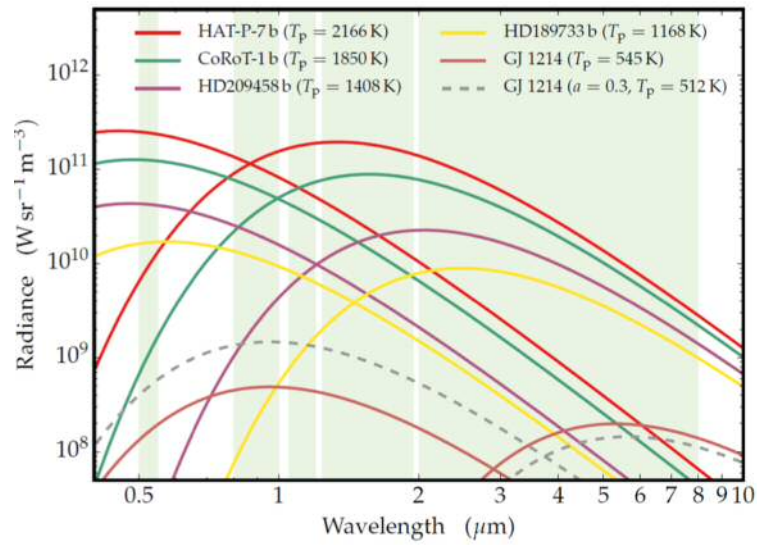


FIGURE 4.3 Black body fluxes for a range of likely ARIEL planet targets. The reflection and thermal emission components are shown for each planet. The thermal emission components peak within the 1-8  $\mu\text{m}$  wavelength range. Figure from ARIEL Yellow Book (ARIEL Consortium, 2017).

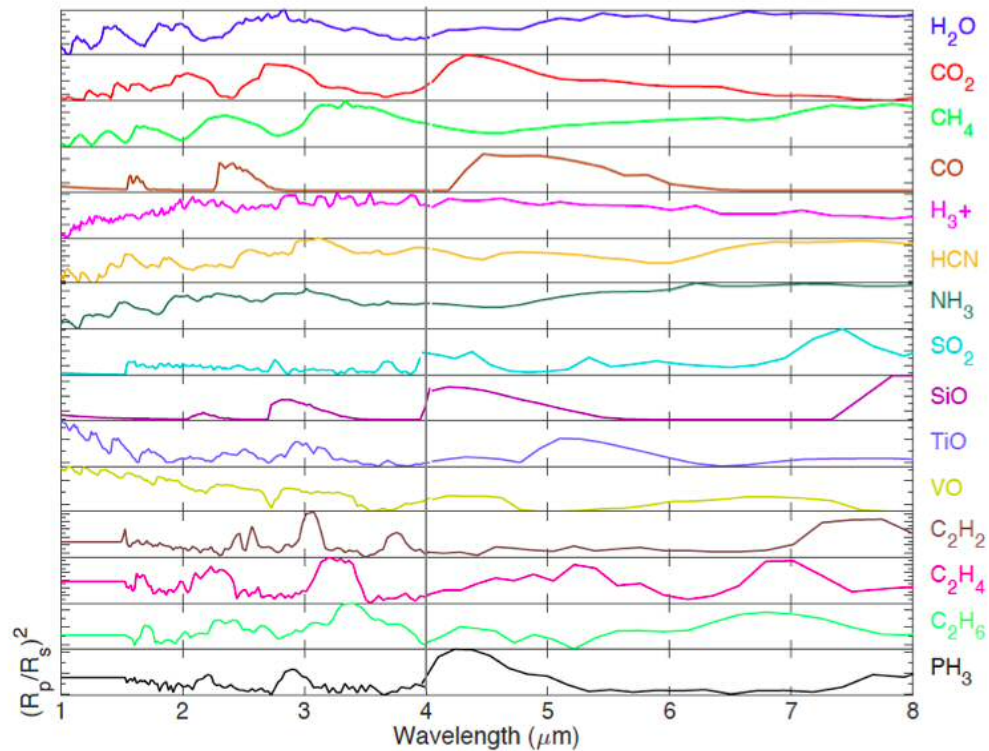


FIGURE 4.4 Spectral features for a variety of molecules likely in ARIEL target planet atmospheres, binned at  $R=100$  upto 4  $\mu\text{m}$  and  $R=30$  above 4  $\mu\text{m}$ . Characteristics of individual species are identifiable at these resolutions. Figure from ARIEL Yellow Book (ARIEL Consortium, 2017).

Later in Phase A, coverage in the NIR and visual range was greatly expanded upon by addition of a third photometric channel and NIRSpec.

#### 4.2.1.2 ALTERNATE 'LOW RESOLUTION' SPECTROMETER

Despite the more stringent criteria above, Figure 4.4 clearly shows that molecular bands can be identified at much lower resolution. In this figure, Ch0 is binned to  $R=100$  and Ch1 to  $R=30$ . All major molecular bands can be still be identified (Figure 4.4), and the signatures of different molecules distinguished. The same paper by Tinetti et al. (2013) also states that  $R=30$  is sufficient to detect most of the molecules at  $\lambda > 5 \mu\text{m}$ , especially at high temperatures, but not the Q-branches of  $\text{CO}_2$ , HCN and other hydrocarbons. Previous spectral retrieval studies at  $R=100$  for the EChO mission (Barstow et al., 2015b) had shown that temperature-pressure profiles and chemical abundances for hot and warm Jupiters and hot Neptunes could be retrieved with an acceptable number of transits for all but the rarer trace species. Thus using  $R=100$  in Ch0 and  $R=30$  in Ch1 appeared an adequate maximum resolution for the goals of tier 2 and tier 3. Spectral retrieval studies as part of ARIEL Phase A by the group at University College London (UCL) on a hot Jupiter and warm Neptune using the NEMESIS and Tau-Rex spectral retrieval codes confirmed that using a maximum resolution of  $R=100$  in Ch0 and  $R=30$  in Ch1 produced accurate retrievals in both tier 2 and tier 3. These fulfilled science requirements, achieving the required SNR of 7 or above in 1-10 transits or eclipses in the majority of cases (ARIEL Consortium, 2017).

Given the improved SNR and reduced number of transits that would be required at lower resolution, an alternative 'low resolution' spectrometer (LRS) design was put forward at the start of the Phase A study in addition to the original 'high resolution' spectrometer design (HRS). The LRS would have an instrumental  $R \approx 100$  in Ch0 and  $R \approx 30$  in Ch1.

A feature of the LRS design was that it had a smaller linear dispersion of the spectrum (i.e. fewer pixels to cover the same spectral-resolution-element-sized bin) compared to the HRS. This meant that it could potentially accommodate detectors with higher dark current or read noise (since the increased noise would be offset by the lower number of pixels per resolution element). This in turn meant it could be compatible with a wider range of possible available detectors than the HRS. The baseline detector for the original HRS design was the the Teledyne H1RG MCT array developed for NEOCam (McMurtry et al., 2013), with a dark current of about  $16 \text{ e}^-/\text{s}$  (ARIEL Consortium, 2015). European manufacturers (Selex-ES,

AIM and CEA/LETI) all had IR detectors in development with mostly higher projected dark currents. The LRS could potentially accommodate these detectors as well as the Teledyne detectors, whereas the HRS would have to accommodate only the Teledyne detector.

Towards the start of the Phase A study therefore, ExoSim was tasked comparing the noise performance of the two designs, as a way to decide on further development of one or other design.

## 4.2.2 EVALUATION OF INITIAL DESIGNS WITH EXOSIM

### 4.2.2.1 NOISE BUDGET METHOD

For the purposes of assessing the ARIEL instrument performance during the Phase A study, I adopt a method of obtaining ‘noise budgets’. In this method, ExoSim simulates an out-of-transit (OOT) observation of a given host star, and the noise in spectral-resolving-element-sized bins is found for different noise sources. For each channel we build up a wavelength-dependent picture of the contribution of each noise type. This characterises the noise performance of the instrument channel for the given target. It can identify which noise sources may be problematic in relation to the photon noise limit, and can be used to assess the efficacy of noise mitigation strategies. The mitigation of noise and systematics can in general be tackled at either the level of the instrument and spacecraft design, or at the level of data reduction, the latter being preferable from the point of view of cost and complexity of the spacecraft.

To allow consistency with other metrics such as those in the ESA radiometric model, the noise is presented as the variance of the signal (‘noise variance’) per unit time in each spectral-resolution-element-sized bin (or photometric channel).

The highest level noise requirement is that photometric stability of the instrument should not add ‘significantly’ to the Poisson noise from the astrophysical sources (star, planet and zodiacal light). What constitutes ‘significant’ ultimately relates back to whether the science of the mission can be fulfilled. In the case of ARIEL, this constitutes the ability to perform the tier 1 transit spectroscopy survey of 1000 planets within the mission lifetime, with an appreciable amount of time left for tier 2 and tier 3 studies.

Noise sources simulated in ExoSim for noise budget tests were: 1) photon noise from the source, 2) dark current shot noise, 3) read out noise, 4) zodiacal

light noise, 5) emission noise<sup>7</sup>, and 6) pointing jitter noise. The latter was broken down into spectral and spatial components for the spectroscopic channels, and left as 'combined' (i.e. undifferentiated in direction) jitter noise for photometric channels.

We are measuring here therefore the noise on the OOT signal and not the noise on the transit depth or contrast ratio. Full transit simulations were deemed unnecessary for the purpose of instrument performance testing since the instrument photometric stability and precision can be measured with respect to the OOT signal, and noise requirements were also defined in relation to the OOT signal. However there is a proportionality between the noise on the OOT signal per bin,  $\sigma_{oot}(\lambda)$ , and the noise or uncertainty on the contrast ratio,  $\sigma_{cr}(\lambda)$ , as elaborated on below.

#### 4.2.2.2 USING OOT NOISE TO ESTIMATE NOISE ON THE CONTRAST RATIO

The OOT noise,  $\sigma_{oot}(\lambda)$ , can be related to the noise on the contrast ratio in each spectral bin (or photometric channel),  $\sigma_{cr}(\lambda)$ , using the following equation:

$$\sigma_{cr}(\lambda) \approx \frac{\sqrt{2} \sigma_{oot}(\lambda)}{\sqrt{\frac{N}{2}} S_{oot}(\lambda)} \approx \frac{\sqrt{2} \sigma_{oot}(\lambda)}{\sqrt{\frac{T_{14}}{\tau}} S_{oot}(\lambda)} \quad (4.1)$$

where  $\sigma_{oot}(\lambda)$  is the OOT noise (variations with exposure) in the spectral bin (or photometric channel),  $S_{oot}(\lambda)$  is the mean stellar OOT signal per exposure in that bin and  $N$  is the total number of exposures during a transit observation (which may vary between channels). The above equation assumes an equal number out-of-transit and in-transit exposures.  $N$  is equal to the twice the transit duration,  $T_{14}$ , divided by the exposure time,  $\tau$ , giving the expression on the right side. This formula also assumes no correlated noise (or insignificant levels), and should be most accurate for flattish light curves, e.g. above  $2 \mu\text{m}$ , where the effects of limb darkening will be minimal.

In a test of this formula, I used ExoSim to simulate the transit of GJ 1214b observed with a 1-m telescope and a R=200 grating spectrometer, with only photon noise simulated. A linear limb darkening coefficient of 0.27 was used. 20 bins were combined to obtain the 'white light curve', consisting of 42 exposures (half of which were out-of-transit). The noise on the white light contrast ratio,  $\sigma_{cr}$ , was obtained using 3 methods: a) using  $\sigma_{oot}$  (obtained after disabling the light curve in the

<sup>7</sup> Noise from thermal emission of instrument and telescope.

TABLE 4.2 Comparing estimates of  $\sigma_{cr}$  from different methods.

Error formula	MCMC posterior	Monte Carlo	
		$\sigma_{sample}$	$\sigma_{fit}$
$4.67 \pm 0.50 \times 10^{-5}$	$4.70 \pm 0.81 \times 10^{-5}$	$4.86 \times 10^{-5}$	$4.81 \times 10^{-5}$

simulation) and the above formula; b) curve fitting with a Markov Chain Monte Carlo (MCMC) code where the standard deviation of the marginalized posterior is used to give the uncertainty on the recovered contrast ratio; c) multi-realization Monte Carlo simulation with repeated curve fits using a downhill simplex algorithm and finding the uncertainty on the contrast ratio through the standard deviation of the distribution of the transit depths (as used in Chapters 2 and 5) (Figure 4.5). 100 simulations were performed for the first 2 methods and the average noise obtained. For the third method, 2 sets of 1000 realizations were performed and the average noise from the 2 simulations obtained. The results are shown in Table 4.2. For the multi-realization Monte Carlo method the results of using the standard deviation calculated from the data ( $\sigma_{sample}$ ) or from a Gaussian fit ( $\sigma_{fit}$ ), are also shown. Despite the presence of limb darkening, we find a good agreement between the 3 methods, the average error formula result being within 4% of the multi-realization Monte Carlo method (using  $\sigma_{sample}$ ) and within 1% of the average result of the MCMC method. The Monte Carlo result lies within the standard deviation of the error formula and MCMC results. For the Monte Carlo method, there is not much difference between using the standard deviation from the Gaussian fit and the calculated standard deviation from the data, the former being 1% lower compared to the latter. This test gives us confidence that the use of the above error formula for estimating the contrast ratio noise from the OOT noise will be accurate to within a few percent. Although the test was performed on the white light curve, in principle it can be applied to each spectral light curve. This relationship between the OOT noise and the contrast ratio noise forms the basis of the contrast ratio noise calculations used in Chapter 6.

#### 4.2.2.3 EXOSIM SIMULATIONS

Each design, HRS and LRS, was implemented in ExoSim with its own input configuration file and associated reference files. Only the main spectrometer (later to become 'AIRS') was simulated. The configurations used in ExoSim for each

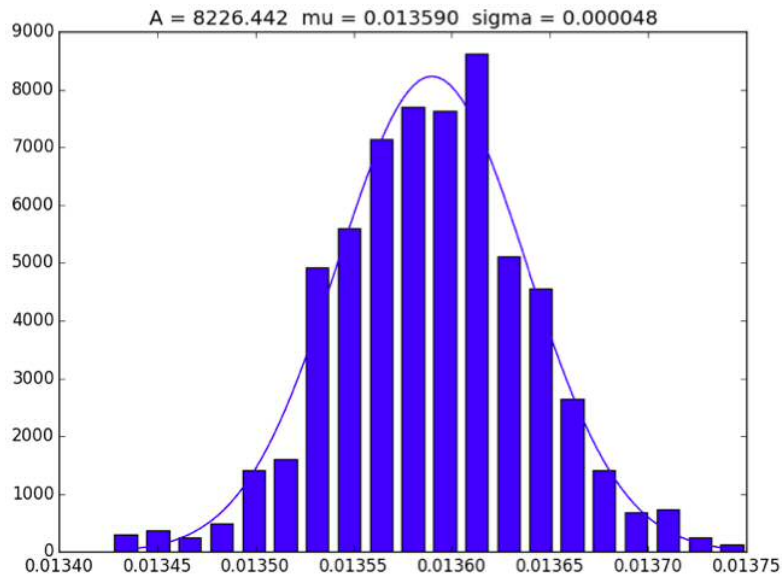


FIGURE 4.5 Finding the uncertainty on the contrast ratio using Monte Carlo simulation. The uncertainty can be quantified by the standard deviation of the distribution, either calculated from the data or through fitting of a Gaussian profile. The results of the Gaussian fit are shown above the chart, with the standard deviation being 48 ppm in this case.

design are shown in Table 4.3. Both these initial designs used gratings for the dispersive element. Note the use of higher dark current detectors in the LRS design (the projected dark currents for European detectors under development). Optical surface emissions were simulated assuming an emissivity of 0.03 for all surfaces and channel temperatures of 60 K. The zodiacal light model described in Chapter 2 was used without adjustment.

Both the HRS and LRS designs were divided into 2 channels (Ch0 and Ch1) with the same f-numbers used in each design. The f-number was chosen ensure Nyquist sampling of the PSF at the blue end, i.e the FWHM of the PSF is sampled by at least 2 pixels. The reason to divide the wavelength range into 2 channels is so that each could be optimized for its particular wavelength range and instrumental R power. This division also controls the width of the PSF and the spectral resolution-element-sized bins at longer wavelengths (which will tend to become very large with a single channel). Also different detectors may also have different optimal and cutoff wavelengths, so that each channel has the option of a dedicated and optimized detector for its particular wavelength range.

The ARIEL telescope was simulated using a 0.9-m diameter mirror and three mirror surfaces with individual transmissions and emissivities of 0.03, all held at 70 K temperature. For these early tests, the Herschel pointing jitter power

TABLE 4.3 Configurations of the Low Resolution Spectrometer (LRS) and High Resolution Spectrometer (HRS) designs implemented in ExoSim. Units of reciprocal linear dispersion are  $\mu\text{m}$  of wavelength per  $\mu\text{m}$  of distance.

Parameter	LRS		HRS	
	<i>Ch0</i>	<i>Ch1</i>	<i>Ch0</i>	<i>Ch1</i>
Wavelength ( $\mu\text{m}$ )	1.95-3.9	3.9-7.8	1.95-3.9	3.9-7.8
R (instrument)	98	29	193	97
Reciprocal linear dispersion ( $\mu\text{m}/\mu\text{m}$ )	$4.896 \times 10^{-4}$	$3.288 \times 10^{-3}$	$2.478 \times 10^{-4}$	$4.953 \times 10^{-4}$
f-number	20.5	10.3	20.5	10.3
Optical efficiency	0.45	0.45	0.45	0.45
Detector QE	0.55	0.55	0.55	0.55
Pixel size ( $\mu\text{m}$ )	18	18	18	18
Pixel scale ( $^\circ/\text{pixel}$ )	$5.583 \times 10^{-5}$	$11.166 \times 10^{-5}$	$5.583 \times 10^{-5}$	$11.166 \times 10^{-5}$
Pixel diffusion length ( $\mu\text{m}$ )	1.7	1.7	1.7	1.7
Slit width (pixels)	11	13	17	13
Dark current ( $e^-/\text{s}$ )	32	120	17	17
Linear well depth ( $ke^-$ )	70	70	70	70
Read noise ( $e^-$ )	22	22	22	22

spectrum was used, which gives a total bi-axial rms of 129 mas. This was thought to be a reasonable preliminary approximation for the expected ARIEL pointing jitter.

Two simulated stellar targets were ‘observed’ out-of-transit using each design. These were 55 Cancri and GJ 1214, representing the brightest and dimmest targets for ARIEL at the time of the test. The PHOENIX spectra used were  $T=5200$  K,  $\log g=4.5$ ,  $[\text{Fe}/\text{H}]=0$  for 55 Cancri, and  $T=3000$  K,  $\log g=5.0$ ,  $[\text{Fe}/\text{H}]=0$  for GJ 1214. Other system parameters were obtained from the Open Exoplanet Catalogue. The brightest target was later changed to HD 219134 after the more recent discovery of this planet and incorporation into the ARIEL target list. Each of these stars have ‘super Earth’ planets orbiting, 55 Cancri e, and GJ 1214 b. The total observing time for each target was set to twice  $T_{14}$  for the super-Earth planet in each system.

The exposure time was determined using a ‘time to saturation’ method: the time taken for the first pixel on the detector to reach full well capacity from the combined count rates (in  $e^-/\text{s}$ ) from the source, dark current, emission and zodia-

cal light, is found, and used to set the total integration time<sup>8</sup>. This is then divided between different subexposures<sup>9</sup>. Time is then allocated for the reset and ground times for the detector. Adding these to the total integration time gives total exposure time. This approach maximises the integration time in relation to the number of reads, which helps to reduce the read noise per unit time. It also maximises the duty cycle. This ‘time to saturation’ method is re-used throughout the remainder of this thesis.

For this particular test the shorter of the two exposure times calculated for each channel was applied to both channels, but in later tests (after it became clear that the integration times could be set independently in different channels) each channel was simulated with its own individual exposure time. The full well capacity (linear well depth) in this particular test was set at 70000 e<sup>-</sup> per pixel. This gave total exposure times of 1.07 s and 2.18 s for 55 Cancri in the LRS and HRS, respectively, and 45.54 s and 156.17 s for GJ 1214 in the LRS and HRS, respectively. The reason for the longer integration time in the HRS design is due to the larger linear dispersion reducing the peak count rate from the stellar spectrum, and thus taking longer to reach full well capacity. A simulation frame rate of 100 Hz was used. A total of 0.02 seconds (2 frames) was allocated to detector reset and ground times, and 0.01 seconds (1 frame) to NDR<sub>0</sub> (i.e. subexposure 0), the first of two NDRs. Two NDRs were used for each exposure (i.e. multiaccum = 2) to allow correlated double sampling (CDS) in data reduction. The CDS exposure (NDR<sub>1</sub>-NDR<sub>0</sub>) therefore had an integration time equal to the exposure times above minus 0.03 seconds.

A quantum efficiency (QE) variation of 5% rms was applied over each detector array. This is based the observed variation of 3% rms in the F105W and F110W LP flats for the Hubble WFC3 quoted in Chapter 3, adding a small additional margin of error. This degree of QE variation is applied in all subsequent simulations in this thesis except where stated otherwise. Intra-pixel variations were based on the ‘bowler hat’ model described in Chapter 2, with a diffusion length of 1.7  $\mu\text{m}$ .

The simulations were repeated with different noise sources activated in isolation, and also with total noise, in order to obtain the noise contributions from individual sources and to construct the wavelength-dependent ‘noise budget’ charts. Each individual noise simulation for each target in each channel generates its own FITS file for subsequent data reduction. Only one realization was performed for

<sup>8</sup> This method gives a first order estimate of the integration time since I assume linearity of the detector response upto the designated full well capacity. In reality detectors would normally work slightly below this limit to avoid non-linearity problems near saturation.

<sup>9</sup> Cumulative addition of subexposures form each non-destructive read (NDR).

each noise type in each case.

Note this basic ‘noise budget method’ was repeated at later stages in Phase A as described below, but with modifications. When described in later sections, I focus on the modifications used for that test.

#### 4.2.2.4 DATA REDUCTION PIPELINE

**‘Basic’ pipeline** A ‘basic’ data reduction pipeline was developed for these initial tests and later modified for use in later Phase A studies (as well as in Chapters 5 and 6). The pipeline takes the individual FITS files for each channel produced after an ExoSim simulation and delivers either an OOT signal and noise per spectral bin, or if full transit simulations are performed, a transit depth per spectral bin. If the latter is used, the noise on the transit depth can be obtained using the variety of methods described earlier and in Chapter 1. The steps in the pipeline are as follows:

- 1) Background subtraction on each NDR. 5 adjacent rows are sampled at each of the top and bottom edges of the image, separated by 5 rows from the edge. The mean count of these pixels is subtracted from all pixels in the NDR.
- 2) Flat fielding. The QE variations introduced in the simulation are flat fielded out but a 0.5% rms uncertainty is left in the flat field. This is based on the uncertainties in pixel-to-pixel responsivity calibration for Spitzer IRAC (IRAC Instrument and Instrument Support Teams, 2015), and flat field uncertainties for the Hubble WFC3 IR (Pirzkal et al., 2011).
- 3) Correlated double sampling (CDS). The first NDR ( $\text{NDR}_0$ ) is subtracted from the final NDR. This mitigates reset noise (not simulated) and is generally used as a baseline read out mode; thus all ExoSim simulations in this chapter use multiaccum setting of 2 (i.e two NDRS). CDS produces a single image for each exposure, that then undergoes further processing. Other read out modes such as up-the-ramp and Fowler sampling may be possible for longer exposures, but are not included in this ‘basic’ pipeline<sup>10</sup>. They have a more complex outcome on the total noise.
- 4) Aperture photometry. An aperture mask is placed over the spectrum to exclude the count from pixels outside the mask. This is used to reduce the instrumental and background noise on each CDS exposure image. The mask is a 2-D array of the same size as the pixel array, with excluded areas having a value of zero and

<sup>10</sup> Up-the-ramp modes can also be useful for removing cosmic ray events; cosmic ray events are not currently simulated in ExoSim but could be added in a future version of the detector model.

included areas a value of 1. This array is then multiplied into the CDS image. The centre of the aperture mask in the spatial direction is aligned with the maximum of the signal.

A nominal width for the aperture in the spatial direction of  $2.44 f\lambda$  is used, i.e. the width of the Airy disc. Each pixel column therefore has its own aperture width based on the wavelength of the pixel column, getting physically narrower at the shorter wavelengths. This nominal width was chosen as it was thought this would minimise the effect of spatial jitter, since the mask edge falls on the first Airy minimum, and so variations in position would result in less jitter noise than for narrower apertures falling on the region of higher gradient. For the initial mask used for this study, the mask width per pixel column was rounded to the nearest whole pixel.

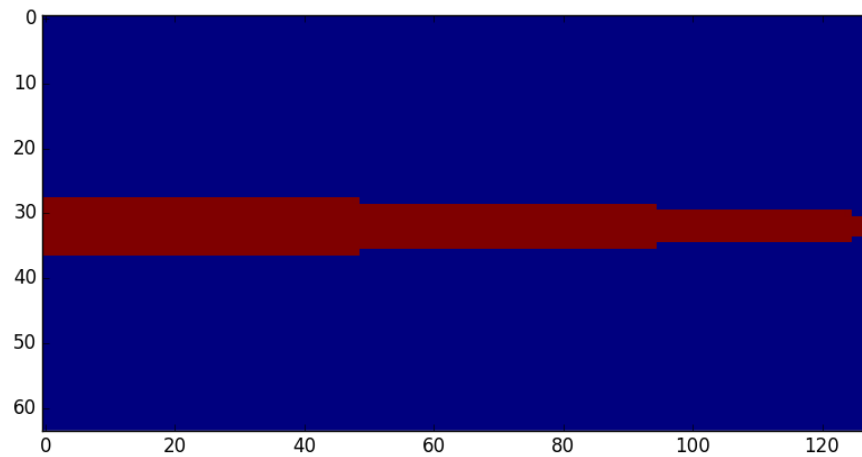
A later iteration of the mask (used for later Phase A studies, and in Chapters 5 and 6) used a sub-pixel modification. Each pixel in the image was subdivided into sub-pixels in the spatial direction, allowing a more accurately sized mask per column and smoother variation in mask width with column. For this version of the mask, after locating the column with the maximum count, a 2-D Gaussian is used to locate the maximum sub-pixel row which is then used to centre the mask in the spatial axis. Some modifications to the nominal mask width were used for later Phase A simulations, as explained in later sections.

Examples of the pixelised and sub-pixelised versions of the aperture mask, applied in later prism-based designs, are shown in Figure 4.6. In this initial test, the nominal width of  $2.44 f\lambda$  was used with the earlier pixelated form of the mask.

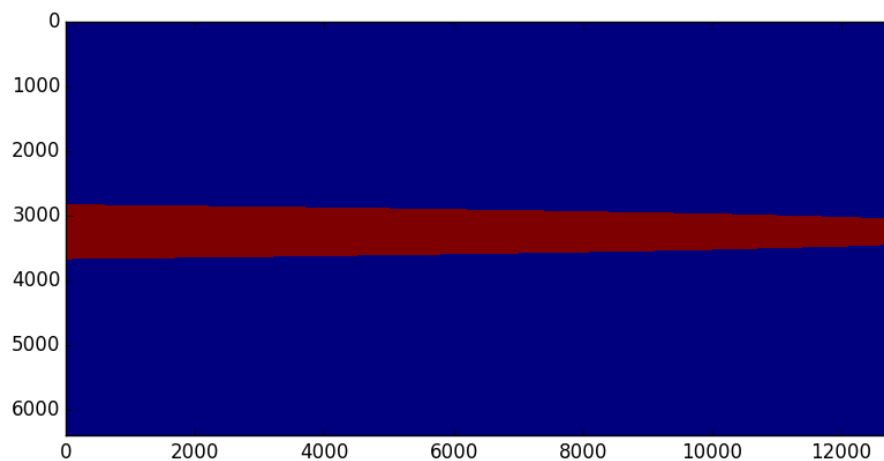
For photometric channels (not simulated in this initial test, but in later Phase A simulations), a circular aperture is applied using the Photutils (Bradley et al., 2016) Python package that utilizes its own sub-pixel method. A 2-D Gaussian is fitted to the image to determine the centre position of the aperture in each CDS exposure. The count within the aperture is then returned for each exposure (thus steps 5 and 6 below are not applicable for the photometric channels). The nominal radius of the aperture (sized to the Airy disc) is  $1.22 f\lambda$  but this is modified to take into account PSF aberrations (see later sections).

**5) Spectrum extraction.** The 1-D spectrum per CDS exposure is obtained by simple integration of the column counts after masking.

**6) Spectral resolution element binning (R-binning).** The 1-D spectra are divided into spectral-resolution-element-sized bins. For this initial test, this was performed using bins sized to match the resolution elements rounded to the nearest whole pixel. This gives a fairly coarse representation of the bin sizes, with sharp changes



(A) Original whole pixel aperture mask



(B) Sub-pixel aperture mask

FIGURE 4.6 Aperture masks used in basic data reduction pipeline. Mask array is multiplied into the image. The blue area has zero value and red area has value of unity per pixel or sub-pixel. Width of the mask is based on  $2.44f\lambda$  and rounded to the nearest whole pixel or sub-pixel. Example shown is for AIRS Ch1. Wavelength decreases to the right (due to prism-based wavelength solution). A: original whole pixel mask. B: modified sub-pixel mask, using a sub-pixelization factor of 100. Axes show pixel or sub-pixel indices. In the pipeline, sub-pixel expansion of the mask is only performed in the y (spatial) direction but for clarity in this picture the x direction has also been expanded.

in bin size across the wavelength range. For later Phase A evaluations (and in Chapters 5 and 6), this was modified to use a sub-pixel method where the count from each whole pixel column was subdivided into sub-pixels<sup>11</sup>. This allowed a more accurate sizing of resolution element sized bins with smoother variation with wavelength.

7) Calculation of the variance of the counts per spectral bin (or per photometric channel) and division by the CDS exposure time.

This pipeline was also modified later by the addition of a jitter decorrelation routine between steps 3) and 4): step 3a). For the purposes of the performance tests in this chapter, the pipeline ends with step 7), however in chapter 5 we use full transit simulations to perform Monte Carlo simulations to obtain the uncertainties on the transmission spectrum due to star spots. For the full transit simulation the following additional step is used.

8) The timeline of signals per exposure in each spectral bin constitutes a 'spectral light curve'. To each spectral light curve, a model Mandel-Agol light curve is fitted. The model (generated using PyTransit) has  $p$  (the square root of the contrast ratio), quadratic limb darkening coefficients and the  $z$  grid as inputs. The OOT flux and  $p$  (and possibly the limb darkening coefficients) are treated as free parameters. The curve fit can be performed either using a downhill simplex algorithm minimizing  $\chi^2$ , or a Monte Carlo Markov Chain (MCMC) routine. This therefore returns the fitted value of the contrast ratio per spectral bin (and also its uncertainty if MCMC is used).

**Correction for 'optimal extraction'** A correction can be considered to the OOT noise results to account for 'optimal extraction' algorithms. Not all studies in transit spectroscopy use optimal extraction, but some have used this method for extracting the 1-D spectra from each exposure, e.g. Kreidberg et al. (2014a). Optimal extraction (Horne, 1986) is a technique to extract 1-D spectra from spectroscopic images using profile fitting. It would replace step 5 in the above pipeline. The technique can reduce the noise contribution of background and instrumental sources (but not photon noise from the source) within the given aperture. The general principle involves fitting a profile to the spectrum in the spatial direction and obtaining a weighted mean of the counts per pixel column. The following formalism follows that in Horne (1986).

Let  $x_1$  and  $x_2$  be the aperture boundaries in pixel units for a pixel column

<sup>11</sup> An interpolation method was also used for the ESA radiometric model cross-validation test as described in Chapter 2.

containing the spectrum at wavelength  $\lambda$ . Then assuming each pixel has variance  $V_x$ , and the simple sum of pixels is used to obtain the spectral signal,  $f_{basic}(\lambda)$  (as in aperture photometry), the total variance for the pixel column using the basic pipeline would be:

$$V_{basic}(\lambda) = (x_2 - x_1)V_x \quad (4.2)$$

In optimal extraction, an unbiased linear estimator of the pixel column count is obtained by fitting a profile to the spectral shape in the spatial direction. This profile represents the probability,  $P_x$ , that a pixel  $x$  in the column will collect a photon, so that the sum of  $P_x$  over all pixels in the column is 1.  $P_x$  will thus have a higher value at the peak of the signal, and less value towards the wings. If  $S_x$  is the signal (after background subtraction) in the pixel  $x$  within the pixel column, an independent unbiased estimate of the signal is given by  $S_x/P_x$ . The independent unbiased estimates for all the pixels in the column will therefore have the same mean but different variances. For each pixel the variance of the independent unbiased estimate is  $V_x/P_x^2$ . The optimal spectrum is obtained as a weighted mean,  $f_{opt}(\lambda)$ , of these independent estimates:

$$f_{opt}(\lambda) = \frac{\sum_x W_x S_x / P_x}{\sum_x W_x} \quad (4.3)$$

where  $W_x$  is the weight on pixel  $x$ . The optimal weights that deliver the minimum variance are given by the inverse of the variances on each random variable. Therefore for each pixel column, the optimal minimum variance spectrum is given by:

$$f_{opt}(\lambda) = \frac{\sum_x P_x S_x / V_x}{\sum_x P_x^2 / V_x} \quad (4.4)$$

The variance on  $f_{opt}(\lambda)$  is given by:

$$V_{opt}(\lambda) = \frac{1}{\sum_x P_x^2 / V_x} \quad (4.5)$$

If  $P_x$  is in the form of a Gaussian of standard deviation  $\sigma$ , we can estimate the ratio of  $V_{basic}(\lambda)$  to  $V_{opt}(\lambda)$ , and from this the improvement in variance for background and instrumental noise sources (i.e. sources where  $V_x$  is the same for all pixels) using optimal extraction compared to basic aperture photometry:

$$\frac{V_{basic}(\lambda)}{V_{opt}(\lambda)} = (x_2 - x_1) \int_{x_1}^{x_2} \frac{e^{-x^2/\sigma^2}}{2\pi\sigma^2} dx \approx \frac{x_2 - x_1}{2\sqrt{\pi}\sigma} \quad (4.6)$$

If the aperture width,  $x_2 - x_1$ , is expressed in units of the Gaussian standard deviation,  $\sigma$ , then a  $6\sigma$  width aperture will have an reduction in variance from instrumental and background sources of a factor of 1.69 if optimal extraction were used instead of aperture photometry. For the Airy functions used in ExoSim, the Gaussian approximation,  $\sigma = 0.42f\lambda$ , can be used to estimate the improvement. Note that if photon noise from the source is considered then  $V_x = P_x$  and no improvement occurs. For jitter noise the variance has some degree of proportionality to the signal and so the variance improvement shown above would not occur for this type of noise either.

During the course of the Phase A study, a prototype optimal extraction routine was developed by A. Papageorgiou, that demonstrated the above expected improvement from profile fitting in a selected case from ExoSim results, but was not sufficiently validated to incorporate into the data reduction pipeline used in this thesis. To ensure however that I did not adversely bias findings due to the non-optimized nature of the 'basic' pipeline, I apply this optimal extraction correction to noise results on the matured design when it comes to setting requirements and testing compliance, anticipating that this will be part of a future pipeline. For this correction to be applied, the variances need to be corrected individually for each background and instrumental noise source and then added in quadrature together with uncorrected sources (source photon noise and jitter noise) to obtain the final total corrected noise. The optimal extraction correction is not applied to the photometric channels as these would require a 2-D profile fit, and will have aberrated PSFs due to wavefront errors (Figure 4.21). Therefore pipelines to apply profile fitting would be more complex for these channels, and it is less clear what the expected improvement in noise would be.

#### 4.2.2.5 RESULTS AND ANALYSIS

The noise budgets for each design are shown in Figure 4.7 for 55 Cancri as a target, and Figure 4.8 for GJ 1214 as a target. The y axis in each chart shows (in log scale) the noise variance per unit time per spectral-resolution-element-sized bin. The results for Ch0 and Ch1 are shown on the same charts covering their respective wavelength ranges.

For the bright source, 55 Cancri, both designs suffer from spectral jitter noise that exceeds the photon noise limit at the blue ends of both channels. The effect is worse in the LRS design where the spectral jitter noise exceeds the photon noise over most of the band in Ch0 and all of Ch1. This probably reflects the smaller

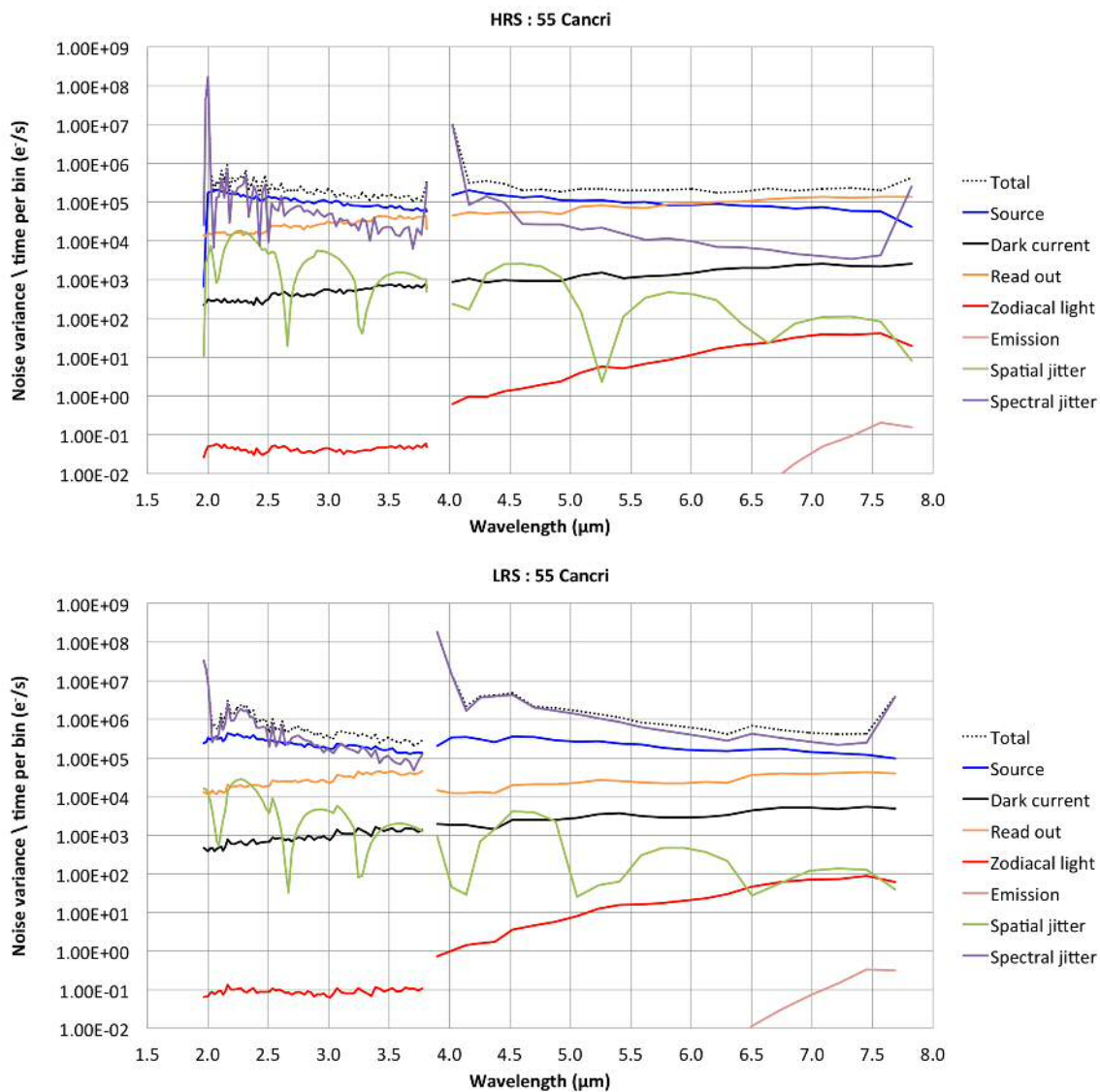


FIGURE 4.7 Noise budgets for HRS and LRS designs for 55 Cancri. Top: HRS. Bottom: LRS.

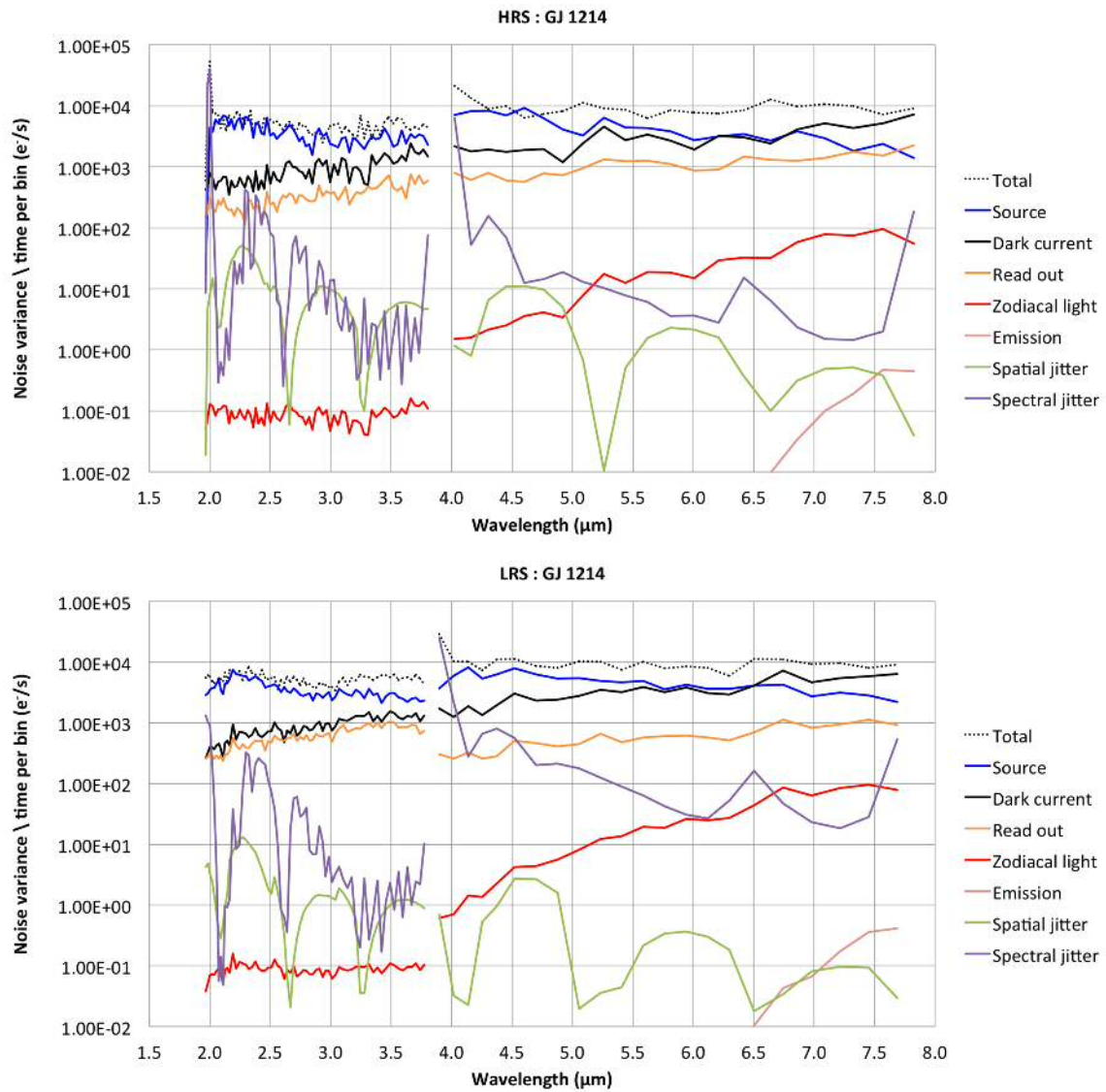


FIGURE 4.8 Noise budgets for HRS and LRS designs for GJ 1214. Top: HRS. Bottom: LRS.

physical spectral bin sizes in the LRS design than the HRS. There will be more variation in the signal in the spectral direction if the bin size is smaller, given the same pixel scale in both designs. I discuss jitter noise dependencies in more detail in the next section.

For the dim source, GJ 1214, the spectral jitter noise is well below photon noise for both designs (except at the extreme edges of the channel, an 'edge' effect discussed further in the next section). Spectral jitter noise therefore appears to be worse for brighter sources with shorter integration times than dim sources with longer integration times.

Spatial jitter noise is well controlled in both designs, well below the photon noise limit. A periodicity is seen in the pattern of the spatial noise which may be due to the interaction of the PSF and mask width as they vary in size at slightly different rates across the array, the mask being highly pixelated.

Read noise in Ch1 is more problematic in the HRS design despite both designs having the same read noise per pixel. This is caused by the higher number of pixels per spectral bin, and the effect is worse for the bright target with more reads per unit time. In the HRS read noise exceeds the photon noise halfway through the Ch1 band for the bright target. Although the HRS has longer integration times that should reduce the read noise per unit time compared to the LRS, this effect is evidently outweighed by the effect of the larger bin sizes.

Dark current noise is well controlled for the bright 55 Cancri in both designs. The higher dark current per pixel used in the LRS design to mimic the use of European detectors is offset by having more compact bins with fewer pixels. However for the dimmer GJ 1214 with the longer integration time, the dark current noise is increased and becomes the dominant instrumental noise source (i.e. exceeding the read noise) in all cases. The effect is however similar in both designs, with the dark current exceeding the photon noise limit at the red end of Ch1.

Noise from zodiacal light<sup>12</sup> and telescope and instrument emission is small compared to these other noise sources. No optimal extraction corrections were applied in these tests.

---

<sup>12</sup> GJ 1214 is at an ecliptic latitude of  $27.9^\circ$ , and as discussed in the Appendix, the baseline zodi model used here should, to a first order, be directly applicable. 55 Cancri is closer to the ecliptic at ecliptic latitude of  $10.4^\circ$ . It is possible that by not adjusting the zodi model to a higher level of emission, I may be underestimating the zodi noise for 55 Cancri in these tests. However since the purpose here is to compare the relative performance of the two designs this will not be of great consequence for this test. In addition, the increase in zodi emission would have be several magnitudes higher than modeled to be of any impact to the total noise in 55 Cancri, which is not predicted in the analysis given in the Appendix, which indicates the zodi intensity would increase by a factor of 1.79.

#### 4.2.2.6 CONCLUSIONS

On comparing the two designs, the noise budget results show an equivalence in performance except for the increased read noise for the bright target in the HRS compared to the LRS, and the increased spectral jitter in the LRS design for the bright target compared to the HRS.

Mitigation of the high read noise in the HRS would be challenging at either the instrument design level or data reduction level. It may be possible to improve the read noise using Fowler sampling or up-the-ramp reads if the detector has a high enough frame rate to allow multiple NDRs in the integration time, but this becomes less likely with very short integration times as used here.

Mitigation of the spectral jitter could also be tackled at the instrument design or data reduction level. A potentially finer jitter rms could be possible, e.g. as on the Hubble, but such a pointing system would be expected to be more expensive. This motivated the study of pointing jitter dependencies through ExoSim, and the evaluation and implementation of mitigation strategies in data reduction, to show that jitter noise could be controlled without a major redesign of the instrument and spacecraft. This study is detailed in the next section, and showed in fact that jitter noise could be controlled through decorrelation in the LRS design.

Therefore the major conclusion after this initial study was that the performance of the LRS was equivalent to and even slightly superior (in terms of read noise performance) to the HRS after jitter decorrelation is factored in. The LRS was more versatile, being able to be used with both Teledyne and European detectors (with the 'pessimistic' dark currents), and from a scientific perspective there was minimal gain from the higher instrumental resolution in the HRS design, with the LRS ( $R=100/R=30$ ) resolution having been shown to be efficacious for the science objective. Together with the expected improvement in SNR from the LRS design compared to the HRS, the consortium decided to pursue development and testing of the LRS design only, which subsequently became the AIRS instrument.

As the Phase A study progressed, the LRS design became AIRS with the main modification being the replacement of the grating with a prism as the dispersive element. This gave a higher throughput and would be potentially easier to manufacture. In the FGS, as mentioned previously, there was addition of the third photometric channel, FGS 2 (at  $1.1 \mu\text{m}$ ) and the low resolution spectrometer, NIRSpec (covering  $1.25\text{-}1.9 \mu\text{m}$  at  $R \approx 10\text{-}20$ ). Together with the two other photometric channels in the original proposal, now named FGS 1 ( $0.9 \mu\text{m}$ ) and VisPhot ( $0.5 \mu\text{m}$ ), these channels would give about 10 data points from  $0.5$  to  $1.9$

$\mu\text{m}$ , to evaluate Rayleigh scattering, albedo, clouds and stellar variability. ExoSim and the data reduction pipeline were modified to accommodate the more complex wavelength solutions resulting from the varying R power in the prism-based designs.

## 4.3 POINTING JITTER AND ITS MITIGATION

Pointing jitter noise is a highly complex type of noise, both in terms of the multiple factors that contribute to it, and how it manifests on the final image. It is a form of correlated noise that is difficult to simulate and quantify at the system level through simple models. ExoSim however provides an excellent tool to estimate jitter noise in both spatial and spectral directions, explore its dependencies and test the effect of mitigation strategies.

With the finding that spectral jitter was a highly significant noise source in both the LRS and HRS designs, on par with or exceeding the photon noise from the source in the case of 55 Cancri, it became clear that it was necessary to find a way (or ways) to mitigate this type of noise.

In addition these early studies showed that there was a clear difference between the magnitude and behaviour of spatial jitter noise and spectral jitter noise. Although not manifesting to a high degree in these early studies, we needed to also know how spatial jitter responds and could be mitigated, should it become an issue in future designs.

The spectral jitter noise was higher in the LRS than in the HRS design, and both types of jitter noise were lower for the dimmer target. These all point to various dependencies of jitter noise, and therefore possible approaches to its mitigation.

In this section, I explore the mechanisms of spatial and spectral jitter noise, discuss possible mitigation strategies, and then show the results of implementing such strategies in the context of Phase A noise budget studies.

### 4.3.1 POINTING JITTER MECHANISM

Jitter noise arises from the movement of the signal (beam or spectrum) over the focal plane. When this movement occurs within an integration period it causes 'smearing' of the PSF or image (unresolved jitter noise). Its effect between different exposures is to cause a photometric count variation (resolved jitter noise).

The ARIEL pointing system consists of a coarse tracking and slewing system based on wide field star trackers, and a Fine Guidance System (FGS) that centroids the main star on one of 2 FGS channels (line-of-sight sensors), and uses a closed loop feedback system to maintain pointing on the star. There are also a system of gyroscopes (inertial sensors). The line of sight and inertial sensor information are fused and then a control algorithm implements the required corrections to attitude. The spacecraft is moved using 3 reaction wheels. Thrusters are included to deload the reaction wheels when they saturate.

The jitter we consider here are the movements occurring while fixed on the main star using the closed-loop feedback system of the FGS. This will be affected by the precision of the FGS, which in turn depends on the centroiding accuracy on the star, the precision of the sensor, gyroscopes and reaction wheels, and the delay within the loop. Other factors adding to the jitter will be drifts in attitude due to vibrational modes of the spacecraft and external factors such as thermal changes or interaction with the solar wind. The accuracy of the FGS will also depend on the brightness of the star. Iverson et al. (2007) estimate the error is proportional to the inverse of the SNR<sup>13</sup>.

Variations in the spacecraft positioning will occur in will occur in all 3 spacecraft axes, but are translated into a 2-D movements in the  $x$  (spectral direction) and  $y$  (spatial direction) on the focal plane. These random movements are correlated in time (and 100% spatially correlated across all spectrometer wavelengths) and, as previously discussed, are represented by a non-white power spectral density (PSD) profile such as that produced from Herschel data (Figure 2.6 in Chapter 2).

I focus here on the mechanism leading to photometric variations (i.e the resolved jitter noise). These can be traced back to 4 basic contributing factors:

- 1) The degree of the movement (jitter) of the signal.
- 2) The degree of detector non-uniformity in responsivity.
- 3) The size of the aperture (or bin) over which the count is being measured.
- 4) The gradient of the signal.

Figure 4.9 shows how these factors interact to produce noise. Each of these factors is now discussed in more detail.

#### 4.3.1.1 DEGREE OF THE MOVEMENT (JITTER) OF THE SIGNAL.

The degree of jitter movement is related to the stability and accuracy of the pointing system, summarised as the root mean square deviation (rms) of the jitter

---

<sup>13</sup> Their Equation B2.

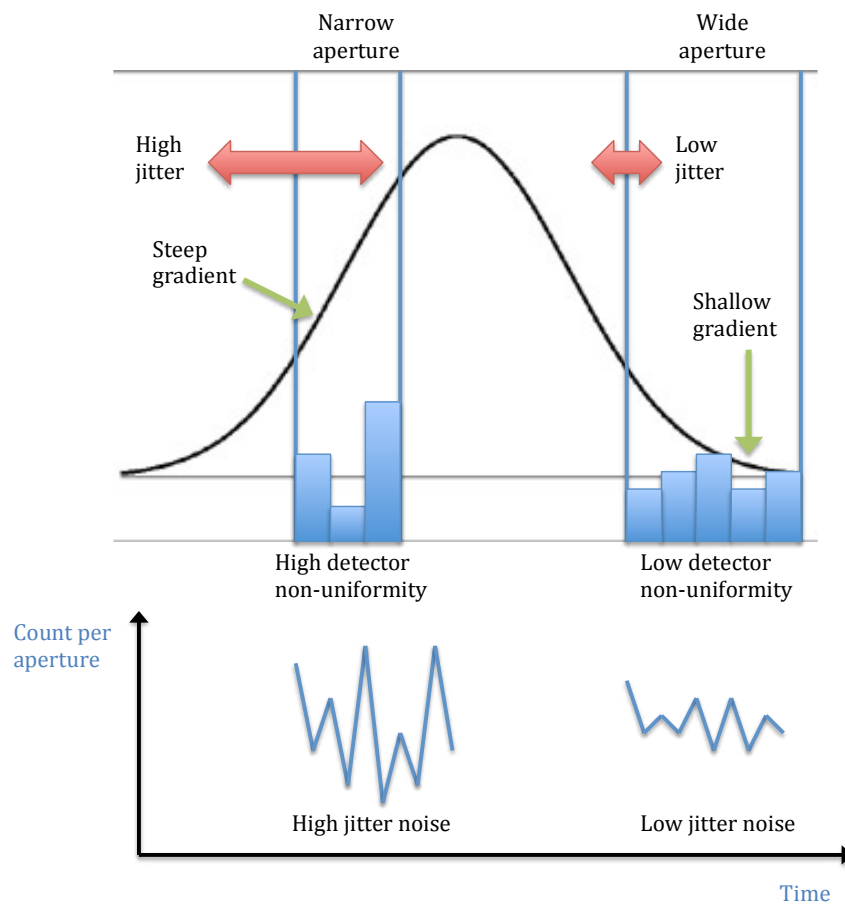


FIGURE 4.9 Jitter mechanism. The diagram shows a 1-D signal (black line) jittering over a detector array with pixels of varying quantum efficiency. The generation of photometric variation from jitter can be reduced to a few fundamental factors that combine to give the final noise. Left: factors that increase jitter noise. Right: factors that reduce jitter noise.

(equal in magnitude to its standard deviation) or the peak-to-peak variation. A higher jitter rms will result in higher jitter noise, both resolved and unresolved. As well as the angular jitter rms due to the pointing accuracy, the degree of movement on the focal plane itself will be affected by the plate scale<sup>14</sup>. Decreasing the plate scale (e.g. by increasing the effective focal length of the instrument) will increase the jitter rms in pixel units the level of the focal plane thereby increasing the jitter noise.

Jitter types have been formalised into a complex scheme documented in the ESA Pointing Error Engineering Handbook (ESA, 2011)<sup>15</sup>. This gives definitions

<sup>14</sup> Or 'pixel scale' which is the angle per pixel length.

<sup>15</sup> [http://peet.estec.esa.int/files/ESSB-HB-E-003-Issue1\(19July2011\).pdf](http://peet.estec.esa.int/files/ESSB-HB-E-003-Issue1(19July2011).pdf)

for various types of pointing error. For the purposes of this study we are most interested in metrics that will allow us to simulate the unresolved jitter within the integration period and the resolved jitter noise between exposures. The error types of interest in this regard are the Relative Performance Error (RPE) and Performance Drift Error (PDE).

The RPE is the difference between the absolute pointing error,  $\epsilon$ , at a given time and mean pointing error within a time interval,  $\Delta t$  (Figure 4.10, top). The 'RPE jitter' is the rms of the RPE, and can be considered the 'high frequency jitter' that occurs on scales of the integration period or shorter. For ARIEL, external engineering modeling (based on cost-effective and feasible pointing system designs) resulted in estimates for RPE and PDE jitter that were formalised as 'requirements' for the Mission Requirements Document (MRD)<sup>16</sup>. The requirement also needed to take into account that the LRS design was simulated with the Herschel power spectrum with a bi-axial rms of 129 mas; as will be shown below, the jitter noise from this was found to be controllable with jitter decorrelation, and thus a pointing system for ARIEL with an overall rms of this order should be viable.

For the RPE jitter, the requirement was set as an bi-axial rms of  $\leq 66.7$  mas for bright targets, and  $\leq 133.3$  mas for dim targets, over a defined frequency band. The lower bound of the frequency band was set by  $1/\Delta t$ , where  $\Delta t$  is based on nominal maximum exposure times required to capture the shape of a light curve. For bright targets this was defined as 90 s and for dim targets, 300 s. The upper bound of the frequency band was set by the presumed cadence of pointing information (5 Hz). Thus the RPE jitter covers jitter frequencies from  $1.11 \times 10^{-3}$  to 5 Hz for bright targets, and  $3.33 \times 10^{-3}$  to 5 Hz for dim targets.

The PDE is the difference between the mean pointing error taken over two time intervals separated by a specified time,  $\Delta t_s$ , within a single observation period (Figure 4.10, bottom). The 'PDE' jitter is the rms of the PDE and quantifies the 'low frequency jitter', that occurs on scales longer than the integration time, upto the length of the observation. The upper frequency bound of the PDE jitter is defined by  $\Delta t$  above (i.e.  $1.11 \times 10^{-3}$  and  $3.33 \times 10^{-3}$  Hz for bright and dim targets respectively). The lower bound is set by the frequency corresponding to the longest expected observation period, defined in the MRD as 10 hours ( $2.78 \times 10^{-5}$  Hz). The rms requirement for the PDE jitter was defined for ARIEL as  $\leq 33.3$  mas for bright targets and  $\leq 100$  mas for dim targets. However what we need for simulating the resolved jitter is the rms of the mean pointing error (the average error

<sup>16</sup> ARIEL Mission Requirements Document, ESA-ARIEL-EST-MIS-RS-001, V1.2, issued 02/09/2016. Available from ESA on request.

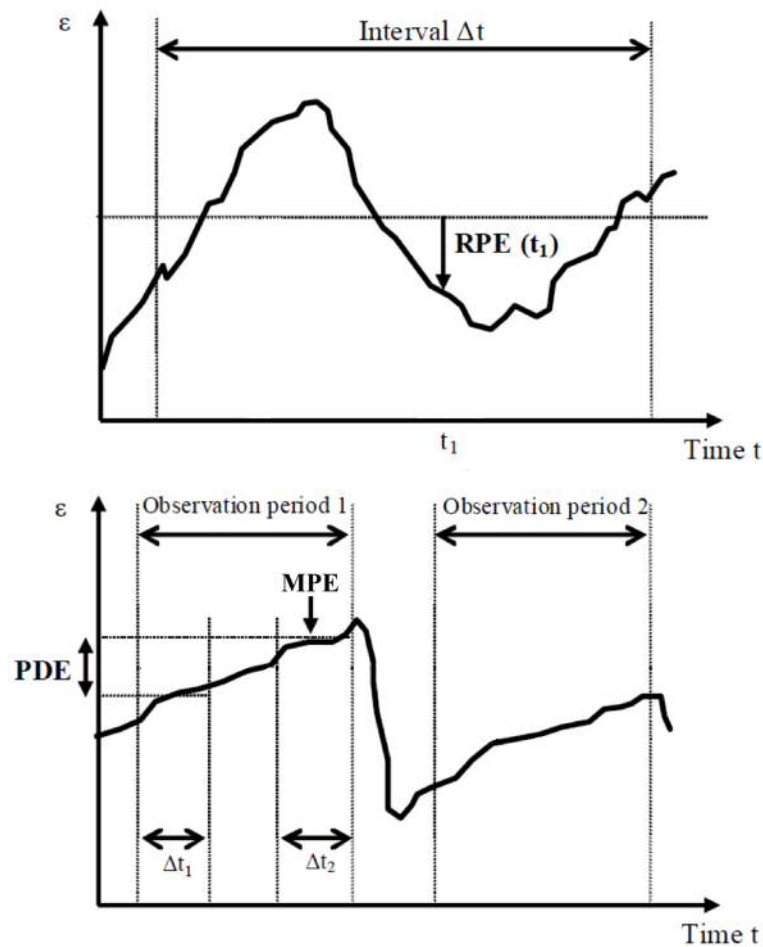


FIGURE 4.10 RPE and PDE definitions. Top: RPE. Bottom: PDE. See text for description. Figures (with slight adaptations) from Waldmann (2013) and the ESA Pointing Error Engineering Handbook (ESA, 2011).

over the time period  $\Delta t$  also known as Mean Performance Error or MPE) rather than its differences. Assuming this does not change over the observational period, the rms of the MPE is  $1/\sqrt{2} \times$  the rms of the PDE.

Using the above frequency ranges for RPE and PDE, and converting the PDE rms to MPE rms, I produced custom PSD profiles (one each for 'bright' and 'dim' targets) for ARIEL pointing jitter that could be used in ExoSim (Figure 4.11). The overall bi-axial rms for the jitter timelines generated from these PSDs were 71 mas for the 'bright' target PSD and 151 mas for the 'dim' target PSD. These were therefore of the same order as (but slightly lower and higher than) the Herschel PSD at 129 mas.

These PSDs were used for later noise budget tests on matured ARIEL configurations described in the next 2 sections. The exact pointing accuracy will vary

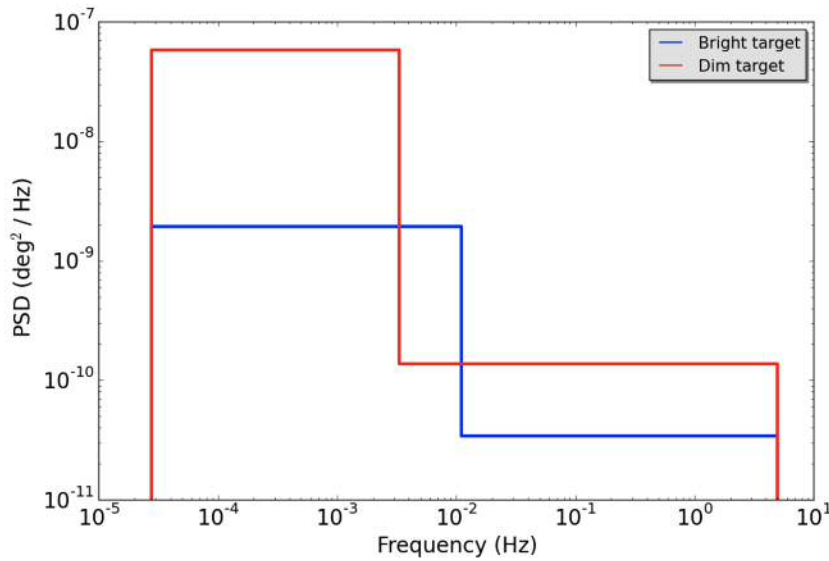


FIGURE 4.11 Power spectral density profiles developed for ExoSim simulations using ARIEL pointing requirements for 'bright' and 'dim' targets. The same PSD is used for both axes. The 'bright' PSD generates a jitter timeline with an overall rms of 50 mas (71 mas bi-axial), and the 'dim' PSD, an overall rms of 107 mas (151 mas bi-axial)

in real situations with the brightness of the star, but for the purposes of these simulations we utilize these generalized PSDs, selecting one or the other depending on whether the star is 'bright' ( $K \text{ mag} \leq 6.3$ ) or 'dim' ( $K \text{ mag} > 6.3$ ).

Another influence on jitter noise is the integration time (usually increased for dimmer sources) in relation to the frequency band of the PSD. As the integration time is increased, more of the higher frequencies in the jitter PSD will be folded into the image. This should increase the unresolved jitter, i.e. the smear within the exposure increases, and decrease the resolved jitter, i.e. the photometric variation between exposures decreases. We first saw this effect in the Hubble study in Chapter 3, where the shorter integration time in staring mode made it more sensitive to jitter noise than the longer integration time in scanning mode. It may also underly the difference in jitter noise seen in the HRS-LRS study, where the jitter noise for the dimmer GJ 1214 with its longer integration time was much lower than for the brighter 55 Cancri with its shorter integration time.

#### 4.3.1.2 DEGREE OF DETECTOR NON-UNIFORMITY IN RESPONSIVITY

Both intra- and inter-pixel non-uniformities can result in photometric variations when coupled with movement of the image. The inter-pixel distance (the

dead space between adjacent detector pixels) effectively contributes to the intra-pixel variation.

If the signal shape (the FWHM of the PSF in the spatial direction and the spectral shape in the spectral direction) is Nyquist sampled by the pixel array, the impact of the intra-pixel response should be mitigated; conversely when the signal is sub-Nyquist sampled, intra-pixel variations dominate and photometric errors will increase. Nyquist sampling of the PSF and spectrum also prevents aliasing of high spatial frequencies, and assists manipulations in frequency space (e.g. for shifting the image in jitter decorrelation) without loss of information.

Increasing the inter-pixel non-uniformity (i.e. the rms of QE variations between pixels) will tend increase the count variations resulting from a moving signal (Figure 4.9). Flat-fielding in data reduction should mitigate this, however perfect flat fielding is never possible due to uncertainties in the QE variations, so a residual (but much smaller) level of non-uniformity will continue to be coupled to the image.

#### 4.3.1.3 SIZE OF THE APERTURE OR BIN

The smaller the aperture the greater the potential variation in the signal with movement (Figure 4.9). This affects jitter in the spatial direction through the width of the aperture mask, and in the spectral direction through the size of the spectral bin. For photometric channels it related to the radius of the circular aperture. This partly explains why both spectral and spatial jitter noises worsen with shorter wavelengths, since the aperture width is reduced in the spatial direction and the size of the spectral-resolution-element-sized bin is reduced in the spectral direction.

#### 4.3.1.4 GRADIENT OF THE SIGNAL

If all other factors are controlled, a high gradient in the signal will result in more variation in the count than a shallow gradient. The gradient produces variation through interacting with both the pixel non-uniformity and the edge of the aperture. A perfectly flat signal for instance should not result in any count variations. In the spatial direction (and in the photometric channels), it is the shape of the PSF that controls this effect. A narrow PSF will have a high gradient causing more jitter noise compared to wide PSF with shallow gradients. In the spectral direction, regions of sharp gradients include spectral features and also the edges of the transmission bands which occur at the ends of the channel wavelength ranges.

We may expect the spectral jitter noise to be increased at the edges which is indeed seen in Figures 4.7 and 4.8. Higher signals will tend have higher gradients (assuming the PSF width and spectral dispersion are unchanged). Thus a high signal should cause more jitter noise than a low signal. This also partly explains the wavelength dependency of spatial and spectral jitter noise, since as the wavelength reduces, the signal generally increases (in the infrared) following the flux of the star. A high signal may also influence the integration time as discussed above, with a shorter integration time resulting in higher levels of resolved jitter noise.

### 4.3.2 JITTER NOISE MITIGATION

Based on the above mechanisms we can suggest some mitigation strategies for jitter noise. These are summarised in Table 4.4. In general, noise mitigation strategies can be implemented at either the spacecraft and instrument design level or data reduction. The latter would usually be the more cost effective approach when possible. Clearly a more accurate and probably more expensive pointing system could reduce the overall jitter rms, as would increasing the plate scale. These design level changes could be considered if jitter noise remains uncontrolled after data reduction methods have been exhausted as tested through ExoSim simulations. Jitter decorrelation is a key data reduction method that would reverse the jitter movements themselves at the level of the individual exposures.

**Moving aperture** One way to do decorrelation would be to move the aperture with the image. In the 'basic' pipeline described, the centre of the aperture mask in the spatial direction is aligned with the maximum of the signal in each exposure. When jitter moves the signal in the spatial direction between exposures, the aperture mask will 'follow' this and could to some degree decorrelate the spatial jitter. This may be one reason why the spatial jitter appears lower in Figures 4.7 and 4.8 than the spectral jitter, if it has been partly decorrelated by the moving aperture. However it is also possible that the baseline spatial jitter noise is lower than the spectral jitter noise without this. I did not explore moving the aperture in the spectral direction as it likely to be much less accurate in following the spectrum since there would be a less clear peak to track and modulations in the spectrum shape may occur in time due the planet transit. A moving aperture could also be an effective way to decorrelate the jitter in photometric channels by aligning the centre of the aperture with the maximum of the signal. This can be done through fitting of a 2-D Gaussian for example to track the movement of the PSF.

TABLE 4.4 Jitter mechanisms and mitigation strategies for each mechanism. Applicability to spatial or spectral jitter noise in spectroscopic channels or combined jitter in photometric channels is indicated for each case.

Mechanism	Mitigation	Spatial	Spectral	Photometric
Jitter movement	• More accurate AOCS	✓	✓	✓
	• Increase plate scale	✓	✓	✓
	• Decorrelate jitter in image	✓	✓	✓
Detector non-uniformity	• Nyquist sample signal	✓	✓	✓
	• Flat field	✓	✓	✓
Aperture size	• Increase width of aperture mask (spatial jitter)	✓	×	×
	• Increase size of spectral bins (spectral jitter)	×	✓	×
	• Increase radius of circular apertures (photometric channels)	×	×	✓
Signal gradient	• Broader PSF (lower f-number, aberrations)	✓	×	✓
	• Increase dispersion of the spectrum	×	✓	×

**Shifting the image** ‘Image shift decorrelation’ (ISD) decorrelates the jitter independent of any moving apertures by shifting the images themselves. This requires 2 steps: the first to obtain the relative offsets of each exposure in the x and y directions, and the second to apply the shifts to each image.

It is important to note that any jitter decorrelation method may fail to remove jitter noise if the images are not flat-fielded first. This is because only flat fielding can remove the noise due to inter-pixel variations. Without this step, the jitter noise will remain coupled to the images even after the jitter is decorrelated.

### 4.3.3 IMPLEMENTING MITIGATION

In this section, I will present results from various jitter evaluations performed during the Phase A study that demonstrate some of the above dependencies and implementation of mitigation methods when needed. The final result is that it is possible to control both spatial and spectral jitter through a combination of methods in data reduction, without recourse to redesign of the instrument or a more accurate pointing system. The combined jitter in the photometric channels can also be controlled to levels below the source photon noise.

#### 4.3.3.1 IMAGE SHIFT DECORRELATION

A set of Python routines were developed by A. Papageorgiou, and then implemented by myself to show the effectiveness of ISD in removing both spatial and spectral jitter.

These routines were designed to be used on CDS exposures, and assume that the initial NDR ( $NDR_0$ ) is sufficiently short and the signal low enough that it does not require separate decorrelation. Flat fielding, background subtraction and CDS are performed first, prior to the decorrelation step, i.e. it is implemented after step 3) in the 'basic' pipeline, as step 3a).

**Methods for obtaining offsets** Two alternate methods were developed to obtain the x and y offsets for each CDS exposure.

The first method assumes FGS pointing information will be available and is of sufficient accuracy and frequency to determine the offsets between exposures. The method uses the ExoSim jitter timeline to mimic the spacecraft pointing information. The median x and y jitter offsets for each exposure are found directly from the timeline. The relative x and y offsets for each exposure are then found by taking the difference of these medians with the values for the first exposure in the series.

In the second method a type of 1-D cross-correlation function is used. The image and reference image (the first exposure) are collapsed in spatial or spectral axes to give 1-D signals. For each axis, a function is used to determine the similarity of the 1-D signals at different relative offsets. The function is the standard deviation of the square of the differences between the 1-D signals over a particular windowed region. This standard deviation is determined at each relative offset and the relationship between standard deviation and relative offset interpolated to a finer grid. The relative offset where the standard deviation is at a minimum is then found. This method is applied in each axis and is used to give the x and y offsets for each CDS exposure relative to the first in the sequence.

The advantage of the cross-correlation method is that it would not be reliant on the FGS information. However testing a method using FGS data is important as there may be situations where the cross-correlation method may become inaccurate such with a very low signal or if there is significant change in the spectral shape during the planet transit.

**Methods for applying shift** To apply the corrective shift, a couple of methods were developed. The first uses a 2-D cubic interpolation of the image, which is re-sampled at the positions corresponding to the offsets obtained in the previous step, giving the shifted image.

The second method uses a 2-D Fourier transform of the image which is shifted in phase in Fourier space, and then inverse Fourier transformed back. This is based on the following property of the Fourier transform:

$$\mathcal{F}[x(t \pm t_0)] = X(i\omega)e^{\pm i\omega t_0} \quad (4.7)$$

where  $\mathcal{F}[x(t)] = X(i\omega)$ . Thus a spatial shift,  $t_0$ , in the signal can be achieved by performing the above operation in frequency space where the Fourier transform of the spatial signal is multiplied by a factor that changes the phase at each frequency, and then inverse Fourier transforming back. In the code by A. Papageorgiou, a 2-D version of the above is performed, applying shifts in both x and y directions, based on the offset values obtained. One advantage of the Fourier method is that if the image is Nyquist sampled (which it should be since the PSF is Nyquist sampled), no information should be lost on performing the shift.

**Improvement in spectral jitter** The ISD method was first applied to the LRS design with the Herschel pointing jitter PSD using the combination of the cross-correlation function method to obtain offsets and the cubic interpolation method to apply the shifts (the Fourier method had not been developed at that time). Figure 4.12 shows that the spectral jitter noise in the LRS design was significantly reduced to a level below the source photon noise after decorrelation. This result supported the further development of the LRS over the HRS since the added spectral jitter noise was shown to be controllable. The improvement on the spatial jitter is much lower, the spatial jitter starting however from a lower baseline.

As noted previously we see the 'edge effect' occurring at the ends of each band where the spectral jitter noise increases in the final bin or two, due to the fall in transmission at the edges of the band causing a large gradient in the spectral shape, and hence large jitter noise in the spectral bins covering the edge region; the absolute values fall with decorrelation but the spectral jitter noise at the edges remains high compared to the rest of the spectrum. The edge regions are also regions of overlap between the spectral bands of adjacent channels. It is anticipated that a future advanced pipeline will combine spectra from different channels such

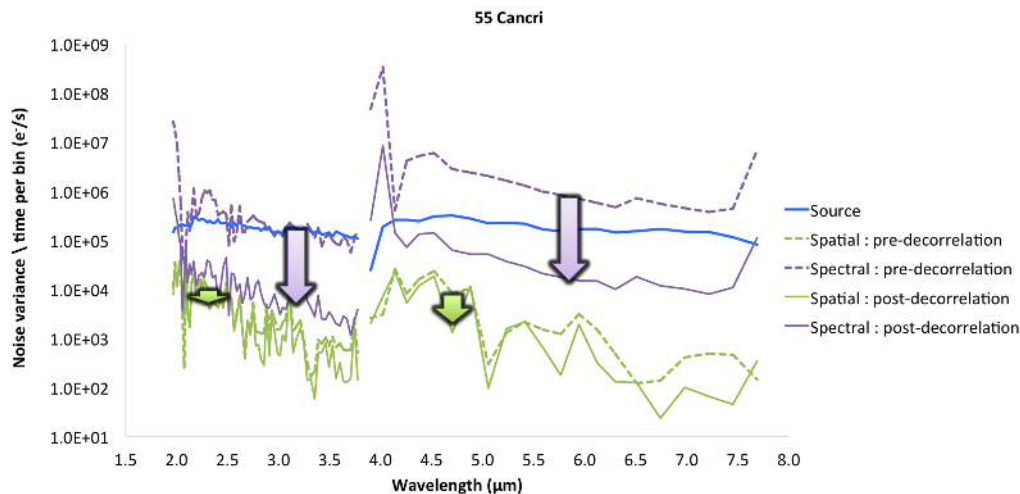


FIGURE 4.12 Effect of image shift decorrelation on LRS jitter noise when observing 55 Cancri. Green arrows indicate degree of improvement in spatial jitter. Purple arrows indicate degree of improvement in spectral jitter.

that the bins in the edge regions will have contributions from both adjacent channels, reducing the variation in the signal from spectral jitter and mitigating this edge effect. For the remainder of this study, I omit the bins at the extreme edges of the bands that display such edge effects from the analysis since they are a feature of the current ‘basic’ pipeline and such effects should be mitigated in a future advanced pipeline.

After this successful demonstration, the ISD method was implemented as step 3a) in the basic pipeline, and used for the remainder of the Phase A study. Using the ARIEL-specific ‘bright’ and ‘dim’ PSDs in ExoSim, the effect of ISD on the stabilised final end of Phase A design (described in Section 4.5) can be seen in Figure 4.13, where we see a similar pattern of jitter noise improvement as in the LRS. In this case the combination of the cross-correlation function method and the Fourier transform method was used. HD 219134 replaces 55 Cancri as the ‘bright’ target, and GJ 1214 remains the ‘dim’ target. These targets were simulated with the ‘bright’ and ‘dim’ target PSDs described above. For both targets, we see a large fall in spectral jitter after ISD compared to pre-decorrelation, and again the spatial jitter baseline pre-decorrelation is lower than spectral jitter and its subsequent improvement with ISD is minimal.

**Need for flat fielding** We predicted above that flat fielding would be an essential prior step to any decorrelation of the jitter. The effect of omitting flat fielding

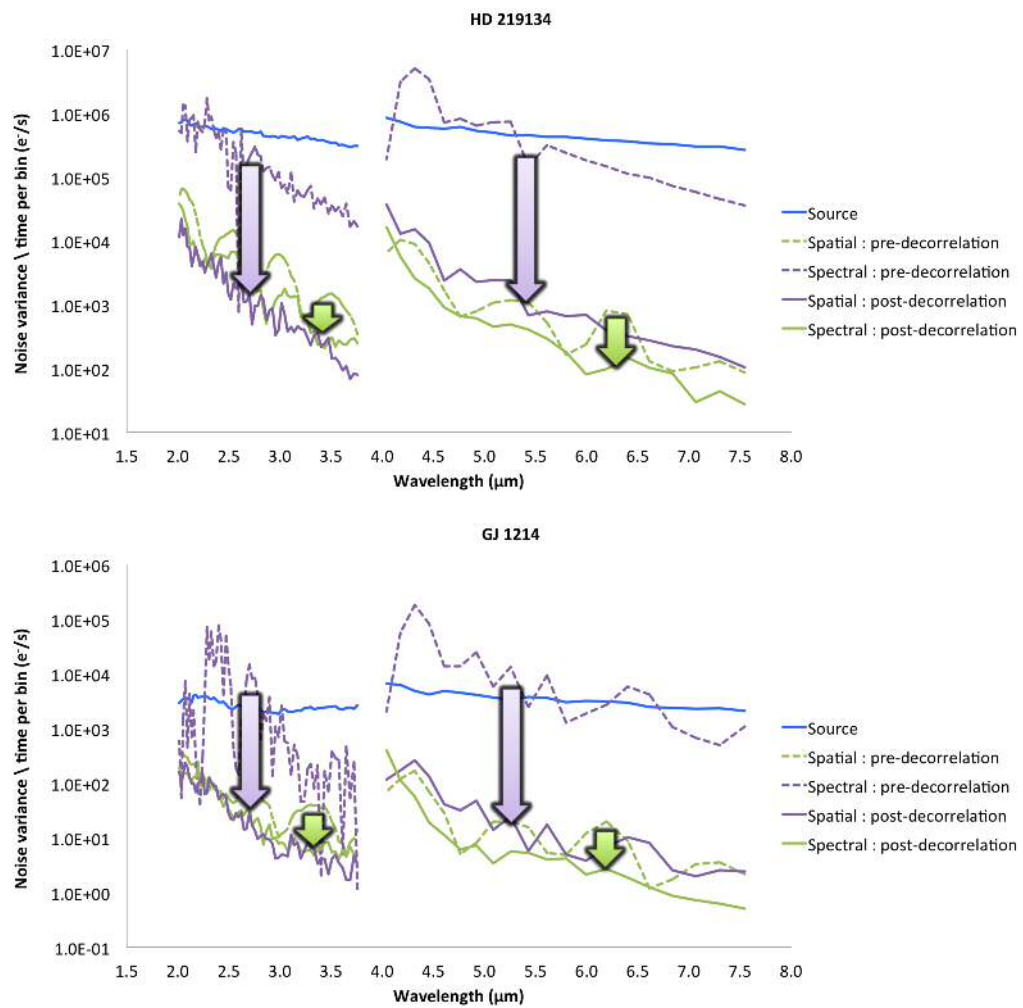


FIGURE 4.13 Effect of image shift decorrelation on jitter noise on the final end-of-Phase A AIRS design. Top: HD 219134. Bottom: GJ 1214. Green arrows indicate degree of improvement in spatial jitter. Purple arrows indicate degree of improvement in spectral jitter.

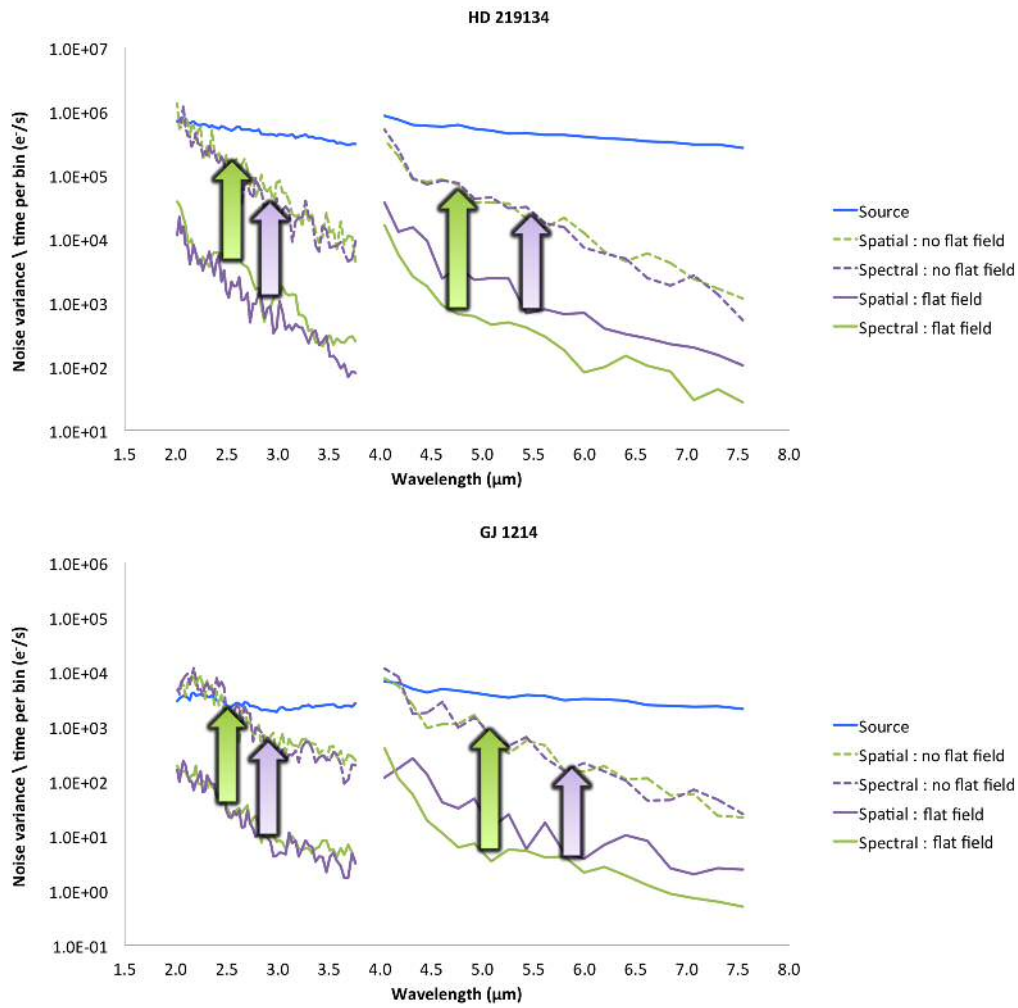


FIGURE 4.14 Importance of flat fielding prior to image shift decorrelation of jitter noise in the final end-of-Phase A AIRS design. Top: HD 219134. Bottom: GJ 1214. Green and purple arrows indicate degree of worsening in spatial and spectra jitter noise respectively if flat fielding is omitted.

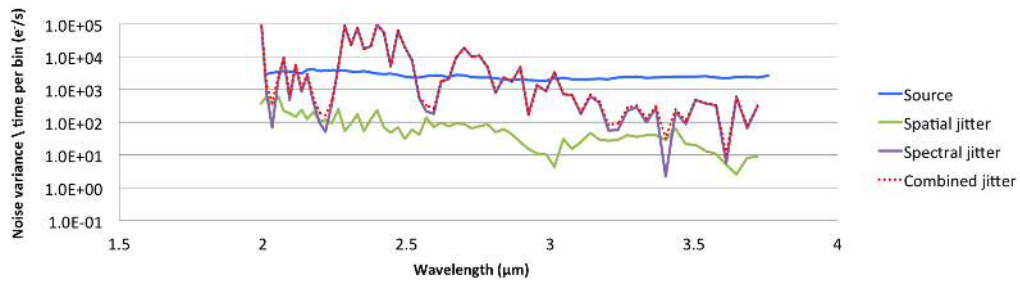
while implementing the ISD method, is shown in Figure 4.14. It can be seen that any improvement due to the decorrelation is lost, with both spectral and spatial jitter remaining high. This exemplifies the fact that interaction of the jittering signal with detector non-uniformity and with apertures (i.e. bins and masks) are essentially separate mechanisms of jitter noise production. Flat fielding is the only way to mitigate the former, while jitter decorrelation mitigates the latter. Both are therefore needed for effective jitter noise mitigation.

**Comparison of ISD techniques** Figure 4.15 compares different combinations of the 2 offset determination methods and the 2 shifting methods, with the non-decorrelated case at the top. I used the case of GJ 1214 and the final end of Phase A design for these comparisons with a single realization for each case. There is no noticeable difference between the various combinations, except that using the interpolation method for applying the shifts tends to result in slightly worse improvement on the spatial component compared to the Fourier method. Thus the Fourier method therefore has an edge on effectiveness. For the tests on the matured ARIEL designs in the next two sections, the cross-correlation method was used to obtain the offsets (and to demonstrate FGS independence) with the Fourier transform method used to apply shifts.

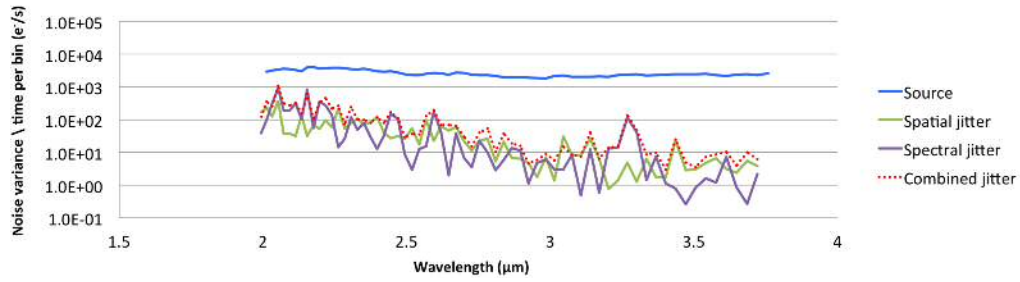
#### 4.3.3.2 APERTURE-BASED DECORRELATION

I predicted above that one reason spatial jitter appears to start at a lower pre-decorrelation baseline than spectral jitter, may be due to partial decorrelation in the spatial direction having already been implemented through the moving of the aperture with each exposure. This is tested in Figure 4.16 where the aperture is not allowed to move, thus the only decorrelation applied is through the ISD. If movement of the aperture produces a decorrelation effect we would expect the pre-ISD spatial jitter to be much higher than in the moving aperture case, and show a greater decrease after ISD.

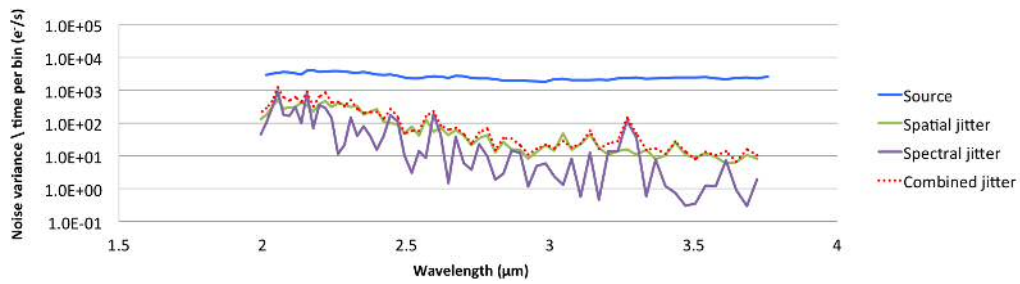
We do in fact see some increase in the pre-ISD spatial jitter in Ch0 in GJ 1214, the difference being a lot higher than if the mask was allowed to move (Figure 4.13, bottom), indicating in this situation that mask movement does appear to partially decorrelate the jitter. However in Ch1 and also in the HD 219134 case the differences are much smaller, and similar to what is seen with a moving mask. This indicates that the spatial jitter is low even without either mask movement or ISD. Since Figure 4.14 shows that omitting the flat field results in a huge rise in



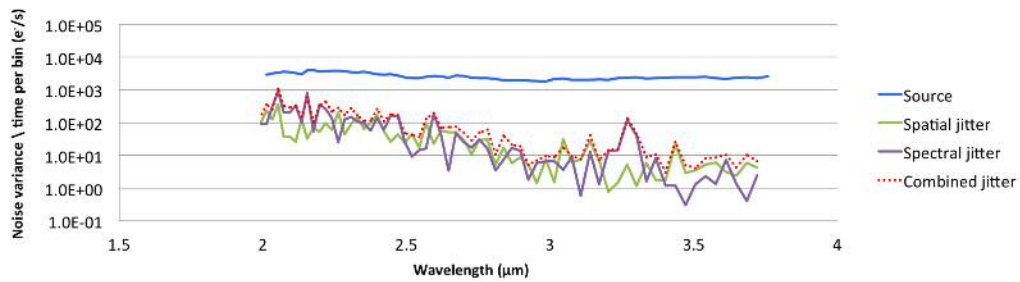
(A) No decorrelation



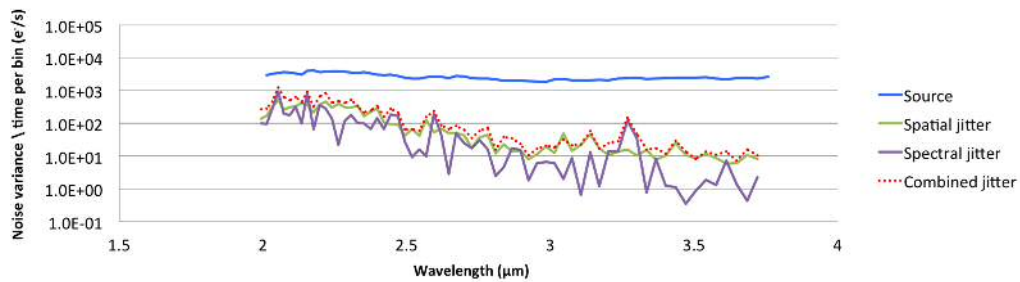
(B) Cross-correlation-Fourier



(C) Cross-correlation-Interpolation



(D) Pointing-Fourier



(E) Pointing-Interpolation

FIGURE 4.15 Comparison of different methods for image shift decorrelation.

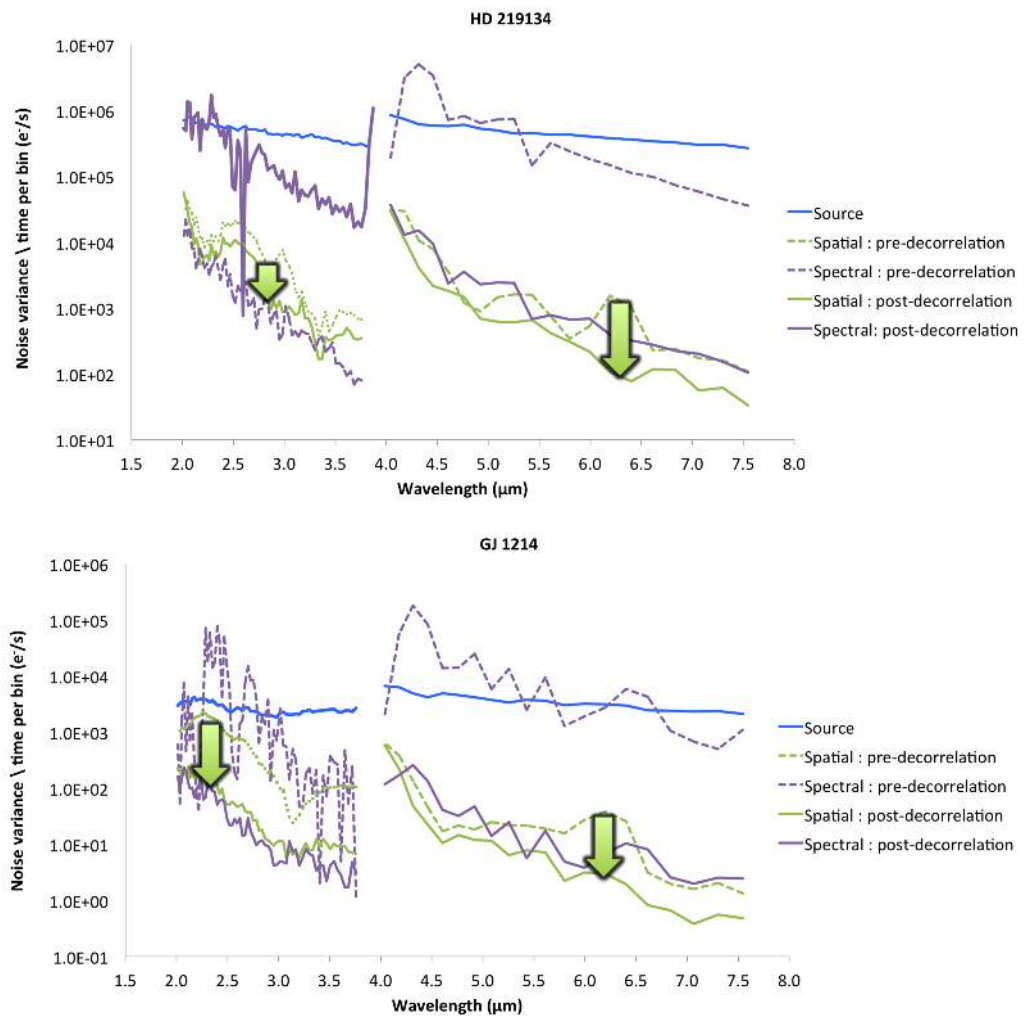


FIGURE 4.16 Effect of image shift decorrelation implemented with a fixed un-moving aperture mask. Top: HD 219134. Bottom: GJ 1214. Green arrows indicate degree of improvement in spatial jitter, which is somewhat increased from the moving aperture case (Figure 4.13).

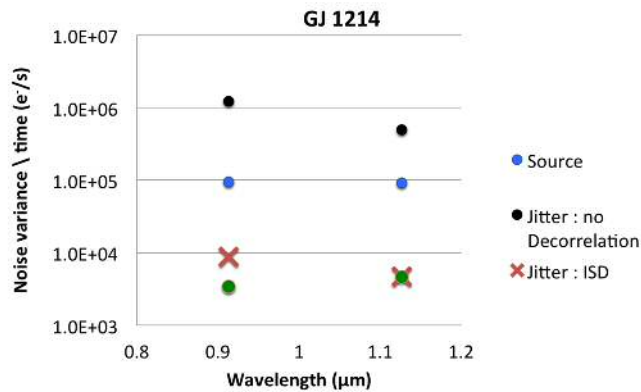


FIGURE 4.17 Comparison of image shift decorrelation vs aperture-based jitter decorrelation in FGS 1 and FGS 2 with GJ 1214 using the final end-of-Phase A design. Aperture sizes for each channel were based on optimal SNR.

spatial jitter, we can conclude that the major factor in mitigating the spatial jitter is flat fielding, with jitter decorrelation, either through the moving aperture or ISD, having much less impact.

The aperture-based decorrelation method was also tested on the photometric channels (Figure 4.17). It was found to be as effective if not more so than the ISD method. As a result for photometric channels I use the aperture-based method as the sole decorrelation technique.

#### 4.3.3.3 APERTURE WIDENING

For noise budget tests on the matured ARIEL designs (Sections 4.4 and 4.5), I used the newer sub-pixel methods for both masking and binning. Compared to the previous highly pixelated mask, the sub-pixel mask more closely follows the desired width of  $2.44f\lambda$  to match the position of the first Airy minima in the spatial direction. One drawback of the new mask was that it appeared to heighten spatial jitter noise at the blue ends of Ch0 and Ch1, despite being allowed to shift position in the spatial direction to match the position of the maximum of the PSF profile. This may have been due to the limited precision of centering the aperture, which becomes proportionally worse as the aperture narrows at the blue ends. The effect was that the spatial jitter was enhanced with the tighter mask.

A solution was proposed to widen the mask at the blue end to reduce spatial jitter noise while maintaining the nominal  $2.44f\lambda$  mask width at the red end, with intermediate widths tapering linearly with wavelength. Widening at the red end would not have improved the spatial jitter noise much since it is already very low in

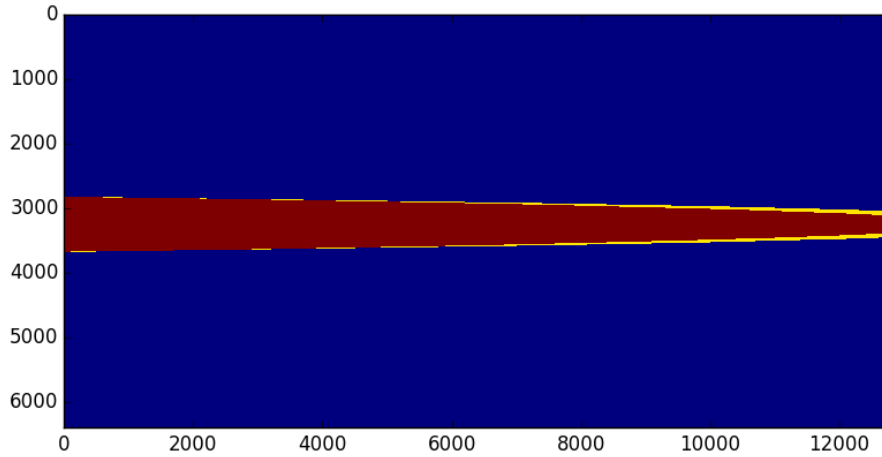


FIGURE 4.18 Blue end widening of the aperture mask. Example shown is for AIRS Ch1. Wavelength decreases to the right. Axes show sub-pixel indices. Nominal mask area based on  $2.44f\lambda$  shown in red. Additional area due to widened mask (in this case widened by 1 pixel at the blue end) shown in yellow. Mask tapers linearly in wavelength space to nominal width at red end. In the pipeline sub-pixel expansion of the mask is only performed in the y (spatial) direction but for clarity in this picture the x direction has also been expanded.

that region and instead would tend to increase the instrumental and background noise component. The instrumental and background noise is low at the blue end of each channel so widening the blue end mask would not impact much on these noise sources but would mitigate the spatial jitter. The mask width,  $w(\lambda)$  (in units of pixels) was therefore modified according to the equation:

$$w(\lambda) = (\lambda - \lambda_{end}) \left( \frac{x}{\lambda_{start} - \lambda_{end}} \right) + \frac{2.44f\lambda}{\Delta_{pix}} \quad (4.8)$$

where  $\lambda$  is the wavelength of the pixel column,  $\lambda_{start}$  is the wavelength at the start of the band,  $\lambda_{end}$  is the wavelength at the end of the band,  $\Delta_{pix}$  is the width of the pixel, and  $x$  is the extra pixel width at  $\lambda_{start}$  (the 'blue end'). Figure 4.18 shows an example of the mask array for Ch1 and how much extra mask area is obtained from this type of widening.

Figure 4.19 shows the change in spatial jitter from this 'blue end' widening, for HD 219134 in Ch0 and Ch1 using the final end-of-Phase A design. The

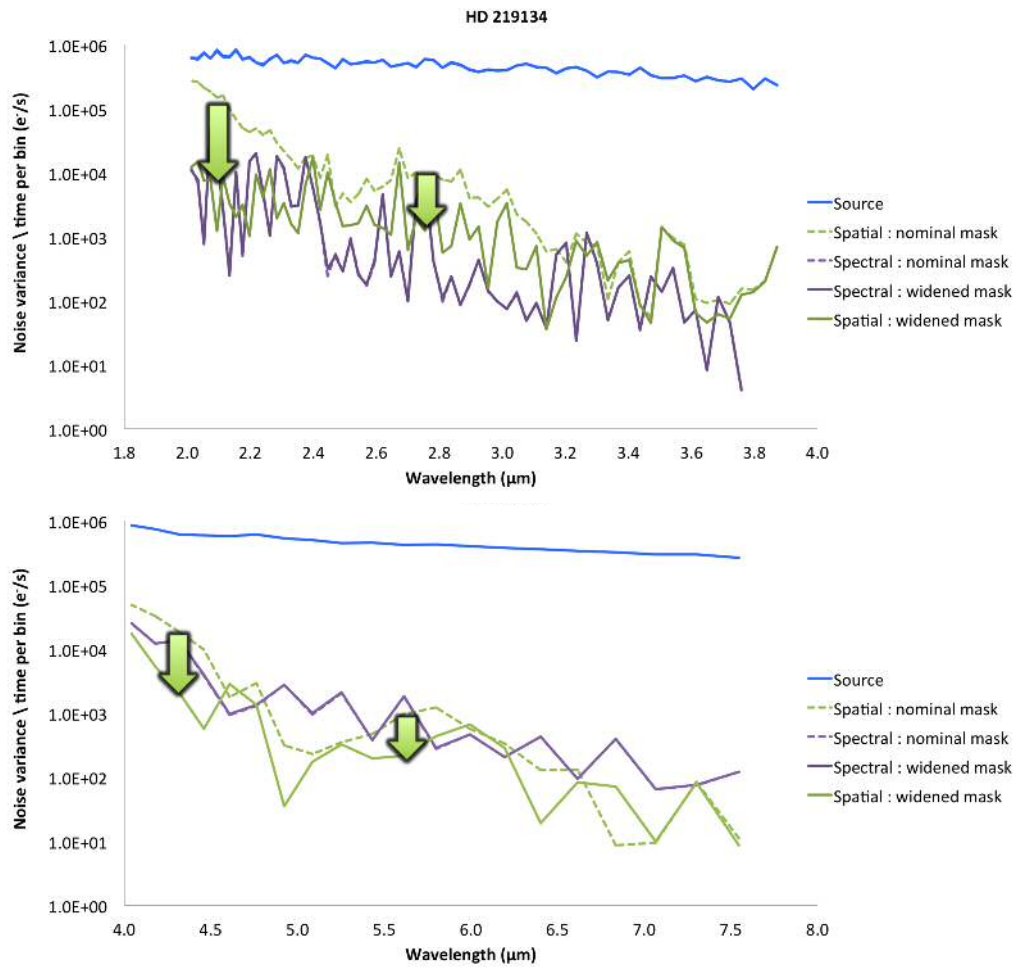


FIGURE 4.19 Effect of aperture mask widening on spatial jitter for HD 219134 in Ch0 (top) and Ch1 (bottom). Example shown uses blue end widening of 1 pixel. Green arrows indicate degree of improvement in spatial jitter noise. Improvement is highest at the blue end. There is no significant change in spectral jitter noise.

widening does not affect the spectral jitter. I use this method in Sections 4.4 and 4.5 to optimize the spatial jitter noise in AIRS Ch0 and Ch1. Aperture widening also improves jitter in the photometric channels, but needs to be balanced against worsening instrumental noise since the aperture increases are much bigger than considered here. This is described further in Section 4.5, where optimal aperture sizes are obtained through following the SNR.

#### 4.3.3.4 PSF ABERRATIONS

Although not implemented as a ‘mitigation strategy’, it is important to simulate aberration in the PSF for channels operating in the wavelength range below the primary mirror diffraction limit<sup>17</sup> to accurately estimate the jitter noise. This is because broader, flatter PSFs will tend to generate less jitter.

Figure 4.20 shows the jitter noise obtained in simulations of FGS 1 and FGS 2 photometric channels using either Airy functions for the PSF or using PSFs that have been modeled to take into account the aberration due to wavefront errors (Figure 4.21). The latter are clearly much flatter and broader. The apertures for the Airy pattern PSFs had a radius of  $1.22f\lambda$ , i.e. to the first minimum, and the apertures used for the aberrated PSFs enclosed the same equivalent encircled energy (86%). The jitter noise obtained with the aberrated PSFs is significantly lower. For example in FGS 1 this effect alone reduces the jitter/photon noise variance ratio from 7 to 0.54 for HD 219134. Thus not taking into account the PSF shape would have led to a gross overestimate of the jitter noise in these channels.

#### 4.3.4 SUMMARY

Pointing jitter noise is complex in its mechanism, dependencies and mitigation strategies. Early studies with the LRS showed this type of noise will be an issue for ARIEL observations but in this section I have shown that it can be mitigated to acceptable levels in data reduction.

Factors influencing jitter noise can be reduced to a few fundamental factors: the magnitude of the jitter, the pixel non-uniformity, the size of apertures and the gradient in the signal. Both spatial and spectral jitter noise show an inverse wavelength dependence in each spectroscopic channel. This is probably due to a combination of increasing signal at shorter wavelengths increasing both types of

<sup>17</sup> Here ‘diffraction limit’ refers to the wavelength below which the Strehl ratio drops to 0.8 or less.

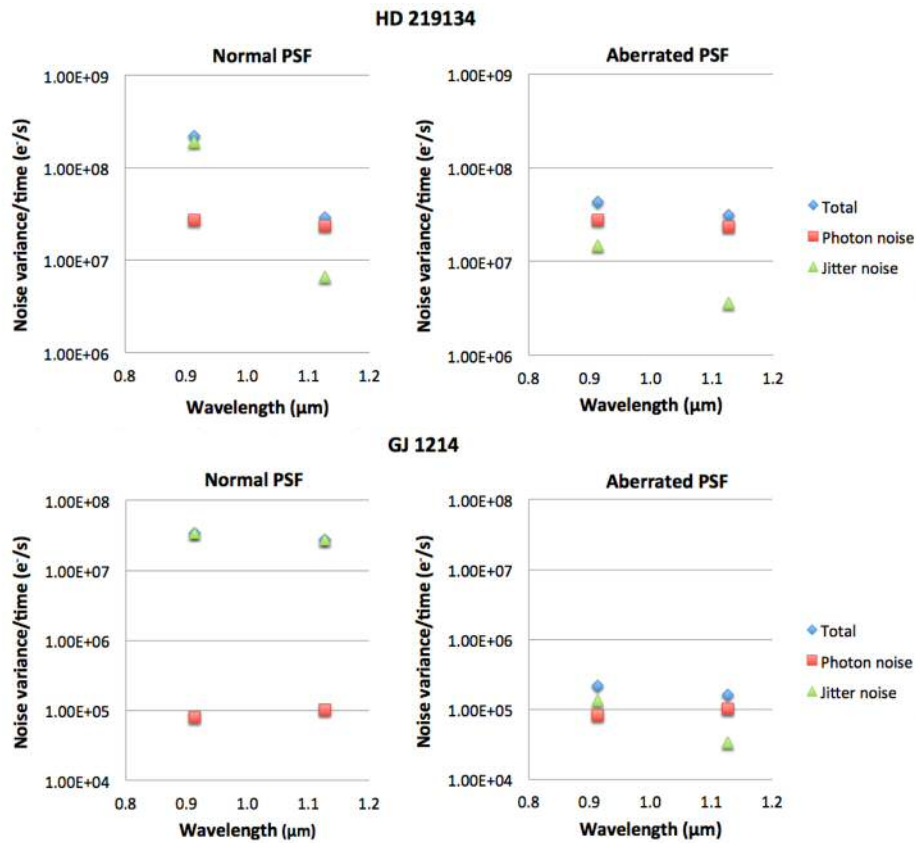


FIGURE 4.20 The importance of using accurate PSF profiles in the simulation of jitter noise. Examples are shown for HD 219134 (top) and GJ 1214 (bottom) in FGS 1 and FGS 2. Left: noise using Airy model PSF. Right: noise using aberrated PSF. Apertures in all cases contain 86% encircled energy. Photon noise is that from the source.

jitter noise, reduced size of spectral-resolving-element-sized bins at shorter wavelengths causing increase in spectral jitter noise, and narrower, steeper PSFs resulting in more spatial jitter.

Bright targets may be more prone to both types of jitter noise not only through increased gradients in the signal, but also through shorter integration times, so that more of the frequency bandwidth is outside the integration time and thus adds to photometric variation. On the other hand this may be offset to some extent by the fact that the pointing accuracy is higher for bright targets over dimmer ones, leading to a lower jitter rms.

'Image shift decorrelation' (ISD) was shown to be effective at mitigating spectral jitter noise in particular, and was added to the basic data reduction pipeline to be used for all ARIEL targets. Spatial jitter noise is mostly reduced through flat fielding, and to a lesser degree by jitter decorrelation.

Flat fielding is essential to reduce both spectral and spatial jitter noise, the

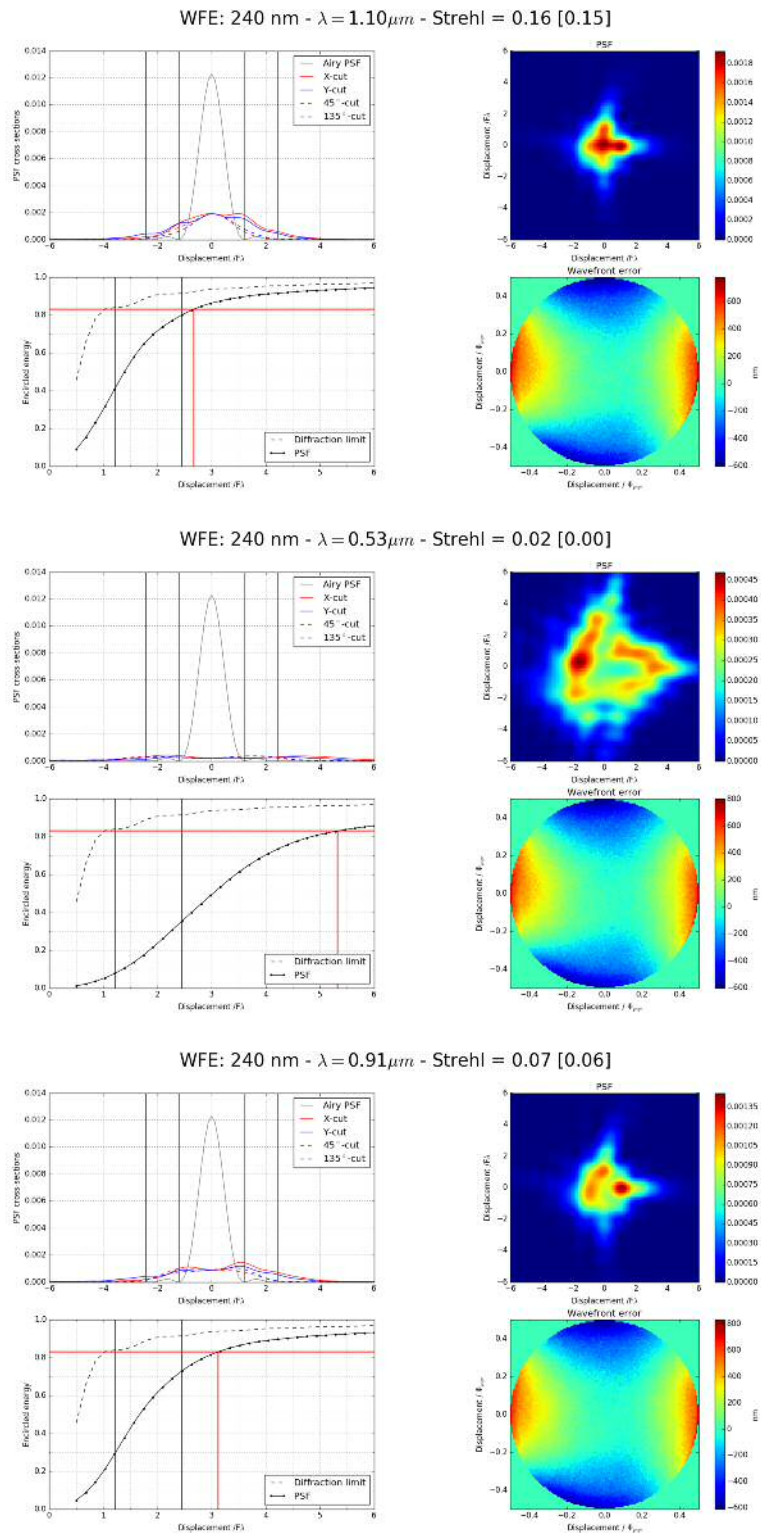


FIGURE 4.21 Wavefront-error-aberrated PSFs for photometric channels used in ExoSim simulations. Top: FGS 2. Middle: FGS 1. Bottom: VisPhot. Model and charts by E. Pascale.

effects of any decorrelation being negated if this is not performed. Jitter noise in the photometric channels can be effectively decorrelated by moving the aperture alone. Aperture widening reduces spatial jitter noise but must be balanced against increased instrumental and background noise. In simulations, PSF aberrations should be taken into account as these will influence the jitter noise estimated particularly in the the visual channels.

#### 4.4 ESTABLISHING NOISE REQUIREMENTS COMPATIBLE WITH SCIENCE CASE

In Chapter 2, we showed how ExoSim cross-validated the ESA Radiometric Model (ERM). This was a crucial validation since the ERM is the tool used to test the ARIEL Mission Reference Sample (MRS) (Zingales et al., 2017)<sup>18</sup>, and to verify the viability of the science case by checking if the target list can be successfully observed within the mission life time. As mentioned in Chapter 2, the ERM models the total noise variance per unit time on any spectral element as:

$$\frac{\sigma^2}{t}(\lambda) = N_0(\lambda) + XN_0(\lambda) + N_{min}(\lambda) \quad (4.9)$$

where  $N_0$  is the signal (in  $e^-/s$ ) in the spectral-resolution-element-sized bin and represents the source photon noise variance per unit time,  $X$  is a factor that accounts for instrumental noise sources that are proportional to the signal, and  $N_{min}$  is an instrumental noise floor (in  $e^-/s$  per spectral element) that is independent of the signal.

In this section I detail how ExoSim was used to obtain values of  $X$  and  $N_{min}$  'measured' from a matured design of the ARIEL instrument (but not the final Phase A design since these tests were performed prior to the final iteration). These were then utilized by the MRS group to run batch simulations using the ERM. The MRS currently consists of 1002 planets, of which around 200 are known planets and the remainder are projected planet discoveries based on stellar and planetary statistics.

Each planet in the MRS has a nominal primary transit atmospheric signal (contrast ratio) assigned to it based on its known or assumed radius, equilibrium temperature, likely atmospheric mean molecular weight, and stellar radius, using

<sup>18</sup> The group developing and testing the MRS is led by G. Tinetti based at University College London.

Equation 1.7 in Chapter 1. Similarly a secondary eclipse signal is obtained using Equation 1.8 in Chapter 1. The noise on these signals is found using a similar equation to Equation 4.1 (i.e. using the OOT signal and noise, to obtain the noise on the contrast ratio). The SNR (atmospheric signal/contrast ratio noise) for 1 transit,  $SNR_1$  is found for each spectral resolution element. The mean  $SNR_1$  per channel is found. The goal SNR used was 7, and so the number of transits,  $N_{transits}$ , needed to reach this goal using the mean  $SNR_1$  per channel is found using Equation 1.16 in Chapter 1. The noisiest channel with the highest  $N_{transits}$  is then used to set the observing time required assuming that the time taken per transit is  $2 \times T_{14}$ . The mean  $SNR_1$  will be higher as the resolution of the observation tier falls, and so fewer transits are needed at tier 1 compared to tier 2, and tier 2 compared to tier 3, but this occurs at the expense of spectral resolution. The mission is considered scientifically viable if the 1000 or so planets (selected to cover a wide range of parameter space in temperature, size, stellar class and metallicity) in the target list, can be observed (i.e. reach the required number of transits needed for each planet) within total mission time at the tier 1 level either in primary transit or secondary eclipse, and leave a significant proportion of time remaining for selected groups of planets to be observed at tier 2 and tier 3 resolutions.

The selected values of  $X$  and  $N_{min}$  used in the MRS simulations will directly determine the SNR obtained for each planet and thus the overall time to observe the target list. ExoSim, being well-validated and able to model the instrument prescription more precisely and realistically than radiometric models, as well as being able to simulate pointing jitter noise and include limitations of data reduction, was tasked with obtaining noise results from the matured ARIEL model with the goal of finding  $X$  and  $N_{min}$  values to use in the ERM to test the target list and mission viability.

#### 4.4.1 FINDING $N_{min}$

In terms of the noise types modeled in ExoSim,  $N_{min}$  (in units of e-/s) will be the sum of the variances per unit time per spectral-resolution-element-sized bin resulting from dark current, zodiacal light and emission. As shown in the LRS noise budget, dark current noise greatly exceeds the latter two and so will be the dominant factor in  $N_{min}$ .  $N_{min}(\lambda)$  gives the noise floor per spectral-resolution-element-sized bin, and thus is dependent on the resolving power,  $R$ , of the spectrum which will vary with the channel simulated. Therefore the results from ExoSim can only

be used directly in the ERM if it simulates the same R values. The ExoSim simulation and data reduction will return results with R=20 in NIRSpec, R=100 in AIRS Ch0 and R=30 in AIRS Ch1. Since tier 1 and tier 2 will be at lower resolution than these, the  $N_{min}(\lambda)$  results obtained by ExoSim will have to be adjusted for in the ERM in order to simulate tier 1 or tier 2 resolutions<sup>19</sup>. For the spectroscopic channels only, a correction factor  $\kappa$  for optimal extraction was applied. For each spectral bin at wavelength  $\lambda$ , the correction is found using Equation 4.6, and assuming the Gaussian approximation to the Airy pattern.

$$\kappa(\lambda) = \frac{0.84f\lambda\sqrt{\pi}}{w(\lambda)} \quad (4.10)$$

where  $w(\lambda)$  is the width of the aperture in the same units as  $\lambda$ . Thus,

$$N_{min}(\lambda) = \kappa(\lambda) \frac{\sigma_{dc}^2(\lambda) + \sigma_{zodi}^2(\lambda) + \sigma_{emm}^2(\lambda)}{\tau} \quad (4.11)$$

where  $\tau$  is the integration time for the CDS exposure (and will vary with target and channel), and  $\kappa=1$  for the photometric channels. From these results for  $N_{min}$  versus wavelength, a power law fit can be obtained for each spectroscopic channel and used to determine an  $N_{min}(\lambda)$  expression for use in the ERM.

#### 4.4.2 FINDING X

In terms of the noise modeled in ExoSim,  $X$  will consist of components from jitter noise ( $X_j$ ) and read noise ( $X_r$ ).  $X$  is the ratio of the variance from these noise sources to the source signal,  $N_0(\lambda)$ . Therefore an aperture correction,  $AC$ , is needed for the ExoSim-derived ratio to be used in the ERM, since the ExoSim aperture mask cuts off part of the signal per bin, which is not the case in for the ERM signal. Thus the ExoSim signal,  $S_{oot}(\lambda) = AC[N_0(\lambda)]$ . Without the aperture correction, the absolute value of the  $X$  noise contribution will be overestimated in the ERM. In addition, a correction factor for optimal extraction,  $\kappa(\lambda)$  (found per spectral bin in the same way as described above) is also applied to the read noise component. Therefore:

$$X(\lambda) = X_j(\lambda) + X_r(\lambda) = AC \frac{\sigma_{jit}^2(\lambda) + \kappa(\lambda)\sigma_{rn}^2(\lambda)}{S_{oot}(\lambda)} \quad (4.12)$$

<sup>19</sup> Another approach used is to run the simulation with the R values fixed at the highest resolutions but to find  $N_{transits}$  for lower resolutions by compensating the goal SNR in the simulation to a lower value.

The value of  $AC$  is found empirically for each bin as described below. Due to the large size of apertures used in the photometric channels (see below), no aperture correction was deemed necessary, thus in the above equation  $\kappa=1$  and  $AC = 1$  for the photometric channels. Note that this expression implies that  $X$  is dependent on wavelength, which is not in fact represented in the ERM model where  $X$  is assumed to be a fixed ratio for a given channel.

### 4.4.3 METHODOLOGY

The ARIEL configuration used for this test is given in Table 4.5. Compared to the LRS, this model now also includes NIRSpec and the three photometric channels. The wavelength solutions used in Ch0, Ch1 and NIRSpec were now based on prisms with varying dispersion and resolution across the focal plane. Rather than using the Herschel jitter PSD, the pointing jitter PSDs described in Subsubsection 4.3.1.1, were used for 'bright' and 'dim targets'. Dark currents used in Ch0 and Ch1 were again 'pessimistic' to demonstrate compliance with requirements for a possible European detector. Telescope and channel emissions were modeled as previously described for the LRS (Subsubsection 4.2.2.3). The zodiacal light model was again used without adjustment<sup>20</sup>.

The ExoSim 'noise budget' method was followed as before with modifications outlined below.

#### 4.4.3.1 EXOSIM SIMULATIONS

The targets 'observed' were now changed to HD 219134 (the revised 'brightest target' for ARIEL), HD 209458 (an intermediate target at K magnitude of 6.3 which represents the boundary condition for a 'bright' target as defined in the mission requirements), and GJ 1214 (the 'dimmiest' target). The same PHOENIX model was used for GJ 1214 as described earlier. For the other two stars, PHOENIX spectra used were:  $T=4700$  K,  $\log g=4.5$ ,  $[Fe/H]=0$  for HD 219134, and  $T=6100$  K,  $\log g=4.5$ ,  $[Fe/H]=0$  for HD 209458. The two brighter targets utilized the 'bright' target jitter PSD (71 mas rms), whilst GJ 1214 simulations use the 'dim' target PSD (151 mas rms).

<sup>20</sup> For the ecliptic latitudes of the targets used in this study it was decided that the baseline model would be adequate. The ecliptic latitudes are as follows: GJ 1214  $27.9^\circ$ , HD 209458  $28.7^\circ$  and HD 219134  $20.5^\circ$ . It is possible that the zodiacal emission for HD 219134 may be slightly underestimated in these simulations, but per the analysis in the Appendix, the increase would amount to about  $1.43\times$  the baseline intensity, and thus would not change the overall simulation results significantly given the low level of zodi noise.

TABLE 4.5 ARIEL instrument prescription used in noise requirements test. WFE PSF refers to use of model PSFs incorporating wavefront error aberrations.

Parameter	VisPhot	FGS 1	FGS 2	NIRSpec	AIRS Ch0	AIRS Ch1
Wavelength ( $\mu\text{m}$ )	0.53 <sup>a</sup>	0.91 <sup>a</sup>	1.13 <sup>a</sup>	1.25-1.90	1.95-3.9	3.9-7.8
R (band start-band end)	N/A	N/A	N/A	20-20	95-163	30-66
f-number	32.14	25.0	34.47	26.42	13.2	6.36
Optical efficiency (mid-band)	0.57	0.59	0.64	0.50	0.45	0.46
Detector QE	0.55	0.55	0.55	0.55	0.55	0.55
Pixel size ( $\mu\text{m}$ )	15	15	15	15	15	15
Pixel scale ( $^{\circ}$ /pixel)	$2.43 \times 10^{-5}$	$3.10 \times 10^{-5}$	$2.23 \times 10^{-5}$	$3.01 \times 10^{-5}$	$6.11 \times 10^{-5}$	$1.23 \times 10^{-4}$
Slit width (pixels)	N/A	N/A	N/A	13	17	13
Pixel diffusion length ( $\mu\text{m}$ )	1.7	1.7	1.7	1.7	1.7	1.7
Dark current ( $\text{e}^-/\text{s}$ )	1	1	1	1	30	50.0
Linear well depth ( $\text{ke}^-$ )	100	100	100	100	70	70
Read noise ( $\text{e}^-$ )	16	16	16	16	16	16
PSF aberration	WFE PSF	WFE PSF	WFE PSF	2xf-number	None	None

<sup>a</sup> central wavelength

TABLE 4.6 Integration times in seconds for each target in each ARIEL channel used in ExoSim simulations for the noise requirements test.

Channel	HD 219134	HD 209458	GJ 1214
AIRS Ch1	0.24	4.06	26.50
AIRS Ch0	0.29	4.78	62.25
NIRSpec	0.43	5.42	85.60
FGS 2	0.14	1.44	29.36
FGS 1	0.10	0.71	23.94
VisPhot	0.54	2.81	2642.90

As before, simulations were repeated with each noise source activated in isolation. In addition to spectral and spatial jitter simulations in isolation, a combined jitter simulation was also run for all channels (as this was needed for  $X_j$ ). The targets were 'observed' for 250 exposures or 2000 seconds whichever was longer (rather than relying on  $T_{14}$  for the principle planet as before) to ensure that a reasonable number of exposures were always obtained to measure the noise. The upper limit of 2000 seconds on the observation was limited by computational efficiency, and thus may not contain the lowest frequencies on the jitter power spectrum ( $< 5 \times 10^{-4}$  Hz), however we still capture 99.8% and 98.4% of the total jitter rms for bright and dim target PSDs respectively. The integration times were again found using the 'time to saturation' method for each target in each channel, but this time each channel was assigned its own integration time rather than the shortest in any channel applied to all channels. This was done as it became clear that each detector could be separately commanded in terms of exposure cycle elements. The integration times used are given in Table 4.6.

If the integration time was less than 0.1 seconds this was rounded to 0.1 seconds, as this was considered the minimum frame rate expected for readout of the detector. This was required in only one situation (FGS 1 with HD 219134)<sup>21</sup>.

For efficiency a variable simulation frame rate was used of about 400 frames per integration time. The detector ground and reset times, and  $NDR_0$  were each allocated 1 frame, thus the time for the CDS exposure ( $NDR_1 - NDR_0$ ) was very close to (but not exactly the same as) the total exposure time.

<sup>21</sup> This situation would require the detector to operate outside its linear regime which may be an acceptable assumption depending on the detector characteristics.

Quantum efficiency variations were modeled as before with a 5% rms inter-pixel QE variation (with uncertainties of 0.5% rms after flat-fielding in data reduction), and using the same intra-pixel variation as before.

The PSF in NIRSpec and the photometric channels will suffer from wavefront error aberrations since these channels operate at wavelengths well below the diffraction limit of the primary mirror. External calculations by K. Middleton at Rutherford Appleton Laboratory (RAL), indicated the aberrated PSF in NIRSpec could be modeled by a flatter, broader PSF of about twice the FWHM of the unaberrated PSF. Thus for this channel, I mimic this aberration by using an f-number twice that of the channel f-number to generate the PSFs. For the photometric channels, the aberrated PSFs were generated by E. Pascale from a model that estimates the effects of wavefront errors from the primary mirror (Figure 4.21). These were then incorporated into ExoSim by myself.

#### 4.4.3.2 DATA REDUCTION

The 'basic' data reduction pipeline was modified to use the sub-pixel mask and binning methods described previously, and also now incorporated the 'image shift decorrelation' routine at step 3a) for the spectroscopic channels (using the cross-correlation and Fourier transform methods). AIRS Ch0 was binned to  $R = 100$ , Ch1 to  $R = 30$  and NIRSpec to  $R = 20$ . The use of the more accurate (and tighter) sub-pixel mask resulted the aforementioned unexpected excess in spatial jitter noise at the blue end of Ch0 and Ch1 due to the limitations of the precision in mask positioning. As described in Subsubsection 4.3.3.3, this was mitigated by widening the blue end of the mask in each channel, in this case, empirically by 2 pixels (tapering to the nominal size of  $2.44 \lambda$  at the red end). The NIRSpec mask did not require widening as the spatial jitter appeared unaffected.

Optimal extraction corrections,  $\kappa(\lambda)$ , for the spectroscopic channels were found for each bin based on the width of its aperture as previously described. The aperture correction for each bin,  $AC(\lambda)$  was found empirically by obtaining the ratio of the noiseless signal with the mask to the noiseless signal without the mask in each bin. This ranged from 0.94 to 0.96.

For the photometric channels, circular aperture radii were used that enclosed an encircled energy equivalent to the 2nd Airy minimum as determined using the encircled energy versus displacement charts on Figure 4.21. The radius for the 2nd Airy minimum was used since it was found that if the radius that enclosed an encircled energy equivalent to the 1st Airy minimum was used, the jitter

noise was excessive and well above the photon noise. In VisPhot this radius occurs off the chart shown at  $7.7 f\lambda$  but the aperture was widened further empirically to  $9f\lambda$  to further reduce jitter noise which was still high for the brightest target, HD 219134. Due to large size of these apertures no aperture corrections were deemed necessary for the photometric channels.

#### 4.4.4 RESULTS

##### 4.4.4.1 $N_{min}$

Figure 4.22, top, shows the results in terms of  $N_{min}$  versus wavelength from all three sources over all six channels. Power law fits are shown for the 3 spectroscopic channels. These appear to follow a  $\lambda^3$  relationship. This reflects the increase in recruitment of pixels with wavelength, and is consistent with a prism wavelength solution where the spectral element bin size varies with  $\lambda^2$ , whilst the aperture width varies with  $\lambda$ . By dividing by  $\lambda^3$  we obtain Figure 4.22, bottom. The highest value in each channel of  $N_{min}/\lambda^3$ ,  $\alpha$ , was found. This was used to set a conservative power law for each channel in the form:  $N_{min}(\lambda) = \alpha\lambda^3$ . The final power laws are given in Table 4.7. For the photometric channels, single values for  $N_{min}$  were obtained. Small margins were added to these empirical values for  $N_{min}$  to give an input for the ERM that for use by the MRS group to test for mission viability.

##### 4.4.4.2 $X$

Figure 4.23 shows  $X_j$ ,  $X_r$  and total  $X$  for each target over all six channels. It can be seen that due to the complex wavelength dependencies of both  $X_j$  and  $X_r$ , total  $X$  cannot be said to have a single value for all wavelengths, as implied in the ERM noise equation. However as this is how the ERM is modeled, it was necessary to find an appropriate value for  $X$  from these data, for each channel. Table 4.7 shows the minimum, maximum and median values for total  $X$  from all targets, in each channel, obtained from ExoSim. Given the wide variation of  $X$  values, it was decided to use the median as the best overall measure of  $X$  in each channel. Based on the medians therefore,  $X$  values were proposed as inputs for the ERM MRS simulation, also shown in Table 4.7.

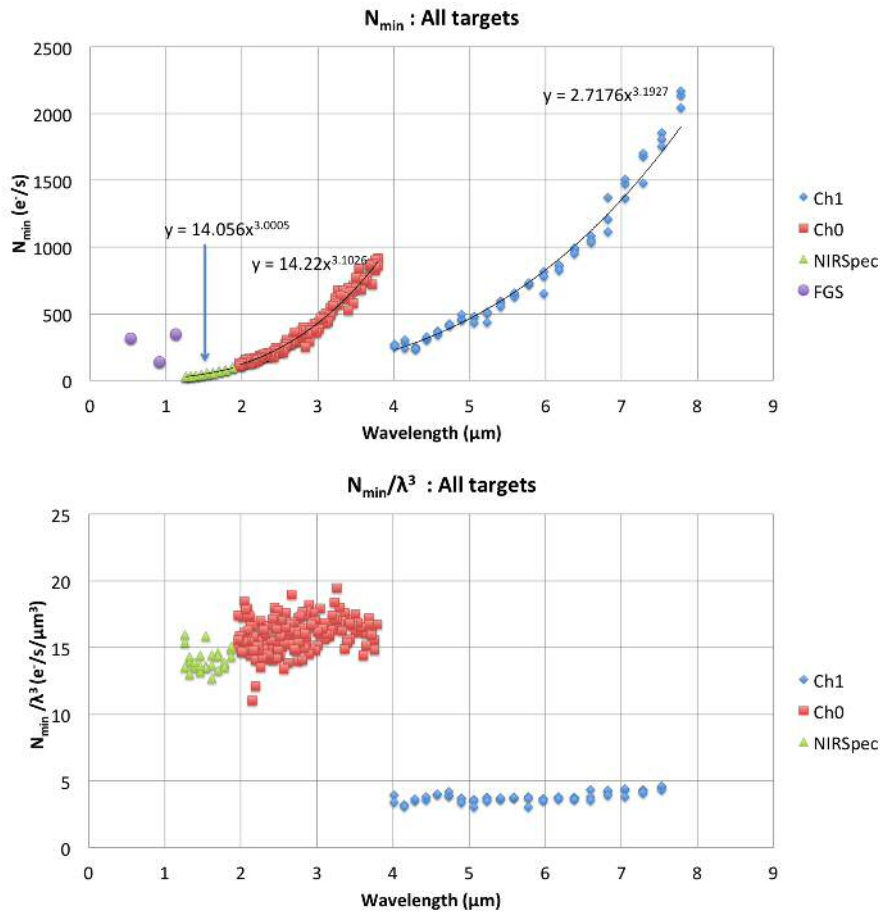


FIGURE 4.22  $N_{min}$  values from ExoSim simulations. Top:  $N_{min}$  vs wavelength,  $\lambda$ . Bottom:  $N_{min}/\lambda^3$  vs  $\lambda$ . Also shown in top diagram are power law fits in each spectroscopic channel.

#### 4.4.5 MISSION VIABILITY

The MRS group, using these input values of  $X$  and  $N_{min}$  in the ERM, determined that that all 1002 target list planets could be successfully surveyed within the mission lifetime with selected groups studied at the higher resolutions (Zingales et al., 2017). The results for the particular sample used were as follows: 3% of the mission time will be at tier 3 only (including time taken during the tier 2 and tier 1 surveys). Tier 3 will examine 67 gaseous planets. 60% of the mission time will be at tier 2 (not including tier 2 time used in tier 3, but including tier 2 time during the tier 1 survey). Tier 2 will examine 502 planets. The remaining 37% of the mission is pure tier 1 (not including tier 1 time used in tier 2 or tier 3). Tier 1 will examine 1002 planets. Figure 4.24 shows that this sample covers a wide range of planet sizes and temperatures. If phase curve spectroscopy studies are performed the number of planets observed in tier 2 falls. The key result is that the

#### 4.4. ESTABLISHING NOISE REQUIREMENTS COMPATIBLE WITH SCIENCE CASE 167

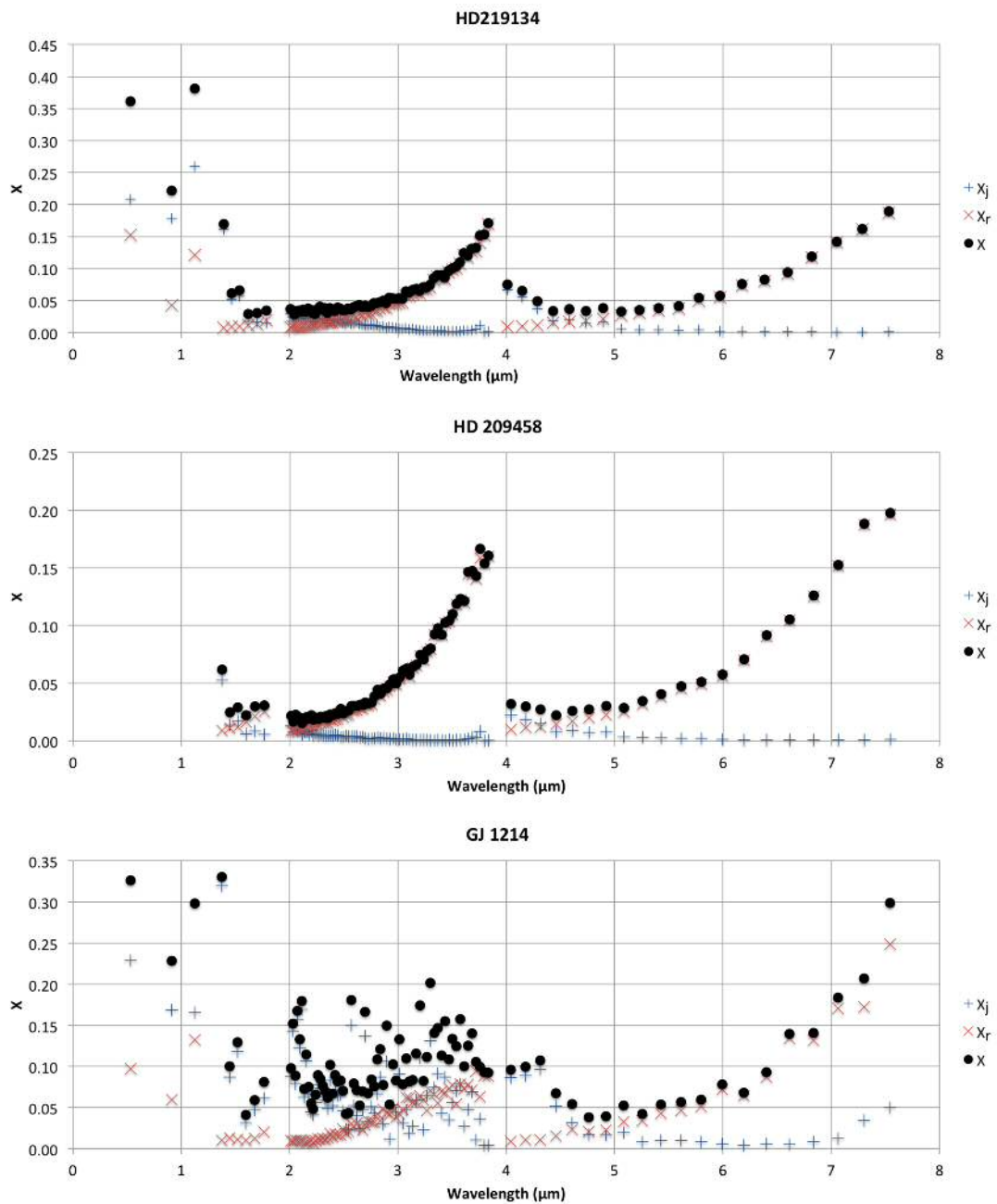


FIGURE 4.23 X values found from ExoSim simulations for each target. Top: HD 219134. Middle: HD 209458. Bottom: GJ 1214.

primary science goal of achieving the 1000 planet survey (covering the wide range of parameter space) is feasible, and significant numbers of planets can be observed at tier 2 and 3. This showed a scientifically viable mission was possible given the noise parameters used. Therefore it was established that these values of  $X_{median}$  and  $N_{min}$  were compatible with the science case.

TABLE 4.7 Summary of  $X$  and  $N_{min}$  results from ExoSim simulations of matured ARIEL design and ERM inputs for the MRS study.

Channel	ExoSim results				ERM inputs	
	$X_{min}$	$X_{max}$	$X_{median}$	$N_{min}$	$X$	$N_{min}$
Ch0	0.02	0.20	0.06	$19.5 \lambda^3$	0.1	$20 \lambda^3$
Ch1	0.02	0.30	0.06	$4.6 \lambda^3$	0.1	$5 \lambda^3$
NIRSpec	0.02	0.33	0.06	$16 \lambda^3$	0.09	$17 \lambda^3$
FGS 2	0.24	0.38	0.3	348	0.3	400
FGS 1	0.22	0.23	0.22	141	0.3	400
VisPhot	0.20	0.36	0.33	316	0.3	400

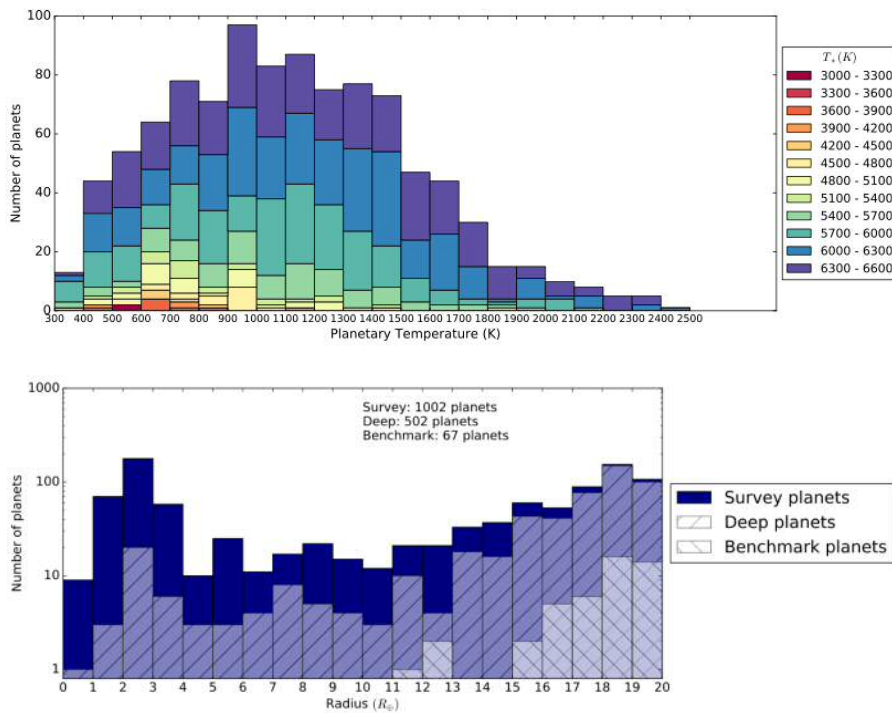


FIGURE 4.24 ARIEL Mission Reference Sample (MRS) results. The MRS study found that 1002 planets could be observed in tier 1, 502 in tier 2, and 67 in tier 3 within the mission lifetime, given the  $X$  and  $N_{min}$  provided from ExoSim. Top: Tier 1 planets organised in by temperature, showing the range of temperatures expected. Bottom: Number of planets observable in each tier arranged by size. Figures from Zingales et al. (2017).

## 4.5 EVALUATION OF FINAL PHASE A DESIGN

The final Phase A instrument design differed slightly from the version used to test the science case in the previous section, due to ongoing design iterations by various working groups. In general the main changes were altered transmissions in each channel, modified f-numbers in NIRSpec and the FGS channels, and changes to the NIRSpec wavelength solution. ExoSim was used to generate complete final noise budgets for this end of phase design, which were used for ESA technical documents summarising the Phase A study, including the ARIEL Performance Analysis Report (Sarkar et al., 2017a). In this section we present the noise breakdown of the stabilised final instrument design, evaluate its noise performance and characteristics and check that it remains compatible with a viable science case.

### 4.5.1 METHODOLOGY

The final configuration tested in ExoSim is shown in Table 4.8. This configuration, as well incorporating the above changes, assumes Teledyne detectors in the FGS and NIRSpec (18  $\mu\text{m}$  pixels and low dark current) but models for European detectors in AIRS (15  $\mu\text{m}$  pixels and high dark current), as it was more likely at this stage that the visual and NIR channels would employ the Teledyne detectors, but European detectors with ‘pessimistic’ dark currents were still possible for AIRS. If the final instrument adopted 18  $\mu\text{m}$  pixels for AIRS as well, the results would still be applicable as long as the f-numbers of the AIRS channels are scaled by 18/15. The noise budget method from the previous section was followed with with the following modifications.

#### 4.5.1.1 EXOSIM SIMULATIONS

The same three stellar targets are simulated in the same way as previously described in Subsubsection 4.4.3.1. Integration times for the new configuration are given in Table 4.9.

An optimal detector readout mode had been established by the ARIEL detector working group for the Teledyne H1RG array and the SIDECAR ASIC that utilised line-by-line resets. Using a read-reset-read mode, a line of pixels can be read out, reset and read again before before moving on to the next line. This dramatically reduces the overheads to the time taken to reset a line and the read time of a single line, both of which are negligible compared to the total frame read time.

TABLE 4.8 ARIEL instrument prescription used for Phase A final noise budget performance analysis.

Parameter	VisPhot	FGS 1	FGS 2	NIRSpec	AIRS Ch0	AIRS Ch1
Wavelength ( $\mu\text{m}$ )	0.53 <sup>a</sup>	0.91 <sup>a</sup>	1.13 <sup>a</sup>	1.25-1.90	1.95-3.9	3.9-7.8
R (band start-band end)	N/A	N/A	N/A	36-55	95-163	30-66
f-number	39.46	24.62	31.30	19.34	13.2	6.36
Optical efficiency (mid-band)	0.53	0.60	0.60	0.65	0.45	0.46
Detector QE	0.55	0.55	0.55	0.55	0.55	0.55
Pixel size ( $\mu\text{m}$ )	18	18	18	18	15	15
Pixel scale ( $^{\circ}$ /pixel)	$2.86 \times 10^{-5}$	$4.58 \times 10^{-5}$	$3.60 \times 10^{-5}$	$4.85 \times 10^{-5}$	$6.11 \times 10^{-5}$	$1.23 \times 10^{-4}$
Pixel diffusion length ( $\mu\text{m}$ )	1.7	1.7	1.7	1.7	1.7	1.7
Slit width (pixels)	N/A	N/A	N/A	13	17	13
Dark current ( $\text{e}^-/\text{s}$ )	1	1	1	1	30	50
Linear well depth ( $\text{ke}^-$ )	100	100	100	100	70	70
Read noise ( $\text{e}^-$ )	16	16	16	16	16	16
PSF aberration	WFE PSF	WFE PSF	WFE PSF	2xf-number	None	None

<sup>a</sup> central wavelength

TABLE 4.9 Integration times in seconds for each target in each ARIEL channel used in ExoSim simulations for Phase A final noise budget performance analysis.

Channel	HD 219134	HD 209458	GJ 1214
AIRS Ch1	0.33	5.84	37.78
AIRS Ch0	0.32	5.53	71.26
NIRSpec	0.11	1.49	23.75
FGS 2	0.13	1.52	30.17
FGS 1	0.10	0.69	23.49
VisPhot	0.78	4.20	3903.27

This means that overheads including the time for  $NDR_0$  can be considered negligible. To reflect this near 100% duty cycle, the simulations assigned zero time to overheads.  $NDR_0$  was generated with read noise (to allow CDS simulation) but zero integration time.

Another modification was that multiple realizations were used for the same noise source to build up an average performance value. This should better reflect the average performance of the instrument without being biased by random variations from a single realization. For all noise sources involving jitter noise (i.e. the spatial, spectral and combined jitter simulations and total noise) I obtained the average from 20 realizations with the QE grid and uncertainties changed randomly with each realization. For the noise sources without jitter the average of only 5 realizations was obtained, since the variations between simulations are much lower.

The PSF aberrations in NIRSpec and the photometric channels were simulated as before.

#### 4.5.1.2 DATA REDUCTION

The ‘basic’ pipeline was used in the same way as in Subsubsection 4.4.3.2, with the following modifications.

The aperture widening at the blue end of Ch0 and Ch1 was guided by following the median improvement in spatial jitter noise over 5 bins at the blue end of each channel as the value of  $x$  in Equation 4.8 was varied. These simulations used HD 219134 as the target with 100 exposures per simulation and a single realization in each case. Figure 4.25 shows that a minimum in spatial jitter noise occurs with only 1 pixel of widening at the blue end in Ch0 and Ch1. Therefore masks based on  $x = 1$  were used for these channels for all simulated targets. For NIRSpec, the change in median spatial jitter noise over all 6 bins unaffected by edge effects was

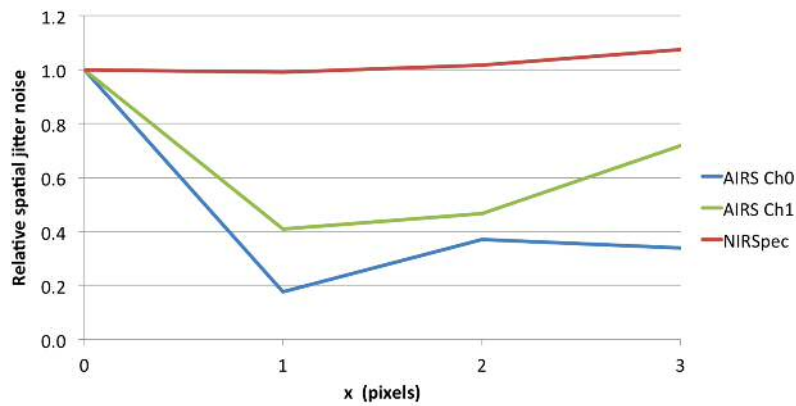


FIGURE 4.25 Finding optimal value for  $x$  (blue end widening) in each channel. Y axis shows the proportional change from  $x = 0$  in the median spatial jitter noise over the 5 bins at the blue end of Ch0 and Ch1, and all 6 spectral bins in NIRSpec.

TABLE 4.10 Apertures used for FGS channels, in units of  $f\lambda$ .

Channel	HD 219134	HD 209458	GJ 1214
FGS 2	5	5	5
FGS 1	6	7	7
VisPhot	9	9	8

followed (Figure 4.25), and no significant improvement occurred in with increasing  $x$ . The mask for this channel was therefore left at the nominal  $2.44 f\lambda$  width over the whole band. As before, an optimal extraction correction factor for each spectral bin was found based on the aperture width in that bin. The aperture correction for each spectral bin was again found empirically from the ratio of the noiseless signal with the mask to the noiseless signal without the mask. This averaged to 0.95 in Ch1 and 0.94 in Ch0 and NIRSpec.

For the photometric channels instead of using the radius equivalent to the 2nd Airy minimum, an optimal aperture was found for each channel by following the SNR (mean signal/total noise). The radius of the aperture is given by  $rf\lambda$ . For each of the three photometric channels,  $r$  was varied until a peak in the SNR for each target was found (Figure 4.26). Widening the aperture tends to reduce the jitter noise but increases the instrumental noise (primarily read noise), thus the maximum SNR is obtained when a balance is reached between these two noise sources. The final apertures in terms of  $r$  are given in Table 4.10 for each channel and target.

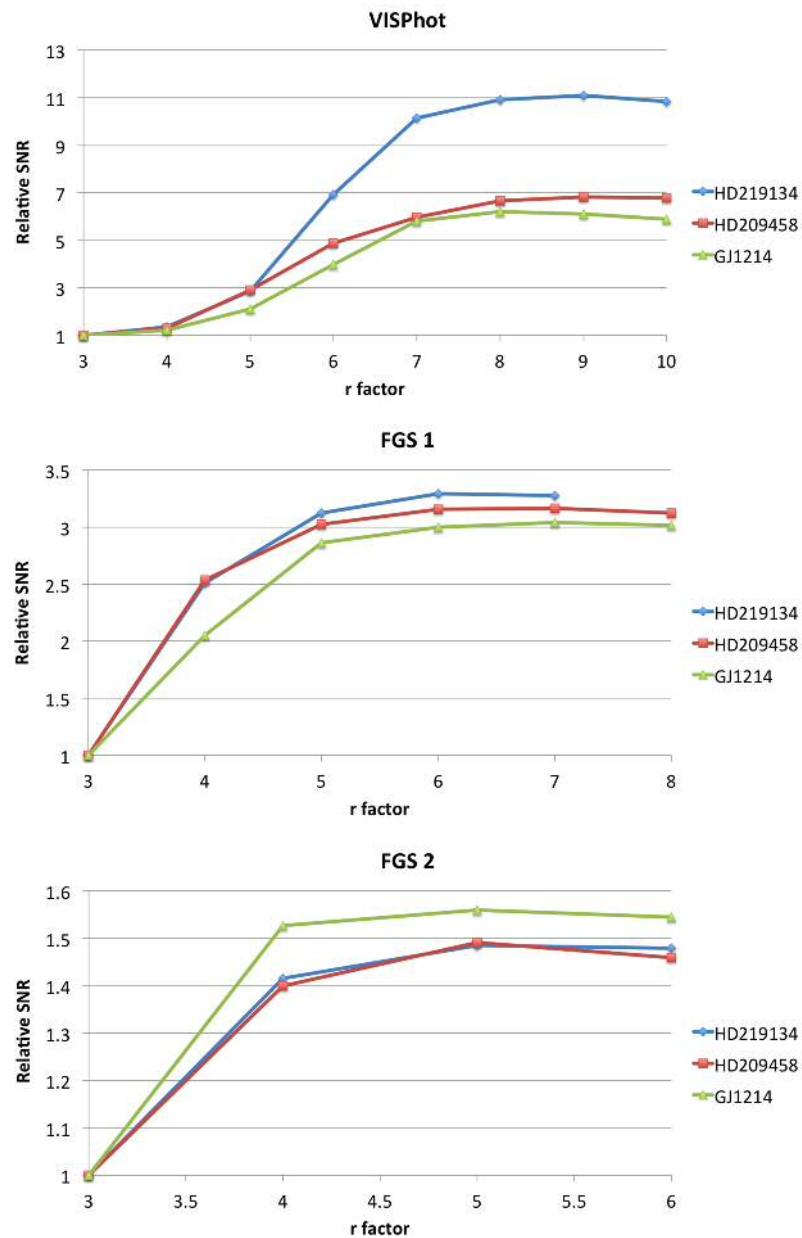


FIGURE 4.26 Relative SNR vs aperture radius factor  $r$  for HD 219134, HD 209458 and GJ 1214 in VisPhot (top), FGS 1 (middle) and FGS 2 (bottom).

## 4.5.2 RESULTS

The final noise budgets for the end-of-Phase A design are given in Figures 4.27 to 4.29. These charts do not include any corrections due to optimal extraction. For each channel a breakdown of individual noise variance per unit time per spectral bin (or photometric channel) is shown for each stellar target observed out-of-transit. Bins that cross the transmission band edge and those that showed 'edge' effects have been omitted. These results give the current best estimate of the noise performance of the ARIEL instrument.

## 4.5.3 ANALYSIS

The final ARIEL design achieves near photon noise limited performance in all channels and for all targets studied, with the exception of the extreme red end of Ch1 in GJ 1214 (which has the longest integration times), where the dark current slightly exceeds the photon noise. However since the final detectors may well have much lower dark current than the pessimistic case simulated here, it is likely that this region will achieve the photon noise limit in the final design. In addition a reduction in the dark current noise variance of by a factor of about 1.7 may be expected in this region due to optimal extraction.

We see the expected wavelength-dependent behaviour in instrumental noise reflecting the R-binning process, with dark current noise and read noise variance increasing with wavelength as the bin sizes and aperture mask widths increase recruiting more pixels. Conversely, the photon noise variance from the source falls with wavelength in accordance with the signal, as does jitter noise variance but at a different rate to the photon noise variance.

The combination of jitter mitigation strategies (flat fielding, optimal apertures and image shift decorrelation) achieve very good control of both spatial and spectral jitter in all channels and across all targets.

I find that emission noise is negligible in this wavelength range and at the temperature of the optics simulated, and only appears on the charts at the red end of Ch1. Zodiacal light noise is also very low being the second lowest noise source in all channels except in Ch1 where it exceeds the jitter noise at longer wavelengths.

Read noise is the dominant instrument noise source (i.e. higher than dark current) for the brighter 2 targets. This is due to their shorter integration times compared to the dim target resulting in more rapid read out rates. However all 3 targets have read noise at the red end of Ch0 and Ch1 that encroaches within 1

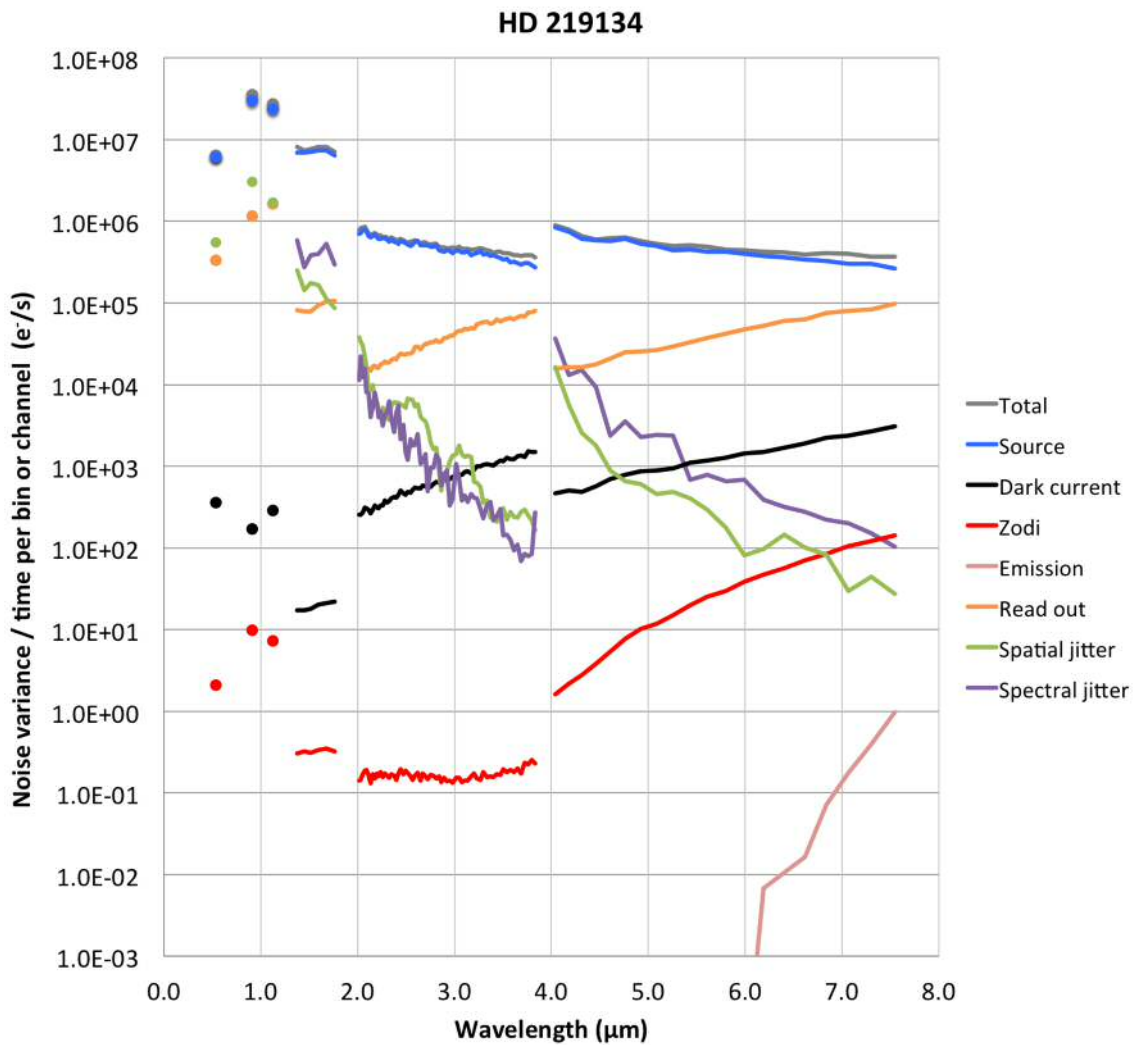


FIGURE 4.27 ARIEL noise budget for OOT observation of HD 219134. Combined jitter shown for photometric channels (green dots).

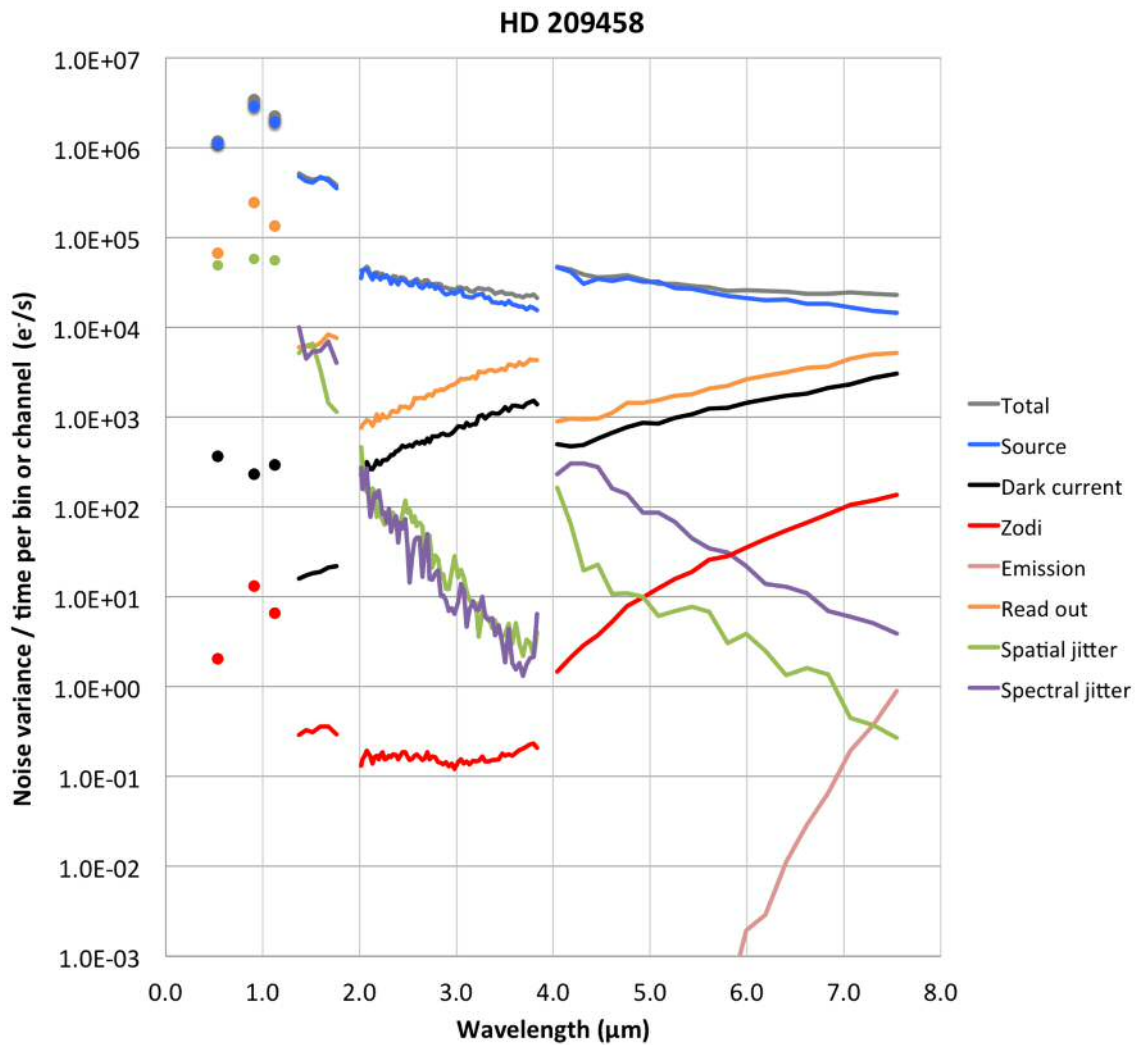


FIGURE 4.28 ARIEL noise budget for OOT observation of HD 209458. Combined jitter shown for photometric channels (green dots).

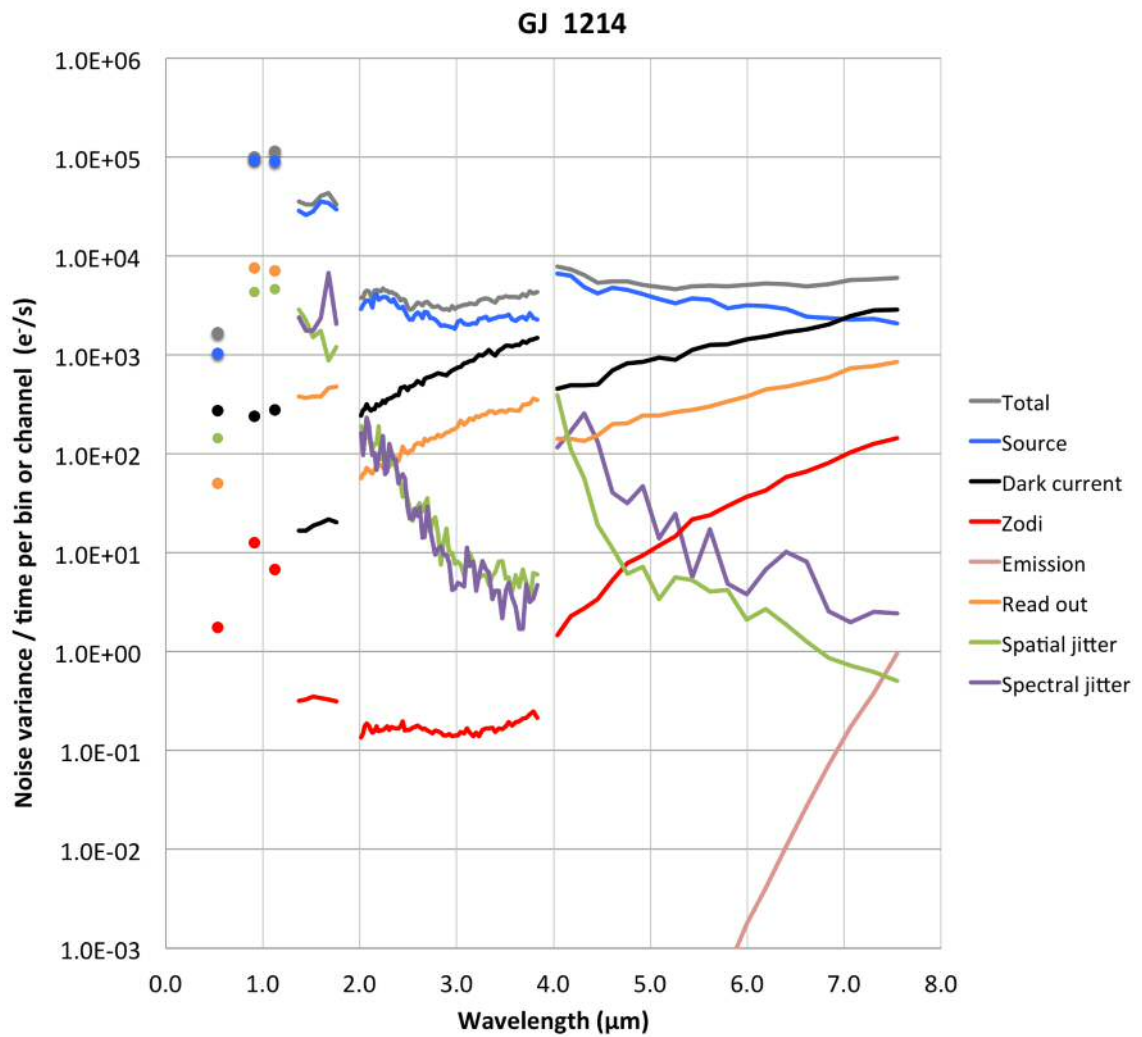


FIGURE 4.29 ARIEL noise budget for OOT observation of GJ 1214. Combined jitter shown for photometric channels (green dots).

magnitude of the source photon noise.

The read noise variance here is of course based on CDS. A future advanced pipeline can incorporate more a sophisticated mode such as up-the-ramp or Fowler sampling. These alternate modes however will also impact Poisson noise adversely so their use will need to be assessed carefully based on optimizing the total noise.

For NIRSpec, spectral jitter noise is the second highest noise for the brightest target, HD 219134, but still at least an order of magnitude below the photon noise. This was probably aided by the increased instrument resolution in the final design compared to the design in Section 4.4. The higher instrumental resolution is matched by greater dispersion and bigger physical sizing of the spectral bins, which tends to mitigate spectral jitter noise.

In most of the photometric channels, the dominant noise sources after photon noise are combined jitter and read out noise. Being close to the peak of the source signal means these channels have high signals with strong gradients, making them particularly vulnerable to jitter noise. Integration times in these channels are also typically short causing them to fold in less jitter into the integration time and suffer from more resolved jitter noise between exposures. Another impact of a shorter integration times would be to increase the number of reads and therefore the read noise per unit time. Thus jitter and read noise are both problematic in these channels but have been controlled through aperture-based decorrelation and optimal sizing of the apertures in these channels based on SNR to balance jitter and read noise. Accurate representation of the aberrated PSF is also essential to not over-estimate the jitter noise.

One exception to this noise pattern is the VisPhot channel for GJ 1214. This simulation has an extremely long integration time, due to the combination of low stellar signal (sampling the Wien region of the SED for this cooler star) and enlarged PSF with a low peak. In practice such a long integration times would not be used for transit observations since the light curve must be sampled at a higher rate. The effects of slit losses were evaluated in a separate simulation by E. Pascale but were found to be negligible.

Finally,  $X$  and  $N_{min}$  were derived from the noise results given here, using the methods described in the previous section (including optimal extraction and aperture corrections for the spectroscopic channels). These will indicate if, despite the changes made for the final iteration, the final design remains compatible with the science case.

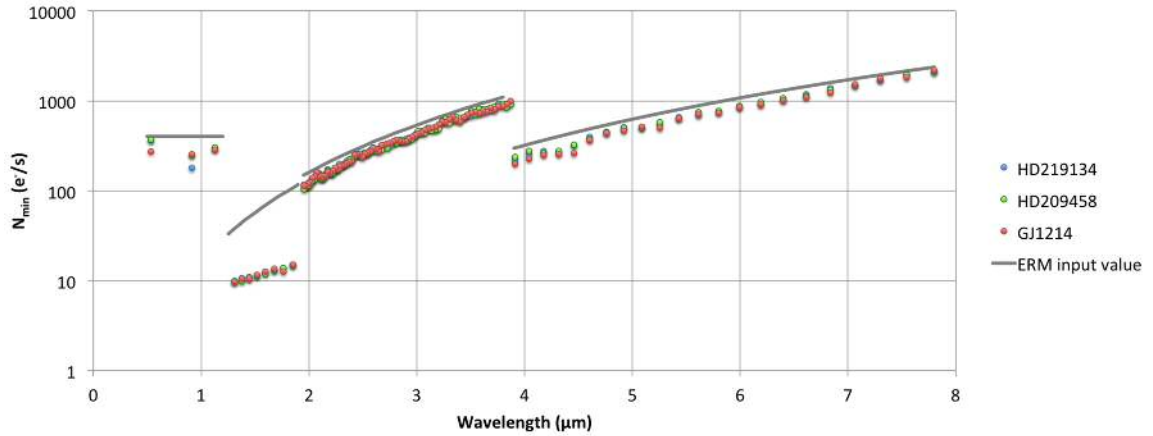


FIGURE 4.30  $N_{min}$  results from ExoSim final Phase A configuration simulations compared to the ERM input value as a requirement for scientifically viable mission. The final results lie within the requirement.

#### 4.5.4 COMPLIANCE WITH REQUIREMENTS

The  $X$  and  $N_{min}$  results obtained from these simulations were compared against the input values used in the ERM when testing the science case in Section 4.4 (Table 4.7), the latter acting as requirements for a scientifically viable mission. Since the ERM  $X$  value was previously established from the ExoSim median  $X$  value, the metric of comparison for the final design needed to be the new ExoSim median  $X$  value. Figure 4.30 shows the comparison for  $N_{min}$ , and Figure 4.31 shows the comparison for  $X_{median}$ , which is the median for all  $X$  values from all sources within a given channel. We find that in all the channels,  $X_{median}$  and  $N_{min}$  do not exceed the previously used ERM input values, for all the targets studied. Therefore these ExoSim simulations indicate that the final end-of-Phase A design remains compatible with a scientifically viable mission.

## 4.6 DISCUSSION

In this chapter, I applied ExoSim in a ‘prospective’ way, as a design phase tool in the ARIEL mission Phase A study, where it played an essential role. The noise budget method was developed as a way of assessing the noise performance characteristics together with a basic data reduction pipeline. The latter as well as being applied in future chapters, can form the nucleus of future more advanced pipeline.

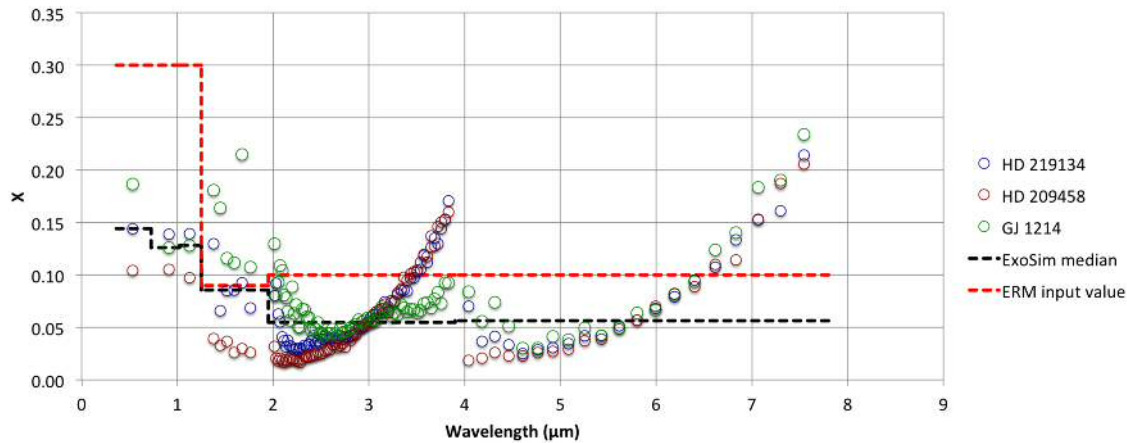


FIGURE 4.31  $X$  results from ExoSim final Phase A configuration simulations.  $X_{median}$  from ExoSim is compared to the ERM  $X$  input value. ExoSim  $X_{median}$  is below both ERM  $X$  input value in all channels.

I showed how ExoSim aided a key design decision between the two initial candidate designs. Using ExoSim, I discovered the issue of spectral jitter noise as a major noise source in ARIEL observations. I then used ExoSim simulations to better understand the mechanism and dependencies of jitter noise both spatial and spectral, and implemented a number of mitigation strategies. These included flat fielding, optimal aperture sizing, and an image shift decorrelation routine. The latter was essential for mitigating spectral jitter noise. I showed that the combination of these methods can reduce both spatial and spectral jitter noise to acceptable levels in data reduction without need for spacecraft or instrument redesign.

Next ExoSim was used to validate the ESA radiometric model as described in Chapter 2. This was essential for the simulation of the ARIEL Mission Reference Sample and thus the validity of the science case. Related to this, ExoSim simulations of the matured design were used to find realistic  $N_{min}$  and  $X$  inputs for the ERM. These were found to be compatible with a scientifically viable mission. Finally the stabilised design at the end of Phase A was tested and was found to remain within the requirement for a viable science case.

ExoSim's unique capabilities were called upon during this Phase A study, including the ability to model the time domain and simulate 2-D jitter, which was crucial in capturing the problem of spectral jitter noise at an early stage in the study phase, and then to test mitigation strategies. The ability of ExoSim to use non-standard PSFs was also crucial to the accurate simulation of jitter noise in the photometric channels as simulations with Gaussians or Airy patterns would have

grossly over-estimated the jitter noise.

Limitations of these simulations included the custom ARIEL jitter PSDs developed, which although generating the appropriate amount of jitter rms overall, were unrealistic in their profiles, being flat values over two frequency ranges. In a future Phase B simulation, more realistic PSD models can be developed. The rms could also be adapted for each individual target (since the accuracy will vary with the target brightness), rather than choosing either the 'bright' or the 'dim' PSD as in this case. Another limitation is that variations in RPE jitter rms were not simulated, which are expected in the real instrument. This is because the current jitter code is unable to vary the overall rms of the timeline once generated for a particular simulation. However this could be addressed in the future by applying an envelope to the generated jitter timeline that can adjust the jitter rms as a function of time.

The basic data reduction pipeline developed here relied on aperture photometry with a correction applied for a future optimal extraction method. An early development in Phase B could be to incorporate a functional optimal extraction routine into the pipeline and demonstrate these improvements.

Despite these limitations, we have shown with ExoSim that the final end-of-Phase A ARIEL design is a near-photon noise limited instrument that is compatible with achieving the primary science goals of the mission. With this design, ARIEL has the potential to transform our current understanding of exoplanet science.



## CHAPTER 5

# THE IMPACT OF STELLAR VARIABILITY AND ACTIVITY

---

---

**S**TELLAR variability represents a major issue in exoplanet transit spectroscopy and photometry. It introduces a form of astrophysical noise into the observations that impacts on the measurement of the transit depth. There are several types of variable phenomena which may impact on an observation. These include convection-related phenomena such as granulation and pulsations, and magnetic activity phenomena such as spots, faculae and flares. In this chapter, I examine the effects of stellar variability and activity as applied to the ARIEL mission, using ExoSim simulations in conjunction with two separate models. The first model simulates pulsations and granulation and was developed by KU Leuven. Timelines of variations from this model were used to modulate OOT simulations in ExoSim, and noise on the signal obtained in the same way as for the performance tests in Chapter 4. The noise contribution from pulsations and granulation can be compared in the overall noise budget. The second model was developed at Cardiff University and simulates star spots and faculae. This was integrated into ExoSim as a prototype ‘stellar variability’ module for the purposes of this chapter. The method of full transit Monte Carlo simulations used in Chapter 3, was used to quantify the added uncertainties due to spots on the primary transit spectrum, and then compare these to the instrument precision defined by the photon noise limit. The effects of occulted and unocculted spots, together with variability, are simulated together. Both these tests were performed using two simulated targets: GJ 1214 as a ‘typical’ M-dwarf target, and HD 209458 as a ‘typical’ G-type star, to encompass the approximate range of stellar types that ARIEL will observe. For the star spot study, a range of spot filling factors were simulated permitting a degree of

extrapolation to other stars with different levels of activity. The goal of these studies was to quantify the raw uncorrected impact of stellar variability and activity on ARIEL observations. Such an assessment helps us to understand the underlying degree of the problem, and when or whether correction methods are required<sup>1</sup>.

## 5.1 PULSATIONS AND GRANULATION

For convective stars such as M-dwarfs and solar-type stars with a convective outer layer, small-scale inhomogeneities appear as granulation on the photosphere and can be the cause of variations in the stellar flux. Such granulation cells are of the order of  $10^8$  cm (Micela, 2015), and have time scales of minutes to hours. Pulsation of the photosphere are caused by convection currents of plasma within the convection zone (p-modes), and have timescales of 5-15 minutes. This contrasts with the timescale of the variability caused by spots of days to weeks. It has been argued that these variations would not significantly impact transit spectroscopy measurements (Micela, 2015), firstly since the spatial scale of granulation is a lot smaller than the planet the effect is averaged over the area occulted by the planet, and for pulsations since they are not a stochastic phenomena they may be modeled using the out-of-transit observations to correct in transit observations (Micela, 2015). However this has not been definitively proven by simulations. In the context of the ARIEL mission, I began an analysis of the effects of stellar variability on ARIEL observations, starting with the stellar noise from granulation and pulsation.

In this section, I adopt the same approach used in Chapter 4 for ARIEL performance testing, finding the noise variance per unit time per spectral bin (or photometric channel) on the OOT stellar signal noise arising from granulation and pulsation which I will term 'stellar convection' noise. I use stellar targets already used in Chapter 4. This then permits a simple comparison of stellar convection noise with other noise sources in the overall noise budgets already found in Chapter 4, to assess its significance and impact on ARIEL observations.

For this I utilize results from a model of stellar convection developed at KU Leuven developed by I. Argyriou and B. Vandenbussche, which is described in detail in Sarkar et al. (2017a). This firstly models pulsations using pulsation mode frequencies and decay times from BiSON solar data rescaled for particular stellar

---

<sup>1</sup> Material from this chapter is presented in Sarkar et al. (2017a).

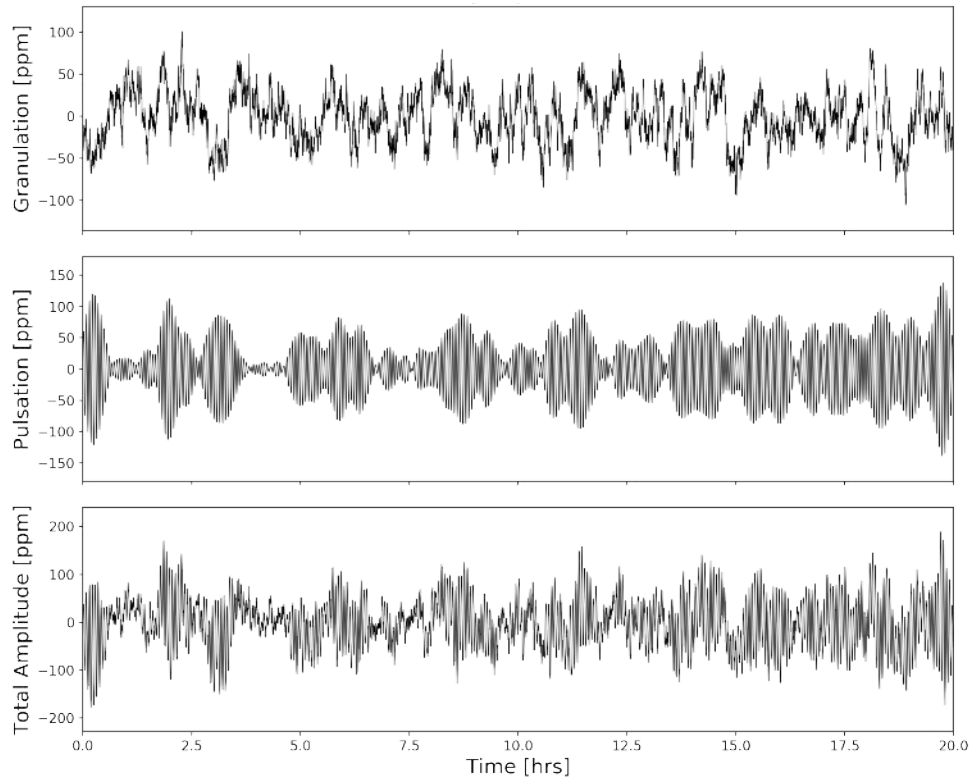


FIGURE 5.1 KU Leuven pulsation and granulation model. Time series showing the effect of simulated granulation and pulsations on the bolometric luminosity of a star of spectral type M2V. Figure credit: Ioannis Argyriou.

types generating a time series of stochastically excited damped modes. Granulation signals are simulated using a process that generates red noise components and depends on granulation timescales and amplitudes. The additive effects of granulation and pulsations on the bolometric luminosity is modelled (Figure 5.1) and thence variations on the stellar spectral energy distribution (SED). The model generates dynamic SEDs for stars of different spectral classes, producing wavelength-dependent timelines of the order of a few seconds that gives the variation around the baseline flux within a given wavelength band.

### 5.1.1 METHODOLOGY

SED timelines from the KU Leuven model above for different stellar types were obtained and then used to modify the OOT timelines generated for specific stellar targets within ExoSim. Two cases were examined representing ‘typical’ G-type and M-type star targets for ARIEL: HD 209458 (G0V) for which a solar SED timeline was used and GJ 1214 (M4.5) for which an M-type star SED was used.

The ExoSim simulation parameters were set in the same way as described in Section 4.5 for each target, but using only one realization per star. As in that section, overheads were assumed to be negligible so that the entire exposure time was attributed to  $\text{NDR}_1$ . All other noise sources were suppressed. In the *Timeline* module, the convection model SED timelines were loaded and the wavelength and timegrids interpolated to the time cadence of the ExoSim simulation frame rate used, and to the wavelength solution of the instrument pixel columns in each channel. For each exposure in the timeline, the proportional modulation per pixel column  $X(\lambda)$  was found by taking the average variation of the SED timeline within each integration time, generating a 2-D array of proportional modulation per integration period versus pixel column analogous to (and replacing) the light curve array  $LC(X, \hat{t})$  from Subsubsection 2.1.3.4. As with the generation of the light curve array, in the case of photometric channels, the central wavelength is assigned to all pixel columns for the purposes of generating this grid. This 2-D modulation array is multiplied into the array cube of subexposures in the *Noise* module in the same way as the light curve array.

Averaging the variations gives a more accurate representation of the overall modulation effects within the integration period than simply sampling the variations at the cadence of the exposures. By averaging the variability within the integration time, the standard deviation of the counts on each exposure is reduced compared to sampling at the cadence of the exposures (but by a lesser degree than expected for white noise, consistent with correlated noise).

An example of the variations obtained per exposure in an ARIEL Ch0 spectral bin is shown for GJ 1214 in Figure 5.2, showing a peak-to-peak variation of the order of 80 ppm. The simulated data was then processed using the same pipeline and methods as in Subsubsection 4.5.1.2 to obtain the OOT noise variance per unit time per spectral bin or photometric channel.

This allows a direct comparison with other noise contributions obtained for the final Phase A design at the end of Section 4.5.

## 5.1.2 RESULTS

The results for stellar convection noise resulting in each channel for each star are shown in Figures 5.3 and 5.4. The noise is shown in comparison to other noise sources obtained in Section 4.5 for each case. Table 5.1 gives the fractional OOT noise (i.e. noise/signal) in the different ARIEL channels from stellar convection as ppm, and Table 5.2 gives the ratio of stellar convection noise variance to the

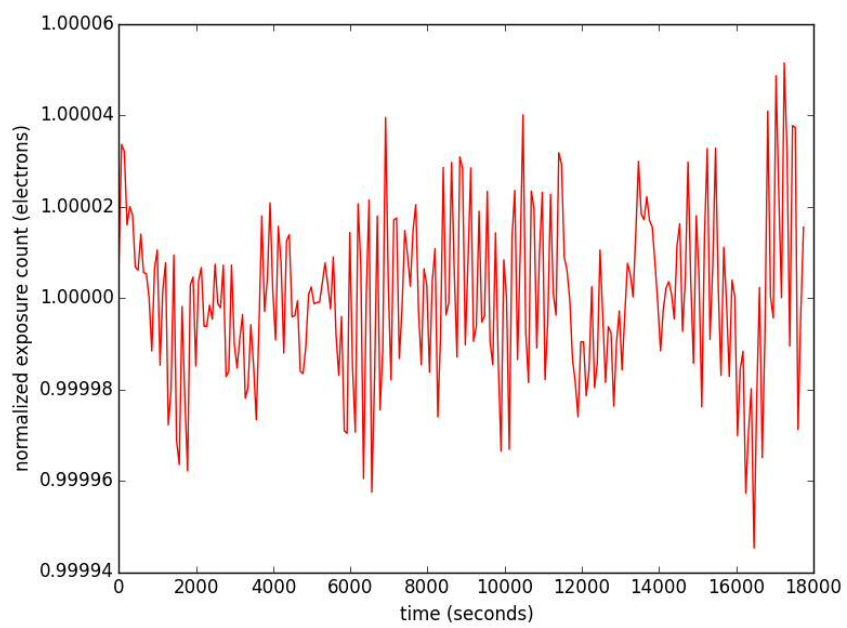


FIGURE 5.2 Timeline of proportional variations in the signal (per exposure) of GJ 1214 due to stellar convection in the  $2.013 \mu\text{m}$  spectral bin in AIRS Ch0.

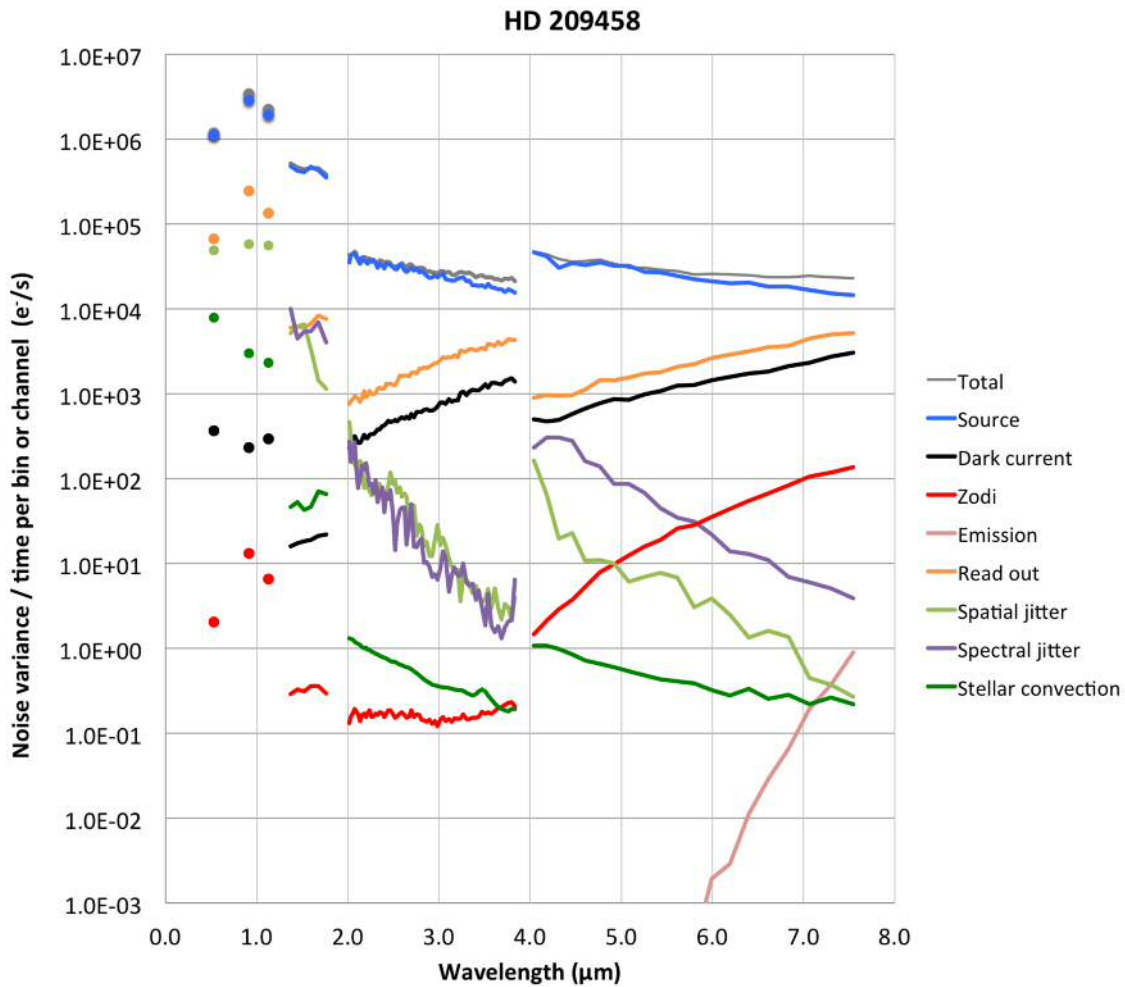


FIGURE 5.3 Stellar convection noise contribution for OOT observation of HD 209458 shown in dark green, compared to overall noise budget.

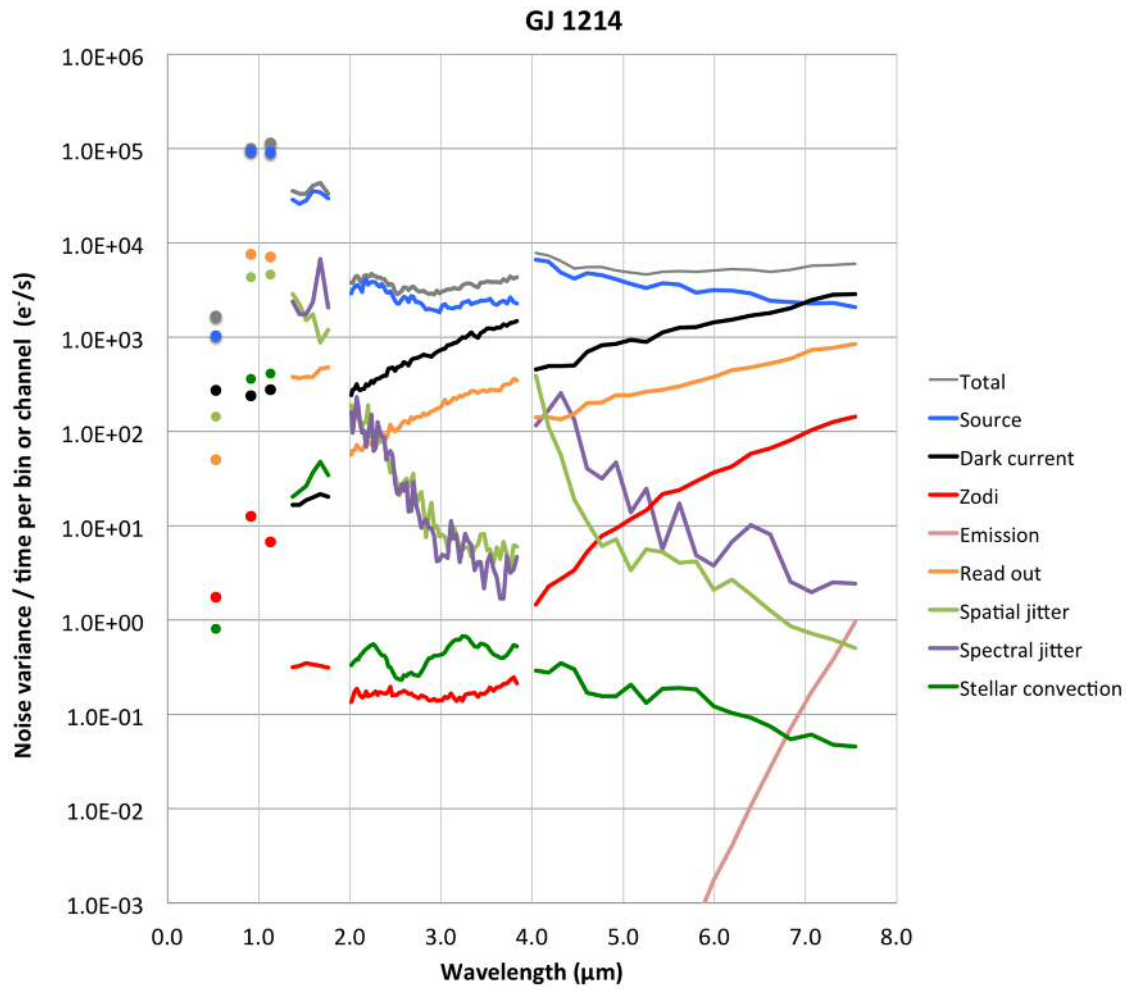


FIGURE 5.4 Stellar convection noise contribution for OOT observation of GJ 1214 shown in dark green, compared to overall noise budget.

TABLE 5.1 Stellar convection noise/signal as ppm (for a channel or spectral bin). Median values shown for spectroscopic channels. The signal is the mean count for a single exposure, and noise is the standard deviation of the signal resulting from stellar variation.

Channel	HD 209458	GJ 1214
AIRS Ch1	9.6	15.4
AIRS Ch0	9.8	24.5
NIRSpec	11.2	32.2
FGS 2	19.6	36.6
FGS 1	21.7	43.6
VisPhot	40.5	13.2

TABLE 5.2 Stellar convection noise variance as a percent of photon noise variance (for a channel or spectral bin). Median values shown for spectroscopic channels (to 3 significant figures).

Channel	HD 209458	GJ 1214
AIRS Ch1	0.00170	0.00381
AIRS Ch0	0.00176	0.0143
NIRSpec	0.0115	0.0978
FGS 2	0.120	0.449
FGS 1	0.104	0.380
VisPhot	0.708	0.0781

source photon noise variance. In these tables, the median values are shown for the spectroscopic channels.

### 5.1.3 ANALYSIS AND DISCUSSION

Firstly in AIRS Ch0, for both stellar targets studied, the noise contribution from stellar convection is extremely low, being only slightly higher than the zodiacal light noise contribution, and well below the source photon noise as well as read noise, dark current noise, and jitter noise. In AIRS Ch1, the noise is lower still, only emission noise being lower except at the red end, where it falls even below the emission noise. In NIRSpec, the stellar convection noise contribution is somewhat higher. For both sources, it exceeds the dark current noise but remains well below the source photon noise, read noise and jitter noise.

The contribution increases again in the visual photometric channels, where the stellar convection noise again exceeds the dark current noise, except for GJ

1214 in VisPhot where the stellar noise contribution falls below most other noise sources, showing a different behaviour to the G-type star in this particular channel (probably reflecting the Wein region of the stellar SED and the very long integration time used for this star in this channel).

The fractional stellar convection noise ranges from 43.6 ppm for GJ 1214 in FGS 1 down to 9.6 ppm for HD 209458 in AIRS Ch1 (Table 5.1). The M-dwarf star, GJ 1214, is a noisier target than the G-type HD 209458. The contribution to the overall noise, as noted, is small compared to other noise sources, Table 5.2 showing that the convection noise variance never reaches more than 1% of the photon noise variance in any channel.

Within the AIRS spectroscopic channels, the convection noise increases at shorter wavelengths, although the gradient is not as clear in GJ 1214 in Ch0. The peak contributions occur in the visual photometric channels, with the exception of GJ 1214 in VisPhot as for the reasons noted above.

Overall we can conclude that this source of stellar variability is not a significant issue for the ARIEL mission, with the noise falling below the precision of the instrument arising from other noise sources, and decorrelation is neither required nor easy to do given the signature of the variability would be hidden within the photon noise. These findings confirm the overall assumption made by Micela (2015) that granulation and pulsations should not be an issue for a smaller-sized exoplanet telescope; the assumption was made for the 1.5 m EChO telescope but would equally apply to ARIEL.

This does not rule out convection noise becoming an issue for higher precision observatories, especially in the NIR and visual regions. This methodology could be applied to examine the stellar convection noise contributions to future JWST or E-ELT transit spectroscopy observations.

## 5.2 STAR SPOTS

### 5.2.1 BACKGROUND

Star spots and their effects on exoplanet measurements are a major issue in transit spectroscopy and photometry, as well as radial velocity studies. Star spots (like sunspots) are features on the stellar surface caused by magnetic activity that are cooler and darker than the surrounding photosphere. Spots are one of a variety of phenomena associated with stellar magnetic fields that include flares, coronal mass ejections, faculae, plagues, as well as UV and X radiation (Berdyugina,

2005). Younger, rapidly rotating stars will have more powerful dynamos and therefore manifest more magnetic features; also cooler stars with prominent convection zones (such as M-dwarfs) are usually more magnetically active.

Plages and faculae are associated features on the chromosphere and photosphere respectively of stars. They are both closely associated with star spots, but appear brighter than the photosphere. For this discussion, 'plages' and 'faculae' are considered synonymous as both terms are used in the literature to describe bright regions on the stellar surface. Both spots and faculae are thought to be concentrations of magnetic flux tubes that inhibit local convection. The brightness of individual flux tubes is an inverse function of their size, with faculae having the smallest tubes compared to spots with the largest (Solanki, 1999). The proportion of the stellar disk covered with spots is termed the 'filling factor' and is related to but not exactly the same as the hemispheric 'spot coverage', which is the proportion of the stellar surface area covered with spots.

The variations in stellar flux seen in main sequence dwarfs over the time period of days to weeks are thought to be primarily due to rotation of the star with a population of spots changing the filling factor as a function of time. The observed flux variations may allow for changes in the filling factor to be followed, but a baseline filling factor may also exist at the peak of the flux. Longer term variations due to changing magnetic activity are likely as well, as evident in the solar cycle. This variability is one of several issues posed by spots that can affect transit photometric and spectroscopic observations, as discussed below. To potentially simulate the effect of spots, we need to have a sense of the likely filling factors that exist.

Techniques for studying the filling factors and temperatures of star spots include light curve modeling, Doppler surface imaging, molecular line modeling (in particular TiO) and line depth ratios (Berdyugina, 2005). Andersen & Korhonen (2015) list a sample of main-sequence stars ranging from G2V to M4V with measured spot temperatures and filling factors using a variety of methods. The following values are from that paper. The filling factor for the Sun varies from 0.03-0.3%, which is lower than any other star in the sample. Among the two other G2V stars in their sample, filling factors vary between 6 and 40% for EK Dra depending on the method used, and a filling factor of 13% is given for HD 307938. Among K-type stars the range of filling factors is 5 to 45%, and from 1 to 60% for M-type stars. Thus a wide range of filling factors have been reported, which are sensitive to the method used. It may be difficult therefore to define a 'typical' filling factor for any given star type, although in general they appear higher for M-type stars.

Sunspots are known to consist of darker and cooler central regions called the ‘umbra’ with a surrounding lighter and warmer ‘penumbra’, however reported stellar filling factors consider only the total spot area. In the Sun, the ratio of the penumbra to umbra area is about 5.5 on average when examining the data in Hathaway (2013).

The ratio of faculae to spot area, the ‘Q’ ratio, has been well studied in the Sun where the ratio can be as high as 16 (Chapman et al., 2001) but varies inversely with the proportion of sunspots (Chapman et al., 1997). Like spots, faculae have the potential to cause stellar flux variations, however a lot less is known about faculae in other stars than spots. In the Sun, the brightness contrast of faculae with the photosphere is complex having a dependency on the radial position, appearing brighter towards the limb where the projection is also smallest. Per Lanza et al. (2007),  $I_f(\lambda, \mu) = I_0(\lambda)[1 + c_f(\lambda)(1 - \mu)]$ , where  $I_f(\lambda, \mu)$  is the intensity at the cosine of the limb angle ( $\mu$ ),  $I_0(\lambda)$  is the intensity at the centre of the disc, and  $c_f(\lambda)$  is a contrast coefficient. Together with the fact that the temperature contrast is lower than for spots, this has led some authors to suggest they do not give significant contribution to stellar variability, e.g. Micela (2015). On the other hand, Shapiro et al. (2014) note that the Sun and other low magnetic activity stars become brighter with increased activity, whereas more magnetically active stars become dimmer. Modeling this behaviour, they conclude that the contribution to stellar variability by spots increases faster with magnetic activity than the facular contribution, causing a transition from faculae-dominated to spot-dominated variability with increased magnetic activity. This is consistent with the inverse relationship between Q and sunspot area found by Chapman et al. (1997), and the findings of Foukal (1998) that the area coverage by sunspots increases more rapidly with chromospheric activity (proxied by emission in the CaII H and K lines) than the coverage by faculae<sup>2</sup>. These findings suggest faculae could be an important factor in variability in less active stars, and should be considered in simulations.

### 5.2.2 IMPACT ON TRANSIT SPECTROSCOPY

Star spots can affect transit spectroscopy observations in a number of ways, and both occulted and unocculted spots will have their own specific effects.

<sup>2</sup> Chapman et al. (1997) observed solar faculae with the Ca II K line (393.4 nm) filter obtaining larger ratio numbers than the white-light faculae measurements by Foukal (1998).

**Spurious spectral features** Spots have their own spectrum distinct from that of the unspotted photosphere, with the overall stellar spectrum being a weighted sum of the spectrum of the unspotted photosphere and the spectrum of the spots. The larger the overall spot area and the greater the temperature contrast, the higher the 'contamination' of the stellar spectrum by the spots will be. Spots being cooler will tend to have a spectral peak at slightly longer wavelengths, and thus the proportional contribution of the spots will have a wavelength dependence. The spectrum of the spot may contain absorption features that do not appear in the unspotted spectrum, e.g. water absorption features have been found in the spectra of sunspots (Wallace et al., 1995). When a planet transits the star (assuming negligible spot occultation) the spot spectrum will tend to contribute more to the overall stellar brightness spectrum during the transit than before. Any spectral features due to spots will tend to be enhanced during the transit, leading to possible contamination and misinterpretation of the final transmission spectrum. Conversely, occulted spots could cause the feature to appear in emission, reducing the strength of actual planet features. Deming et al. (2013) estimated these effects for HD 209458b observed with the HST WFC3 IR, assuming spots with water features, and concluded the effects would not be significant at the precision of the instrument. On the other hand, Barstow et al. (2015a) examined the effect of 10% filling factor on M-dwarf and 3% filling factor on G-type stars on simulated observations by JWST, using the spectral retrievals method, finding that for high SNR targets such as a hot Neptune-M-dwarf combination, the water abundance was overestimated by up to an order of magnitude.

**Biasing the contrast ratio** Unocculted and occulted spots can bias the measured contrast ratio in opposite directions. In the case of unocculted spots, the contrast ratio will tend to be overestimated, since the spots will reduce the baseline brightness of the star, causing a proportionally larger transit depth by the planet as it crosses the unspotted regions of the star (Figure 5.5) or a proportionally larger flux ratio in secondary eclipse. Occultation of the spots in primary transit will manifest as an upward 'bump' on the light curve, which can cause a bias on curve fitting resulting in a smaller contrast ratio (Figure 5.5). Faculae in principle will have the opposite effects reducing the contrast ratio when not occulted, and increasing it when occulted with a downward bump in the transit light curve.

For the case of unocculted spots, the change in the contrast ratio can be estimated using black body functions (or model stellar spectra) to represent the star and spot spectra. If the contrast ratio in primary transit without spots is  $CR_1(\lambda) =$

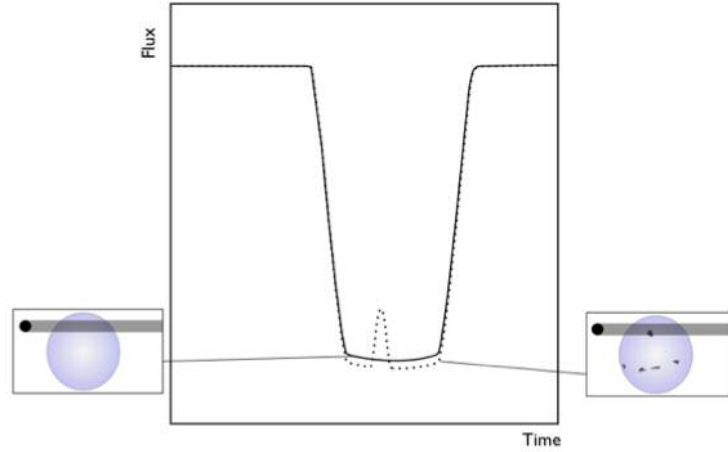


FIGURE 5.5 Effects of occulted and unocculted spots on the transit depth. Figure from Pont et al. (2013).

$(R_p/R_s)^2(\lambda)$ , then the contrast ratio in the presence of unocculted spots with a filling factor,  $s$ ,  $CR_2$  is given by:

$$CR_2(\lambda) = \left(\frac{R_p}{R_s}\right)^2(\lambda) \left[ \frac{B_\lambda(T_{star})}{(1-s)B_\lambda(T_{star}) + sB_\lambda(T_{spot})} \right] \quad (5.1)$$

where  $B_\lambda(T_{star})$  is the surface brightness of the unspotted stellar photosphere at temperature  $T_{star}$ , and  $B_\lambda(T_{spot})$  is the surface brightness of the spotted photosphere at temperature  $T_{spot}$ . The second term on the RHS therefore gives the ratio of the brightness of the unspotted star to the spotted star. If we call this term  $\alpha(\lambda)$ , the apparent increase in  $R_p(\lambda)$ , assuming no change in  $R_s(\lambda)$  is  $\sqrt{\alpha(\lambda)} - 1$ . This is a similar formalism to that seen in many papers including Pont et al. (2013) and Zellem et al. (2017). The same factor  $\alpha$  will modify secondary eclipse transit depths modulating the planet star flux ratio ( $F_p/F_s$ ) rather than the area ratio.

To estimate the transit depth decrease due to spot occultation the numerator in  $\alpha(\lambda)$  can be changed to  $(1 - s_i)B_\lambda(T_{star}) + s_iB_\lambda(T_{spot})$ , where  $s_i$  is the filling factor of the occulted region.  $s_i$  will change with time within the transit, as the planet transit chord passes over randomly distributed spots of different sizes. It will also vary unpredictably between visits for the same reason.

For a perfectly homogeneously spotted star,  $s_i$  will equal the filling factor of the unocculted region, with the two opposing biases cancelling out any changes to the contrast ratio. This is unlikely in any single real case, but may be approached if a large number of observations were performed and combined (assuming the spots

do not cluster to preferred latitudes or locations). Due to the random nature of  $s_i$ , it is far more difficult to estimate the impact on the transit depth due to occulted spots than unocculted spots in any single case. Spot occultations will not be an factor in secondary eclipse spectra.

Although it can be argued that if the occulted spot is visible on the light curve it can be decorrelated out of the data, and any spots not seen indicate that occulted spots did not impact the observation, as argued in Fraine et al. (2014) for the study of HAT-P-11b<sup>3</sup>. This does not rule out the effect of unobserved occulted spots. The effects of many small occulted spots may not be so obvious as to have a visual impact, and yet may still have a significant cumulative effect on the transit depth.

The bias due to both occulted and unocculted spots on the contrast ratio is wavelength-dependent, and thus both have the potential to distort the final transmission spectrum. Both types of bias are stronger towards shorter wavelengths as the spot-star contrast increases. Occulted spot features will be more pronounced at shorter wavelengths. Fraine et al. (2014) found that spot features were obvious in the visible range Kepler light curve, somewhat observable at 3.6  $\mu\text{m}$  in the simultaneously measured Spitzer light curve, but not at all at 4.5  $\mu\text{m}$ . Coupled with the fact that the fraction photon noise<sup>4</sup> increases with wavelength, the effects of spots will be more obvious in the visible than in the infrared.

The impact of faculae on the transmission spectrum has been less well studied. Oshagh et al. (2014) examined the impact of spots and plages on transmission spectra using the code SOAP-T which simulates light curves of planets transiting spots or faculae. 20 cases of Neptune- or Jupiter-sized planets transiting M- or G-type stars with various spot or plage filling factors were simulated. They found that plage crossings could deviate the spectrum by upto 10% mimicking the Rayleigh scattering slopes of HD 189733b and GJ 3470b. However there were some major limitations of this study. Firstly, no Monte Carlo approach taken, so that it is possible that the relationships found will vary with random placement of the spots or faculae. The same plage may have more or less impact on a repeated realization. Secondly, only 10 spots are simulated in SOAP-T, which may be unrealistic and will not take into account the expected size distribution. Simulations

---

<sup>3</sup> HAT-P-11b is in a highly inclined orbit (almost polar) relative to the spin of its star, i.e. high stellar obliquity. This unusual configuration allows star spot anomalies identified on transit light curves to map the active latitudes on the stellar surface, e.g. Sanchis-Ojeda & Winn (2011) and Deming et al. (2011).

<sup>4</sup> The fraction photon noise is the absolute photon noise divided by the signal.

also appear to consider plage and spot effects separately, which again is not realistic especially for plages, which are usually associated with spots. Finally, very small filling factors are used (1% or less for spots, < 6.25% for plages) which again may not be realistic for active stars.

**Variability** As well as these static effects at fixed filling factors, variations due to rotation and changes in activity can cause changes in the filling factor between epochs. This has the potential to generate different stellar spectra at different times depending on the degree of spot contamination. If the filling factor increases between observations, then the star will appear dimmer, and the planet radius measurements become larger (if the effects of unocculted spots alone are considered<sup>5</sup>). The integrated stellar spectrum will also change as the spot contribution increases changing the wavelength-dependency of the distortion in the contrast ratio spectrum as per Equation 5.1.

The variations in flux caused by this effect are typically of the order of a few percent in active stars in the visible range. For example, for HD 189733, considered a highly active K dwarf, Pont et al. (2013) noted a 1-2% reduction in the visible range flux, which is comparable to the planet transit. A 1% peak-to-peak variation has been noted in the visible range for GJ 1214 (Berta et al., 2011) which was estimated to produce a 100 ppm change in the visible range contrast ratio attributable to spots. Thus for more active stars, it may be important to attempt to calibrate for changes in filling factor when combining or comparing results across epochs, especially if there is clear evidence that spot effects are present, such as changes in the white light transit depths between epochs. In some cases, the effects of variability were assessed to be not significant. For example, Kreidberg et al. (2014a) observing GJ 1214b found consistent transit depths over all epochs, which they took to indicate that no significant variability had occurred.

**Corrections for unocculted spots** A number of correction methods have been proposed. These compensate for changes in filling factor between observations, attempting to reverse the distortion in the contrast ratio spectrum due to unocculted spots to the level expected for a spot-free star. These rely on the reasonable assumption that the spot patterns do not change significantly during the course of a transit. Typically the flux is monitored in the visible range where variations are strongest. For any single observation, the fractional change in flux,  $\Delta f(\lambda)$  from the

<sup>5</sup> The situation is more complicated than this since the probability of spot occultation will also increase countering this effect.

unspotted star is estimated through models or inferences from data (since the peak flux may still have a baseline level of spots). Then:

$$\Delta f(\lambda) = s \left( 1 - \frac{B_\lambda(T_{spot})}{B_\lambda(T_{star})} \right) \quad (5.2)$$

where  $s$  is the filling factor.  $\Delta f$  is related to  $\alpha(\lambda)$  through  $\Delta f = 1 - 1/\alpha(\lambda)$ . Thus at the measured wavelength, the correction can be applied through the estimation of  $\Delta f(\lambda)$  from measurements, without recourse to measuring the filling factor or spot temperature directly. However when extrapolating to other wavelengths, e.g the infrared, a spectrum model is needed (e.g. Planck function as below) for both the star and spots, and thus an estimate of the star and spot temperatures is needed. This forms the basis of the formalism used by Sing et al. (2011) and Berta et al. (2011) to correct the spectrum at all wavelengths, including infrared wavelengths, based on the flux variations in the visible.

$$\frac{\Delta d}{d} = \Delta f(\lambda_0, t) \left( 1 - \frac{B_\lambda(T_{spot})}{B_\lambda(T_{star})} \right) \bigg/ \left( 1 - \frac{B_{\lambda_0}(T_{spot})}{B_{\lambda_0}(T_{star})} \right) \quad (5.3)$$

where  $\frac{\Delta d}{d} = (CR_2 - CR_1)/CR_2$  at wavelength  $\lambda$ .  $\Delta d/d = 1 - 1/\alpha$ , where  $1/\alpha$  is the correction factor that needs to be applied to the measured contrast ratio,  $CR_2$ . The spot temperature in some cases, e.g. Sing et al. (2011) is found through fitting of models to the shape and wavelength-dependency of occulted spot features.

Variations in flux in the infrared will be much smaller than in the visible range. For example, Knutson et al. (2007) found for HD 189773, a  $\pm 1.5\%$  variation in the visible range over its 13.4 day rotation period translated to a linear increase in flux of about  $\pm 0.1\%$  at  $8\ \mu\text{m}$  over the 33 hour phase curve observation of that planet. From the 1% peak-to-peak variation in GJ 1214 in the visual range, Berta et al. (2011) calculated a contrast ratio variation of 40 and 30 ppm in the Spitzer 3.6 and  $4.5\ \mu\text{m}$  pass bands compared to 100 ppm in the visible. It may be the case that the photometric variation returns a contrast ratio variation due to spots that will be smaller than the precision of the data. For example, Kreidberg et al. (2015) observing WASP 12b with the HST WFC3, using the above formalism and assuming a 0.3% variability in flux caused by spots, found a change in the contrast ratio of 10 ppm which was below the precision in the final spectrum which averages to 51 ppm.

Micela (2015) describes another method for correcting variations in stellar

spectra in different epochs due to varying spot contribution. The visible part of the spectrum is projected into space defined by principal components computed from a grid of spectra. This identifies the spot temperature and filling factor of the observed spectrum and using the related spotless spectrum applies a correction to the complete wavelength range including the infrared.

All the above methods will tend to calibrate the observed stellar spectrum to the 'quiet' star level. If however this calibration is inaccurate and the baseline is not truly spot-free, a wavelength-dependent bias could remain that could manifest as a slope mimicking, for example, Rayleigh scattering. This has been suggested by McCullough et al. (2014) as a possible explanation for the slope seen in the visible and NIR spectrum of HD 189773b, originally explained through Rayleigh scattering caused by hydrogen molecules. They suggest that unocculted star spots could explain most of the slope seen.

**Corrections for occulted spots** If the occulted spot is large and the effect clearly observable on the light curve, its effect may be removed from the data. The simplest method would be to omit the light curve points that shown the spot feature, e.g. Sing et al. (2011)<sup>6</sup>. If the luxury of many transits are available, simply excluding those that show spot crossings is another option, e.g. 2 transits excluded from the 'deep field' observation of GJ 1214b by Kreidberg et al. (2014a).

However, as noted above, it may be the case that the occulted spots are not visibly detectable and yet have a cumulative impact on the measurement. Detecting this effect, and correcting for it is highly challenging.

Pont et al. (2013) observing HD 189773b, attempted to correct for both occulted and unocculted spots in the infrared Spitzer IRAC 8  $\mu\text{m}$  band (where spot crossings were not visible) based on flux variations in the visible range, where spots were obvious. They considered the limiting case of the filling factor of the occulted region equaling the filling factor of the unocculted region, i.e. the bias cancelling out. However, an added statistical uncertainty in the transit depth is introduced due to the stochastic nature of the occulted spot effect. This is estimated in the visual range by taking the standard deviation of the residuals of the light curves showing effects of spot crossings, and scaling to the infrared, from which they calculate an additional uncertainty of 0.3% on the transit depth<sup>7</sup>.

<sup>6</sup> Since occulted and unocculted spots bias the measured transit depth in different directions, the removal of occulted spot features from the light curve could actually result in an increased bias from the unocculted spots which is now unopposed. An ideal approach therefore needs to correct for both the occulted and unocculted spot effects.

<sup>7</sup> Two additional methods mentioned in the paper gave a similar uncertainty.

### 5.2.3 STAR SPOT STUDY WITH EXOSIM

We can see that the overall effect on a primary transit spectrum due to spots is quite complex involving a wavelength-dependent bias and variations in this between epochs caused by variations in the unocculted spot background and the random occurrence of spot crossings. For any single transit, many factors contribute to the overall effect on the final transit depth at any wavelength, including the relative temperatures of the star and spots, the sizes and distribution of the spots, the spot filling factor, and the relative effects of unocculted and occulted spots. There is also the question of faculae, which the above corrections mostly ignore, but which may have a significant opposing effect to spots.

Analytical approaches that can account for all these effects are limited. Overall a great deal of uncertainty still exists in the field regarding the impact of spots on transmission spectra. This opens up the opportunity to use ExoSim to investigate this issue.

Therefore in the context of evaluating the effect of stellar variability and activity for the ARIEL mission, I perform a study to examine the raw, uncorrected effects of spots, with and without faculae, directly on the transmission spectrum. The study will elucidate in each transit simulation, the bias on the transmission spectrum due to the combined effects of occulted and unocculted spots. A Monte Carlo approach is adopted, as in Chapter 3, so that with repeated realizations, where the spot crossings are randomized together with a filling factor variation, we will obtain the distribution of transit depths at any wavelength. This gives a direct measure of the uncertainty in the transmission spectrum due to spots.

I focus only on the effects on wavelength-dependent bias and uncertainty in the transit depth, and not on effects of enhancement or diminution of spectral features, which could be the focus of a future study. The results can be used to quantify the problem at hand for ARIEL. Under what circumstances do spots pose a problem requiring correction methods, and under what circumstances can they safely be ignored? This may in turn depend on the underlying instrument precision. Therefore a comparison is required with the equivalent uncertainty due to photon noise from the source obtained through the same Monte Carlo method.

I focus again on the same two targets studied for stellar convection noise: GJ 1214 and HD 209458, this time modeled in primary transit by their planets (GJ 1214b and HD 209458b). The filling factor for GJ 1214 is unknown, but a value of 10% has been used in simulations by Barstow et al. (2015a). de Mooij et al. (2012) estimated a filling factor variation of 2.5% based on the variability of the

star but indicate that the baseline filling factor is likely to be much larger. Filling factors between 2.5-10% could thus be considered representative for this star. HD 209458 is not thought to be a highly active star. Deming et al. (2013) consider the Sun a good analogue with a maximum filling factor of 0.3%. Although these are reasonable estimates for the filling factors of these stars, a range of filling factors will be simulated to explore more generally the effects of activity on the planet spectrum.

A dedicated star spot model which allows the simulation of both spots and faculae will be used in conjunction with ExoSim. The combination of using a time domain simulation of transit spectroscopy modulated by star spots and faculae, integrated with an instrument model, and elucidating the combined effects of occulted and unocculted spots directly on the transmission spectrum through Monte Carlo simulations, is a novel approach in this field.

#### 5.2.3.1 SPOTSIM

A star spot model, 'SpotSim', was developed<sup>8</sup>. The features of the original model are described below, followed by a description of the modifications performed by myself for this study.

SpotSim models the visible disk of a star with spots and faculae within a 2-D array, producing a pixelised image (Figure 5.6). It then simulates the transit of a planet along a chord on the stellar disk in small steps generating a transit light curve numerically. The light curve will thus reflect the increased transit depth due to unocculted spots, and also the upward bumps due to spot occultations. Downward bumps are generated when faculae are crossed. The model can simulate different star classes, with spots and faculae of different sizes, temperatures and spatial distributions. Spots are modeled as perfect discs with a projection effect, and are assumed to have uniform brightness, with no distinction made between umbra and penumbra. Faculae are modeled as regions encircling the spots following the model by Herrero et al. (2015). This allows for a fixed area ratio ( $Q$ ) between faculae and spot areas which is realistic, although in reality faculae do not usually encircle the spots in a regular fashion. The quiet star, spot and faculae are assigned a temperature each. Using black body functions, at the simulated wavelength, the relevant spectral brightness is applied to each pixel in the simulated disk according to whether it represents the quiet star, spot or faculae. Limb darkening is then

---

<sup>8</sup> The original version was part of a 4th year undergraduate project by L. Johnson, actively supervised by myself and E. Pascale, with later code optimization by A. Papageorgiou. Projection effects for the spots and faculae were added by myself to the model.

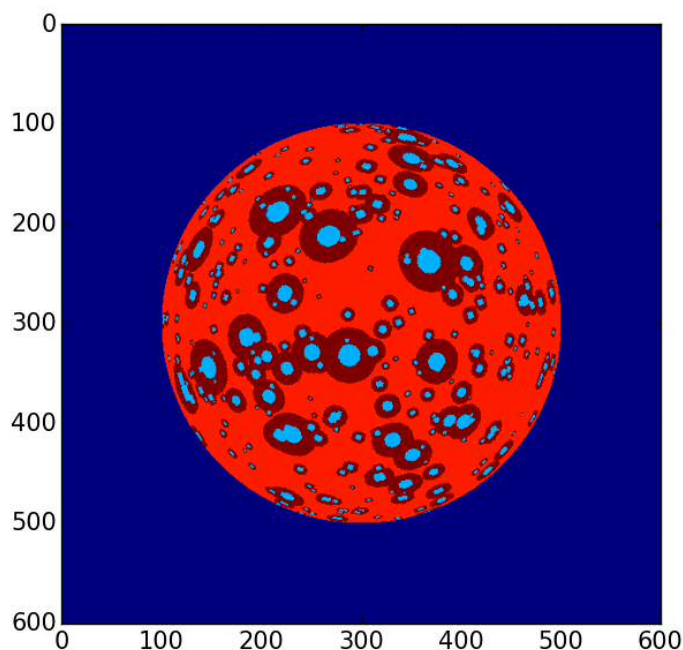


FIGURE 5.6 SpotSim: the dedicated ExoSim star spot simulator. Example of a star with 10% spot coverage. Cold spots are shown in light blue. Hot faculae are in brown surrounding each spot. The temperature contrast with the photosphere is higher for spots than faculae.

applied across the star using a quadratic limb darkening law. The planet transit is then simulated by moving a circular aperture (whose radius in proportion to that of the model stellar disc is  $R_p/R_s$ ) across the transit chord in small steps<sup>9</sup>. At each step, the sum in the aperture is subtracted from the total image sum generating the light curve. For different wavelengths the process is repeated with new brightness values for the star, spots and faculae, generating different light curves. Also the planet radius may change with wavelength in accordance with the transmission spectrum, as may the limb darkening. For each spotted light curve an equivalent unspotted light curve is also generated in the same way using an unspotted star disc. The level of pixelation in the model can be varied, although higher resolutions will considerably slow the simulation. To reduce the errors due to pixelation the ratio of the spotted to unspotted light curves is used to generate a correction factor which is then applied to the equivalent analytic Mandel-Agol light curve, modifying it for the effects of spots.

<sup>9</sup> The Python package Photutils is utilized for this purpose.

### 5.2.3.2 SPOTSIM MODIFICATIONS

A number of modifications to SpotSim were implemented for this study, not only for incorporation with ExoSim, but also to permit more computationally efficient light curve generation for the purposes of Monte Carlo simulations. In addition a number of new methods were added to calculate key parameters for the model.

The main reasons for integrating SpotSim with ExoSim were to allow ExoSim parameters to directly act as inputs to the spot model, and for the spot model to generate specific light curves for the ExoSim instrument model, forming a prototype 'stellar variability' module. This way the impact of spots for specific targets with a specific instrument can be evaluated. Although in this test we will separate out the effects of spots from other noise as means of evaluating the spot contribution in isolation, integrating the spot model allows future use of this set up where 'spot noise' can be modeled in combination with other noise sources in ExoSim and the total effects on the spectrum evaluated. This could be used for example to test the efficacy of spot noise correction methods in the 'realistic' setting of all other noise sources.

**Generation of the light curves** This was modified so that the transit of the planet needed be simulated just once for multiple wavelengths (rather than repeating the passage of the aperture each time for each wavelength). This modification greatly reduces the simulation time for channels with many pixel columns such as AIRS Ch0, each of which would need its own light curve.

The circular aperture method was used as before to produce light curves, but this time separate image matrices were used for the star only (a spotless star matrix with spot and faculae areas subtracted), spots only and faculae only, generating a single individual light curve for each. This method depends on there being a fixed planet radius across all wavelengths (i.e. a flat contrast ratio), which is fine for the purposes of this study, where we are interested in the bias and uncertainties produced at each wavelength rather than the effects on specific spectral features.

These three light curves are then multiplied by the relevant Planck brightness over the range of wavelengths needed, generating (in a single step) for each case, a 2-D array of wavelength-dependent light curves. These three arrays are then summed together to give the light curve array for the star including both spots and faculae. If a simulation with spots only is required, then the faculae light curves are omitted in the above process (and the star-only light curves are

generated from the star matrix with only the spots subtracted). The above process is repeated for the unspotted star case, with a single numerical transit of the stellar disc (this time with no areas subtracted for the spots and faculae) and then generating the array of wavelength-dependent light curves as before.

Finally limb darkening can be applied at each wavelength by obtaining the ratio of the analytic Mandel-Agol light curve with limb darkening, to the analytic light curve with no limb darkening, and applying this as a correction to the final light curves from both the spotted and unspotted cases.

I tested the light curves generated using this modified version against the original and found excellent agreement, but this newer method allows for the rapid production of wavelength-dependent light curves essential for the Monte Carlo approach in this study.

**Size and spatial distribution of spots** The original SpotSim code had no clear method for the size distribution of the spots. I added a function to allocate a realistic size distribution of spots, following the log-normal relationship of umbral areas on the Sun, first proposed by Bogdan et al. (1988):

$$\frac{dN}{dA} = \left(\frac{dN}{dA}\right)_m \exp\left[-\frac{(\ln A - \ln \langle A \rangle)^2}{2 \ln \sigma_A}\right] \quad (5.4)$$

where  $N$  is the number of spots,  $A$  is the area of the spot umbral area,  $\langle A \rangle$  is the mean spot umbral area,  $\left(\frac{dN}{dA}\right)_m$  is the maximum of the distribution and  $\sigma_A$  is the standard deviation of the distribution.

I utilize the relationship between spot coverage and  $\sigma_A$  given in Solanki & Unruh (2004), where  $\sigma_A$  increases linearly with coverage, and use the same fixed  $\langle A \rangle$  as they used of 0.57 (similar to the average for the Sun). As  $\sigma_A$  increases, so the average spot umbral size also increases. The spot coverage<sup>10</sup> is a user-defined input for each simulation (e.g. 10%).

The code adjusts  $\left(\frac{dN}{dA}\right)_m$  until the overall area of spots (in the integrated solution), assuming a spot-umbra area ratio (SUR) of 6.5<sup>11</sup>, equals that for the target spot coverage. Having found the three parameters,  $\sigma_A$ ,  $\langle A \rangle$  and  $\left(\frac{dN}{dA}\right)_m$ , that define the log-normal distribution, the code integrates equation 5.4 to produce a histogram of number of spots versus area of spot umbral areas. The number of spots per area bin are then multiplied by scaling factor of 100, and rounded to the

<sup>10</sup> Note this is the 'hemispheric spot coverage' with umbral and penumbral areas together, and not the 'filling factor' as distinguished earlier.

<sup>11</sup> Based on the average penumbra:umbra ratio for Sun of about 5.5 from data in Hathaway (2013).

nearest non-zero integer. This produces a baseline distribution of spot umbral areas. The code then repeatedly samples this distribution, random uniformly, until the required spot coverage, assuming SUR of 6.5, is attained. Each umbral area is multiplied by the SUR to obtain the corresponding whole spot area. The final result is a set of spots with randomly distributed sizes per realization, that conforms to the log-normal distribution and the inputted spot coverage.

For the spatial distribution, I use a uniform random distribution over the surface assuming no prior knowledge of the spatial distribution on the star, but future simulations could cluster the spots to certain latitudes.

The ‘filling factor’ of the final spotted stellar disc, can be measured in the simulation by obtaining the ratio of the number of pixels allocated to the spots to the number for the whole star. The same can be performed for the faculae to obtain a faculae filling factor. Due to the projection effect, the filling factor may be expected to be approximately  $\cos(\pi/4) \times$  the spot coverage. Final results are in fact close to this expectation (Table 5.3). For the final analysis, I utilize the measured filling factors rather than the input spot coverage as this gives a better basis for comparison with observed targets where filling factors are typically measured.

**Q ratio** The Q number, the ratio of faculae area to spot area, is probably not fixed but varies with the activity of the star as discussed above. Previous simulations by Herrero et al. (2015), and Lanza et al. (2003), have used Q factors of 7 and 10 respectively. Gondoin (2008) fitting models with different Q values to MOST light curves of 2 active young dwarfs,  $\epsilon$  Eri and  $\kappa$  Ceti, found that low Q values gave the best description. Overall, the Q factor appears to go down with increasing activity, i.e. with increasing spot coverage.

It therefore seems unlikely that a very active star with 50% spot coverage will have the same Q ratio as one with 1% coverage. As mentioned previously, in the Sun, Chapman et al. (1997) found a relationship between facular coverage and spot coverage that could be fitted by a second order polynomial (Figure 5.7).

If we use this polynomial to extrapolate to larger spot filling factors (for more active stars) a non-physical down turn occurs in the curve. I therefore re-sample the data points, using WebPlotDigitizer (Rohatgi, 2017), and fit a power law to the data:  $y = 82.97x^{0.772}$  (correlation coefficient of 0.95). This power law gives a Q factor of 14.7 at 0.2% spot coverage (Figure 5.8). At 20% this falls to 5.1. Although there will be an uncertainty in using this power law extrapolation, it allows the simulation to take into account varying contributions of faculae and spots depending on the activity level, proxied here by the spot coverage.

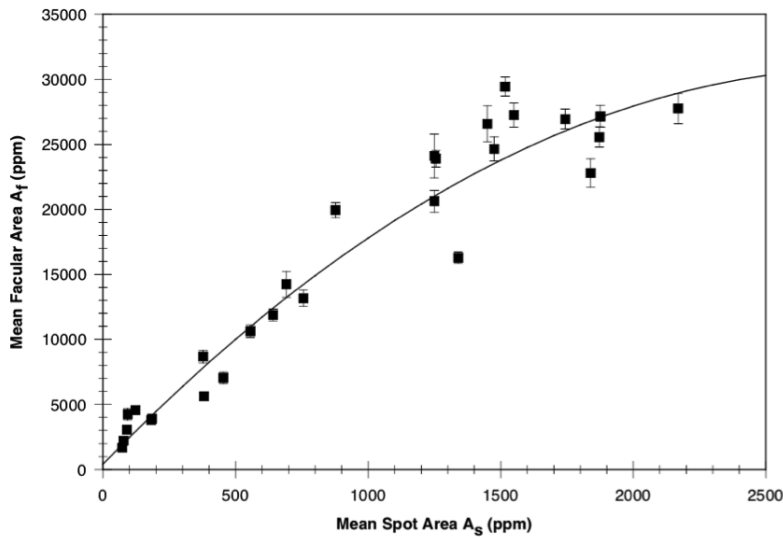


FIGURE 5.7 Mean facular area vs mean spot area for the Sun. Figure from Chapman et al. (1997).

It was found that due to a combination of pixelation effects at small spot sizes and faculae overlaps at large sizes, the final Q ratio on the actual images produced (the ratio of the number of facula to spot pixels), is somewhat lower than the input Q number (Table 5.3). Given the uncertainty in the actual Q values that would occur in reality, I elect to quote the directly measured Q values in the analysis, as they remain within the plausible range of Q values we might expect.

**Spot and faculae temperature** A positive relationship between star temperature and spot temperature contrast is shown in Andersen & Korhonen (2015) (Figure 5.9). The red dashed line, which better captures the temperature contrast of cooler stars, is sampled using WebPlotDigitizer (Rohatgi, 2017) and fits the polynomial relationship:  $y = 0.0001343x^2 - 0.6849x + 1180$ . Using this relationship GJ 1214 at 3026 K has a spot temperature contrast of -337 K (i.e. spots are 337 K cooler than the unspotted star). HD 209458 at 6075 K has a spot temperature contrast of -1976 K. These values for spot temperature contrast are used as inputs in these simulations.

How the facular temperature scales with photospheric temperature is not as well understood. For the Sun, Meunier et al. (2010) found that data best fitted a model with spot temperature of -663 K and a facular contrast temperature that varied with the cosine of the limb angle,  $\mu$ , according to the relationship  $190.9\mu^2 - 407.7\mu + 250.9$  K. The simulation currently cannot account for the variation in facula brightness and temperature with  $\mu$ , thus I find an average value for

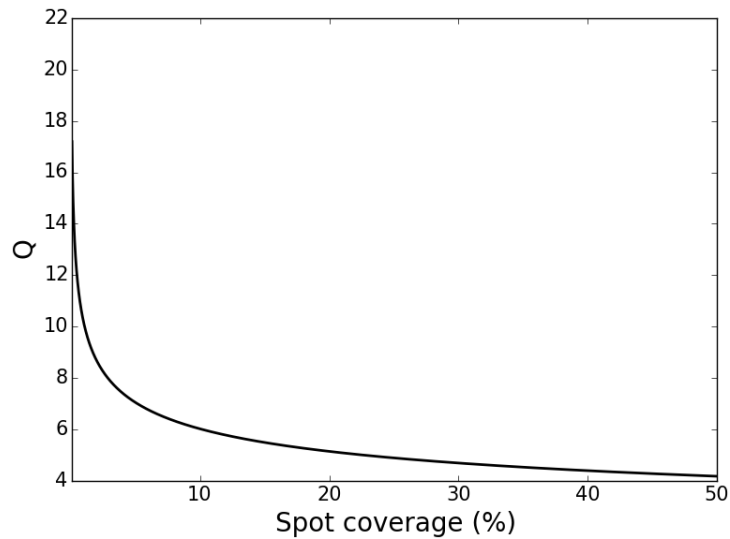


FIGURE 5.8 Power law Q factor prediction for different spot coverages.

the facula contrast temperature by transforming the relationship from  $\mu$  to the limb angle,  $\theta$ , and obtaining the mean contrast temperature over all angles, which gives +87.4 K. It might be reasonable to assume that since the spot temperature scales with the photosphere temperature, the faculae temperature may also do so, and by the same proportion. Thus I use the ratio of the solar faculae to spot temperature contrast (87.4/663), to obtain faculae temperatures for these simulations by multiplying the spot temperature contrast by this factor. For HD 209458 this gives a facular temperature contrast of +260 K and for GJ 1214b, +44 K.

The faculae portion of these simulations is therefore somewhat less accurate and more speculative than the spots, given the Q factor extrapolation and uncertainty about temperature behaviour, as well as not taking into account the limb angle-brightness relationship. Also it is true to say that faculae would not usually not appear completely encircling spots, thus the profile of the occultation on the transit light curve may be less accurately represented. Nevertheless, they may give a first order indication of how the facular content modifies the effects due to cold spots alone.

Therefore, I ran simulations with and without faculae content. The latter case (i.e.  $Q = 0$ ) may be particularly reasonable for active stars such as GJ 1214, but perhaps less so for HD 209458b, which if it behaves like the Sun would have a substantial Q ratio.

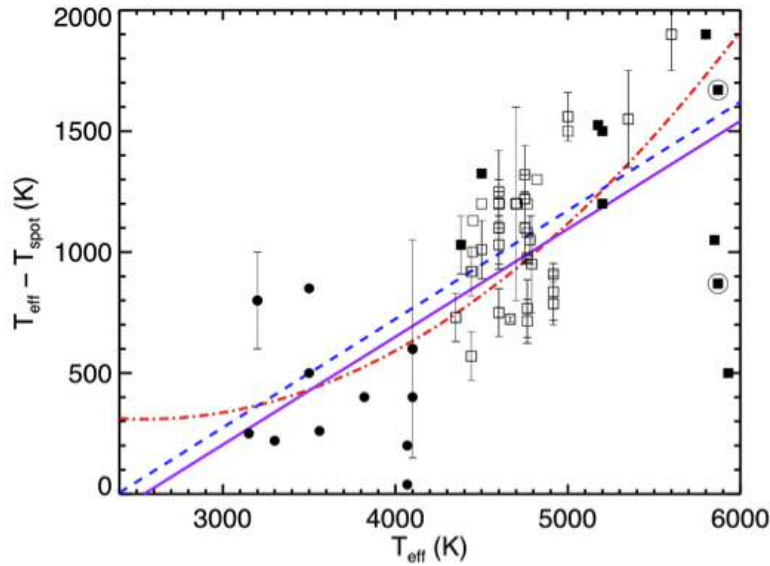


FIGURE 5.9 Spot temperature contrast vs star temperature. Figure from Andersen & Korhonen (2015). I adopt the polynomial relationship of the red dashed line for these simulations.

### 5.2.3.3 EXOSIM MODIFICATIONS

SpotSim is called within the *Timeline* module, and the star and planet parameters fed into SpotSim, which then returns light curve corrections for each wavelength to be applied to the corresponding ExoSim analytic Mandel-Agol light curves. A separate light curve correction is therefore generated for each pixel column for the spectroscopic channels (each with a different wavelength), and a single light curve correction is generated for the photometric channels (with a single wavelength).

To allow the effects of spot and faculae crossings occurring within the integration time of an exposure to be accounted for, the generation of light curves in ExoSim is changed as follows. The timegrid resolution is made much higher and based on the frame time of the simulation, not on the time stamps of the subexposures<sup>12</sup>. Once the SpotSim corrections are applied to these high resolution light curves, each light curve is reformed from the average value within each subexposure period. This gives an ‘integrated’ light curve at the cadence of the subexposures which more accurately contains the effects of changes within the integration time. The new 2-D ‘integrated’ light curve array is then multiplied in the usual way in the *Noise* module into the array of subexposures.

<sup>12</sup> Since smaller star spots could modulate the light curve within the integration time it was thought this modification would result in a more accurate capture of spot effects.

The ExoSim light curves are generated in the *Timeline* module based on this new high resolution timegrid. However this would severely slow the SpotSim transit simulation if the  $z$  grid from ExoSim was directly used in SpotSim, since this would require a very high resolution for its 2-D array. An image size of  $601 \times 601$  pixels was used in SpotSim and found to give a reasonable balance between accuracy of light curve generation and speed to permit Monte Carlo simulations. Thus SpotSim was run on its own low resolution  $z$  grid (of 601 points), and its outputted light curve corrections, interpolated to the ExoSim high resolution  $z$  grid prior to modifying the ExoSim light curves.

Examples of the light curves generated by the SpotSim-ExoSim combination are shown in Figure 5.10, for GJ 1214b in AIRS Ch0, at two wavelengths, 2.1 and 3.8  $\mu\text{m}$ , for an instance of 10% spot coverage, with and without faculae. The 2.1  $\mu\text{m}$  curve has a lower transit depth overall (due to unocculted spots), and spot features in the light curve (upward 'bumps' due to occulted spots) have greater amplitude than at the longer wavelength (Figure 5.10 A and B). This demonstrates the known fact that spot effects (both for unocculted and occulted spots) are more pronounced at shorter wavelengths. When faculae are added in the simulation, the general effect is to oppose the spot effects, with the transit depths and the amplitudes of the in-transit features both reduced (Figure 5.10 C and D).

#### 5.2.4 METHODOLOGY

The method used here consists of the following steps with details described subsequently:

- 1) For a given star-planet combination, an ExoSim full transit spectroscopy simulation is performed with the final Phase A ARIEL model (from Chapter 4 Table 4.8), outputting FITS files for each channel. Flat input contrast ratios are used.
- 2) Within the ExoSim simulation, SpotSim is used to generate the effects of occulted and unocculted star spots and faculae, with the SpotSim input parameters obtained from ExoSim or from the aforementioned methods. A particular spot coverage is chosen. The ExoSim simulation suppresses all other noise sources.
- 3) The ExoSim FITS files undergo data reduction producing light curves per spectral bin or photometric channel that are then fitted with model light curves to extract the planet transmission spectrum.
- 4) Steps 1-3 are repeated 200 times, with the size and spatial distribution of the spots and faculae recalculated between realizations. This comprises the Monte Carlo simulation.

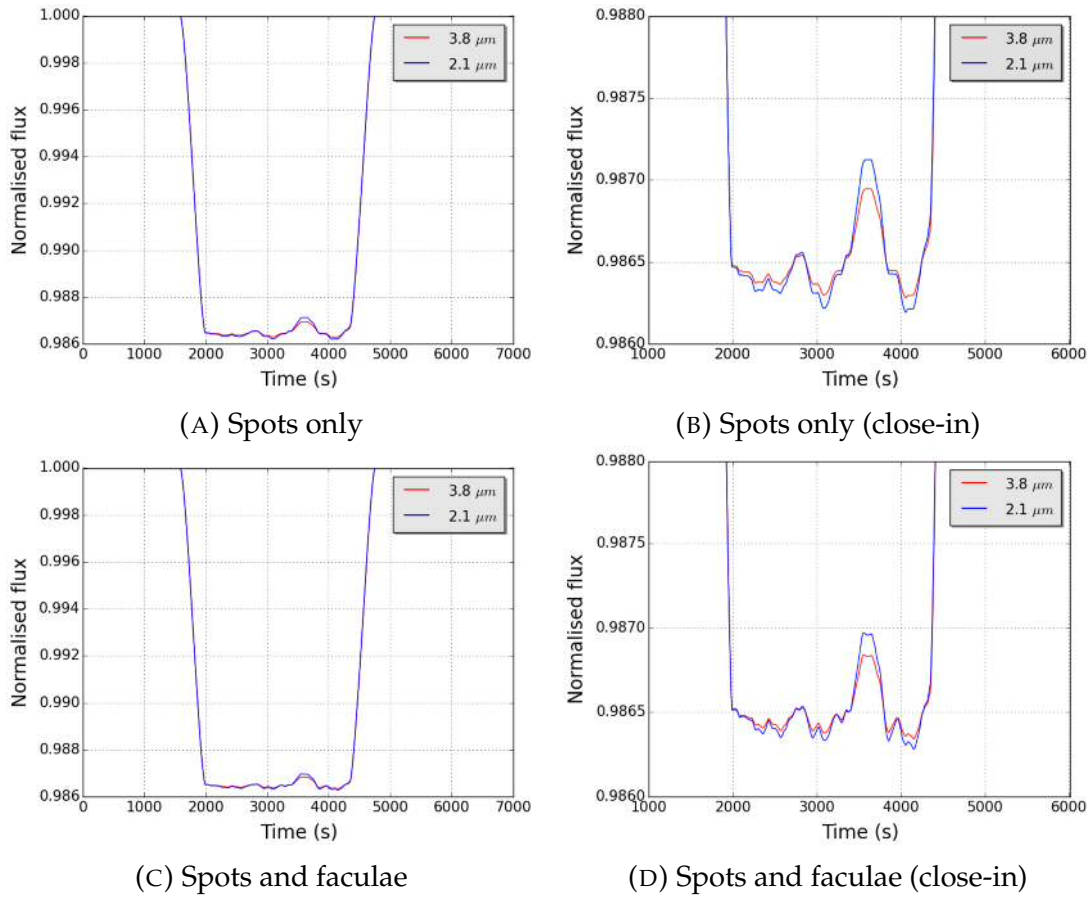


FIGURE 5.10 Example light curves from SpotSim-ExoSim showing the effects of spots and faculae. Blue curve: 2.1  $\mu\text{m}$ . Red curve: 3.8  $\mu\text{m}$ . A: Spots only. B: Spots only (close-in view). C: Spots and faculae. D: Spots and faculae (close-in view).

5) A distribution of transit depths is obtained per spectral bin from which the standard deviation gives a measure of the the uncertainty on the contrast ratio at each wavelength,  $\sigma_{cr}(\lambda)$ . This can be called 'spot noise' ( $\sigma_{spot}$ ) when  $\sigma_{cr}$  is caused by the presence of spots alone<sup>13</sup>.

6) The above method is repeated at different spot coverage values, and with and without faculae. The wavelength-dependent 'spot noise' is found in each case.

7) The corresponding uncertainty on the contrast ratio from photon noise,  $\sigma_{photon}$ , is obtained by repeating the Monte Carlo simulation, deactivating SpotSim and activating the source photon noise only. This is then adjusted to account for the

<sup>13</sup> The term 'spot noise' is used loosely, referring to the fact that the contrast ratio encountered from spot effects on any particular visit will have an error from the true value, and that error may be randomly distributed between repeated observations, allowing an 'uncertainty' to be assigned for any given measurement. It does not however resemble 'noise' as a stochastic process within any single observation, since in any given observation the error manifests as a bias from the true spectrum.

dimming occurring at different spot coverages. This allows comparison between the ‘spot noise’ ( $\sigma_{spot}$ ) and the photon noise limit ( $\sigma_{photon}$ ) in each case.

**ExoSim simulations** Full primary transit simulations were performed with GJ 1214b and HD 209458b using the same ARIEL configuration and integration times as in Section 4.5. The total observing time was  $2 \times T_{14}$ , with  $T_{14}/2$  before and after the transit. Black body spectra were used for the stars rather than PHOENIX spectra for consistency with SpotSim which currently uses black body functions<sup>14</sup>.

Flat input planet-star contrast ratio spectra were used:  $(R_p/R_s)^2 = 0.0135$  for GJ 1214b,  $(R_p/R_s)^2 = 0.01464$  for HD 209458b. These area ratios are also applied in the SpotSim model.

All other noise sources were suppressed and QE variations were deactivated, so that the effects of the spots (with or without faculae) alone can be assessed in isolation. A low frame rate of 1 Hz was used; this was considered adequate to capture the effects of spots within the integration period, while permitting a fast simulation.

The integration times for each target and channel were set by the ‘time to saturation’ method, and are similar to those in Chapter 4 Table 4.9, but rounded to the nearest second (due to the lower simulation frame rate). The exception is that the maximum integration time is limited to 300 seconds to allow adequate cadence to capture a light curve; this affects only GJ 1214 in VisPhot. Again we assume zero overheads so the exposure time is the same as the CDS time. The downlink rate for each exposure is assumed to be 0.25 Hz, meaning that onboard co-adding of exposures is required for exposure times shorter than this (e.g. for HD 209458 in NIRSpec, FGS 2 and FGS 1); in such cases, since no overhead time is assigned and read noise is not simulated, this can be mimicked by increasing the integration time to the minimum value above 4 seconds that contains an integer number of exposure times.

It was assumed that the effects of limb darkening will be minimal at the longer wavelengths of AIRS Ch0 and Ch1, and thus no limb darkening was simulated in these channels. However limb darkening was applied in NIRSpec and the FGS channels, with the equivalent limb darkening coefficients also used in SpotSim. Photon noise only simulations were also performed for each target using the source photon noise simulated in isolation to obtain the comparison ‘photon noise

<sup>14</sup> This can be modified in the future to using PHOENIX spectra with different spectra for the spotted and unspotted star. This could be used for example to investigate the enhancement of water features during a planet transit.

limit’.

Each spotted star simulation was repeated for different spot coverage inputs for each star, and again without the faculae component. 200 realizations were performed in each case, with each realization processed to extract the transmission spectrum as described below.

**SpotSim simulations** The different spot coverages used were 0.1, 1, 10, 25 and 50%. These translated into measured mean filling factors of 0.13, 1.09, 7.91, 16.99 and 29.48% (mean of the 200 realizations) (Table 5.3). The corresponding expected filling factors assuming the filling factor is  $\cos(\pi/4) \times$  the area coverage would be 0.071, 0.707, 7.07, 17.68 and 35.35%, thus the simulations are reasonably close to the predictions. The measured Q factors are also given in Table 5.3 for each filling factor, and range between 42-62% of the input values.

Small variations in measured filling factors occur over the 200 random simulations, shown in Table 5.3 as the standard deviations of the filling factors. These produce associated variations in the brightness of the simulated star. For the visible (700-1000 nm) and NIR (2-4  $\mu\text{m}$ ) ranges, the brightness variations assuming black body spectra were calculated for each case (Table 5.3). If faculae are included in the simulations, these variations are reduced. Thus the simulations have an in-built degree of ‘stellar variability’ arising from the random generation of the spotted star in each case.

If we assume a 0.13% filling factor as representative for HD 209458, this gives a measured variability from the simulations of 0.16% in the visual with spots only, and 0.15% with spots and faculae. This compares well with the typical visual range variability for G-type stars in Zellem et al. (2017) obtained from Kepler studies of about 0.07% semi-amplitude, and therefore 0.14% peak-to-peak variation.

If we consider the 7.9% spot filling factor representative for GJ 1214, this gives a 1.58% peak-to-peak variation in the visible for the spots only case, and 0.82% peak-to-peak variation for spots and faculae together. This compares reasonably with the 1% peak-to-peak variation reported by Berta et al. (2011), and the 1.14 and 1.51% amplitudes from Nascimbeni et al. (2015). In the IR range, the measured variability for GJ 1214 in these simulations is 0.72% peak-to-peak with spots only, and 0.43% with spots and faculae (Table 5.3). This compares reasonably well with real measurements by Zellem et al. (2017) who report a variation of 0.279% semi-amplitude (and therefore 0.558% peak-to-peak) for GJ 1214 in the near infrared.

TABLE 5.3 Measured simulation filling factors, brightness variations and Q factors, for each input spot coverage.

Spot coverage (%)	Filling factor (%)			Brightness variation (%)						Input Q	Measured Q		
	spots	faculae	spots + faculae	HD 209458			GJ 1214						
				Visual		NIR		Visual				NIR	
				spots only	spots + faculae	spots only	spots + faculae	spots only	spots + faculae			spots only	spots + faculae
0.1	0.13 (±0.03)	1.23 (±0.34)	1.35 (±0.37)	0.16	0.15	0.10	0.06	0.11	0.09	0.05	0.03	17.2	9.7 (±1.0)
1	1.09 (±0.12)	6.73 (±0.80)	7.82 (±0.92)	0.47	0.15	0.30	0.10	0.31	0.10	0.14	0.05	10.2	6.2 (±0.2)
10	7.91 (±0.52)	29.43 (±1.78)	37.34 (±2.26)	2.42	1.19	1.51	0.89	1.58	0.82	0.72	0.43	6.0	3.7 (±0.1)
25	16.99 (±1.25)	44.72 (±2.26)	61.71 (±3.31)	6.03	4.50	3.65	2.98	3.82	2.97	1.70	1.41	4.9	2.6 (±0.1)
50	29.48 (±1.95)	52.24 (±1.78)	81.72 (±3.12)	10.23	9.02	5.91	5.51	6.20	5.68	2.65	2.53	4.2	1.8 (±0.1)

Thus the variations introduced into these simulations from the random processing of the spot coverage in each realization fortuitously generates brightness variations that appear consistent with likely real behaviour of HD 209458 and GJ 1214. This therefore adds a realistic level of stellar variability into the results, at least for the filling factors that most likely represent these stars.

**Data reduction** The output from each realization is processed using the basic data reduction pipeline from Chapter 4, omitting CDS, background subtraction and flat fielding, to give data light curves binned to  $R=100$  in AIRS Ch0,  $R=30$  in AIRS Ch2, and  $R=20$  in NIRSpec. The same apertures were used as in Section 4.5 for the spectroscopic and photometric channels. Each spectroscopic and photometric light curve was then fitted with a Mandel-Agol model using a downhill simplex algorithm minimising  $\chi^2$  in the same way as in Chapter 3. Free parameters in the fits were the out-of-transit flux and the planet-star radius ratio. Quadratic limb darkening coefficients were also included as free parameters for fits for NIRSpec and the photometric channels, and fixed at zero for the 2 AIRS channels. For each realization, this returns the final reconstructed spectrum of recovered contrast ratios for each spectroscopic channel, or a single value for each photometric channel. From the 200 realizations for each Monte Carlo simulation, the mean and standard deviation ( $\sigma_{cr}$ ) of the distribution of contrast ratios,  $(R_p/R_s)^2$ , at each wavelength is obtained.

### 5.2.5 RESULTS

Figure 5.11 shows the results from the Monte Carlo simulations for photon noise only. The y axis shows the percent change from the input contrast ratio with wavelength, grey dots show the individual results from each realization with error bars showing the  $\pm 1\sigma_{cr}(\lambda)$  range in any wavelength bin (or photometric channel), where  $\sigma_{cr}(\lambda)$  is the final uncertainty on the contrast ratio. The equivalent Monte Carlo simulation results for spot only simulations, and spot with faculae simulations, are shown in Figures 5.12 and 5.13 for HD 209458b and Figures 5.17 and 5.18 for GJ 1214b. The results for the 5 different spot filling factors are shown in each figure.

In Figures 5.12 and 5.17 the blue circles show the expected 'baseline' deviation in the spectrum expected due to unocculted spots alone given the average spot filling factors from Table 5.3, simulation spot and star temperatures and the application of Equation 5.1. The equivalent baseline, if faculae are included, is

shown by the blue circles in Figures 5.13 and 5.18, where the faculae filling factor and temperature are taken into account.

The  $\sigma_{cr}(\lambda)$  at each filling factor due to both spots only, spots and faculae, and photon noise are converted into ppm and shown in 5.14 for HD 209458b and Figure 5.19 for GJ 1214b. These figures allows a comparison of the absolute spot (or spot and faculae) noise between different filling factors and in relation to uncertainties due to photon noise.

The contrast ratio uncertainties due to photon noise ( $\sigma_{photon}$ ) obtained for the unspotted stars were corrected (using Planck functions and the simulation temperatures of the star, spots and faculae) to take into account the filling factors allocated to spots and faculae in each case. To 2 decimal places, for the spots only simulations the correction factors ranged from 1.00 to 1.16 for HD 209458 and 1.00 to 1.12 for GJ 1214. For spots and faculae the correction factors ranged from 1.00 to 1.09 for HD 209458 and 1.00 to 1.07 for GJ 1214. These adjusted values were used when finding the  $\sigma_{spot}/\sigma_{photon}$  ratios in Figures 5.15, 5.16, 5.20 and 5.21. Since the variation is small in log space, for clarity in Figures 5.14 and 5.19 only the uncorrected photon noise is shown.

The ratio of the spot (or spot and faculae) noise to photon noise (adjusted as above for filling factors) at each wavelength is shown in Figure 5.15 for HD 209458b and Figure 5.20 for GJ 1214b. Here  $\sigma_{cr}$  due to spots (or spots and faculae) is termed  $\sigma_{spot}$  and that due to photon noise from the source,  $\sigma_{photon}$ .

A channel-by-channel chart of  $\sigma_{spot}/\sigma_{photon}$  versus filling factor is shown for each planet, Figure 5.16 for HD 209458b and Figure 5.21 for GJ 1214b, summarising the impact of spots (or spots and faculae) in relation to precision of each ARIEL channel. The lines show the  $\sigma_{spot}/\sigma_{photon}$  ratio for the representative wavelength in the middle of each band: 2.93  $\mu\text{m}$  for Ch0, 5.80  $\mu\text{m}$  for Ch1 and 1.52  $\mu\text{m}$  for NIRSpec. The shaded areas are bounded by the maximum and minimum values within each channel. The central wavelengths for the FGS channels are 1.13  $\mu\text{m}$  for FGS 2, 0.91  $\mu\text{m}$  for FGS 1 and 0.53  $\mu\text{m}$  for VisPhot.

Using the above channel-by-channel charts, Table 5.4 gives  $\sigma_{spot}/\sigma_{photon}$  ratios for GJ 1214b and HD 209458b for the mid-band wavelength of each ARIEL channel, assuming a filling factor of 10% for GJ 1214 with no faculae, and 1% for HD 209458 with faculae. Also shown are corresponding increases to the final uncertainty on the contrast ratio,  $\Delta\sigma_{cr}$ .

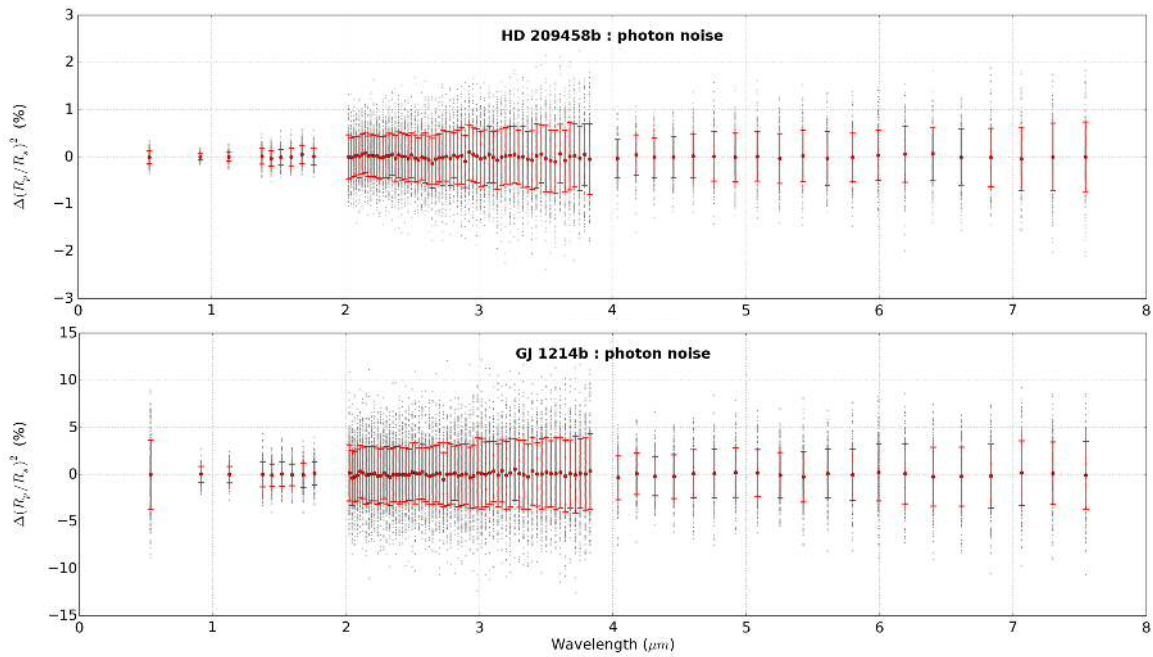


FIGURE 5.11 Monte Carlo simulations for HD 209458b (top) and GJ 1214b (bottom) with photon noise only, showing % variation from input contrast ratio. Grey dots: individual results. Red dots and error bars: mean and standard deviation of the distribution at each wavelength.

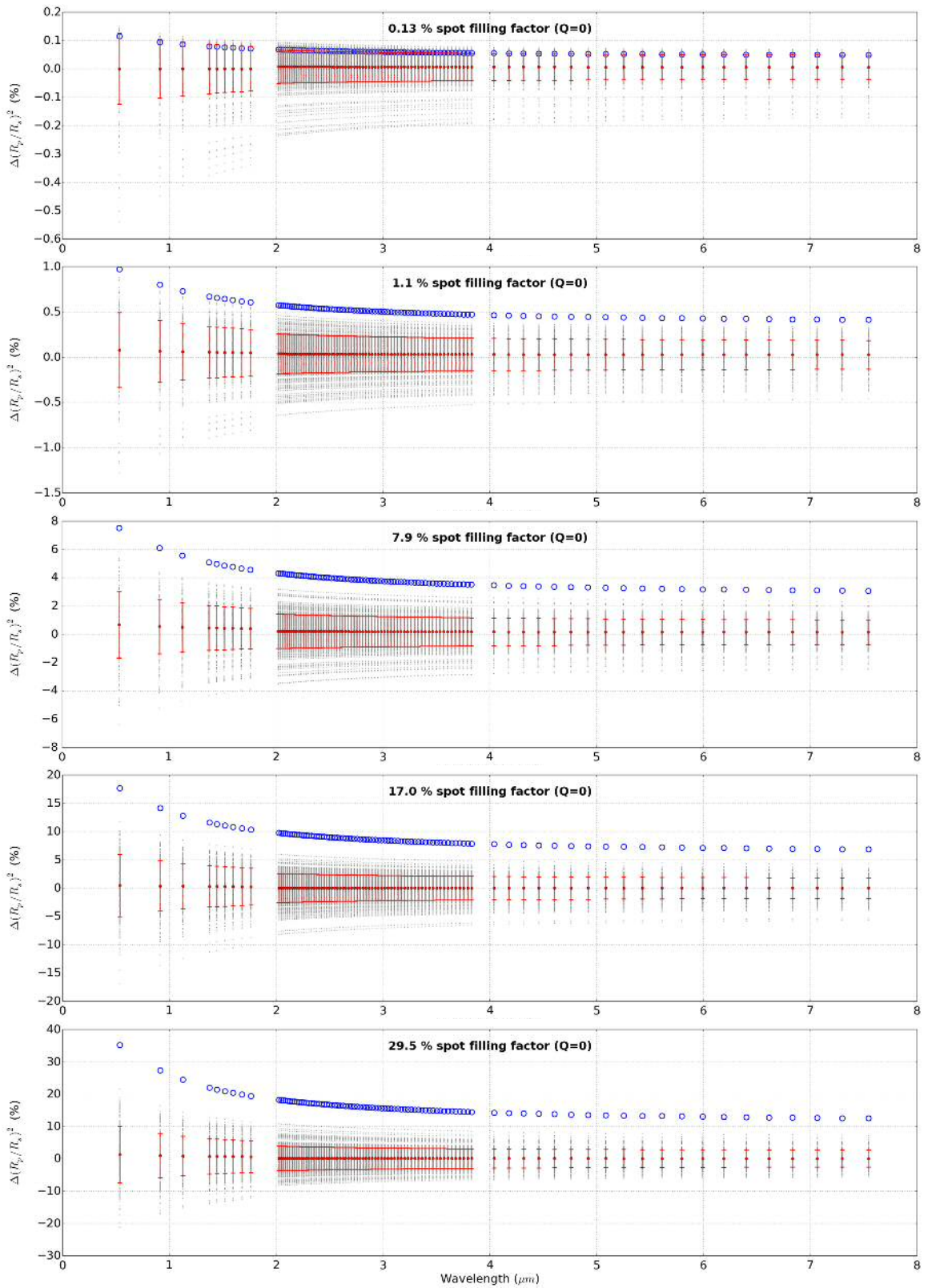


FIGURE 5.12 Monte Carlo simulations for HD 209458b with spots only, at different spot filling factors, showing % variation from input contrast ratio. Grey dots: individual results. Blue circles: 'baseline' with for unocculted spots. Red dots and error bars: mean and standard deviation of the distribution at each wavelength.

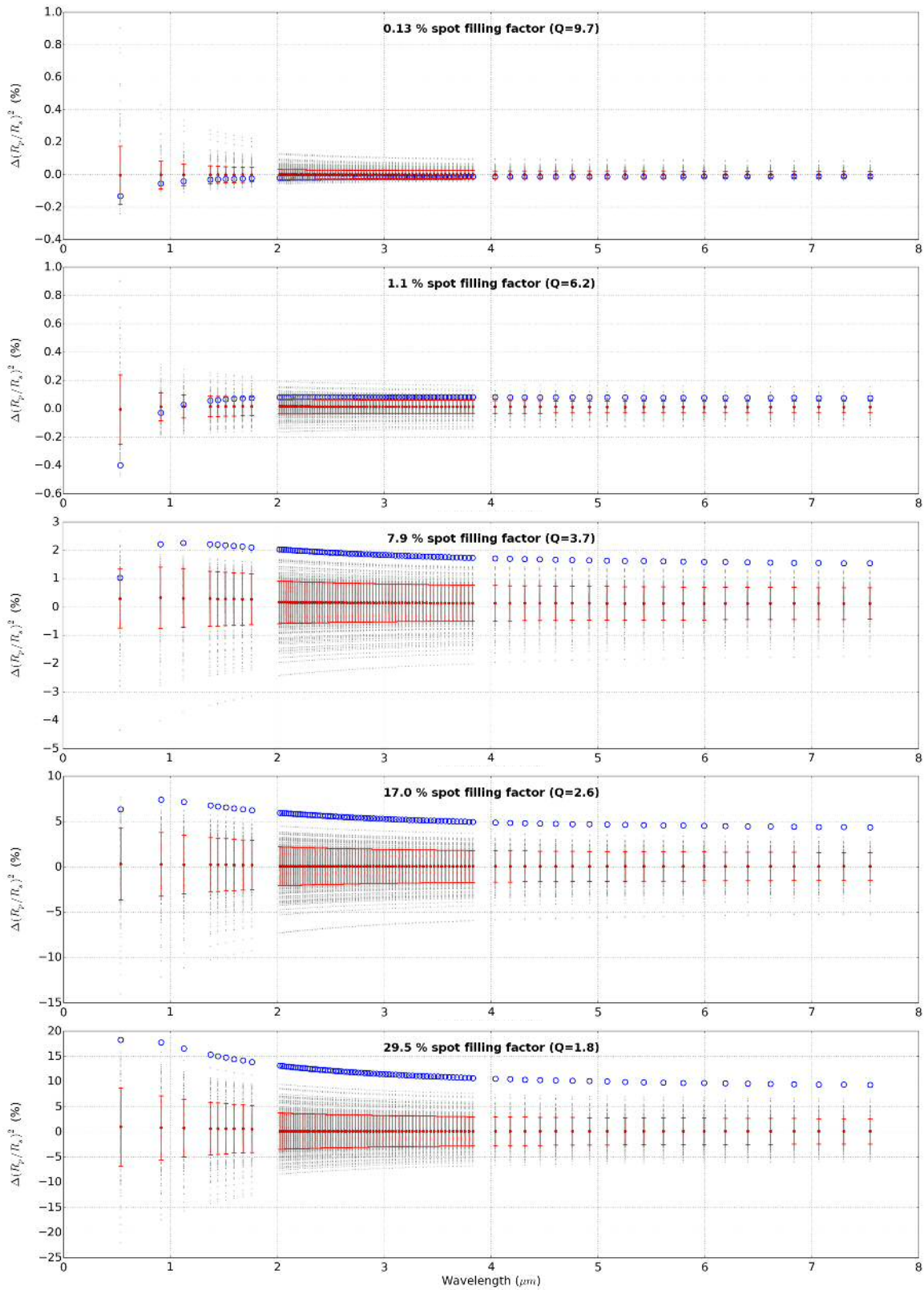


FIGURE 5.13 Monte Carlo simulations for HD 209458b with spots and faculae, at different spot filling factors, showing % variation from input contrast ratio. Grey dots: individual results. Blue circles: 'baseline' with for unocculted spots and faculae. Red dots and error bars: mean and standard deviation of the distribution at each wavelength.

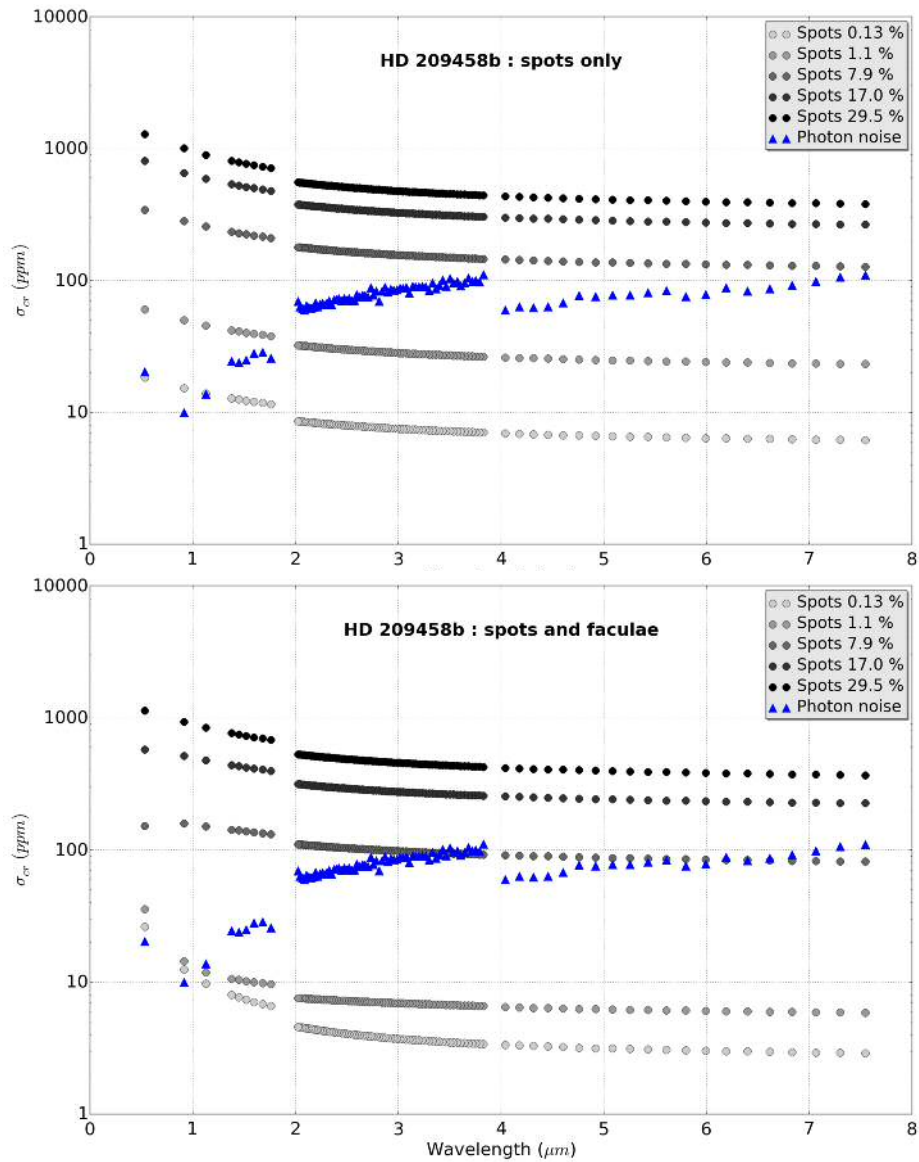


FIGURE 5.14 HD 209458b: uncertainty on the contrast ratio ( $\sigma_{cr}$ ) in ppm vs wavelength from spots only, spots and faculae and photon noise only. Top: spots only (at different spot filling factors) and photon noise. Bottom: spots and faculae (at different spot filling factors) and photon noise.

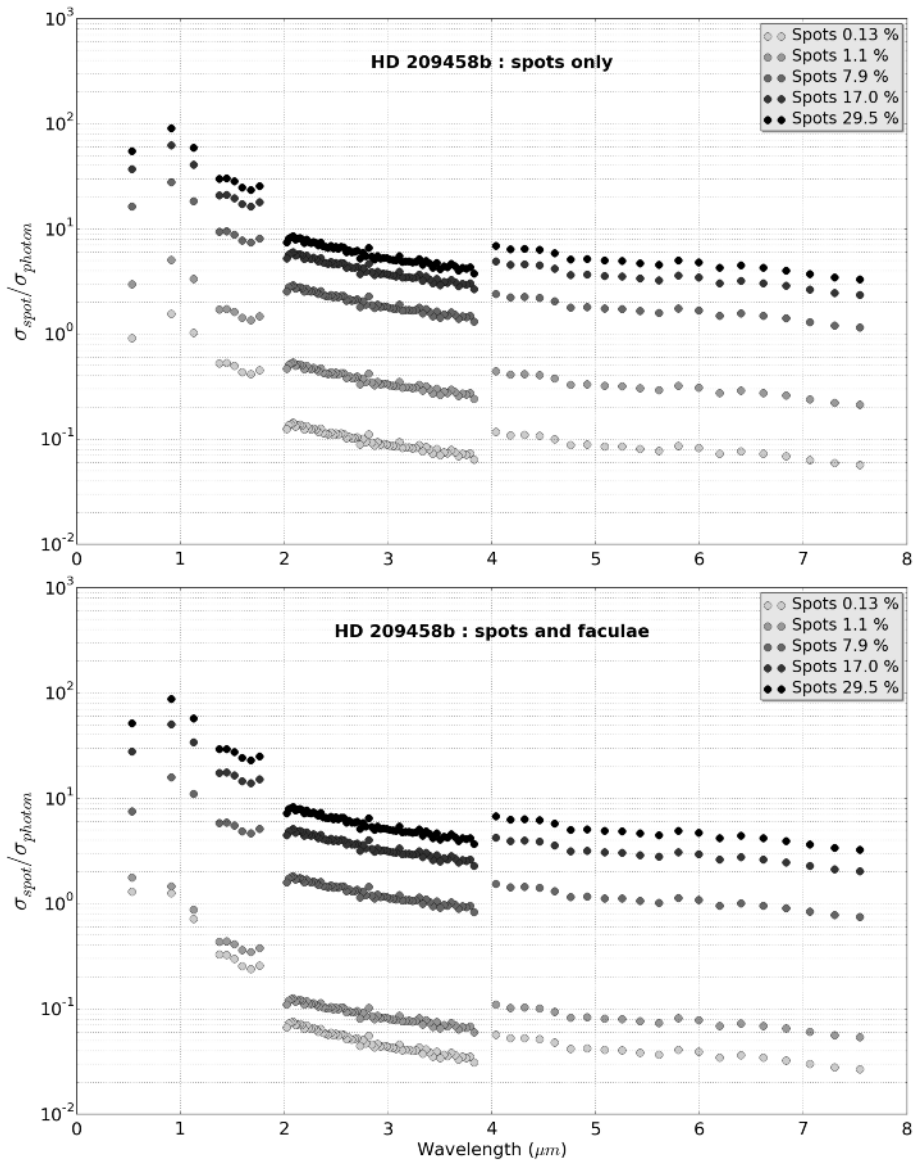


FIGURE 5.15 HD 209458b: ratio of the uncertainty on the contrast ratio due to spots (or spots and faculae), 'spot noise' ( $\sigma_{spot}$ ), to the uncertainty on the contrast ratio due to photon noise, ( $\sigma_{photon}$ ), vs wavelength. Top: spots only (at different spot filling factors). Bottom: spots and faculae (at different spot filling factors).

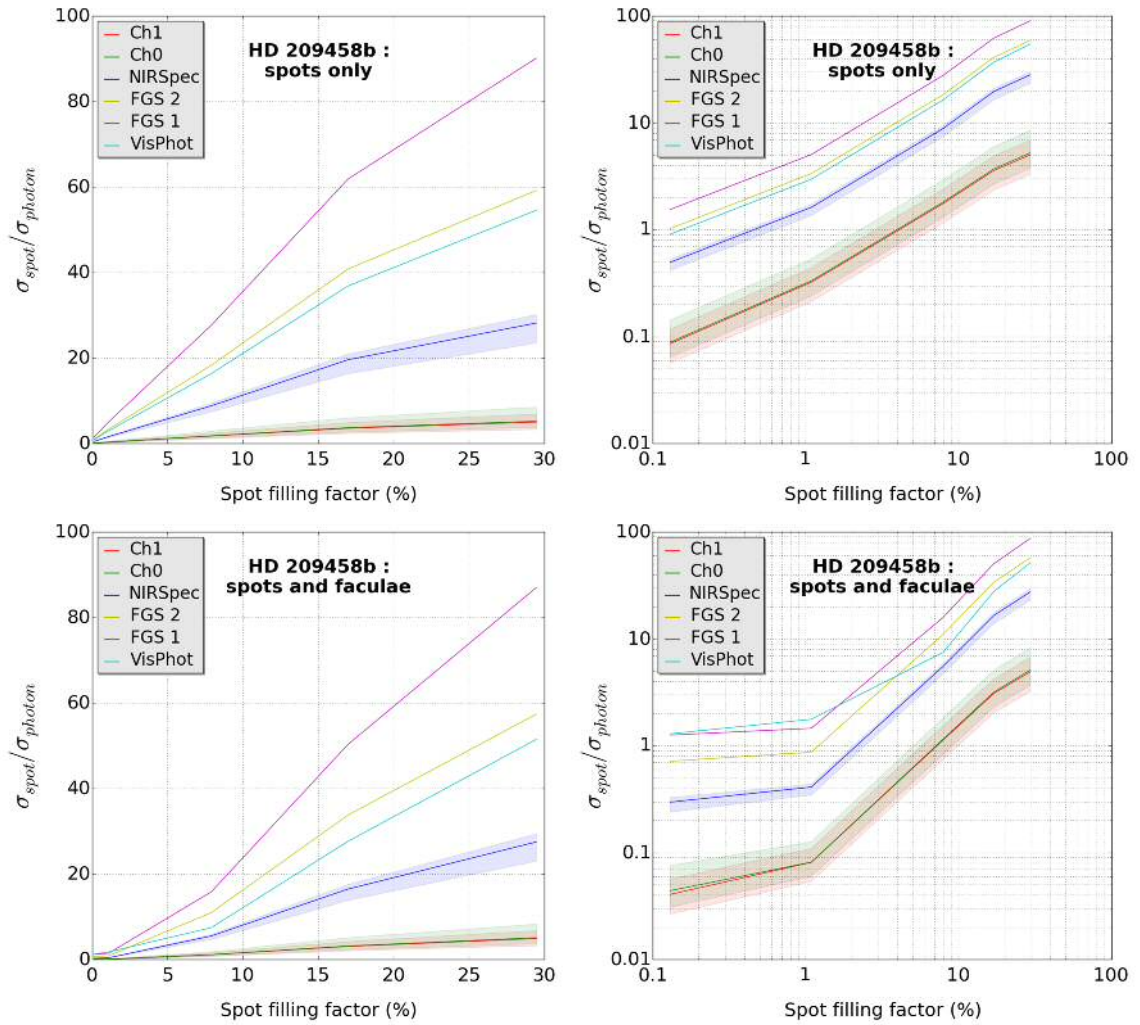


FIGURE 5.16 HD 209458b:  $\sigma_{spot}/\sigma_{photon}$  vs spot filling factor, for each ARIEL channel. Lines show the ratio at representative wavelengths in the middle of each band, with shaded areas bounded by maximum and minimum values in each channel. Details given in the text. Top: spots only. Bottom: spots and faculae. Left: normal scale. Right log:log scale.

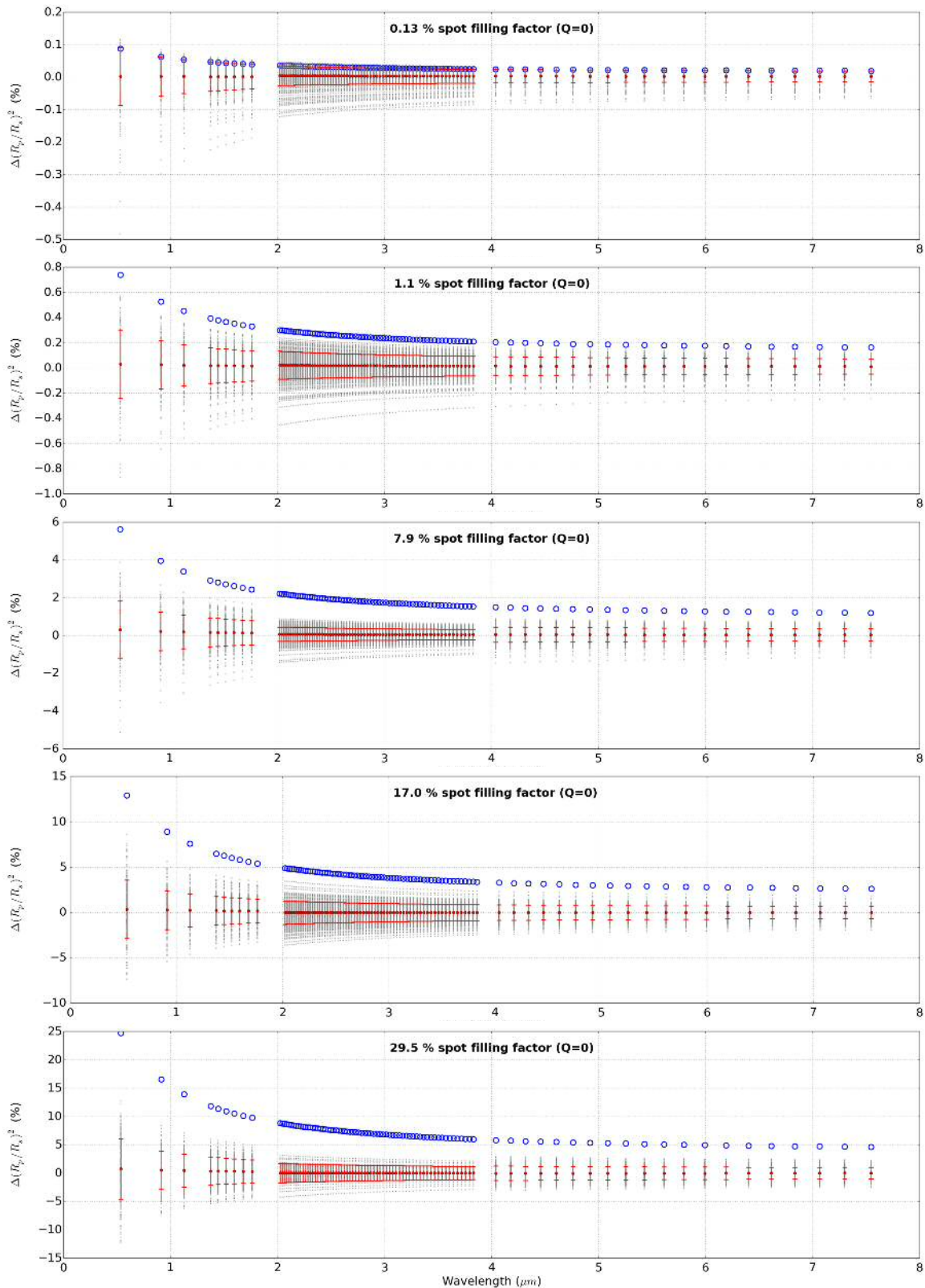


FIGURE 5.17 Monte Carlo simulations for GJ 1214b with spots only, at different spot filling factors, showing % variation from input contrast ratio. Grey dots: individual results. Blue circles: 'baseline' with for unocculted spots. Red dots and error bars: mean and standard deviation of the distribution at each wavelength.

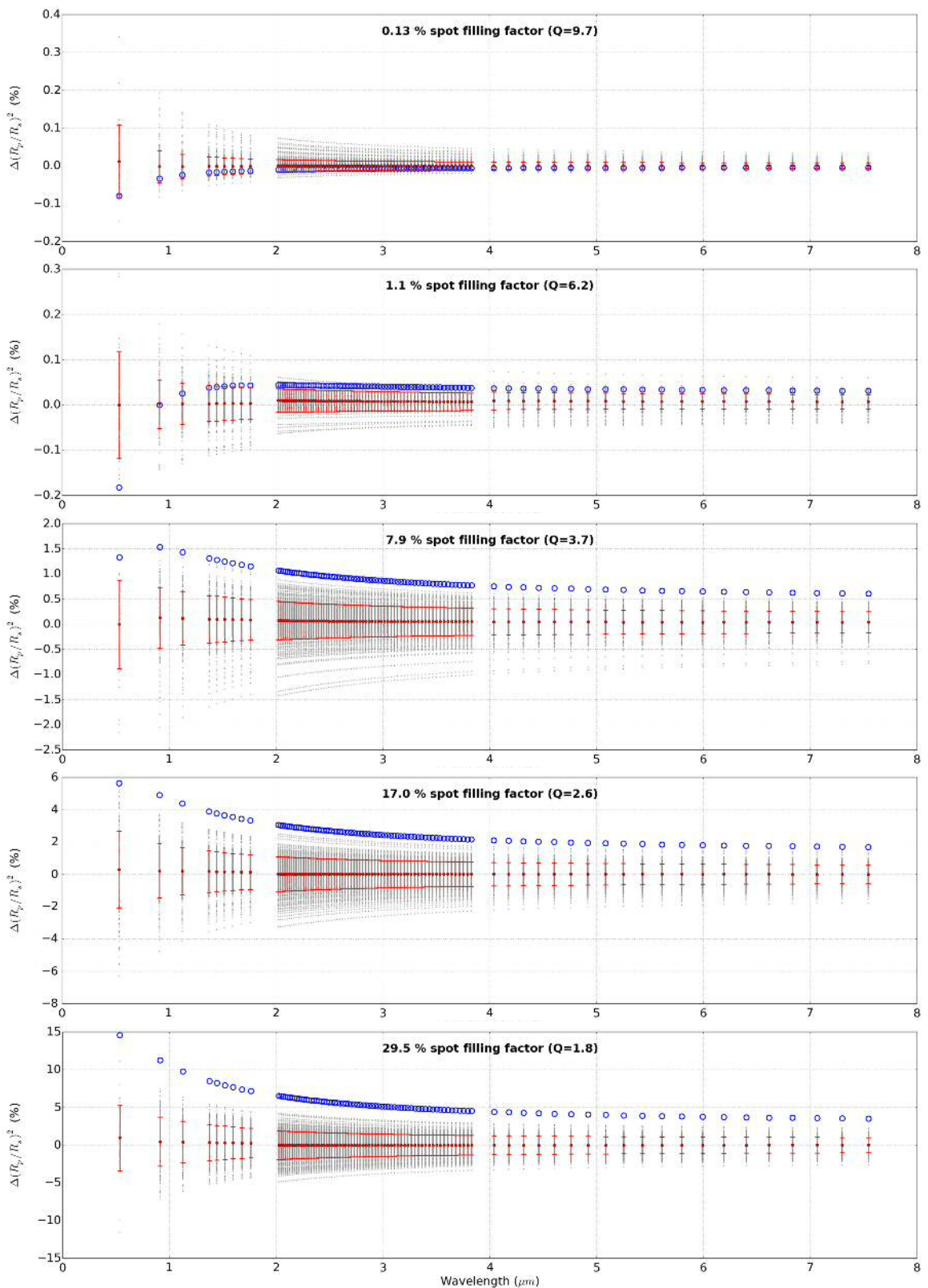


FIGURE 5.18 Monte Carlo simulations for GJ 1214b with spots and faculae, at different spot filling factors, showing % variation from input contrast ratio. Grey dots: individual results. Blue circles: 'baseline' with for unocculted spots and faculae. Red dots and error bars: mean and standard deviation of the distribution at each wavelength.

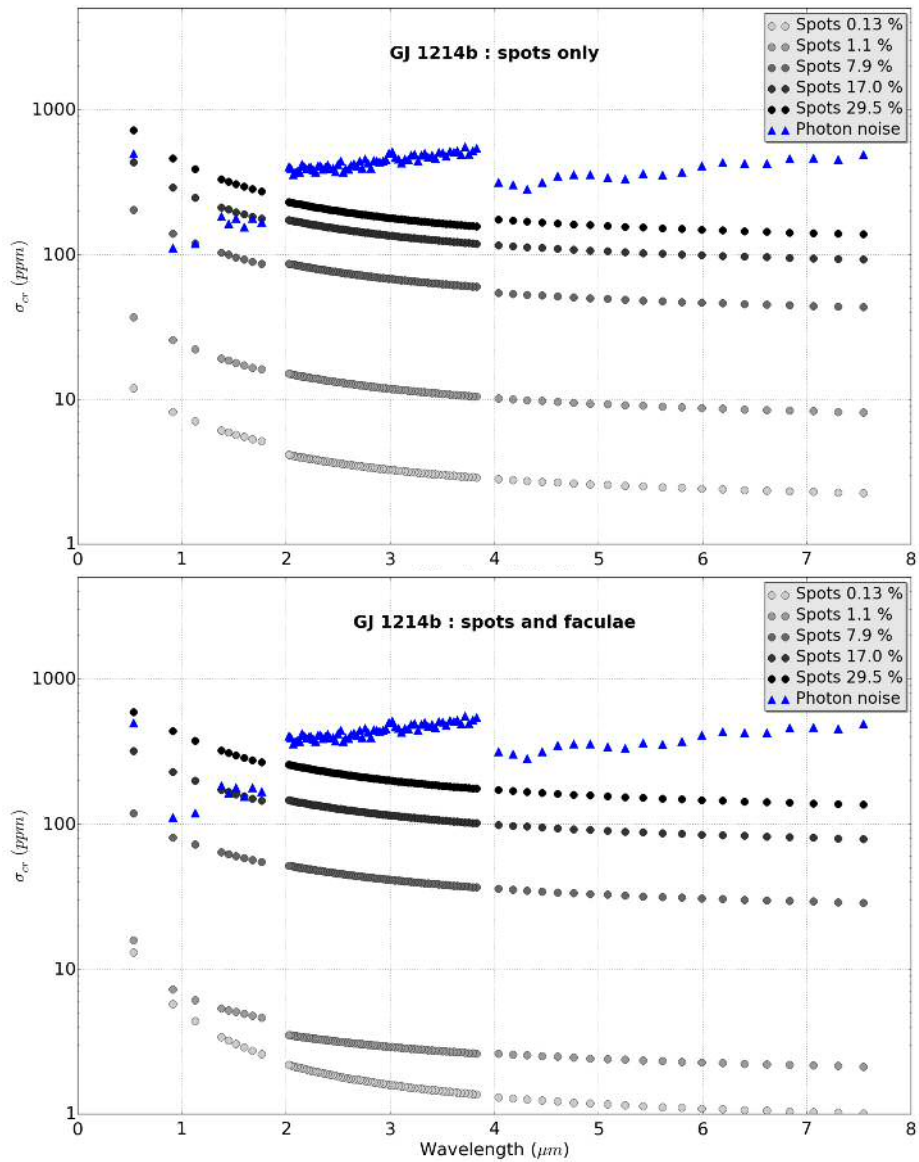


FIGURE 5.19 GJ 1214b: uncertainty on the contrast ratio ( $\sigma_{cr}$ ) in ppm vs wavelength from spots only, spots and faculae and photon noise only. Top: spots only (at different spot filling factors) and photon noise. Bottom: spots and faculae (at different spot filling factors) and photon noise.

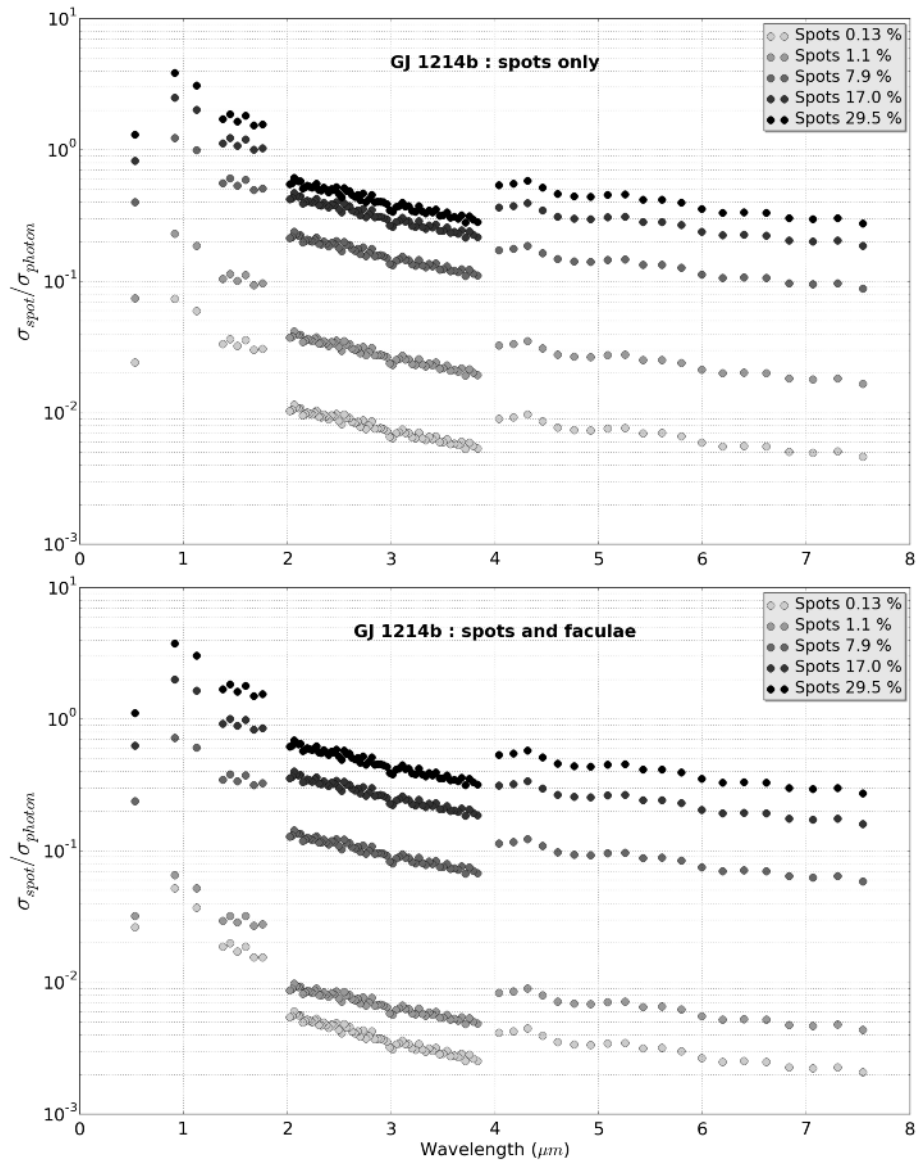


FIGURE 5.20 GJ 1214b: ratio of the uncertainty on the contrast ratio due to spots (or spots and faculae), 'spot noise' ( $\sigma_{spot}$ ), to the uncertainty on the contrast ratio due to photon noise, ( $\sigma_{photon}$ ), vs wavelength. Top: spots only (at different spot filling factors). Bottom: spots and faculae (at different spot filling factors).

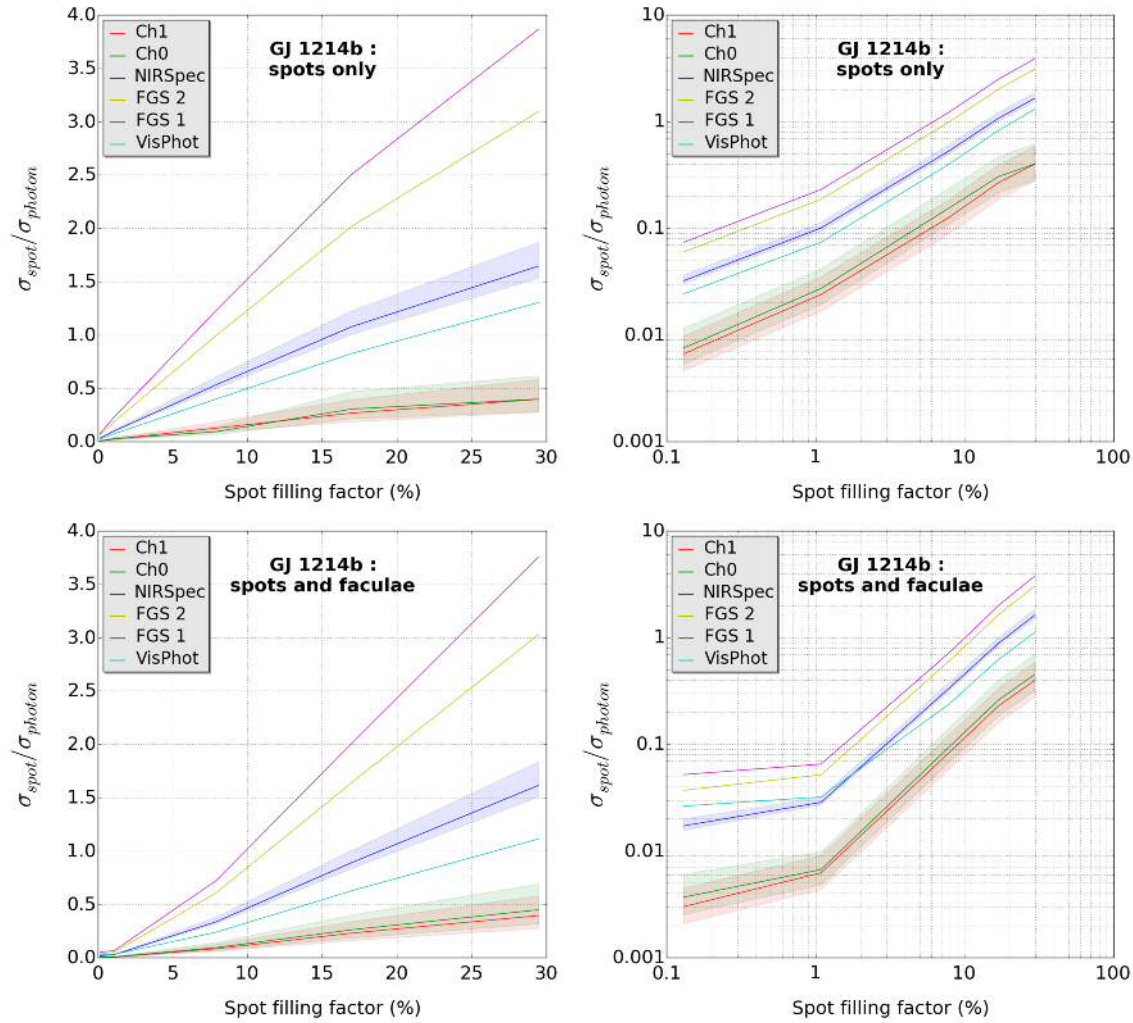


FIGURE 5.21 GJ 1214b:  $\sigma_{spot}/\sigma_{photon}$  vs spot filling factor, for each ARIEL channel. Lines show the ratio at representative wavelengths in the middle of each band, with shaded areas bounded by maximum and minimum values in each channel. Details given in the text. Top: spots only. Bottom: spots and faculae. Left: normal scale. Right log:log scale.

TABLE 5.4  $\sigma_{spot}/\sigma_{photon}$  for GJ 1214b and HD 209458b for each ARIEL channel, for mid-band wavelength, assuming filling factor of 10% for GJ 1214 with no faculae, and 1% for HD 209458 with faculae. Also shown are corresponding increases to the final uncertainty on the contrast ratio,  $\Delta\sigma_{cr}$ .

Channel	HD 209458b		GJ 1214b	
	$\sigma_{spot}/\sigma_{photon}$ (%)	$\Delta\sigma_{cr}$ (%)	$\sigma_{spot}/\sigma_{photon}$ (%)	$\Delta\sigma_{cr}$ (%)
AIRS Ch1	8	0.3	16	1.3
AIRS Ch0	8	0.3	14	1.0
NIRSpec	40	7.7	66	19.8
FGS 2	86	32.0	123	58.5
FGS 1	144	75.3	152	81.9
VisPhot	172	99.0	50	11.8

### 5.2.6 ANALYSIS

**Percentage change to the transmission spectrum** Figure 5.11 shows the percentage change from the ‘true’ input contrast ratio due to the photon noise only simulations for HD 209458b and GJ 1214b assuming a spot-free star. As would be expected, the brighter star HD 209458b elicits the lower fractional photon noise resulting in narrower distributions. For example in Ch0, there is an average standard deviation of 0.55% in HD 209458b and 3.24% in GJ 1214b. This becomes important when considering the relative impact of the spot noise. The absolute values of  $\sigma_{cr}$  from photon noise in ppm are shown in Figures 5.14 and 5.19. For example, in Ch0, the average noise is 80 ppm for HD 209458b and 437 ppm for GJ 1214b<sup>15</sup>.

Figures 5.12 and 5.13 show the percent variation from the input contrast ratio for spots only and spots and faculae respectively for HD 209458b at different spot filling factors. Figures 5.17 and 5.18 give the equivalent results for GJ 1214b. In both exosystems we see an increase in the ‘spot noise’ with shorter wavelengths and with increasing filling factors. It is reduced somewhat if faculae are included in the simulations, as these tend to oppose the effects of spots on the light curve.

We can see that the spots cause a wavelength-dependent bias that varies in

<sup>15</sup> We can compare these values to  $\sigma_{cr}$  derived from the OOT source photon noise obtained in Section 4.5 using Equation 4.1. Using that method, the average  $\sigma_{cr}$  in Ch0 is 82 ppm for HD 209458b and 486 ppm for GJ 1214b. The slight discrepancy in the GJ 1214b noise result with the result obtained here is probably due to the fact I use black body functions in this study compared to PHOENIX spectra in Chapter 4, causing a difference in the signal and thus the photon noise. For HD 209458, in contrast, we have an excellent agreement, which may reflect the greater similarity of the PHOENIX spectra to a black body function for hotter stars.

size between realizations, in contrast to the photon noise which shows no correlation between wavelengths. As expected from the earlier discussion, the bias is highest at shorter wavelengths. The spectrum deviates above or below the true value, by about the same amount, with the mean value close to zero (i.e close to the true contrast ratio). This appears to bear out the prediction from the earlier discussion that over a large number of observations, the effects of the occulted spots and unocculted spots will 'balance out' nullifying the bias.

The distortion therefore varies in any individual visit. If we consider the 7.9% filling factor spots only case as a likely one for GJ 1214b, then we find a range of distortion of +0.9 to -1.4% in Ch0 and +0.9 to -1.5% in Ch1, increasing to up to a maximum of +3.9 to -5.2% in VisPhot. These values, despite having been processed through the ARIEL model and binned to the ARIEL resolution, are more a function of the star spot model than the instrument model, and thus are not special to ARIEL specifically.

The effect of adding faculae to the spots is to reduce the range of variation, e.g. if faculae are added, the VisPhot range falls to +2.7 to -4.4% at the 7.9% filling factor. It also tends to shift the range to more positive values compared to the faculae-free case, which is noticeable particularly at low spot filling factors where the faculae proportions are higher, e.g. for GJ 1214b with no faculae the VisPhot range at 0.13% filling factor is +0.9 to -1.3%, while with faculae it is +0.9 to -0.5%

For HD 209458b, under the same conditions of 7.9% filling factor with spots only, the distortions are higher than for GJ 1214b: +3.2 to -3.5% in Ch0 and +2.6 to -2.8% in Ch1, and rising to +5.4 to -6.4% in VisPhot. However, if we consider a more likely scenario to be a 1.1% filling factor with faculae included, the distortions are a lot less: +0.9 to -0.5% in VisPhot, +0.2 to -0.2% in Ch0 and +0.2 to -0.1% in Ch1.

Since the filling factor is essentially constant between realizations (except for the small variations shown in Table 5.3), the unocculted spot fractions should result in about the same bias on each realization.

The blue circles on these figures show this 'baseline' bias with unocculted spots and faculae (if included) only. Considering the spots only cases (Figures 5.12 and 5.17), the baseline exists above the distributions seen in the Monte Carlo simulations. This makes sense as the baseline marks the limit of how high the contrast ratio could get if no spots were occulted, and the unocculted spot effect was completely unopposed. The downward distribution from this level reflects the effect of reducing the transit depth due to spot crossings that vary from visit to visit depending on the numbers and sizes of spots occulted. A small amount of variation may occur due to variation in the unocculted spot fraction, but the vast majority

will be due to a 'stochastic' variation of unocculted spots crossings with each visit. As the filling factor increases so the baseline appears more separated from the upper bounds of Monte Carlo distribution; this can be explained by the fact that as the filling factor increases, so the probability of spot crossings and the average spot size will increase; thus it become less and less likely that any simulations will be close to the 'baseline' of no spot crossings; a gap opens up therefore between the blue circles and the distribution.

In the case of adding faculae (Figures 5.13 and 5.18), the baseline becomes slightly more complex due to the opposing effects of faculae to cold spots. As the spot filling factor falls, so the Q factor increases, and the influence of the faculae increases, pulling the baseline downward starting at the shorter wavelengths. By 0.13% spot filling factor with a Q of 9.7, faculae are dominant in establishing the baseline, which falls at the lower bound of the Monte Carlo distribution.

Thus the distribution in transit depths seen is caused mostly by the random element of the occulted spot effect opposing the baseline unocculted spot bias. Over many simulations the two effects appear to cancel out, which supports the analytical treatment by Pont et al. (2013) for spot noise in the Spitzer 8  $\mu\text{m}$  band for HD 189733b, where they assumed the bias to be zero, and an uncertainty added to the results due to spot occultations. It is possible that if the spots are concentrated in particular regions, e.g. preferred latitudes, then the distributions seen will be skewed one way or the other, and repeated measurements may not 'balance' out the bias as seen here.

**Absolute noise on the contrast ratio in ppm** Figures 5.14 and 5.19 give the absolute values for the contrast ratio uncertainty due to spot noise at different filling factors (and with and without faculae) and photon noise. As expected,  $\sigma_{cr}$  is less if faculae are included in the simulations. The 'spot noise' in ppm, is higher in the G-type star case than the M-dwarf case for the same filling factor, e.g. at the 7.9% (spots only), the average 'spot noise' in Ch0 is 72 ppm in the GJ 1214b simulation, compared to 161 ppm in the HD 209458b simulation. This reflects the higher temperature contrasts between the baseline star and the spots in G-type stars compared to M-type stars. However we expect M-dwarfs to be more active with higher filling factors. This probably outweighs the temperature effect, i.e. GJ 1214b with 7.9% filling factor for the host star, has over 10 times the spot noise of HD 209458b with 1.1% filling factor (or less) for the host star. The impact on the transmission spectrum by spots may be considered in relation to the observational precision limit represented by the photon noise, which is shown as the blue points

on Figures 5.14 and 5.19.

**Ratio of spot noise to photon noise** If the uncertainty on the contrast ratio seen due to spots is smaller than the uncertainty due to photon noise at a given wavelength, it could be argued that decorrelation or detrending may not be required or may even be undesirable in that it could introduce more uncertainty than it removes. Exactly what proportion of photon noise is considered an acceptable level of spot noise may not be straightforward to define. We could take a 5% increase in the final error bar (uncertainty) due to spot noise as an ‘acceptable’ level, which amounts to a  $\sigma_{spot}$  to  $\sigma_{photon}$  ratio of 32%. Figures 5.15 and 5.20 show the ratio of  $\sigma_{spot}$  to  $\sigma_{photon}$  per wavelength bin and Figures 5.16 and 5.21 show how the ratio of  $\sigma_{spot}$  to  $\sigma_{photon}$  varies with filling factor for each ARIEL channel for the two targets.

For HD 209458b, ‘likely’ filling factors for the host star of those simulated (being considered by some a solar analogue) could range from the lowest filling factor simulated here of 0.13% upto about 1%. Faculae could also be considered more likely to have an impact on this star as they are features of less active stars.

For the AIRS channels, if we focus on Figure 5.16 on the spots and faculae case, we find that at 0.13% filling factor we are at only just above 4% for the  $\sigma_{spot}$  to  $\sigma_{photon}$  ratio for the middle of each band (the maximum values in each band remaining within 10%). For both AIRS channels, we reach reach the 32% ‘limit’ (at which the error bar is increased by 5%) for the middle of the bands at around 2.6% filling factor, which might be a less likely filling factor for this Sun-like star.

The results in Table 5.4 use the interpolated values from Figure 5.16 (spots and faculae case) to give a likely result for HD 209458b assuming 1% filling spot factor. Thus for the AIRS channels, the 8%  $\sigma_{spot}$  to  $\sigma_{photon}$  ratio does not significantly increase the final error bar (0.3%), and therefore corrections can be omitted in these channels.

The ratios are a lot higher in NIRSpec and the FGS channels (Figure 5.16) and in the spots and faculae case, at the lowest filling factor of 0.13% are already at 30% in NIRSpec, and at 130%, 126% and 72% in VisPhot, FGS 1 and FGS 2 respectively (equating to 64%, 61% and 23% increases respectively in the final uncertainty or error bar). Therefore all the visual photometric channels exceed the the 32% ‘limit’ at the lowest spot filling factor, and it is reached at just 0.32% filling factor in NIRSpec.

Table 5.4 indicates that for HD 209458b at 1% filling factor we can expect a 40%  $\sigma_{spot}$  to  $\sigma_{photon}$  ratio in NIRSpec causing a 7.7% increase in  $\sigma_{cr}$ . This increases to a 172%  $\sigma_{spot}$  to  $\sigma_{photon}$  ratio in VisPhot with a 99% increase in the final error

bar. Thus it is very likely that all the photometric channels and NIRSpec will be vulnerable to significant spot effects, requiring corrections or otherwise accounting for in the final error budget.

For GJ 1214b we could consider likely filling factors to range between 5-15%, 7.9% probably being the most likely filling factor of those simulated here, and others have previously simulated GJ 1214 with a 10% filling factor. For this discussion, I focus on the results from the spots only case for GJ 1214b. This may be reasonable for a more active star with a low Q ratio, and represent a more 'pessimistic' case than with faculae included.

If we consider the two AIRS channels in the spots only case, we find that for GJ 1214b the 32% ratio 'limit' (at which the error bar is increased by 5%) is reached for the mid-band wavelength bin at filling factors of 18.9% and 21.9% for Ch0 and Ch1 respectively (Figure 5.21). This is reflected in Figure 5.20, where the 7.9% filling factor results are well below the 32% level in these channels.

Table 5.4 gives a 'likely' result for GJ 1214b assuming a 10% filling with no faculae. In the AIRS channels, the  $\sigma_{spot}$  to  $\sigma_{photon}$  ratio is 14-16%, giving error bar increases of just 1.0-1.3% which we can consider not significant.

We could therefore conclude that if the filling factor for GJ 1214 is below 15%, spot effects may not be detectable or require correction for Ch0 and Ch1, as they will be buried well beneath the photon noise, and will contribute no more than 5% to the final uncertainty. If however the actual filling factor for GJ 1214 is higher, say closer to 30% then we reach a 40% ratio in Ch0 and Ch1 (increasing the error bars by about 8%) where we may wish to consider spot correction methods.

In NIRSpec and the FGS channels, the  $\sigma_{spot}$  to  $\sigma_{photon}$  ratios are much higher than in AIRS, as for HD 209458. In the spots only case, the 32% 'threshold' is reached at a spot filling factor of only 4.5% in NIRSpec's mid-band wavelength bin, and just 1.7% and 2.2% in FGS 1 and FGS 2 respectively. Thus, if GJ 1214 has a low filling factor of < 4%, we could propose that NIRSpec too will not display significant spot effects, though it appears FGS 1 and 2 will be very sensitive to spots down to a few percent filling factor. In VisPhot (0.53  $\mu\text{m}$ ) the tolerance to spot noise is slightly actually higher compared to the other FGS channels, with the 32% 'limit' reached at 6.2% filling factor, reflecting the fall in the SED of the M-dwarf star in this wavelength range, and thus an increase in the fractional photon noise.

Table 5.4 projects that for GJ 1214b at 10% filling factor,  $\sigma_{spot}/\sigma_{photon}$  reaches 66% in NIRSpec which would result in a 19.8% increase in the final uncertainty or error bar, and reaches a maximum of 152% in FGS 1 resulting in an 81.9% increase

in  $\sigma_{cr}$ . The ratio actually is lower in VisPhot than the other FGS channels, probably reflecting increased photon noise in that channel as the stellar signal falls in the Wien region of the GJ 1214 SED. Thus as for HD 209458, spot correction methods or accounting for the increased uncertainty will be essential for NIRSpec and the FGS channels.

For both exosystems, therefore, the visual range FGS channels are particularly sensitive to spots. This may be of course useful for stellar variability monitoring and possibly using the spot profiles in these channels to decorrelate more subtle spot effects in the AIRS channels and NIRSpec. Although AIRS appears 'safe' from spot effects for HD 209458, this will clearly not be the case for more active stars such as HD 189733b. This is a highly active K-type star, and likely to have an appreciable filling factor. Poppenhaeger et al. (2013) estimate this must be at least 5%. We can see that if such a filling factor were present on HD 209458, we would obtain about a very significant 70%  $\sigma_{spot}$  to  $\sigma_{photon}$  ratio in the AIRS channels with faculae included (and parity in the spots only simulations). HD 189733 is slightly brighter than HD 209458 in the K band, so the ratio may be even higher (as the fractional photon noise falls), although the lower photospheric temperature of the K star would reduce the spot temperature contrast which would tend to reduce the ratio. This indicates that active K-type stars could suffer from significant spot noise in AIRS channels, but we should ideally do a future study to look the case of such exosystems specifically.

These findings only apply to the highest resolutions of ARIEL used here (i.e. tier 3 resolutions). If the the resolution was reduced (e.g. for tier 1 or 2 observations),  $\sigma_{photon}$  will fall and the ratios will increase. This can be a subject for a future study.

Since the fractional photon noise will decrease with distance, these findings can be applied to similar exosystems located at the similar or greater distances, as  $\sigma_{spot}$  to  $\sigma_{photon}$  will be no greater than found here. However at closer distances, as  $\sigma_{photon}$  falls, the ratios will increase. Thus a future study could also look at the distance relationship of  $\sigma_{spot}$  to  $\sigma_{photon}$ .

In telescopes with larger apertures, such as JWST, the photon noise limit will be lower and thus the ratios will increase compared to these results. Again to what extent could be a subject for follow-on studies.

### 5.2.7 DISCUSSION

In the second part of this chapter, I examined the contribution of spot-related effects to transit spectroscopy measurements by ARIEL using the two example exoplanets HD 209458b and GJ 1214b simulated in primary transit across their host stars.

The effects of spots is complex, with multiple contributing factors causing wavelength-dependent biases that change in time in an unpredictable way. Using the time domain method performed here with the SpotSim-ExoSim combination in a Monte Carlo approach, simulation of the final impact on the transit spectrum was possible. The simulations included the opposing effects of occulted and unocculted spots as well as realistic levels of variability.

In general we can say that unocculted spots and faculae produce a 'baseline' deviation or distortion in the transmission spectrum, which may vary a small amount with each visit due to changes in filling factor. Correction methods for unocculted spots attempt to de-bias such deviations. However the simulations show that a distribution of possible transit depths arises from this baseline, such that the bias of the baseline unocculted spots over many visits is effectly nullified. This is due to the opposing effects of occulted spots which tend to bias the spectrum in the opposing direction. However for any individual visit, the bias could exist at any point in the distribution. I interpret this to be an 'uncertainty' in the transit depth, due to the combined effects of the baseline deviation of the unocculted spots and the random degree of opposition due to occulted spots. If not corrected for, this uncertainty should be added to the overall uncertainty in the contrast ratio from other noise sources.

Since the distortion is correlated across wavelengths, its effect may not be to make the appearance of spectral features harder to detect (as in photon noise), but it can complicate the fitting of atmospheric models including cloud diagnostics or mimic Rayleigh scattering, and lead to inaccurate conclusions. It would be correct to say that the uncertainty at any wavelength is increased (the 'spot noise') as the difference from the true value of the contrast ratio is increased.

The range of distortion in the contrast ratio spectrum for GJ 1214b is upto +12.7 to -12.2 % at 0.53  $\mu\text{m}$  at the maximum filling simulated factor of 29.5% (with no faculae), but a more likely filling factor of 7.9% gives a range of distortion of +3.9 to - 5.2%. For HD 209458 (assuming faculae), the range of distortion at 0.53  $\mu\text{m}$  reaches +19.9 to -22.1% at 29.5% spot filling factor. However much more likely is a filling factor of 1% which gives a range of +0.9 to -0.5% (assuming faculae).

I find that for 'likely' filling factors in the host stars for HD 209458b (1% with faculae) and GJ 1214b (10% without faculae) that the uncertainties due to spot effects will be significantly below those due to photon noise in both AIRS channels, i.e. well below the precision of the instrument. This reflects a 'protective' effect at mid-IR wavelengths of the increasing photon noise and decreasing spot noise. In AIRS, I project increases in the final uncertainty on the contrast ratio,  $\sigma_{cr}$ , of just 0.3% and 1.0-1.3% for HD 209458b and GJ 1214b respectively. Thus decorrelation may not be indicated or desirable in these cases. However for NIRSspec and the FGS channels, is it very likely that spots will have a significant effect and must be accounted for, with increases in  $\sigma_{cr}$  of upto 99% for HD 209458b and upto 81.9% for GJ 1214b in the FGS channels.

Although in this study I have focussed on these stars alone, this set up can be used for future simulations for other exosystems, other instruments and the testing of spot correction methods. The modifications made for this chapter can be incorporated formally into future versions of ExoSim.

Although M-dwarfs are considered the most active of stars, these simulations show that for the same filling factor, the G-type star will have more spot-related uncertainty on the contrast ratio ('spot noise') due to the higher temperature contrasts of the spots. The increased spot noise in M-dwarfs depend on their increased filling factor. M-dwarfs being dimmer than the G-type stars will also have a higher photon noise uncertainty on the contrast ratio, which again will tend to make the spot effects less relevant despite their greater activity. The sample of G- to M- dwarfs in Andersen & Korhonen (2015) shows a wide range of filling factors. Not all G-type stars will be as quiet as the Sun (as presumably HD 209458 is). Both the G-types stars in that sample have filling factors between 6 to 40%, and thus would certainly have a significant spot noise component in the AIRS band were they at the distance of HD 2094598.

Hence the effect (or not) of spots is highly dependent not only on the star activity in terms of filling factor, and the star class which is related to the temperature contrast of the spots, but also on the baseline photon noise which will be a function of the star brightness (and thus its class and distance) and the telescope, instrument and final binning. The photon noise will vary for each exosystem as will the activity, making generalizations to other exosystems difficult for a given instrument. It may be useful, as mentioned above, to consider a follow on study constructing distance-noise relationship for a given archetypal system, which for a given instrument, may allow an estimate of the spot noise in proportion to photon noise in any given case. This can be used to adjust the size of error bars in real

studies, or to direct the need for correction methods.

From Figures 5.12 and 5.17 we can see that the baseline bias due to unocculted spots is of the order of the size of the error bars (from all spot effects), although getting progressively larger than the error bar with increasing filling factor. If this baseline bias could be determined, then this could be the basis of using observational data to estimate the overall spot-related uncertainty (at any wavelength) for that exosystem. The presence of faculae will complicate this assumption as it affects the baseline, and so it might be most applicable for active stars where the faculae effect is lower.

If the patterns seen in these simulations occur in real stars, then there is a potential pitfall in applying corrections for unocculted spots without also correcting for occulted spots. Ignoring faculae, the corrections, such those based on Equations 5.1 and 5.3, aim to correct the contrast ratio spectrum to that for the unspotted star, effectively applying the correction factor  $1/\alpha(\lambda)$  to  $CR_2(\lambda)$  at all wavelengths. However most commonly this is based on variations in the OOT flux which is a function of the unocculted spot fraction, and does not consider what happens in the transit itself. Thus the correction should work for the unocculted spot baseline distortion (the blue circles in Figures 5.12 and 5.17), as shown in Figure 5.22 A, but in reality for any particular visit, the spectrum will not be at this baseline but somewhere in the distribution below, which appears approximately symmetrical about the true contrast ratio. Thus the correction for unocculted spots will overcorrect in these cases, with a 'corrected' spectrum now falling below the true value, as shown in Figure 5.22 B. A worst case scenario is shown in Figure 5.22 C where the correction results in about twice the error compared to the random uncertainty (grey region) if no correction is applied. Thus it would be important to correct both unocculted and occulted spots, removing the bias of each. The latter is not straightforward and may involved novel methods such as principal components analysis to detect and remove spot effects at the level of the light curves. Figure 5.22 D shows the effect of occulted spot decorrelation reducing the potential region of distribution so that the correction factor is more accurate when applied. It is possible that if spots are concentrated at certain latitudes then the 'grey zone' will be distributed differently, but the potential inaccuracies due to unaccounted for spot occultations would remain depending on the range of occulted filling factors encountered. If faculae are present, these too tend to oppose the occulted spot effect, shifting the 'baseline' bias as shown in Figures 5.13 and 5.18, which also would make the corrections that account only for unocculted spots less accurate. Thus if a robust method for decorrelating occulted spots is not possible, or it is not

possible to rule out spot crossings, it may be better to not attempt to correct the bias at all but to add an uncertainty to the data<sup>16</sup> which would be on the order of  $\pm (CR_2(\lambda) - CR_1(\lambda))$ , as this approximates the distribution around the true value.

Distortions of a few percent in the direction of increasing contrast ratio could mimic the Rayleigh scattering slope as has been suggested by some authors (McCullough et al., 2014; Oshagh et al., 2014). The maximum positive distortions in this study could indeed achieve this effect. However for this to be a consistent finding across observations, the unocculted spots baseline distortion must not be significantly opposed by spot crossings and the distribution of possible spectra in the 'grey zone' needs to be narrow (much like the appearance of the grey zone in Figure 5.22 D). This may be possible if spots are concentrated in latitudinal bands that the planet does not cross or barely crosses.

As mentioned earlier, the study by Oshagh et al. (2014) claimed a deviation of upto 10% could occur in the planet radius estimated from spot and and plage crossings, and that plage crossings in particular could explain slopes attributed to Rayleigh scattering. The results of this study although supportive of the fact that plage crossings would increase the transit depth, generally do not support their findings. Even accounting for small differences in temperature and planet/star radius between the two studies, the deviations obtained in their simulations greatly overestimate the likely effect of occultations. Firstly, this is because they do not appear to include the effects of unocculted spots which will always be present and will tend to oppose the effect of the occultation. Secondly, they appear to consider faculae in isolation rather than with corresponding occulted spots which tend to oppose the occultation effect of faculae. Thirdly, they do not use realistic size distributions for the spots and faculae as used in this study, meaning that a single spot or faculae can cause a large impact on the light curve if all the filling factor is concentrated in one or a few places. This seems an unlikely situation. As an example, the highest distortion in their simulations is the case of an M-dwarf star with 6.25% filling factor with occulted plages alone (which is unrealistic), which causes about a 10% increase in the planet radius, at 0.5  $\mu\text{m}$ , where the baseline  $R_p/R_s$  was 0.15. This is about a 20% increase in the contrast ratio. In these simulations, the highest positive distortion we see for the M-dwarf star at 0.5  $\mu\text{m}$  is about +12.7% in contrast ratio but this occurs at a filling factor of 29.5% (with spots only). In another case, Oshagh et al. (2014) using spots only with 1% filling factor, find a 4% decrease in planet radius due to spot crossings at 0.5  $\mu\text{m}$ , which amounts to about -8% change in contrast ratio. In this study we obtain only a maximum -0.9%

---

<sup>16</sup> Such an approach was taken by Southworth (2011) in his analysis of Kepler light curves.

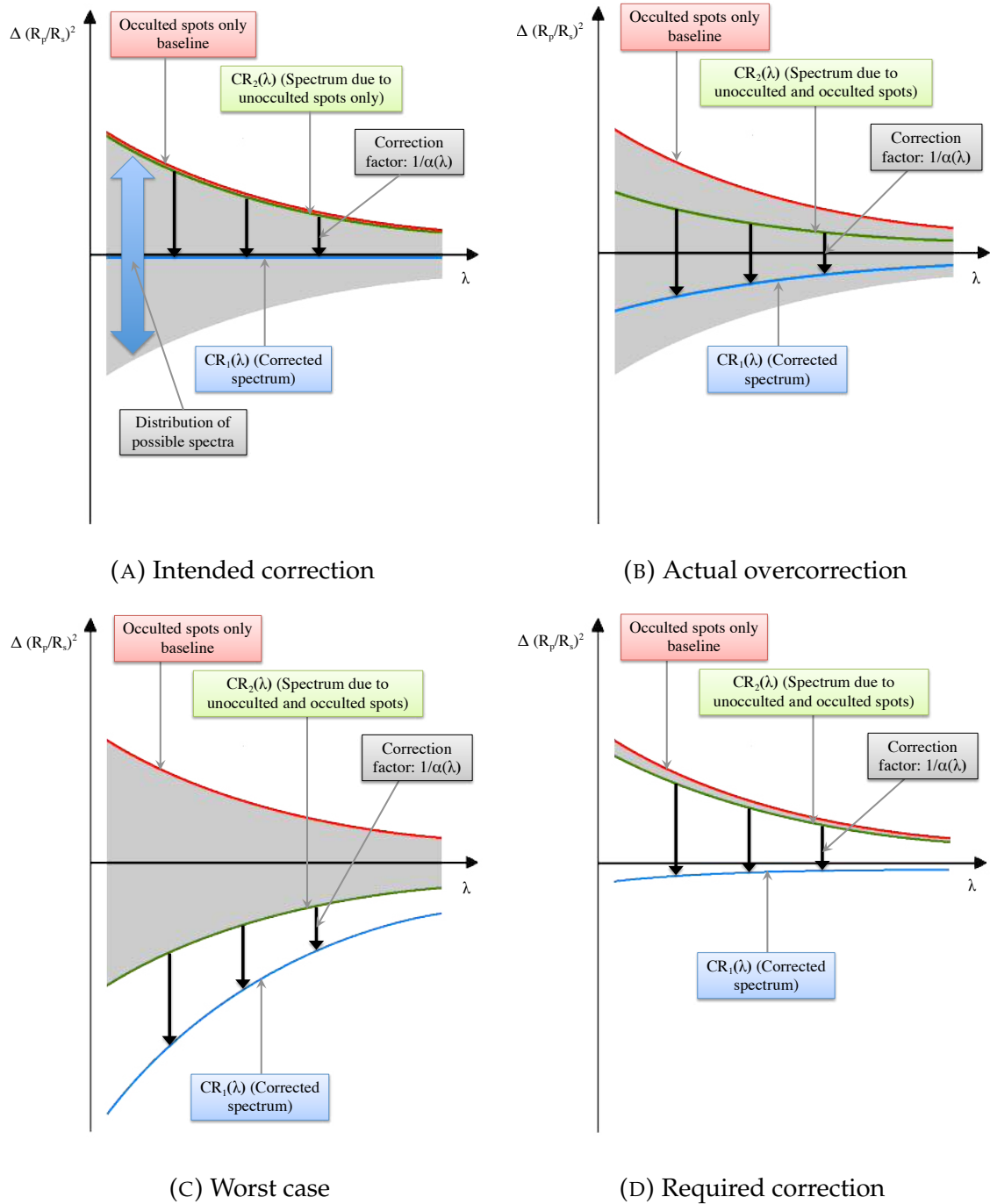


FIGURE 5.22 Potential issues with correction for unocculted spots. A: Intended correction aims to reverse the bias due to unocculted spots. However a potential distribution of biased spectra exist in the grey region due to opposing effects of occulted spots. B: This can lead to an overcorrection if the occulted spot effect is not corrected too. C: In the worst case the error from the true contrast ratio can be made much worse than the uncertainty in the grey zone. D: If the occultation effect is corrected reducing the potential distribution from the baseline, then the correction to the unocculted spots is likely to be more accurate.

distortion in the contrast ratio at the same wavelength and filling factor assuming spots only. They also do not account for the the effect of repeated observations. Since the occultation effect is to some extent 'random', the distortion obtained on another occasion may be different. This is taken into account in this study through the Monte Carlo simulation.

It is difficult to verify the accuracy of these simulations given the paucity of data and uncertainties in interpretation regarding the true effect of spots. We could however in future studies look to simulate known active stars with transiting planets such as the well-studied HD 189733b system, to see if we can replicate some aspects of the data, such as the brightness variations expected or the observed spot occultation frequency and amplitudes. However the paucity of data is also one reason to actually do such simulations, to give a first order idea of the extent of the problem and how it could impact observations. Other limitations of this study include the accuracy of the faculae simulations preformed here. The shape of realistic faculae were not well represented, the limb-brightness relationship was not simulated and I made a speculation of how the temperature will scale with star spot temperature. Also, although I make an informed prediction for the Q values, there is no quantitative data at higher filling factors to verify the exact extrapolation made. Despite these limitations the simulations were overall successful in elucidating the effect of spots and probably to a first order the counter-effects of faculae. I also did not examine one of the important effects of spots, that of spectral feature enhancement. This again could be examined with the framework set up here in a future study using realistic model stellar spectra rather than blackbodies.

---

In this chapter, I applied the generic time domain simulator to one of the key problematic issues in transit spectroscopy, that of stellar variability and activity. This was examined extensively looking at the effects of both convection-driven mechanisms and magnetic activity mechanisms. Flares were not studied. The effects of noise from pulsations and granulation and the more complex effects of spots and faculae were quantified for two well-studied exosystems, for which we are now able to make predictions about the stellar noise contribution to ARIEL observations.

## CHAPTER 6

# OBSERVING TRAPPIST-1 PLANETS WITH ARIEL

---

**E**ARTH-LIKE planets represent amongst the most challenging but also most intriguing of targets for transit spectroscopy. Having utilized the generic transit spectroscopy simulator in the context of characterising both instrumental and astrophysical noise sources, in this chapter, I apply it to the question of the detectability of the atmospheres of Earth-like and Earth-sized planets. I use ExoSim to examine the question of ARIEL's capacity to observe temperate terrestrial planets by focusing on the case of the recently-discovered TRAPPIST-1 planets (Gillon et al., 2017), a system of 7 terrestrial planets with 4 in the habitable zone of an ultra-cool M star. This system is currently of great interest in the exoplanet community as it exemplifies an ideal case for transit spectroscopy of terrestrial planets, orbiting a nearby M-dwarf star. ARIEL's design and science goals were focused more on warmer planets ( $>400$  K), however it is of interest to know if the mission could detect atmospheres on temperate terrestrial planets, under which spectral resolution, and what types of atmosphere.

## 6.1 THE TRAPPIST-1 EXOSYSTEM

### 6.1.1 BACKGROUND

TRAPPIST-1 is an ultra-cool M8 dwarf ( $0.08 M_{\odot}$ ,  $0.0117 R_{\odot}$ , K mag 10.3) located 12.1 pc away, that is known to host 7 terrestrial-sized planets (Gillon et al., 2016, 2017). Planet parameters are shown in Table 6.1. According to Planetary

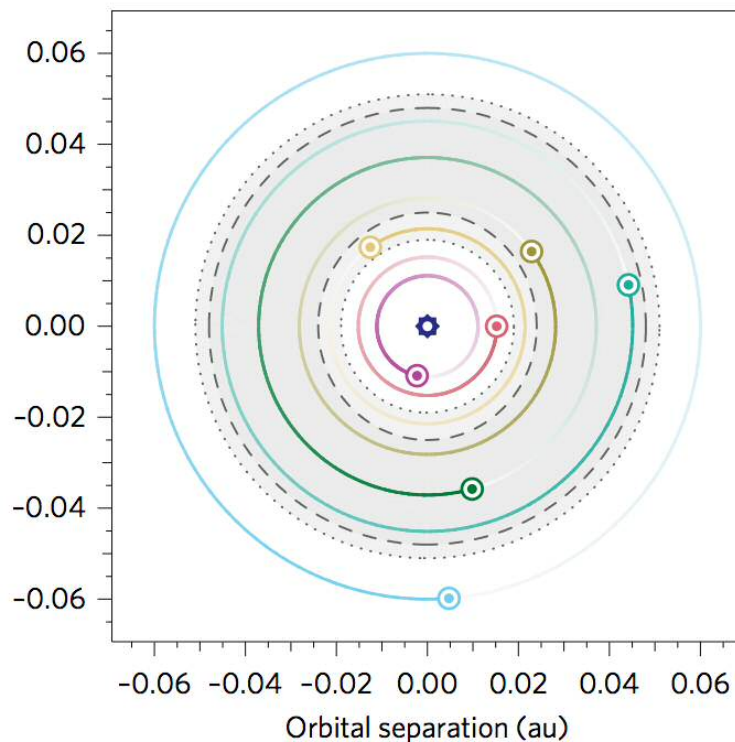


FIGURE 6.1 TRAPPIST-1 system of seven terrestrial planets. Grey region shows habitable zone, with conservative and optimistic limits marked. Planets e, f and g fall in the conservative zone, while planet d is within the optimistic zone. Figure from Luger et al. (2017).

Habitability Laboratory of the University of Puerto Rico at Arecibo<sup>1</sup> and also illustrated in Luger et al. (2017), planets e, f and g are in the 'conservative' habitable zone with planet d in the 'optimistic' habitable zone as defined by Kopparapu (2013) (Figure 6.1). The planets exist in a 7-member resonant chain (Luger et al., 2017).

These planets are of great interest currently as potential targets for transit spectroscopy by existing and future observatories. All 7 planets are rocky, giving excellent opportunities to study several terrestrial planets in a system that may be highly revealing in terms of constraining planet formation theories pertaining to small stars, as well as a potential opportunity in the search for habitable worlds. Barstow & Irwin (2016) evaluated the potential of JWST in performing transit spectroscopy of the system, and found that Earth levels of ozone could be detectable in 60 transits for planet b and 30 transits for planets c and d.

de Wit et al. (2016) conducted the first transit spectroscopy study of the

<sup>1</sup> <http://phl.upr.edu/>

TABLE 6.1 TRAPPIST-1 system parameters.

Planet	b	c	d	e	f	g	h
Period (d) <sup>a</sup>	1.51	2.42	4.05	6.10	9.21	12.35	18.77 <sup>b</sup>
Radius ( $R_{\oplus}$ ) <sup>a</sup>	1.086	1.056	0.772	0.918	1.045	1.127	0.752 <sup>b</sup>
Mass ( $M_{\oplus}$ ) <sup>a</sup>	0.85	1.38	0.41	0.62	0.68	1.34	0.086 <sup>c</sup>
Density(g/cm <sup>3</sup> )	3.66	6.46	4.91	4.42	3.29	5.16	1.12
$T_{14}$ (s)	2193.3	2550.9	2957.5	3448.7	3760.0	4115.4	4523.8
$T_{eq}$ (K)	435.6	372.3	313.6	273.6	238.4	216.2	188.5

<sup>a</sup> From Gillon et al. (2017) except where stated.

<sup>b</sup> From Luger et al. (2017).

<sup>c</sup> From Wang et al. (2017) which is awaiting publication.

TRAPPIST-1 system using the Hubble WFC3 IR instrument in scanning mode, obtaining a combined transmission spectrum for planets b and c. This was found to be featureless but ruled out hydrogen-dominated atmospheres at 10 sigma. Coinciding transits of the many planets in this system may complicate future studies.

Another issue for transit spectroscopic studies may be the stellar activity of the host star, which potentially could present astrophysical noise, as examined in Chapter 5. Wheatley et al. (2017a) found that the TRAPPIST-1 planets will be highly irradiated by X- and EUV radiation many times stronger than the Earth, with the potential to alter primary and secondary atmospheres. This may also affect the potential for life especially in the absence of a protective magnetosphere or photochemical shielding in the upper atmosphere.

Tidal locking may also reduce the strength of a magnetic field generated by the planet. According to Kasting's classic habitable zone diagram (Figure 6.2) all of these planets would be within the tidal lock zone. The formula by Peale (1977) gives the distance  $r$  from the star at which a planet will become tidally locked after  $t$  years:

$$r = 0.027(p_0 t / Q)^{1/6} M_s^{1/3} \quad (6.1)$$

all in cgs units, where  $p_0$  is the original rotation period, set here to 24 hours,  $Q$  is a 'dissipation' factor, set here at 100 after Kasting et al. (1993), and  $M_s$  is the stellar mass in unit of solar mass,  $M_{\odot}$ . Analysis of K2 data by Luger et al. (2017) finds a rotational period for the star of 3.3 days consistent with an age of 3-8 billion years. This gives a tidal lock distance of 0.2038-0.24 AU using the above formula. This would indicate tidal locking for all planets.

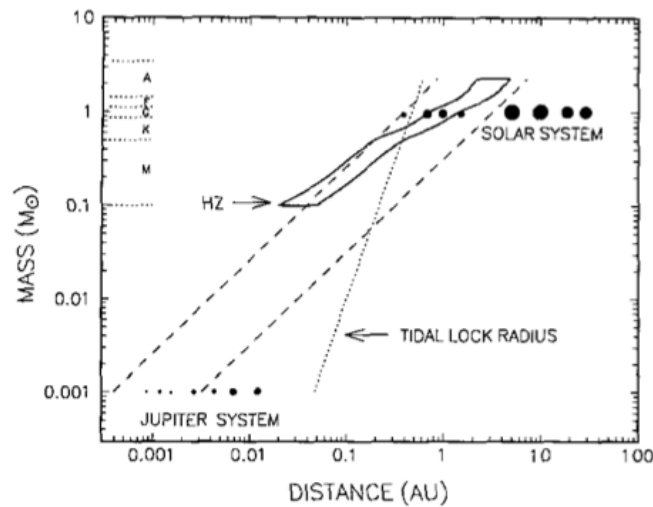


FIGURE 6.2 ZAMS habitable zone and tidal lock limit. Figure from Kasting et al. (1993).

This is supported by N-body simulations of the system by Luger et al. (2017) who determine the planets' spins to be tidally synchronized with small obliquities. Tidal locking increases the equilibrium temperature of the planet, and will tend to reduce the Coriolis effect, both of which will impact the global circulation of the atmosphere and temperature distribution. Luger et al. (2017) find that planet b could have a tidal heat flux similar to that of Io, and planets c-e have tidal fluxes in excess of the internal heat flux of the Earth. Such high tidal fluxes could result in vulcanism with implications for internal structure and atmospheric composition.

In terms of internal composition, Gillon et al. (2017) found densities for the inner 6 planets consistent with rocky planets, with a lower density for planet f consistent with a high volatile content ( $0.6 \times$  Earth density, consistent with the calculated value in Table 6.1), which could be in the form of an ice layer and/or an atmosphere. This possible composition for planet f would be consistent with a formation scenario further out from the star with subsequent inward migration.

The density of planet h however appears much lower than the other planets (Table 6.1), consistent with a 'water world' scenario, or perhaps a large primordial  $H_2$ -He envelope. Luger et al. (2017) has speculated that in terms of an atmosphere, planet h could be dry from hydrodynamic escapes of its primordial atmosphere during the super-luminous phase<sup>2</sup>, or could also be consistent with retaining a primordial hydrogen-rich atmospheres which in turn could provide sufficient insulation and greenhouse effect to retain liquid water.

<sup>2</sup> It is thought that ultra-cool dwarfs go through an early hot pre-main sequence phase that could subject close-in planets to intense temperatures.

The exact composition of the atmospheres will depend on many factors including original location of formation in the disc and disc composition, subsequent migration history, and evolution through local thermodynamic equilibrium (LTE) and non-LTE chemical processes, effects of stellar irradiation, vulcanism, replenishment by impacts, consequences of tidal effects and, perhaps, biology.

As noted above, the system has several planets in the habitable zone, Gillon et al. (2017) noting that planets c, d and f have stellar irradiation very close to that of Venus, Earth and Mars, respectively. They also speculate that all the planets could, under various circumstances, harbour liquid water. Using climate models, they find that planets e, f and g could sustain liquid water oceans assuming Earth-like atmospheres. The models of planets b, c and d result in runaway greenhouse effects, but they suggest that limited regions of water could continue to exist if these survive the super-luminous phase. A scenario where the planet h could harbour water would involve tidal heating or retention of a primordial H<sub>2</sub>-He atmosphere, as mentioned above.

Wolf (2017) on the other hand, using 3-D climate modeling with atmospheres restricted to N<sub>2</sub>, CO<sub>2</sub> and H<sub>2</sub>O, and assuming abundant water, suggests that only planet e is likely to retain liquid water. As with Gillon et al. (2017), a runaway greenhouse effect occurs on the inner 3 planets leaving them dry, and the outer 3 planets result in freezing. While planet e receives 0.662 of the Earth's irradiation from the Sun (Gillon et al., 2017), Wolf (2017) finds various atmospheres could result in greenhouse warming of the planet to sustain liquid water on the surface. Planet e was thus considered the most 'habitable' planet.

Pierrehumbert & Gaidos (2011) showed using a 1-D radiative-convective model and a model of hydrogen escape that primordial H<sub>2</sub>-He atmospheres could be retained on a 3  $M_{\oplus}$ -sized rocky planet at sufficient distance from the host star, and that these planets could have a greenhouse effects that extend the habitable zone much further out than normally considered.

Such primordial atmospheres could be potentially highly detectable in primary transit given the likely large scale height and thus could be within the capabilities of the ARIEL telescope and instrument.

### 6.1.2 THE FEASIBILITY OF ARIEL OBSERVATIONS

For ARIEL these planets are intriguing targets that could be high priority given the unique nature of the system, giving one of the best opportunities to date

to study the atmospheres of temperate terrestrial planets. Being a dedicated exoplanet space telescope, ARIEL would be in a unique position for repeated measurements of the various planets.

However the star is 2 magnitudes dimmer in K band than GJ 1214, considered one of the dimmest targets for the mission. The fractional photon noise will therefore be high. In addition, the pointing accuracy of the AOCS worsens with a dimmer target, resulting in more jitter noise.

Atmospheres of temperate terrestrial planets will of course present extremely small signals, and thus are extremely challenging targets for ARIEL. It may be the case however that certain atmospheres such as a primordial atmosphere theorised above might exist and would represent more feasible targets. Signatures of outgassed molecules could potentially be detectable under the high scale heights of such an atmosphere.

Combining all these factors together to assess the atmospheric signal and noise obtained by ARIEL is another excellent utilization of the ExoSim simulator. Therefore in this chapter, I use ExoSim to assess the feasibility of ARIEL to detect the atmospheres of each TRAPPIST-1 planet. I examine a range of possible atmospheric types, as well the feasibility at different spectral resolutions corresponding to each 'tier' in the ARIEL observational strategy.

## 6.2 METHODOLOGY

The method used here has the following steps, which are subsequently described in more detail.

- 1) Estimate the 'signal' for each planet's atmosphere assuming a 'maximum amplitude' spectral feature,  $A_{pt}$ , in primary transit and  $A_{se}(\lambda)$  in secondary eclipse. The former is repeated for atmospheres of different mean molecular masses.
- 2) Perform out-of-transit (OOT) noise simulations in ExoSim for the host star, which are then processed to obtain the contrast ratio noise per spectral bin, or photometric channel,  $\sigma_{cr}(\lambda)$ .
- 3) In each spectral bin or photometric channel obtain the SNR for the maximum amplitude spectral feature for 1 transit for each channel, and then calculate the number of transits,  $N_{transits}$ , needed to obtain a goal SNR of 5. This is carried out for the different observational 'tiers' in the ARIEL science strategy which represent different binned spectral resolutions. The overall behaviour of the spectroscopic channels can be represented by the median  $N_{transits}$  for the channel
- 4) Compare the number of transits required with the maximum possible number

of transits for each planet during the ARIEL mission lifetime.

### 6.2.1 ESTIMATING THE SIGNAL

Since the TRAPPIST-1 planets are not constrained in terms of possible atmosphere types, with the partial exception of planets b and c, I adopt a general approach assuming detection of a maximum-sized spectral feature for atmospheres with a range of mean molecular weights.

For each of the 7 planets, nominal maximum primary transit and secondary eclipse amplitudes can be estimated using Equations 1.7 and 1.8 from Chapter 1, to give  $A_{pt}$  (which has no wavelength dependency) and  $A_{se}(\lambda)$ .

For  $A_{pt}$ , the scale height  $H$  must be estimated for each planet (Chapter 1 Equation 1.6). Thus we need to calculate a surface gravity,  $g$ , an atmospheric temperature,  $T_p$  (assumed here to be equal to the equilibrium temperature,  $T_{eq}$ ), and obtain a mean molecular mass for the atmosphere,  $\mu$ .

The gravity in each case can be calculated from the mass and radius given in Table 6.1, and the equilibrium temperature for a tidally locked planet found with:

$$T_{eq} = (1 - \rho)^{0.25} (1/2)^{0.25} (R_s/a)^{0.5} T_s \quad (6.2)$$

where  $\rho$  is the Bond albedo,  $R_s$  and  $T_s$  are the stellar radius and temperature, respectively, and  $a$  is the semi-major axis<sup>3</sup>. It would probably not be correct to use a zero albedo for such planets as both Mars and Earth have appreciable Bond albedo of 0.25 and 0.3, respectively. Gas giants in the solar system have an albedos of around 0.3. Venus is an outlier with a very high Bond albedo of 0.77, and Mercury has a low albedo of 0.068<sup>4</sup>. I thus assume a likely Bond albedo value of 0.3 for each planet.  $T_s$  is set at 2559 K (Gillon et al., 2017). The calculated values for  $T_{eq}$  are given for each planet in Table 6.1. These temperatures are somewhat higher than those in Gillon et al. (2017) where it appears they did not take into account tidal locking and used a zero albedo.

Since the mean molecular mass is unconstrained, I use a range of values for  $\mu$ : 2.22 g/mol (H<sub>2</sub>-He dominated, Jupiter-like), 18.0 g/mol (water-dominated), 28.97 g/mol (Earth-like), 43.45 g/mol (Venus-like), and intermediate values: 5, 8

<sup>3</sup> This equation assumes that the tidally locked planet re-radiates heat from only half of its surface area, i.e. from the dayside hemisphere with no advection of heat to the nightside.

<sup>4</sup> Except where mentioned otherwise, albedo and mean molecular masses quoted in this section are obtained from NASA Planetary Fact Sheets:  
<https://nssdc.gsfc.nasa.gov/planetary/planetfact.html>

and 12 g/mol. The Venus-like mean molecular weight is typical of a CO<sub>2</sub>-N<sub>2</sub> atmosphere, e.g. Mars (43.34 g/mol). The Earth's atmosphere of course bears the hallmark of O<sub>2</sub>, but its mean molecular weight is similar to that of Titan's CH<sub>4</sub>-N<sub>2</sub> atmosphere, measured between 27.2-29.3 g/mol (Hathi et al., 2008). Thus the Earth-like mean molecular weight can act as a marker for potential Titan-like atmospheres as well. The value of  $A_{pt}$  for each planet and at each value of  $\mu$  is given in Table 6.3.

$A_{se}(\lambda)$  was found for each spectral bin (or photometric channel) for each planet. In Equation 1.8,  $T_p$  is approximated by  $T_{eq}$  obtained above and  $T_s$  is 2559 K. The radius of the star,  $R_s$ , is set to  $0.117 R_\odot$  (Gillon et al., 2017), and  $R_p$  is obtained from Table 6.1 for each case. The median values for  $A_{se}(\lambda)$  in each channel (binned at tier 1 resolution) for each planet are given in Table 6.4.

## 6.2.2 NOISE SIMULATION

Although ExoSim could obtain the noise on the contrast ratio spectrum through full transit Monte Carlo simulations of each planet in turn, as performed in Chapters 3 and 5, this would be a very time-consuming and computationally intensive approach, considering 7 different planets are being evaluated. I thus use the OOT noise approximation, described in Subsubsection 4.2.2.2, using Equation 4.1 to find the contrast ratio noise,  $\sigma_{cr}(\lambda)$  for each planet. I use the following version of the equation here:

$$\sigma_{cr}(\lambda) \approx \frac{\sqrt{2}}{\sqrt{\frac{T_{14}}{\tau_{int}(\lambda)}}} \frac{\sigma_{oot}(\lambda)}{S_{oot}(\lambda)} \quad (6.3)$$

$T_{14}$ , the transit duration was calculated for each planet from its system parameters, with the results shown in Table 6.1. The remaining parameters were obtained directly from the ExoSim simulation.

For the ExoSim simulation, I follow the 'noise budget' methodology as described in Section 4.5. The ARIEL model used (Table 6.2) for this study matches the one used in that section, the 'final' end-of-Phase A design, with the exception that 18  $\mu\text{m}$  pixels are modeled in AIRS Ch0 and Ch1 with f-numbers scaled in proportion, and the dark currents used here are more optimistic assuming the use of Teledyne H1RG or H2RG detectors where the dark current increases with the cutoff wavelength; the values simulated are 0.05 e<sup>-</sup>/s in the visual channels and NIRSpec, 1 e<sup>-</sup>/s in Ch0 and 18 e<sup>-</sup>/s in Ch1. VisPhot was excluded in this study

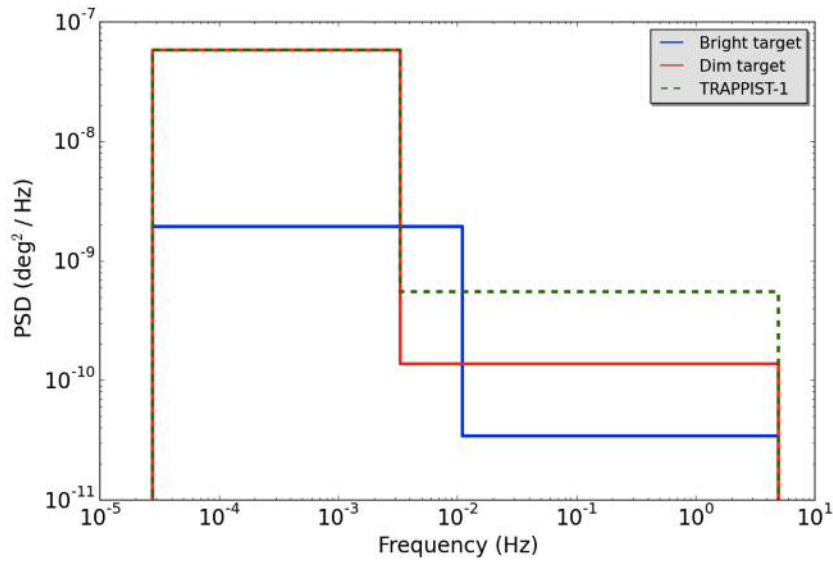


FIGURE 6.3 Pointing jitter power spectral density profile for TRAPPIST-1. ‘Bright’ and ‘dim’ PSDs developed for the ARIEL Phase A study are shown in comparison.

due to the very low signal obtained in that channel, requiring extremely long integration times. Aberrated PSFs were modeled as before (described in Chapter 4).

A custom pointing jitter power spectral density (PSD) frequency profile was produced for this simulation, based on the estimated accuracy of the ARIEL fine guidance system to track a star with the magnitude of TRAPPIST-1<sup>5</sup>. This PSD is similar to the ‘dim’ target PSD developed in Chapter 4 except that the RPE (high frequency) jitter rms is doubled, giving an overall bi-axial rms of 276 mas (or 195 mas per axis). The TRAPPIST-1 PSD is shown in comparison to the ‘dim’ and ‘bright’ PSDs from Chapter 4 in Figure 6.3.

The host star was modeled with a PHOENIX stellar spectrum ( $T=2600$  K,  $\log g=5$ ,  $[Fe/H]=0$ ) and parameters for TRAPPIST-1 and its planets obtained via the Open Exoplanet Catalogue, which correspond to values given in Gillon et al. (2017). The exception is for planet h where the period, radius and orbital parameters were taken from Luger et al. (2017), with the mass taken from the unpublished paper, Wang et al. (2017). The latter is the only current mass estimate for this planet. The integration times,  $\tau_{int}$ , for each channel obtained using the ‘time to saturation’ method, are given in Table 6.2. In each simulation, TRAPPIST-1 was ‘observed’ for 35971 seconds, a time interval that captures the lowest frequency in

<sup>5</sup> Estimated pointing accuracy calculation performed by E. Pascale.

the pointing jitter power spectrum used.

As in Section 4.5, each simulated observation consisted of double NDR exposures, to permit correlated double sampling (CDS) in post-processing, where  $\text{NDR}_0$  had negligible integration time, and negligible overheads were assumed per exposure cycle. Since TRAPPIST-1 planets will be most likely observed with up-the-ramp reads, the CDS read out noise obtained here is pessimistic.

Noise sources included in the simulations were the same as used in Section 4.5, each run in isolation as well as combined for total noise, and again 20 realizations were run for noise sources containing jitter noise to obtain the average noise obtained, and 5 realizations for noise sources without jitter. As before, QE variations of 5% rms were applied to each channel's pixel array and later flat fielded out in data reduction with a 0.5% rms uncertainty remaining.

The ecliptic latitude of TRAPPIST-1 is  $0.63^\circ$ . This close to the ecliptic, the zodiacal dust is will be appreciably denser than modeled for in the baseline formula. Based on the analysis shown in the Appendix, I multiply the zodi flux from the formula by a factor of 2.23, for these simulations.

### 6.2.3 DATA REDUCTION

The same data reduction pipeline as used in Section 4.5 was used again. The optimal apertures were established using the same methods. There was appreciable added post-ISD spatial jitter noise at the blue end of Ch0, probably resulting from the increased jitter rms in this simulation compared to previously. This was reduced considerably by widening the aperture at the blue end by 3 pixels, i.e. applying a mask as calculated in Chapter 4 Equation 4.8, using  $x = 3$ . Similarly a mask with  $x = 1$  was used for Ch1 to reduce spatial jitter noise, and no widening was needed in NIRSpec. For the photometric channels, optimal SNR was obtained with  $r = 6$  for FGS 2 and  $r = 7$  for FGS 1, where the aperture radius is  $r f \lambda$ . Optimal extraction correction factors, for each spectral bin in the spectroscopic channels, were calculated in the way previously described.

Unlike in Section 4.5, the results for each spectroscopic channel are binned to three different spectral resolutions each corresponding to an observing 'tier'. The R powers in each tier for each channel are given in Table 6.2. For each tier, the mean signal,  $S_{out}(\lambda)$ , and noise,  $\sigma_{out}(\lambda)$ , per spectral bin (or photometric channel) were found for each noise source and for total noise, in each realization, with average values obtained for each

Thus all the required parameters to calculate  $\sigma_{cr}(\lambda)$  in Equation 6.3 were

TABLE 6.2 ARIEL instrument prescription used for TRAPPIST-1 study, also showing binned spectral resolutions per observing tier and integration times used per channel.

Parameter	FGS 1	FGS 2	NIRSpec	AIRS Ch0	AIRS Ch1
Wavelength ( $\mu\text{m}$ )	0.91 <sup>a</sup>	1.13 <sup>a</sup>	1.25-1.90	1.95-3.9	3.9-7.8
R (band start-band end)	N/A	N/A	36-55	95-163	30-66
Binned R (tier 1,2,3)	-	-	5,10,20	10,30,100	5,15,30
f-number	24.62	31.30	19.34	15.84	7.63
Optical efficiency (mid-band)	0.60	0.60	0.65	0.45	0.46
Detector QE	0.55	0.55	0.55	0.55	0.55
Pixel size ( $\mu\text{m}$ )	18	18	18	18	18
Pixel scale ( $^{\circ}$ /pixel)	4.58 x10 <sup>-5</sup>	3.60 x10 <sup>-5</sup>	4.85 x10 <sup>-5</sup>	6.11 x10 <sup>-5</sup>	1.23 x10 <sup>-4</sup>
Pixel diffusion length ( $\mu\text{m}$ )	1.7	1.7	1.7	1.7	1.7
Slit width (pixels)	N/A	N/A	13	17	13
Dark current (e <sup>-</sup> /s)	0.05	0.05	0.05	1.0	18.0
Linear well depth (ke <sup>-</sup> )	100	100	100	70	70
Read noise (e <sup>-</sup> )	16	16	16	16	16
PSF aberration	WFE PSF	WFE PSF	2xf-number	None	None
Integration time (s)	130.1	126.1	90.4	232.7	104.6

<sup>a</sup> central wavelength

obtained.

For interest we can look at the OOT 'noise budget' for ARIEL observing TRAPPIST-1 presented in the same way as those in Section 4.5. This is shown in Figure 6.5 for the 'tier 3' level of spectral resolution. The dotted lines show the expected reduction in variance due to optimal extraction. AIRS Ch0, FGS 1 and FGS 2 appear close to photon-noise limited. In NIRSpec we see spectral jitter noise exceeds source photon noise in one spectral bin. In AIRS Ch1, the total noise is progressively increased above the source photon noise with longer wavelengths, reflecting the contribution of dark current, read noise and zodiacal noise. The dark current in particular exceeds the source photon noise at the red end of this channel. Optimal extraction only improves the total noise noticeably at the red end of Ch1, and generally does not make a difference in the other 2 spectroscopic channels.

As seen in Figure 6.5, the assumption of no correlated noise for Equation 6.3 is a good one for all channels except perhaps NIRSpec, due to the spike in spectral jitter noise, jitter noise being the only correlated noise simulated. I tested for correlated noise in the total noise in NIRSpec by performing 'time averaging' as described in Chapter 1. Figure 6.4 shows how the noise from the simulations in two selected spectral bins at tier 3 resolution ( $R=20$ ) falls with  $N$ , the number of points in each bin, upto  $N = 8$ , compared to the predicted noise from Chapter 1 Equation 1.21. There is virtually no difference with the prediction. Over all six spectral bins the measured noise did not exceed the prediction by more than 1.3% and on average was only 0.04% higher. This indicates no significant element of time correlation in the noise.

The reason why we do not see a significant correlated component may be partly due to the choice of PSD, where 2 flat frequency profiles are used; this approximation although accounting for the likely rms of the jitter, may manifest in more uncorrelated behaviour of the jitter noise than may be the case in reality.

#### 6.2.4 SNR AND $N_{transits}$ CALCULATION

Feasibility is assessed through determining the number of transits,  $N_{transits}$ , needed to achieve the goal SNR for detecting the amplitude of a spectral feature in the final transmission spectrum, and then comparing this to the number of observable transits possible in the mission lifetime.

Following the discussion in Subsection 1.2.3, the noise on the nominal maximum primary transit and secondary eclipse amplitude signals are given by Equations 1.12 and 1.15, respectively. In those equations  $S_{oot}$  is the *total* signal collected

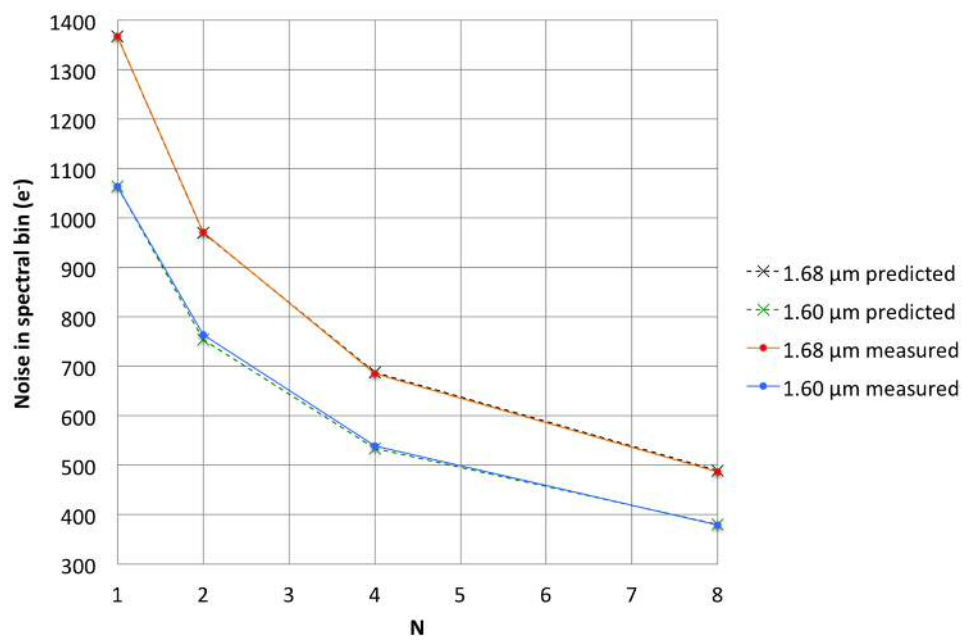


FIGURE 6.4 Testing for correlated noise in NIRSpec by time averaging.

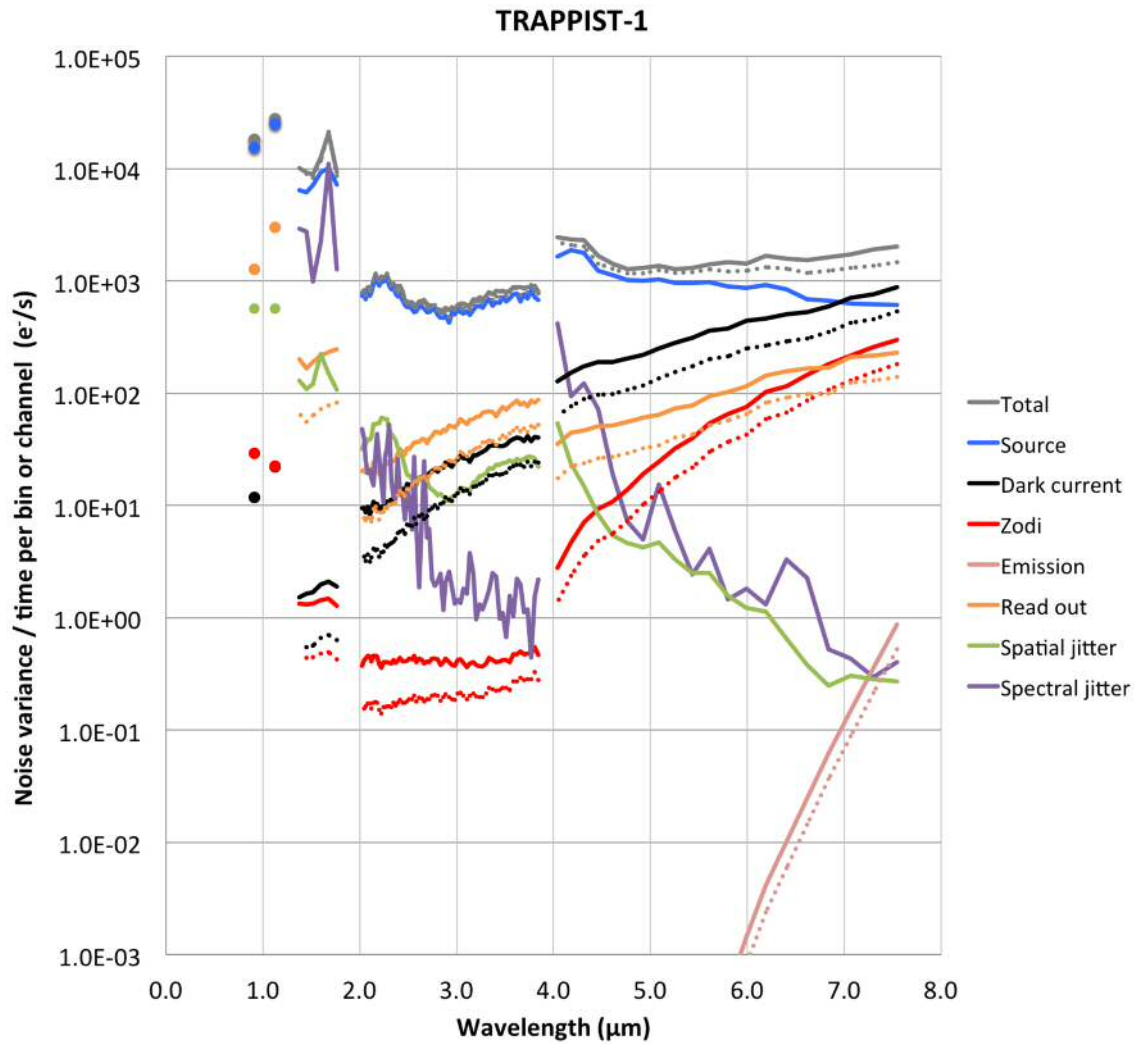


FIGURE 6.5 ARIEL noise budget for OOT observation of TRAPPIST-1. Combined jitter shown for photometric channels (green dots). Dashed lines show expected improvement due to optimal extraction. In FGS 2, the dark current noise marker (black dot) is obscured by the zodiacal noise marker (red dot).

OOT, assuming an equal amount of time observed in- and out-of-transit, which we can term here  $S'_{oot}$  here for clarity. In this chapter  $S_{oot}$  refers to the mean signal per exposure, so that  $S_{oot} = S'_{oot}/(N/2)$ , where  $N$  is the total number of exposures, and  $N = 2 \times T_{14}/\tau_{int}$ . Hence the noise on  $A_{pt}$  in any spectral bin at wavelength  $\lambda$  is given by:

$$\sigma_{A_{pt}}(\lambda) \approx \frac{\sqrt{2} \sigma_{oot}(\lambda)}{\sqrt{\frac{T_{14}}{\tau_{int}}} S_{oot}(\lambda)} \quad (6.4)$$

Which is the same as the noise on the contrast ratio from Equation 6.3, following the discussion in Subsection 1.2.3. Thus the SNR is given by:

$$SNR_{A_{pt}}(\lambda) = \frac{A_{pt}}{\sigma_{A_{pt}}(\lambda)} \quad (6.5)$$

In the same way:

$$\sigma_{A_{se}}(\lambda) \approx \frac{\sqrt{2} \sigma_{oot}(\lambda)}{\sqrt{\frac{T_{14}}{\tau_{int}}} S_{oot}(\lambda)} \quad (6.6)$$

and

$$SNR_{A_{se}}(\lambda) = \frac{A_{se}(\lambda)}{\sigma_{A_{se}}(\lambda)} \quad (6.7)$$

The measured values from the ExoSim simulations will give the SNR per spectral bin (or per photometric channel) for 1 transit.

Previous studies such as Rauer et al. (2011) and Tessenyi et al. (2013) have adopted a goal SNR for detection of a spectral feature of 3. However an SNR of 5 is more widely considered to be a criterion for a solid detection. I therefore use  $SNR_{goal} = 5$  in this study.

If  $SNR_1$  is the SNR in each spectral bin (or photometric channel) for 1 transit (which will equal the values of  $SNR_{A_{pt}}(\lambda)$  or  $SNR_{A_{se}}(\lambda)$  from above), then the number of transits to achieve the goal SNR is given by:

$$N_{transits} = \left( \frac{SNR_{goal}}{SNR_1} \right)^2 \quad (6.8)$$

Since  $SNR_1$  will vary across the spectroscopic bins in each channel, for the purposes of reaching conclusions about the performance of each channel as a whole, I use the median value of  $N_{transits}$  in each channel. This can then be compared to the number of transits possible,  $N_{limit}$ , if the telescope were to observe every transit of

a given planet in the operation observing lifetime of the mission:

$$N_{limit} = \frac{L_{tel}}{P} \quad (6.9)$$

where  $P$  is the orbital period of the planet (given in Table 6.1), and  $L_{tel}$  is the operational lifetime of the mission. Here I use 3.5 years as  $L_{tel}$  for ARIEL.

For the purposes of assessing the feasibility of observations for the instrument as a whole (across all channels), we can focus on the performance of the 'limiting' (i.e the noisiest) channel at any particular tier, and its median and interquartile range  $N_{transits}$  results.

The above process is repeated for each spectroscopic channel at different binned R-powers corresponding to the 3 different observing tiers. We would expect as the spectral resolution decreases,  $SNR_1$  will increase and median  $N_{transits}$  will decrease. Thus tier 1 will have lower median  $N_{transits}$  than tier 2, and tier 2 will have lower than tier 3. However this is at the expense of spectral resolution and the ability to detect features in the spectrum. The relative utility of each 'tier' was discussed in Subsection 4.1.1.1 and summarised in Table 4.1.

### 6.3 RESULTS

The calculated scale height,  $H$ , and atmospheric signal,  $A_{pt}$ , in primary transit for atmospheres of different mean molecular weights,  $\mu$ , for each planet are shown in Table 6.3. The scale heights for each planet are also shown in Figure 6.6 for the  $\mu = 28.97$  g/mol Earth-like atmosphere, although the relative scale heights between the planets will be the same across all molecular weights.

For secondary eclipse, Table 6.4 presents for each planet, the median value of  $A_{se}$  in each channel, with the corresponding value of median  $N_{transits}$  in tier 1 assuming the optimal extraction correction (i.e. the most optimistic case). Figure 6.7 also shows the median  $A_{se}$  for each planet in Ch0 and Ch1 (again assuming optimal extraction).

The  $N_{limit}$  for each planet is shown in Figures 6.8 - 6.15 as well as listed in Table 6.5, which also gives the percentage of the mission operation lifetime (assuming this is 3.5 years, and assuming each transit observation lasts  $2 \times T_{14}$ ) for  $N_{limit}$  number of transits.  $N_{limit}$  values have all been rounded down to the nearest whole number.

Figures 6.8 - 6.14 show for each planet, median  $N_{transits}$  per channel versus mean molecular weight,  $\mu$ , with basic pipeline results on the left and optimal

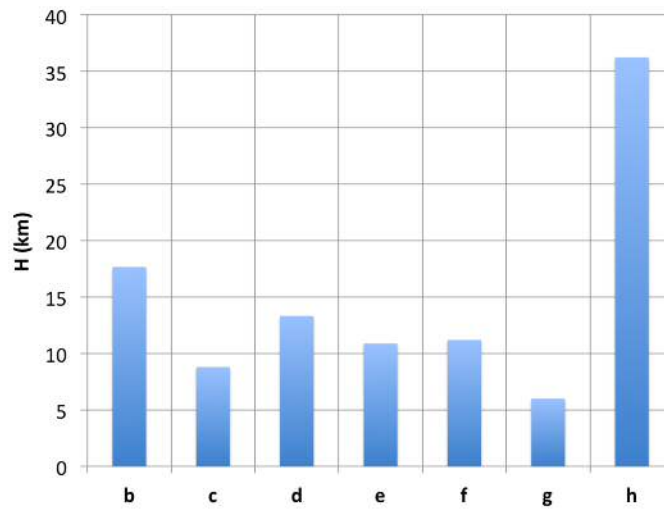


FIGURE 6.6 Scale heights,  $H$ , for each planet for a  $\mu = 28.97$  g/mol atmosphere.

extraction corrected results shown on the right. The results are separated by observing tier.

Figure 6.15 shows for each planet, the median and interquartile range (IQR) for  $N_{transits}$  in the limiting channel in each tier. This gives an idea of the spread of  $N_{transits}$  within each channel.

Table 6.5 also lists for each planet, the value of  $\mu$  when  $N_{transits}$  in the limiting channel reaches  $N_{limit}$  in each tier. Results are given for the median  $N_{transits}$  in each channel and also for the first and third quartiles. This gives an estimate of the maximum mean molecular weight of atmosphere observable for each planet at each tier.

Table 6.6 gives for each planet,  $N_{transits}$  (rounded up to the nearest whole number) in the limiting channel needed to detect the  $\mu = 2.22$  g/mol atmosphere, at the different tiers (again assuming optimal extraction). Results are again given for the median  $N_{transits}$  in each channel and for the first and third quartiles. The percentage of the mission operation lifetime taken for median  $N_{transits}$  is shown.

The limiting channel is Ch1 in all tiers except tier 3 where it is Ch0.

TABLE 6.3 Scale height,  $H$ , and primary transit atmospheric signal,  $A_{pt}$ , at different mean molecular weights,  $\mu$ , for each TRAPPIST-1 planet. Units for  $\mu$  are g/mol. Units for  $H$  are km.

Planet	$\mu = 2.22$	$\mu = 5$	$\mu = 8$	$\mu = 12$	$\mu = 18$	$\mu = 28.97$	$\mu = 43.45$
b	$H$	230.49	102.34	63.96	42.64	28.43	17.66
	$A_{pt}$	$2.41 \times 10^{-3}$	$1.07 \times 10^{-3}$	$6.68 \times 10^{-4}$	$4.45 \times 10^{-4}$	$2.97 \times 10^{-4}$	$1.85 \times 10^{-4}$
c	$H$	114.73	50.94	31.84	21.23	14.15	8.79
	$A_{pt}$	$1.17 \times 10^{-3}$	$5.17 \times 10^{-4}$	$3.23 \times 10^{-4}$	$2.16 \times 10^{-4}$	$1.44 \times 10^{-4}$	$8.93 \times 10^{-5}$
d	$H$	173.80	77.17	48.23	32.15	21.44	13.32
	$A_{pt}$	$1.29 \times 10^{-3}$	$5.73 \times 10^{-4}$	$3.58 \times 10^{-4}$	$2.39 \times 10^{-4}$	$1.59 \times 10^{-4}$	$9.89 \times 10^{-5}$
e	$H$	141.83	62.97	39.36	26.24	17.49	10.87
	$A_{pt}$	$1.25 \times 10^{-3}$	$5.56 \times 10^{-4}$	$3.47 \times 10^{-4}$	$2.32 \times 10^{-4}$	$1.54 \times 10^{-4}$	$9.59 \times 10^{-5}$
f	$H$	146.00	64.82	40.51	27.01	18.01	11.19
	$A_{pt}$	$1.467 \times 10^{-3}$	$6.514 \times 10^{-4}$	$4.07 \times 10^{-4}$	$2.71 \times 10^{-4}$	$1.81 \times 10^{-4}$	$1.12 \times 10^{-4}$
g	$H$	78.16	34.70	21.69	14.46	9.64	5.99
	$A_{pt}$	$8.47 \times 10^{-4}$	$3.76 \times 10^{-4}$	$2.35 \times 10^{-4}$	$1.57 \times 10^{-4}$	$1.05 \times 10^{-4}$	$6.49 \times 10^{-5}$
h	$H$	472.82	209.93	131.21	87.47	58.32	36.23
	$A_{pt}$	$3.42 \times 10^{-3}$	$1.52 \times 10^{-3}$	$9.49 \times 10^{-4}$	$6.33 \times 10^{-4}$	$4.22 \times 10^{-4}$	$2.62 \times 10^{-4}$

TABLE 6.4 Median secondary eclipse signal,  $A_{se}$ , in each channel and median  $N_{transits}$  to achieve goal SNR. Results shown for tier 1 with optimal extraction correction included.

Planet		FGS 1	FGS 2	NIRSpec	AIRS Ch0	AIRS Ch1
b	$A_{se}$	$5.20 \times 10^{-6}$	$5.20 \times 10^{-6}$	$5.20 \times 10^{-6}$	$5.58 \times 10^{-6}$	$3.92 \times 10^{-5}$
	$N_{transits}$	$5.84 \times 10^4$	$3.89 \times 10^4$	$3.04 \times 10^4$	$1.14 \times 10^5$	$3.19 \times 10^3$
c	$A_{se}$	$2.62 \times 10^{-6}$	$2.62 \times 10^{-6}$	$2.62 \times 10^{-6}$	$2.67 \times 10^{-6}$	$1.44 \times 10^{-5}$
	$N_{transits}$	$1.97 \times 10^5$	$1.31 \times 10^5$	$1.03 \times 10^5$	$4.50 \times 10^5$	$2.05 \times 10^4$
d	$A_{se}$	$7.05 \times 10^{-7}$	$7.05 \times 10^{-7}$	$7.05 \times 10^{-7}$	$7.08 \times 10^{-7}$	$2.42 \times 10^{-6}$
	$N_{transits}$	$2.35 \times 10^6$	$1.57 \times 10^6$	$1.22 \times 10^6$	$6.07 \times 10^6$	$6.21 \times 10^5$
e	$A_{se}$	$5.78 \times 10^{-7}$	$5.78 \times 10^{-7}$	$5.78 \times 10^{-7}$	$5.78 \times 10^{-7}$	$1.31 \times 10^{-6}$
	$N_{transits}$	$3.01 \times 10^6$	$2.00 \times 10^6$	$1.56 \times 10^6$	$8.17 \times 10^6$	$1.83 \times 10^6$
f	$A_{se}$	$4.32 \times 10^{-7}$	$4.32 \times 10^{-7}$	$4.32 \times 10^{-7}$	$4.32 \times 10^{-7}$	$6.67 \times 10^{-7}$
	$N_{transits}$	$4.94 \times 10^6$	$3.29 \times 10^6$	$2.57 \times 10^6$	$1.36 \times 10^7$	$6.43 \times 10^6$
g	$A_{se}$	$3.40 \times 10^{-7}$	$3.40 \times 10^{-7}$	$3.40 \times 10^{-7}$	$3.40 \times 10^{-7}$	$4.30 \times 10^{-7}$
	$N_{transits}$	$7.29 \times 10^6$	$4.86 \times 10^6$	$3.79 \times 10^6$	$2.02 \times 10^7$	$1.41 \times 10^7$
h	$A_{se}$	$8.75 \times 10^{-8}$	$8.75 \times 10^{-8}$	$7.81 \times 10^{-8}$	$7.81 \times 10^{-8}$	$8.28 \times 10^{-8}$
	$N_{transits}$	$1.00 \times 10^8$	$6.66 \times 10^7$	$6.51 \times 10^7$	$3.47 \times 10^8$	$2.77 \times 10^8$

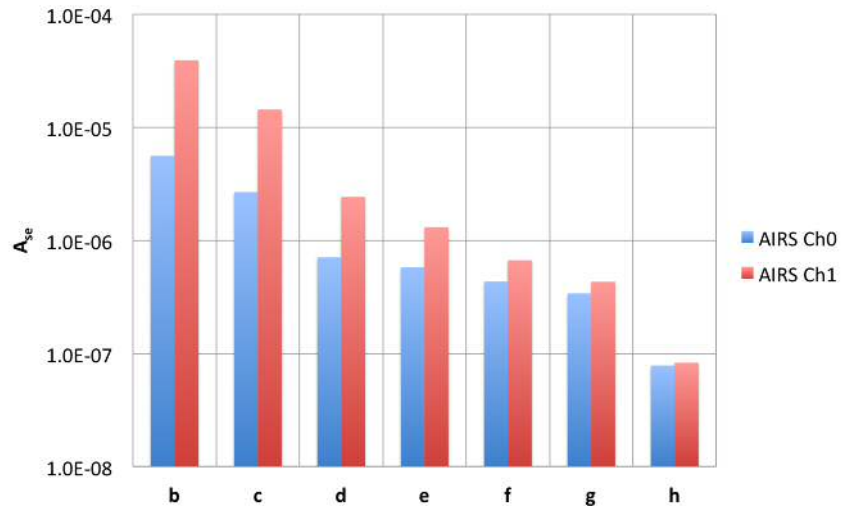
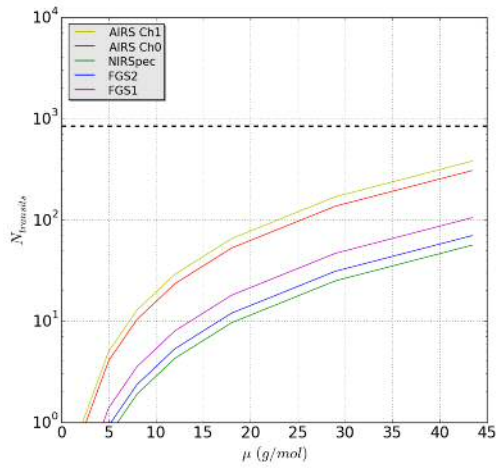
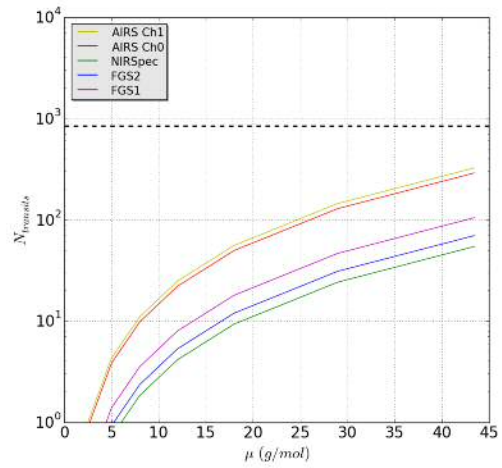


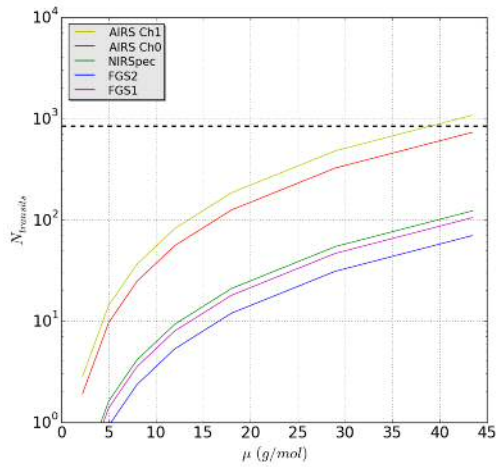
FIGURE 6.7 Median  $A_{se}$  for each planet in Ch0 and Ch1 (assumes optimal extraction).



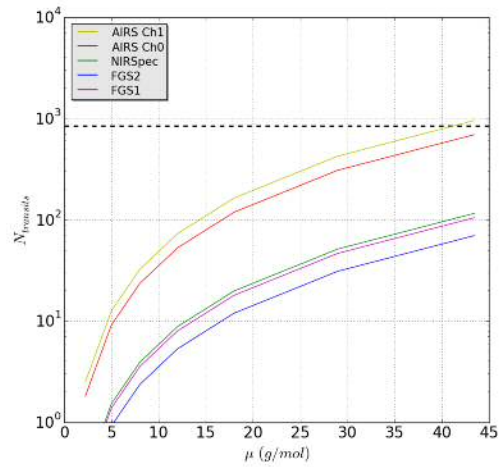
(A) Tier 1 basic



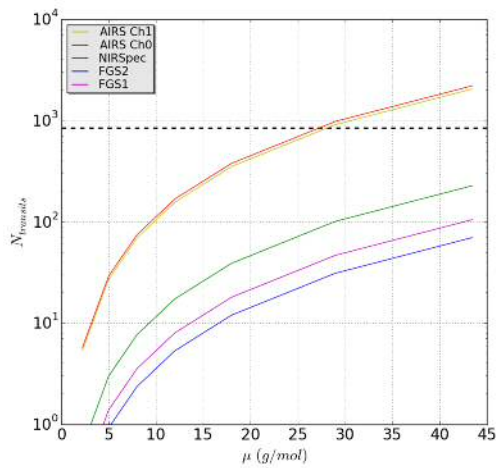
(B) Tier 1 optimal



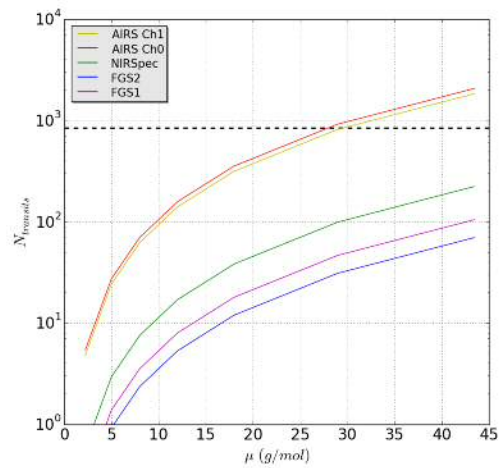
(C) Tier 2 basic



(D) Tier 2 optimal

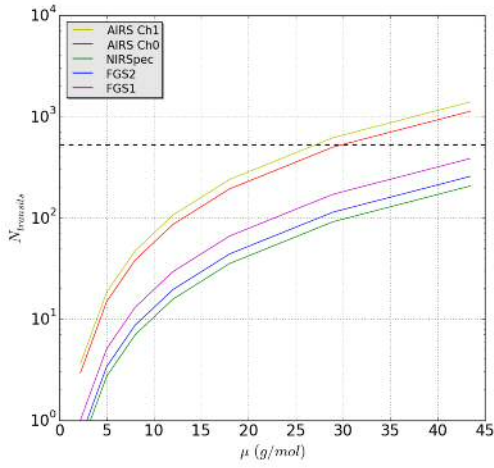


(E) Tier 3 basic

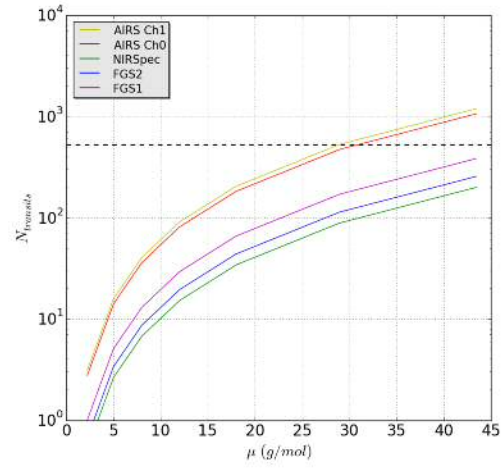


(F) Tier 3 optimal

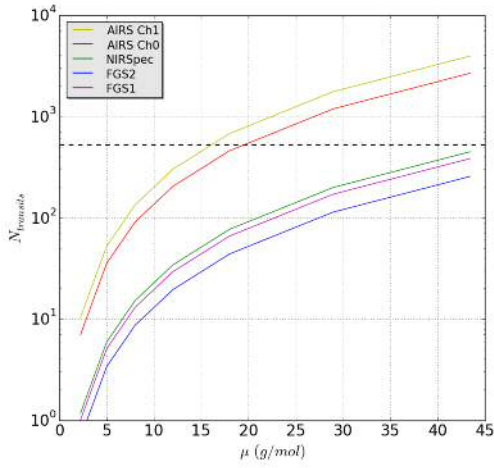
FIGURE 6.8 Planet b:  $N_{transits}$  to achieve  $SNR_{goal}$  vs mean molecular mass of atmosphere,  $\mu$ . Median values shown for each spectroscopic channel. Dashed line shows  $N_{limit}$ .



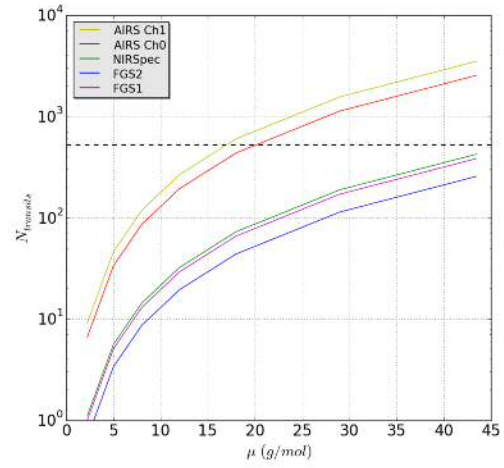
(A) Tier 1 basic



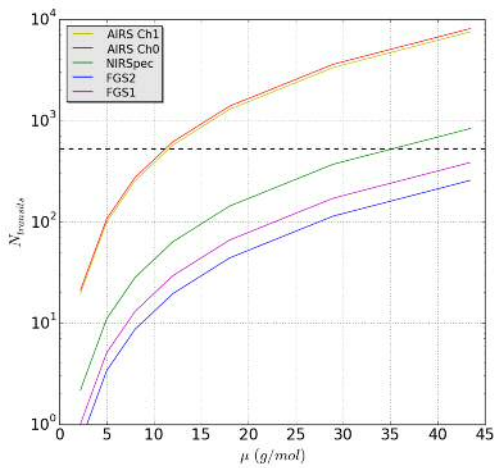
(B) Tier 1 optimal



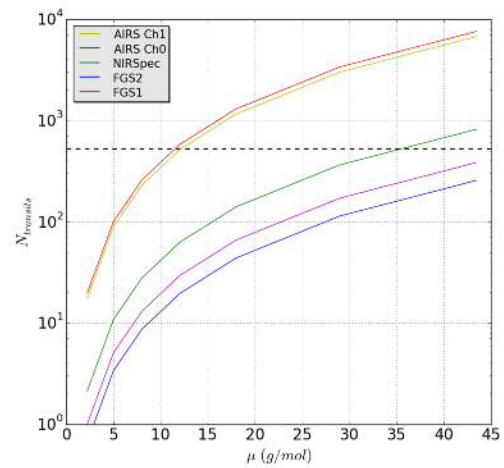
(C) Tier 2 basic



(D) Tier 2 optimal

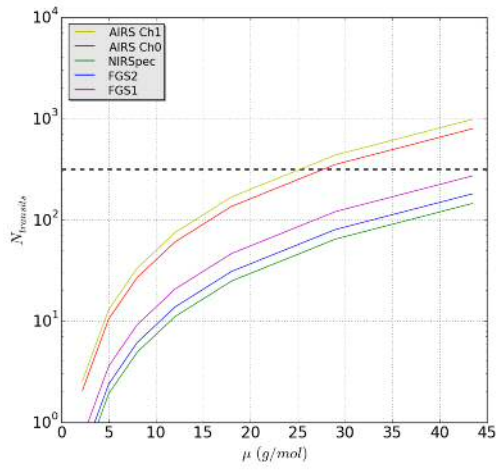


(E) Tier 3 basic

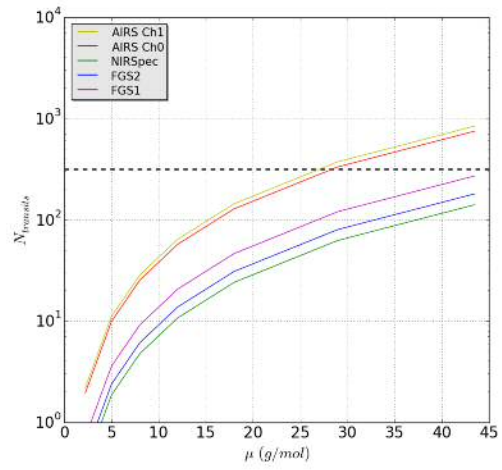


(F) Tier 3 optimal

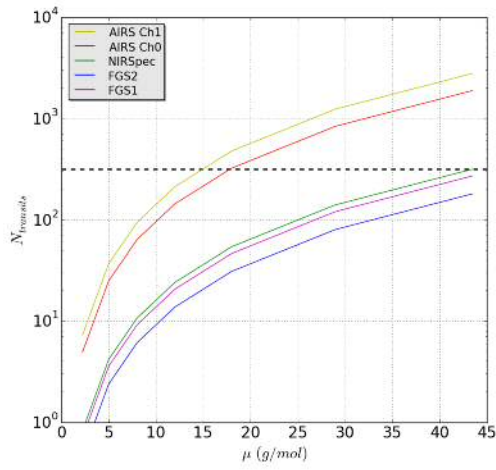
FIGURE 6.9 Planet c:  $N_{transits}$  to achieve  $SNR_{goal}$  vs mean molecular mass of atmosphere,  $\mu$ . Median values shown for each spectroscopic channel. Dashed line shows  $N_{limit}$ .



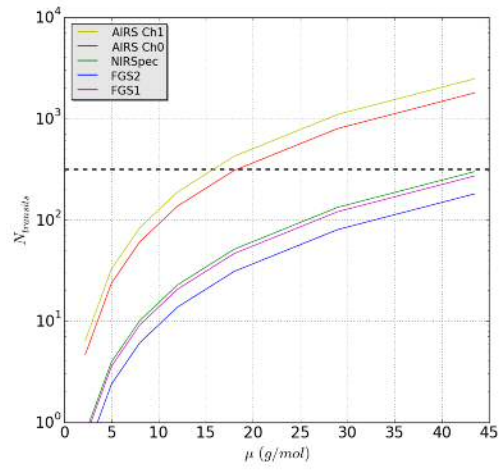
(A) Tier 1 basic



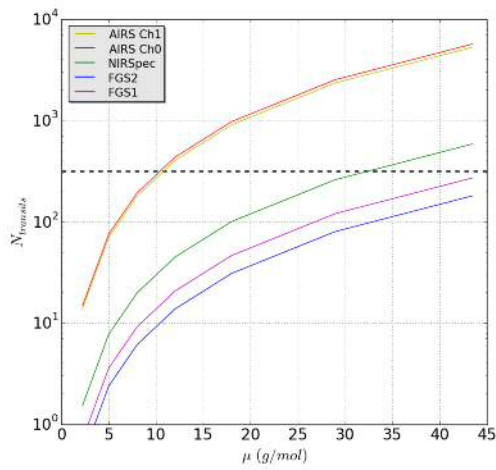
(B) Tier 1 optimal



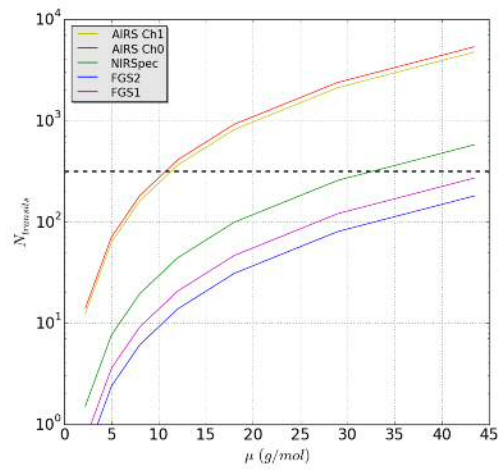
(C) Tier 2 basic



(D) Tier 2 optimal



(E) Tier 3 basic



(F) Tier 3 optimal

FIGURE 6.10 Planet d:  $N_{transits}$  to achieve  $SNR_{goal}$  vs mean molecular mass of atmosphere,  $\mu$ . Median values shown for each spectroscopic channel. Dashed line shows  $N_{limit}$ .

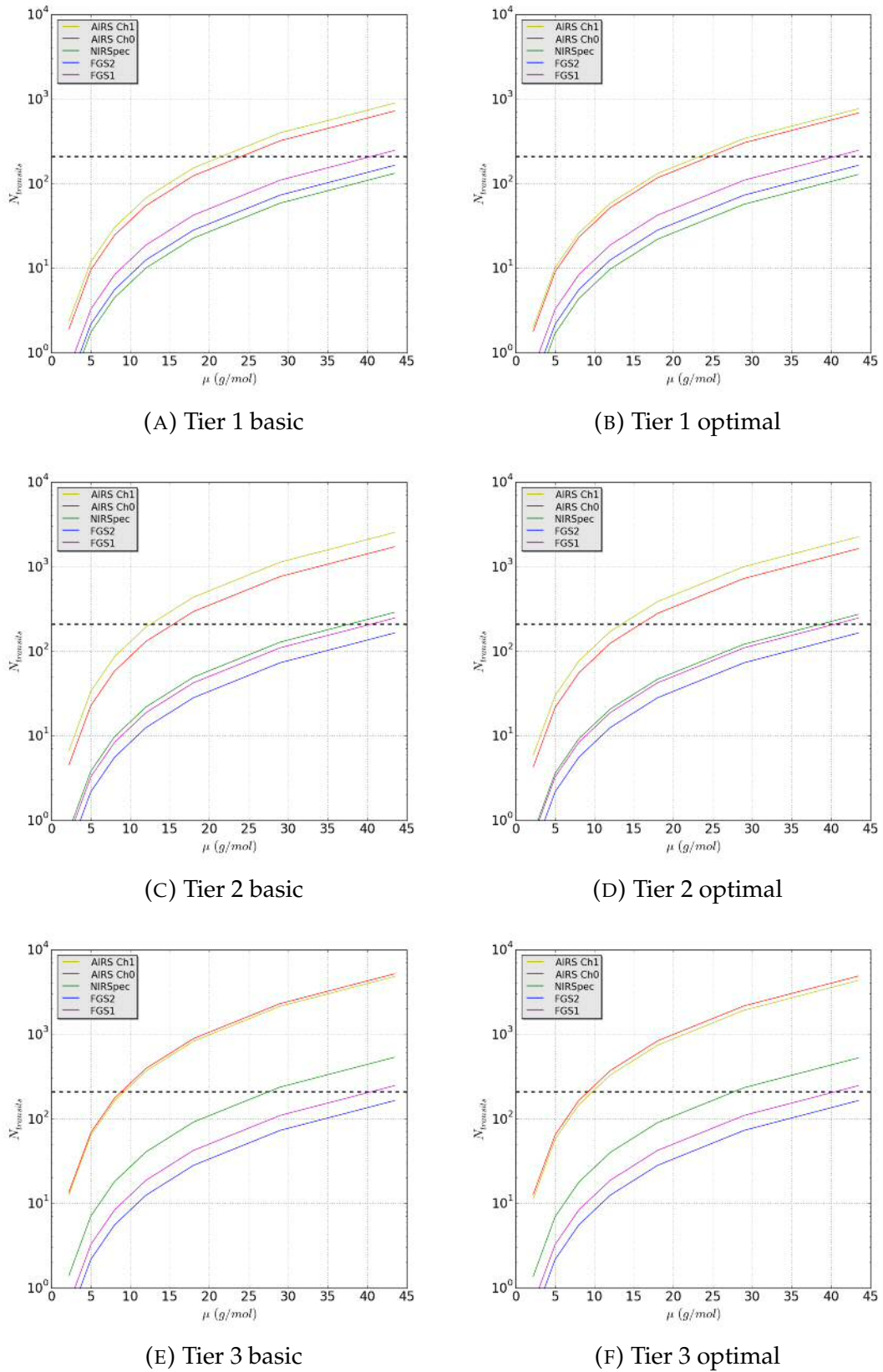
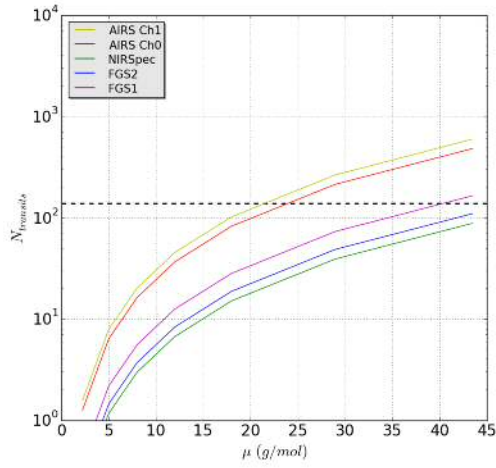
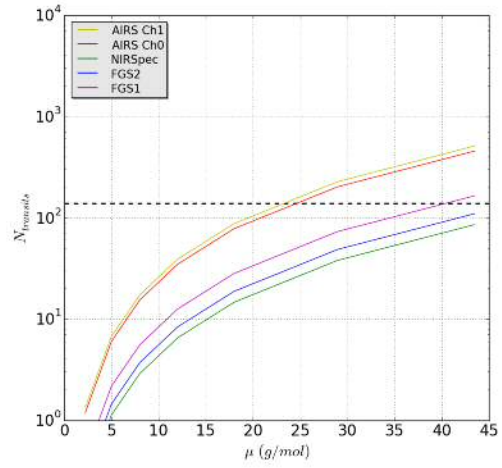


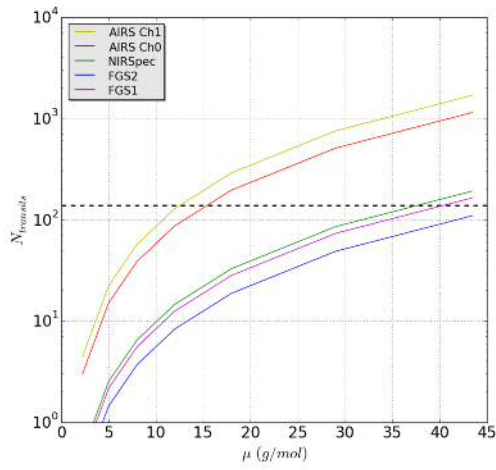
FIGURE 6.11 Planet e:  $N_{transits}$  to achieve  $SNR_{goal}$  vs mean molecular mass of atmosphere,  $\mu$ . Median values shown for each spectroscopic channel. Dashed line shows  $N_{limit}$ .



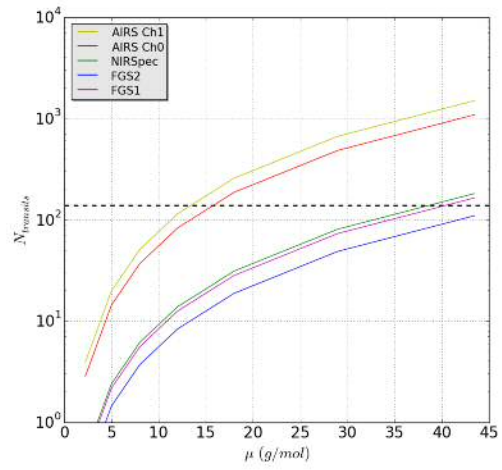
(A) Tier 1 basic



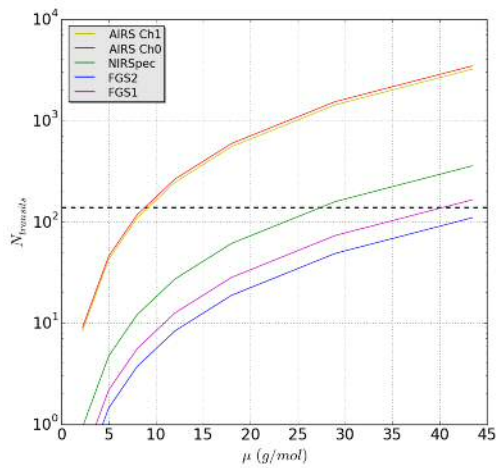
(B) Tier 1 optimal



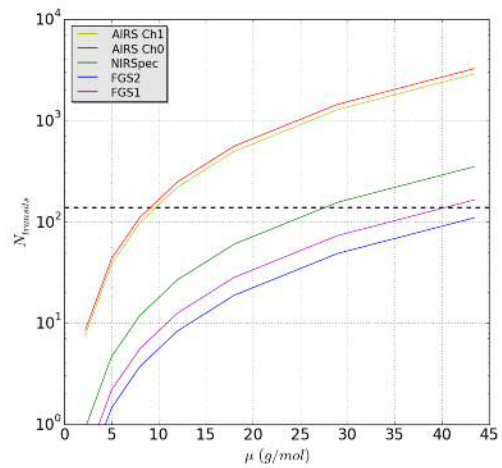
(C) Tier 2 basic



(D) Tier 2 optimal

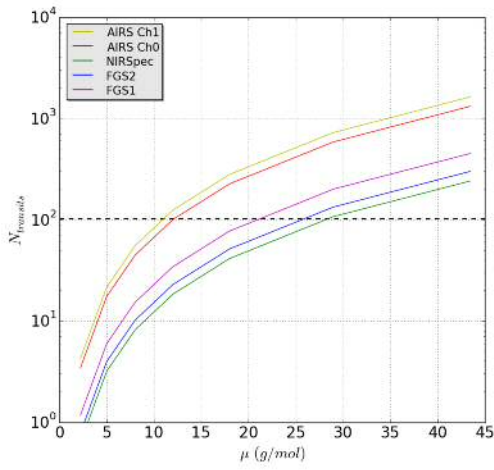


(E) Tier 3 basic

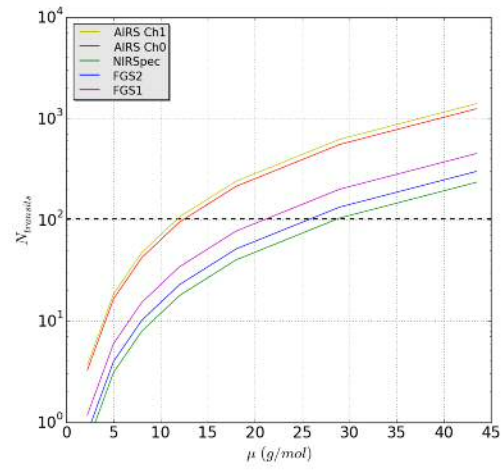


(F) Tier 3 optimal

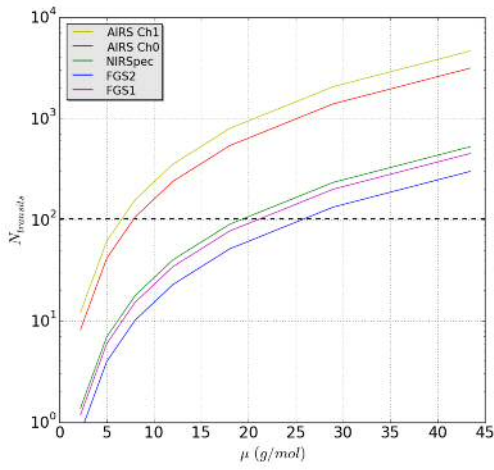
FIGURE 6.12 Planet f:  $N_{transits}$  to achieve  $SNR_{goal}$  vs mean molecular mass of atmosphere,  $\mu$ . Median values shown for each spectroscopic channel. Dashed line shows  $N_{limit}$ .



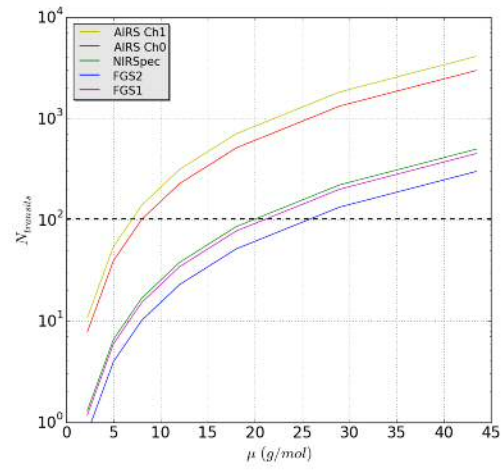
(A) Tier 1 basic



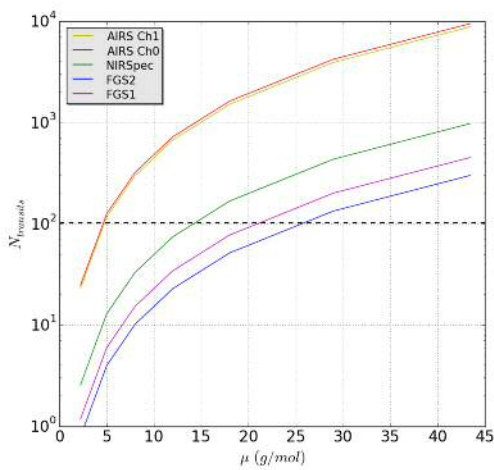
(B) Tier 1 optimal



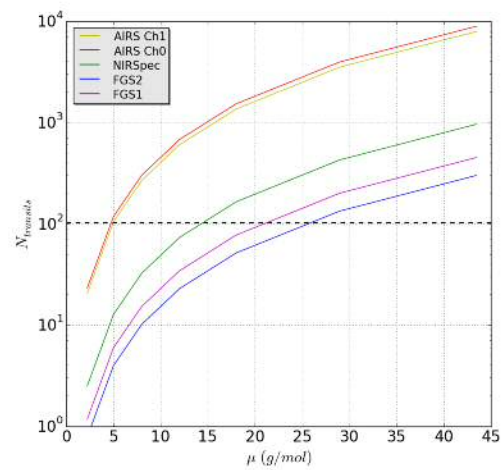
(C) Tier 2 basic



(D) Tier 2 optimal

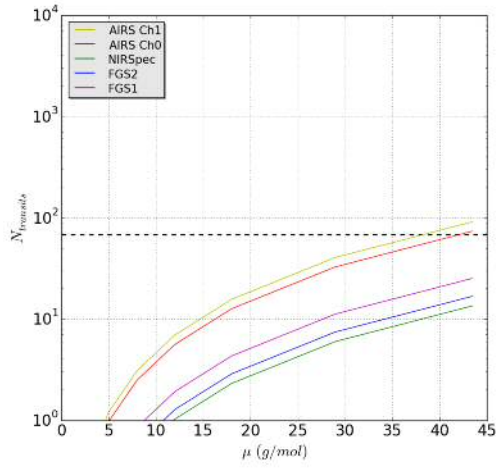


(E) Tier 3 basic

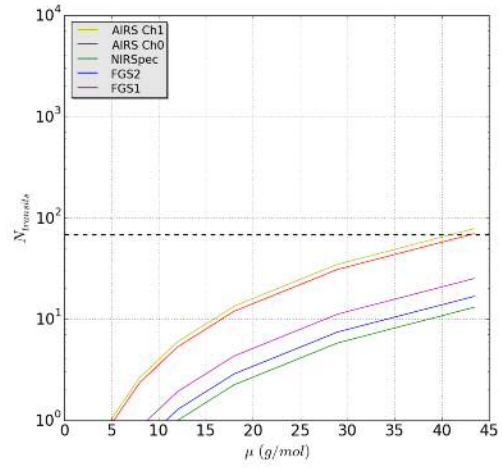


(F) Tier 3 optimal

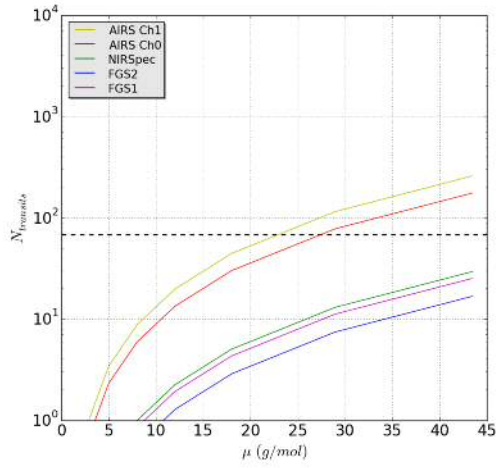
FIGURE 6.13 Planet g:  $N_{transits}$  to achieve  $SNR_{goal}$  vs mean molecular mass of atmosphere,  $\mu$ . Median values shown for each spectroscopic channel. Dashed line shows  $N_{limit}$ .



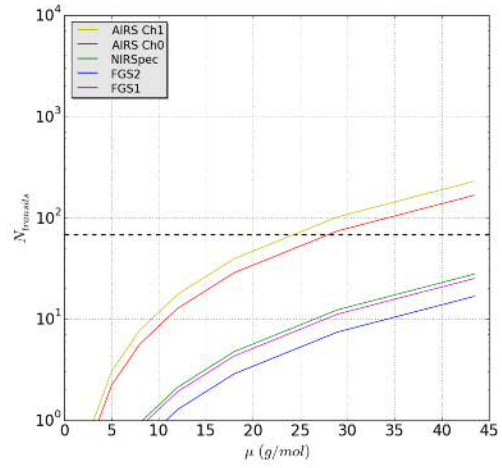
(A) Tier 1 basic



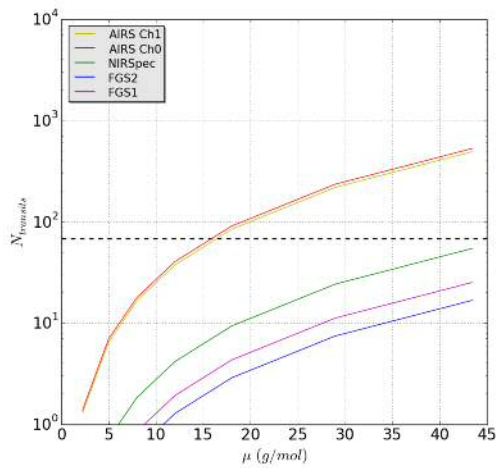
(B) Tier 1 optimal



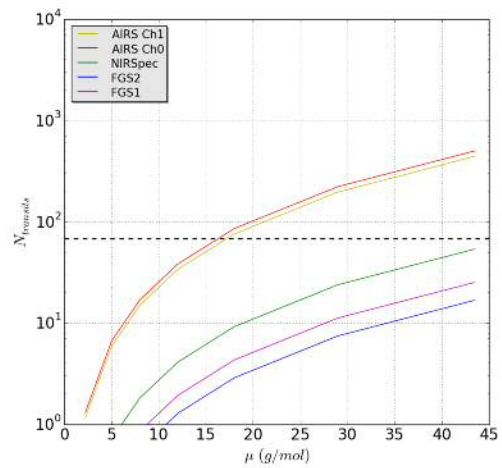
(C) Tier 2 basic



(D) Tier 2 optimal



(E) Tier 3 basic



(F) Tier 3 optimal

FIGURE 6.14 Planet h:  $N_{transits}$  to achieve  $SNR_{goal}$  vs mean molecular mass of atmosphere,  $\mu$ . Median values shown for each spectroscopic channel. Dashed line shows  $N_{limit}$ .

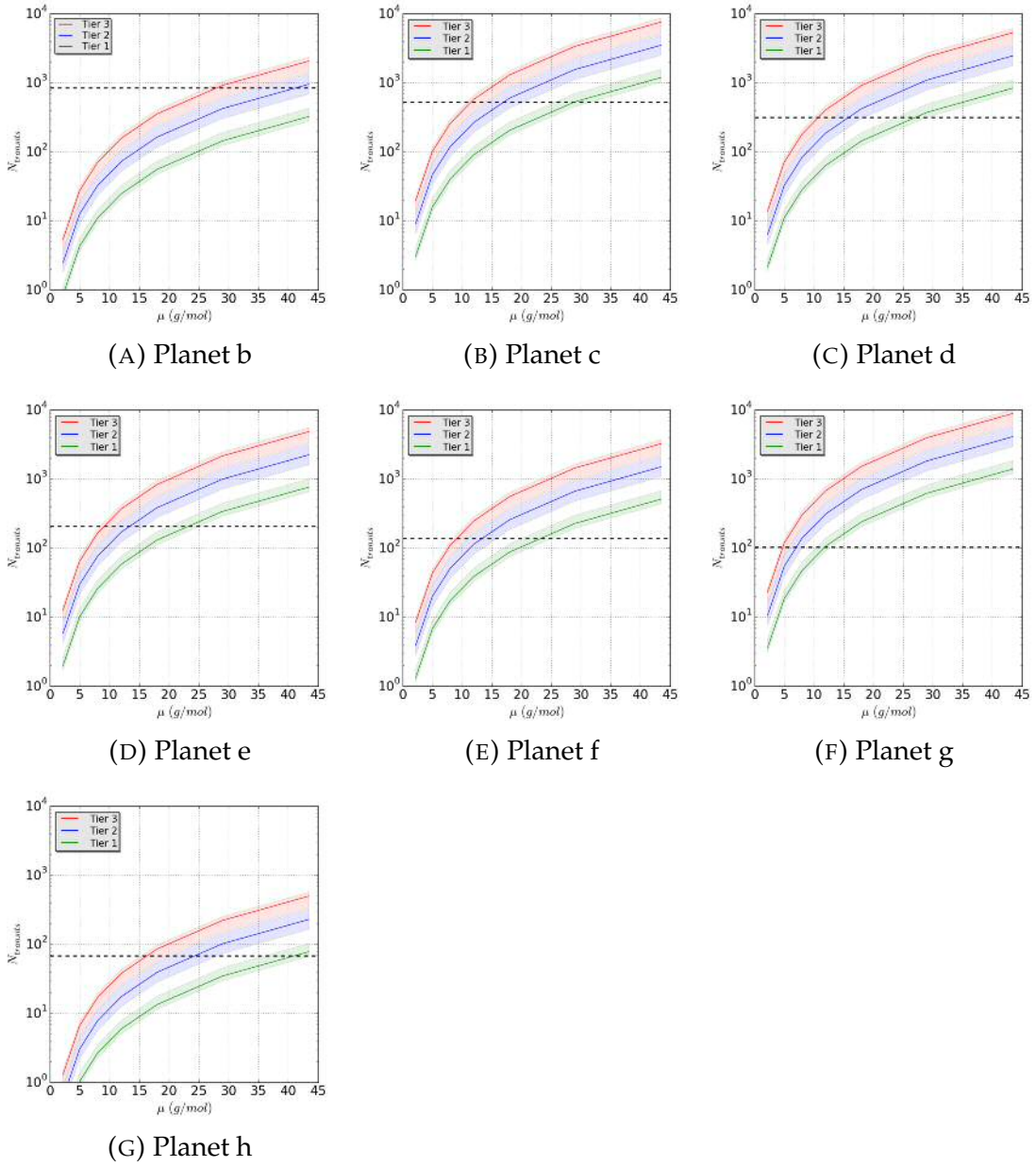


FIGURE 6.15 Median  $N_{transits}$  and IQR for limiting channel vs mean molecular mass,  $\mu$ , for each TRAPPIST-1 planet. Limiting channel in tier 3 is Ch0, and in tiers 1 and 2 is Ch1. Solid line shows the median and shaded area is the interquartile range for each channel. Dashed lines show  $N_{limit}$ .

TABLE 6.5  $N_{limit}$  for different TRAPPIST-1 planets, and maximum mean molecular mass of atmosphere,  $\mu$ , detectable at each tier in the limiting channel (assuming optimal extraction). Median and IQR (in brackets) shown for  $\mu$ . Percentage of total mission time for  $N_{limit}$  is also shown.

Planet	$N_{limit}$	% mission	Maximum $\mu$ (g/mol)		
			Tier 1	Tier 2	Tier 3
b	846	3.36	>43.45 (>43.45->43.45)	41.3 (35.1->43.45)	28.0 (26.5-34.3)
c	528	2.44	28.9 (25.7-31.8)	17.1 (14.5-20.4)	11.6 (10.9-14.2)
d	315	1.69	27.1 (23.8-28.9)	15.8 (13.3-18.4)	10.7 (10.1-12.9)
e	209	1.31	23.4 (20.2-25.2)	13.5 (11.3-15.9)	9.2 (8.5-11.1)
f	138	0.94	23.3 (20.1-25.1)	13.4 (11.2-15.9)	9.1 (8.4-11.0)
g	103	0.77	11.8 (10.5-12.9)	7.0 (5.9-8.2)	4.8 (4.5-5.8)
h	68	0.56	41.0 (36.0-43.9)	24.3 (20.3-28.2)	16.3 (15.3-19.8)

TABLE 6.6  $N_{transits}$  to detect primordial  $\mu = 2.22$  g/mol atmosphere for different TRAPPIST-1 planets at different tiers (assuming optimal extraction) in the limiting channel. Median and IQR (in brackets) shown. Percentage of total mission time for the median number of transits is shown.

Planet	Tier 1		Tier 2		Tier 3	
	$N_{transits}$	% mission	$N_{transits}$	% mission	$N_{transits}$	% mission
b	1 (1-1)	0.00	3 (2-4)	0.01	6 (4-7)	0.02
c	4 (3-5)	0.02	10 (7-13)	0.05	20 (14-23)	0.09
d	3 (2-3)	0.02	7 (5-10)	0.04	14 (10-16)	0.07
e	3 (2-3)	0.02	6 (5-9)	0.04	13 (9-14)	0.08
f	2 (2-2)	0.01	4 (3-6)	0.03	9 (6-10)	0.06
g	4 (4-5)	0.03	11 (8-16)	0.08	24 (16-27)	0.18
h	1 (1-1)	0.01	1 (1-1)	0.01	2 (1-2)	0.02
All planets		0.11		0.25		0.53

## 6.4 ANALYSIS

Although optimal extraction does not substantially improve the noise results except for at the red of Ch1, for clarity, I will focus on the optimal extraction results rather than the basic pipeline results for this analysis and discussion.

### 6.4.1 PRIMARY TRANSIT

**Planet b** Planet b is one of two planets that has had a transit spectroscopy study performed already that ruled out a H<sub>2</sub>-He dominated atmosphere. The planet is hot, with an equilibrium temperature of 436 K per my calculation (which assumes tidal locking and an albedo of 0.3) and therefore well outside the habitable zone. This temperature however results in higher scale heights potentially giving better a atmospheric signal. Figure 6.6 shows that planet b has the second highest scale height relative to the other planets.

Due to its proximity to the star, the short period of 1.51 days means that 846 transits (Table 6.5) would be available to observe during ARIEL's lifetime, the largest number of transits available for any of the system planets.

Planet b would be a good target for ARIEL. Although requiring potentially hundreds of transit observations, high molecular weight atmospheres could potentially be characterised at tier 2 and tier 3 levels (Table 6.5).

At tier 3, the results indicate around a 28.0 g/mol atmosphere could potentially be characterised (limited by Ch0) if the  $N_{limit}$  number of transits is performed and combined, and upto around 41.3 g/mol at tier 2 (limited by Ch1). The IQR shows than within the channels there is some variation in the detectability ranging from 26.5 to 34.3 g/mol in tier 3 and from 35.1 to >43.45 g/mol in tier 2. To a first-order we can say that tier 3 studies may bring us in the range of characterising water-dominated, O<sub>2</sub>-N<sub>2</sub> or CH<sub>4</sub>-N<sub>2</sub> atmospheres (making it a potential 'benchmark' planet), and possibly even heavier Venus- or Mars-like CO<sub>2</sub>-N<sub>2</sub> atmospheres could be detected at tier 2.

Primordial H<sub>2</sub>-He atmospheres (perhaps with mixed in secondary species) could be characterised with a median of only 6 transits at tier 3 (IQR 4-7 transits), and 3 transits at tier 2 (IQR 2-4 transits) (Table 6.6). However the results of de Wit et al. (2016) would suggest this composition is unlikely.

**Planet c** Planet c also lies outside of the habitable zone, with an equilibrium temperature of 372 K, just below the boiling point of water. Higher albedos, cloud coverage or increased planet rotation, could possibly shift this temperature to lower values. However, modeling by Gillon et al. (2017) found that cloud feedback was inefficient for short period objects and a runaway greenhouse effect would result.

ARIEL would be able to observe a maximum of 528 transits of this planet (Table 6.5). Together with planet b, de Wit et al. (2016) ruled out an extended H<sub>2</sub>-He atmosphere for this planet. This is also the densest of the TRAPPIST-1 planets at 6.46 g/cm<sup>3</sup>, consistent with a high iron content rocky planet. The high surface gravity and resulting lower scale heights will tend to make this a tougher target for transit spectroscopy than planet b. It has the second lowest scale height relative to the other planets (Figure 6.6).

This is reflected in needing a median of 20 transits (IQR 14-23) to achieve goal SNR in the limiting channels for the 'easy' H<sub>2</sub>-He atmosphere in tier 3 compared to 6 for planet b (Table 6.6). In fact planet c requires the second largest number of transits of any of the planets to characterise a H<sub>2</sub>-He atmosphere. Detecting higher molecular weight atmospheres will be challenging, with a median limit of 11.3 g/mol at tier 3 and 17.1 g/mol at tier 2. The IQR at tier 2 is 14.5-20.4 g/mol, so a water-dominated atmosphere may be possible to detect, but given the large number of transits needed (528) this may be too costly in terms of likely science return. O<sub>2</sub>-N<sub>2</sub>, CO<sub>2</sub>-N<sub>2</sub> and CH<sub>4</sub>-N<sub>2</sub> atmospheres are unlikely to be characterisable.

**Planet d** Planet d is the first of the planets heading outwards from the star to be placed in the optimistic habitable zone, with an equilibrium temperature of 314 K, and an Earth-like density of 4.91 g/cm<sup>3</sup> (Earth bulk density is 5.51 g/cm<sup>3</sup>). An  $N_{limit}$  of 315 transits could potentially be observed by ARIEL (Table 6.5).

This presents a similar level of difficulty as planet c though somewhat 'easier' in terms of detecting a H<sub>2</sub>-He atmosphere needing a median of 14 transits (IQR 10-16) at tier 3 to achieve goal SNR in the limiting channel (Table 6.6). Again, it is unlikely ARIEL could probe higher mean molecular mass atmospheres of interest, since  $N_{limit}$  is reached at a median of 10.7 g/mol at tier 3 in the limiting channel and 15.8 g/mol at tier 2. However tier 1 could still perform gross detection of atmospheres up to a median of 27.1 g/mol in the limiting channel but would be unable to resolve specific spectral features.

**Planet e** Planet e is potentially the most 'Earth-like' of the TRAPPIST-1 planets with an equilibrium temperature of 273 K and a radius of 0.9  $R_{\oplus}$ . It may differ from

the Earth due to tidal locking which could affect weather systems, the distribution of temperature, and possibly the strength of the planetary magnetic field, and is also subject to more intense X and EUV radiation.

ARIEL could perform a maximum of 209 transit observations of this planet within its mission lifetime (Table 6.5). Again a H<sub>2</sub>-He dominated atmosphere would be very feasible to characterise. At tier 3 this would take a median of 13 transits (IQR 9-14), 6 transits (IQR 5-9) at tier 2, and 3 transits (IQR 2-3) at tier 1 (Table 6.6) in the limiting channel.

For higher molecular weight atmospheres the performance is less promising. Tier 2 resolution allows the largest ro-vibrational bands in Ch0 and Ch1 to be detected. The maximum mean molecular weight of an atmosphere characterisable at this tier is 13.5 (IQR 11.3-15.9) g/mol in the limiting channel, well below that for the Earth, Titan, Mars or Venus, or potential water worlds (Table 6.5). This makes it very unlikely that ARIEL could characterise a O<sub>2</sub>-N<sub>2</sub>, CH<sub>4</sub>-N<sub>2</sub> or CO<sub>2</sub>-N<sub>2</sub> atmosphere on this planet. Gross detection of upto 23.4 (IQR 20.2-25.2) g/mol atmospheres may be possible in tier 1 resolution without resolving specific features.

NIRSpec, FGS 1 and FGS 2 combined could reach 27.8 g/mol at tier 3 (the median value in NIRSpec), however this would be of limited utility since the resolution is too low to detect the spectral features in this wavelength range such as oxygen or alkali metals. These channels could however constrain the continuum in this region, detecting Rayleigh scattering, obtaining the albedo and performing cloud diagnostics.

Note if the mass given in the preliminary paper by Wang et al. (2017) is confirmed of just 0.24  $M_{\oplus}$ , this would give the planet a much higher scale height and a potentially more detectable atmosphere.

**Planet f** is the third planet in the habitable zone with an equilibrium temperature of 238 K and a radius very close to that of the Earth. It gives scale heights close to but slightly higher than planet e (Table 6.3, Figure 6.6).

The feasibility picture is similar to that for planet e, which is unfortunate given the potential similarity to the Earth. We are again limited to low molecular weight atmospheres, reaching only 13.4 (IQR 11.2-15.9) g/mol at tier 2 if all 138 transits are combined. Again NIRSpec and the visual channels allow probing to higher molecular weights, but will have little utility for spectral feature detection.

Gross detection of high molecular weight atmosphere might be possible upto 23.3 (IQR 20.1-25.1) g/mol in tier 1 but is unlikely to warrant the investment of time given the low resolution of tier 1.

Again the H<sub>2</sub>-He atmosphere should be fairly easily detected with a median of 9 transits (IQR 6-10) required at tier 3 (Table 6.6).

**Planet g** This is the last of the habitable zone planets, with an  $N_{limit}$  of 103 transits observable within the ARIEL lifetime (Table 6.5). The planet is Earth-sized with a radius of  $1.13 R_{\oplus}$  and has an Earth-like density of  $5.16 \text{ g/cm}^3$  (Table 6.1). The equilibrium temperature is 216 K assuming tidal locking with an albedo of 0.3. Being colder and more massive than the other habitable zone planets it has the smallest scale height of all (Table 6.3, Figure 6.6).

Tier 1 allows gross characterisation of atmospheres up to only 11.8 (IQR 10.5-12.9) g/mol (Table 6.5). The limiting mean molecular weights at tier 2 and tier 3 are 7.0 (IQR 5.9-8.2) and 4.8 (IQR 4.5-5.8) g/mol respectively. Thus this planet is even more difficult to probe than planets e and f. Again detection of the H<sub>2</sub>-He atmosphere would be feasible with median of just 4 transits (IQR 4-5) in tier 1, and 24 transits (IQR 16-27) in tier 3 (Table 6.6). This is the largest number of transits required for such an atmosphere of any of the planets. Planet g appears to be the least favourable planet in terms of feasibility.

**Planet h** This outermost planet is intriguing due its low bulk density which I calculate at  $1.12 \text{ g/cm}^3$  (Table 6.1) based on the mass measurement by Wang et al. (2017), and the radius from Luger et al. (2017). The error on this mass measurement is large ( $\pm 0.084 M_{\oplus}$ ), giving an upper limit of  $2.2 \text{ g/cm}^3$  on the density. This upper limit is of the same order as the density of GJ 1214, and lower than rocky planets such as the Earth, giving this planet a potentially unusual composition, consistent with a high content of volatiles which includes a water-dominated world or potentially a primordial H<sub>2</sub>-He-dominated envelope. It should be noted that the preliminary paper by Wang et al. (2017) has recalculated all the masses of the TRAPPIST-1 planets which results in the outer 4 planets having such low densities that they are all consistent with water worlds.

The low gravity resulting from this low mass gives this fairly cold planet the largest scale height of any of the TRAPPIST-1 planets (Table 6.3, Figure 6.6) and thus it has a potentially strong signal in primary transit. It has the lowest number of transits required to reach goal SNR at any particular value of  $\mu$  of any of the planets, as exemplified for the  $\mu = 2.22 \text{ g/mol}$  atmosphere in Table 6.6.

At tier 3, a  $\mu = 16.3$  (IQR 15.3-19.8) g/mol atmosphere could be characterised at  $N_{limit}$  transits in the limiting channel, and at tier 2,  $\mu = 24.13$  (IQR

20.3-28.2) g/mol atmosphere could be similarly characterised. This places water-dominated atmospheres and possibly Titan- or Earth-like atmospheres in reach. These results would also indicate that heavier CO<sub>2</sub>-N<sub>2</sub> atmospheres are out of reach at tier 2 or above. Although the latter would be within reach at tier 1, the resolution would not permit characterisation of specific features.

A primordial  $\mu = 2.22$  g/mol atmosphere (with any mixed in secondary species) could be easily characterised at tier 3 in just 2 transits (IQR 1-2), making this is 'easiest' planet in terms of number of transits required (Figure 6.8). It is also the most efficient planet in terms of mission observing time, with this 'primordial' tier 3 observation taking only 0.02% of the total mission time (Table 6.6), and the full  $N_{limit}$  number of transits taking 0.56% of the mission lifetime (Table 6.6), the shortest of any planet.

In the earlier discussion various authors have speculated about such a primordial atmosphere and how it could extend the habitable zone to reach this planet's orbit, increasing the atmospheric temperature through insulation of the internal heat and the greenhouse effect. Since this is also consistent with the apparent low density of the planet, this would be an intriguing planet to study. The large scale height will amplify the spectral features from mixed in gases that may allow identification of high molecular weight species and biomarkers.

Together with planet b, planet h represents one of the best targets for ARIEL.

#### 6.4.2 SECONDARY ECLIPSE

Table 6.4 shows that the signals obtained in secondary eclipse are at least 2 orders of magnitude lower than the primary transit signals in Table 6.3. This is because of the temperate nature of the planets coupled with small values of  $R_p$ . The signals worsen with distance from the star as the equilibrium temperatures of the planets fall (Figure 6.7). The highest median value of  $A_{se}$  is 39 ppm in AIRS Ch1 for planet b, but even this would require over 3000 transits to reach the goal SNR for an atmospheric feature in the most optimistic case (tier 1 with optimal extraction). The lowest median value of  $A_{se}$  is for planet h with  $7.81 \times 10^{-8}$  in NIRSpec and AIRS Ch0, but the highest number of median  $N_{transits}$  is for AIRS Ch0 due to its higher noise, reaching  $3.47 \times 10^8$ . It appears very conclusive that secondary eclipse spectroscopy will not be feasible with ARIEL on any of the TRAPPIST-1 planets.

## 6.5 DISCUSSION

This study gives a first-order assessment of the potential of ARIEL to spectroscopically characterise the TRAPPIST-1 planets at the different observing tiers in the ARIEL science strategy. We have seen the challenge and difficulty of terrestrial planet characterisation by transit spectroscopy.

I exclude the possibility of secondary eclipse spectroscopy by ARIEL on any of these planets, and thus also phase curve spectroscopy. In primary transit, there is a clear order of magnitude difference in difficulty between characterising the  $\mu = 2.22$  g/mol, H<sub>2</sub>-He-dominated, 'primordial' atmosphere scenario and high molecular weight secondary atmospheres as seen on rocky bodies in our Solar System. I find that if these planets retained some of the primordial H<sub>2</sub>-He envelope, thus giving rise to strong spectral features for mixed in species such as CH<sub>4</sub> or H<sub>2</sub>O, all of the planets would be feasible candidates for characterisation even at the highest resolution for ARIEL. If all planets were allocated the median  $N_{transits}$  needed to characterise the primordial atmosphere at tier 3 resolution, this would take up a total of 0.53% of the mission observing lifetime (Table 6.6). This may be an acceptable commitment in terms of time for possible science return. At tier 2, this falls to 0.25% and at tier 1 just 0.11%. Thus there is a strong argument to study all planets at at least tier 1 resolution, and possibly tier 2 or tier 3 resolution, upto the  $N_{transits}$  given in Table 6.6.

Tier 1 observations could potentially probe higher molecular weight atmospheres, and though not allowing detailed characterisation may be able to detect the gross presence of the atmosphere, clouds, and the slope of the continuum. However for most planets (with the exception of planet h) to reach high molecular weights ( $\mu \geq 18$  g/mol) even at tier 1 would require 100 to many 100s of transits, a time commitment which may not be compatible with the overall goals of the mission. Tier 1 is designed for 'reconnaissance survey', with one or just a few transits for each planet, and would not provide the quality of data that justifies many hundreds of transit observations.

Based purely on the number of transits needed to achieve goal SNR in all channels for the H<sub>2</sub>-He atmosphere (Table 6.6), we can say that planet h presents the 'easiest' target, and planet g, the 'hardest' target for ARIEL. However of course much depends on the actual atmospheres present on these planets.

There are also a lot of uncertainties that have not been factored into these results. These include the errors on the radii, periods and masses, as well as the assumptions made in the calculation of the equilibrium temperature about the

albedo (set at 0.3) and tidal locking. The impact of any greenhouse effect is another uncertainty. A re-evaluation using more certain data in the future may be warranted. The impact of coinciding transits and stellar variability have also not been considered in this study, but would be factors to consider for a future study.

The maximum amplitude approximation used here gives a first order measure of the strongest spectral feature possible, but of course many features will be smaller than this; a future study using candidate model spectra could be considered, evaluating the SNR for detectability by spectral feature.

In terms of high molecular weight secondary atmospheres similar to those seen in our solar system for rocky planets, the picture is pessimistic for most of these planets. This includes the habitable zone planets, d, e, f and g, so that unless otherwise indicated by findings in a tier 1 survey, spending large amounts of the available observing time in tier 2 or 3 on these 'habitable' planets would probably be unrevealing. Planet c also is a poor candidate given that high molecular weight atmospheric characterisation is likely to be unfeasible and a H<sub>2</sub>-He atmosphere has already been ruled out by de Wit et al. (2016).

Assuming 'primordial' atmospheres are not detected, one or two of the best targets could be evaluated for higher molecular weight atmospheres with investment of large numbers of transits in tier 2 or 3.

From this analysis the best target in this regard is probably planet h, given the 'ease' of detection, and science questions regarding its low density. If  $N_{limit}$  transits are observed, a  $\mu = 24.3$  (IQR 20.3-28.2) g/mol mean molecular weight atmosphere could be characterised in tier 2, and  $\mu = 16.3$  (IQR 15.3-19.8) g/mol in tier 3. Thus planet h could potentially have a primordial or water-world like atmospheres characterised. Earth-like atmospheres are not far outside the range in tier 2, but very high mean molecular weight atmospheres akin to Venus look less promising.  $N_{limit}$  for planet h constitutes 0.56% of a 3.5 year mission assuming each transit observation is  $2 \times T_{14}$  in duration. This would be a good investment in available observing time for likely science return.

Another good target would be planet b, where a  $\mu = 41.3$  (IQR 35.1->43.5) g/mol atmosphere could be characterised in  $N_{limit}$  transits in tier 2, and  $\mu = 28.0$  (IQR 26.5-34.3) g/mol in tier 3. The main issue here might be that  $N_{limit}$  for this planet constitutes 3.36% of the mission lifetime, which is a large proportion devoted to a single planet. This may however be worth the effort to obtain a potentially high quality spectrum of an Earth-sized exoplanet.



# CHAPTER 7

## CONCLUSIONS

---

**I**N this thesis, I developed a generic simulator of transit and eclipse spectroscopic observations, validated its accuracy and then applied it to diverse problems in the field of transit spectroscopy, with specific findings resulting from each of these applied studies. In this final chapter, I conclude the thesis by restating the general and specific goals, and how these were achieved. I discuss the overall approach taken to the development and validation of ExoSim, followed by a summary of the key findings from each of the applied studies. I then discuss limitations of ExoSim, its data reduction pipeline and the specific studies. I conclude by proposing future directions for these areas of work.

### 7.1 GOALS OF THE THESIS

The general goals of this thesis were to:

**A1)** develop a novel simulator of transit spectroscopy observations that models the time domain, and thus can simulate time-dependent effects such as correlated noise and systematics, and that generates a realistic time series of images, which can allow the effects of multiple error sources to be examined at the level of the final data products;

**A2)** make this simulator generically applicable to different instruments both existing and future, and diverse observing modes, so as to make it versatile enough to address many different questions pertaining to transit spectroscopy signal and noise;

**A3)** extensively test and validate the results of the simulator for accuracy;

**A4)** apply the simulator to several diverse problems in transit spectroscopy,

demonstrating its versatility in ‘prospective’ and ‘retrospective’ studies, and elucidating the effects of both complex astrophysical and instrumental noise sources.

From the selected problems to which ExoSim was applied there were more specific goals. These were:

**B1)** elucidate the noise from scanning mode on the Hubble WFC3 IR instrument and whether this introduces significant levels of correlated noise that may not be accounted for in existing studies;

**B2)** apply ExoSim to the design of the proposed ARIEL transit spectroscopy telescope during its Phase A study, using it to assess and solve noise problems at the system level, leading to a design that has low risk and complexity, and is able to fulfil the science goals of the mission;

**B3)** elucidate noise from stellar variability and activity in the context of the ARIEL mission, and how such noise will impact transit spectroscopy observations;

**B4)** examine the feasibility of observing Earth-like planets in transit spectroscopy in the context of the TRAPPIST-1 exosystem and the ARIEL mission.

## 7.2 APPROACH TO DEVELOPMENT AND VALIDATION

In Chapter 1, the proposed simulator was contrasted with previous simulators and a case made for its development in the setting of the signal and noise challenges of transit spectroscopy. In Chapter 2, I described the algorithm and validation testing of the simulator. ExoSim was developed with the view to ensure it was not hard-coded for any specific instrument and cognizant of the current issues pertaining to transit spectroscopy observations and its variants. A modular structure was used that allows for future upgrades, and interfacing with external models. The latter was demonstrated later in Chapter 5 by interfacing with the results from an external model of stellar pulsation and granulation developed by KU Leuven, and our own SpotSim star spot model. ExoSim adopts a similar modular nomenclature to EChOSim (Pascale et al., 2015), and reuses limited code for some simple functions, but the vast majority of the ExoSim code has been written *de novo* for the purpose of developing a generic and highly versatile simulator. Uniquely ExoSim models the time domain in small steps much smaller than the integration time. This allows ExoSim to capture complex time domain effects other simulators cannot. In contrast to EChOSim and other simulators, ExoSim can simulate pointing jitter in 2-D on the focal plane, capturing both spectral and spatial jitter. This was crucial in Chapter 4, where ExoSim simulations discovered spectral jitter noise to be an issue for ARIEL observations, and specific solutions were

found pertaining to each type of jitter. In contrast to previous simulators, ExoSim captures the effect of folding jitter frequencies into the integration period, which is part of the complex mechanism of jitter noise, impacting on the final photometric noise. Other novel elements are the capabilities to use non-standard PSFs, to simulate spatial scanning and to simulate phase curves at multiple wavelengths. This is all done in the context of keeping ExoSim generic, so unlike previous simulators, all specific information for the instrument and observation is contained in exchangeable Input Configuration Files (linked to sets of reference files). The simulation using small time steps in ExoSim is a function that has great utility beyond pointing jitter. It allowed ExoSim to model the correlated noise from stellar convection and allowed for light curve modifications from the star spots in Chapter 5. ExoSim validation tests were performed using a variety of comparisons including independent simulations, analytical predictions, the ESA Radiometric Model (Puig et al., 2015), and real data from Kreidberg et al. (2014a) and Berta et al. (2012). ExoSim was accurate to within 5% of most of the comparisons. Therefore goals A1-A3 above were achieved.

## 7.3 KEY FINDINGS

In this section I summarise the key findings from Chapters 3-6, which addresses goals A4 and B1-B4.

### 7.3.1 CHAPTER 3

ExoSim was used in a 'retrospective' manner modeling complex instrumental noise from spatial scanning mode in the Hubble WFC IR instrument. I simulated observations closely matching those in Kreidberg et al. (2014a) and Berta et al. (2012). The main findings were as follows:

- 1)** In contrast to Swain et al. (2013b), I find that scanning mode appears superior to normal staring mode in terms of noise on the final spectrum, with a 38% decrease in average  $\sigma_{cr}$ . This is mostly the result of an increased duty cycle producing a reduced fractional photon noise.
- 2)** I find no evidence of significant extra noise resulting from scanning mode itself, which may be a testament to lack of intra-pixel non-uniformity in the instrument and excellent pointing stability of Hubble. When experimental intra-pixel non-uniformity was introduced some extra noise arising from scanning was detected but did not impact the overall noise significantly.

- 3) The excellent pointing precision of Hubble means that even without any jitter decorrelation the jitter noise-related impact on  $\sigma_{cr}$  was only of the order of 2-3% of the overall value.
- 4) I find  $\sigma_{cr}$  values consistent with the published results in Kreidberg et al. (2014a), which is therefore supportive of their claim that GJ 1214b spectrum fits a flat line consistent with a cloudy atmosphere.
- 5) I find that the backward scans of Kreidberg et al. (2014a) have an additional sawtooth-like amplitude of upto 20 mas that does not appear to have been previously reported. This was not simulated in this test, and is still small compared to the angular size of the pixel.

### 7.3.2 CHAPTER 4

ExoSim was used in a 'prospective' manner in the Phase A design study for the proposed ARIEL mission. ARIEL aims to perform the first ever spectroscopic survey of exoplanets with the potential for transformative science in this field. The key findings from this chapter were as follows:

- 1) ARIEL observations are associated with high levels of spectral jitter noise. This is generally worse for bright targets.
- 2) Spectral jitter noise is effectively reduced using an 'image shift decorrelation' method but only in the setting of effective flat fielding.
- 3) Spatial jitter noise is much lower than spectral jitter noise at baseline but is increased through tight apertures; it is mitigated through effective flat fielding and optimal sizing of the aperture.
- 4) General jitter noise in photometric channels can be controlled through shifting of the aperture alone together with optimal aperture sizing.
- 5) Simulation of jitter needs accurate representation of the PSF aberration (which is an ExoSim feature) not to overestimate the resulting noise in the visual and NIR channels.
- 6) It is possible to control pointing jitter noise in ARIEL to acceptable levels in data reduction without need to redesign the instrument.
- 7) The final ARIEL design was tested and found to have near-photon noise limited performance in most spectral bins, and was compatible with a viable science case where 1002 exoplanets covering a wide parameter space can be observed in tier 1 within the mission lifetime, with sufficient time left for a significant number of planets to be studied in tiers 2 and 3.

### 7.3.3 CHAPTER 5

Stellar variability and activity are major concerns in exoplanet transit spectroscopy, so ExoSim was coupled to two different models to elucidate the impact of convection-driven stellar noise (pulsation and granulation) and star spot noise on ARIEL observations of GJ 1214b and HD 209458b. The main findings were as follows:

- 1) Stellar convection noise increases somewhat at shorter wavelengths, and is higher in the M-dwarf case as might be expected for the more active star, e.g. 24.5 ppm in AIRS Ch0 compared to 9.8 ppm for HD 209458.
- 2) Stellar convection noise variance is a tiny proportion of the source photon noise variance, e.g. 0.0143% in AIRS Ch0 for GJ 1214, and for both targets studied it never exceeds 1% of the photon noise variance. It is therefore not a significant noise source and does not require decorrelation.
- 3) The effect of unocculted spots is to cause an upward 'baseline' bias on the contrast ratio spectrum that increases with shorter wavelengths. The simulations show this bias this could mimic Rayleigh scattering as suggested by Oshagh et al. (2014) and McCullough et al. (2014), reaching a distortion at 0.53  $\mu\text{m}$  of upto 19.9% in HD 209458b and +12.7% in GJ 1214b at 29.5% filling factors. At the most likely filling factors for each host star, the maximum positive distortion is + 3.9% for GJ 1214b and + 0.9% for HD 209458b. However for this to be consistent, the occulted spot effect must remain minimal across observations.
- 4) Occulted spots oppose the unocculted spot bias and in strong cases can result overall downward bias. The degree of the opposing bias varies from visit to visit. At 0.53  $\mu\text{m}$ , the distortion in the contrast ratio spectrum ranges from +0.9 to -0.5% for HD 209458b and +3.9 to -5.2% for GJ 1214b at the most likely filling factors.
- 5) The above mentioned variation gives a 'spot noise' on the transmission spectrum. This is worse at shorter wavelengths, at higher filling factors and lower Q values. The impact of spot noise also decreases with increasing wavelength due to an increase in photon noise.
- 6) For the same filling factor, the spot noise is greater for G-type stars than M-type stars due to the higher spot temperature contrast, however M-type stars will usually have higher filling factors than G-type stars and probably lower Q ratios.
- 7) For ARIEL, in the AIRS channels, HD 209458b and GJ 1214b (at probable filling factors of 1% and 10% respectively) are likely to not require spot corrections, with increases in the final uncertainties of just 0.3% and 1.0-1.3% respectively. However accounting or correcting for spots is needed in NIRSpec and the FGS channels,

with increased uncertainties of upto 99% in HD 209458b and 81.9% in GJ 1214b.

8) Current methods that de-bias the effect of unocculted spots may be inaccurate if the occulted spot effect or faculae content are not taken into account, and could result in worsened error. The best correction will decorrelate the occulted spot effect and then de-bias the residual unocculted spot bias. In some situations it may be better to add an uncertainty to the spectrum rather than to attempt corrections.

### 7.3.4 CHAPTER 6

ExoSim was used to assess the feasibility of observing the TRAPPIST-1 planets using ARIEL. The key findings are as follows:

- 1) The possibility of secondary eclipse spectroscopy by ARIEL on any of these planets, and thus also phase curve spectroscopy, is excluded.
- 2) In primary transit, all 7 planets should be studied in tier 1 as H<sub>2</sub>-He-dominated 'primordial' atmospheres would be detectable for all planets in a few transits comprising altogether 0.11% of the 3.5 year total mission observing time. The time to perform the number of transits needed to characterise primordial atmospheres on all 7 planets at tier 3 resolution would comprise 0.53% of the available total observing time, and 0.25% at tier 2. Consideration should thus be given to studying these planets at tier 2 or tier 3 upto the projected number of transits needed to detect a primordial atmosphere. Of note however de Wit et al. (2016) has rejected such atmospheres on planets b and c.
- 3) For most planets including habitable zone planets (d, e, f and g), high mean molecular weight atmospheres will not be detectable in primary transit without hundreds of transits and then only at tier 1 resolution, which is not an effective use of observing time. Thus the habitable zone planets are not good targets for detailed characterisation by ARIEL.
- 4) Planets h and b could potentially have high molecular weight atmospheres characterised at tier 2 or tier 3 resolution. Planet h could have a high molecular weight atmosphere of upto 24.3 g/mol characterised at tier 2 in 0.56% of the mission lifetime. Planet b could have a high molecular weight atmosphere of upto 41.3 g/mol characterised at tier 2 in 3.36% of the mission lifetime.

## 7.4 LIMITATIONS

In terms of the realism of the simulations, validation testing shows a reasonable accuracy but much depends on the exact models used to simulate the star and

planet, as well as the accuracy of the instrument model. In terms of the functionality in the instrument model, the current code does not have a specific function dedicated to a generic time-dependent systematic, although specific time domain modulations such as the transit light curves and stellar variability effects have been coded for. ExoSim however is set up for time-dependent systematic effects to be modeled and so adding a generic systematic function should be a fairly simple addition to the code, and could be used to model for example the Hubble persistence 'ramp' or effects of thermal changes. The baseline ExoSim code uses 'instantaneous' light curves rather than light curves that integrate the modulation over the integration time. This might result in some inaccuracy especially at longer integration times where the discrepancy between the instantaneous and integrated curves may become more apparent. I did implement an experimental 'integrated' light curve in Chapter 5 which is theoretically more accurate, so this functionality could be formally incorporated into the code. However the comparison with the white light curve from Kreidberg et al. (2014a) suggests the current code is still very accurate upto at least 90s of integration time. The effects of detector non-linearity and cosmic rays were not modeled, but again could be added in a future version. In general, there may be limits to how far a 'generic' simulator can go before some level of specific 'hard coding' is needed. For example, a more detailed WFC3 IR model may include the geometric distortion of the detector grid, the slight tilt in the spectrum and the small variations in wavelength solution with row. Some of these effects might be possible by upgrading the current ExoSim code while keeping it generic in structure (e.g. a small adjustment to the coadding of PSFs could model the latter two effects), but some instrument effects may become detailed enough that specific 'hacks' will be required. However the goal here is to minimise the need for such specific coding in the core algorithm. Nevertheless the thesis has shown how the baseline ExoSim code can be used for two highly different optical systems, the Hubble WFC IR and ARIEL, and thus it could be the nucleus of simulators for other transit spectroscopy instruments, such as a JWST and its suite of instruments.

The basic data reduction pipeline developed in Chapter 4 had some limitations, notably the lack of a real optimal extraction method, instead relying on a correction factor to account for this. This may be acceptable in terms of the problems examined here in giving a first order estimate of the expected improvement, but ideally this should be demonstrated with an active method.

The balance between speed and accuracy can be an issue with ExoSim. For Monte Carlo simulations to be practical, simulations must be completed rapidly (in

the order of seconds to a minute), which may prompt the use of lower simulation frame rates. The frame rate will limit the range of values the exposure time can be rounded to, but should not affect the accuracy of the jitter simulation as shown in Chapter 2. Low pointing jitter slows the simulation since the oversampling of the convolved focal plane array is increased; a fix for this was found in the case of Hubble by reducing the oversampling to a third of the calculated value, which tests in Chapter 2 showed was an acceptable change. Larger focal planes will result in slower simulations, so if the simulation slows, cropping the focal plane to the bare minimum needed may help to increase speed.

The WFC3 model used here had some omissions including the persistence ramp systematic, and the effects of Earth occultations as well as the factors mentioned above. This may have implications for the final noise results that were not factored in. Scanning mode has been performed at many different rates, not just the rate tested here, and it is possible that at higher rates different results may occur. I also did not factor in the sawtooth effect discovered for the backward scans. It should be possible to add these factors in a future version of the simulation.

Limitations of the pointing jitter model (used particularly for ARIEL noise performance testing in Chapter 4), include that it currently does not permit simulation of changes in the jitter rms with time during an observation, which may be a feature of a realistic pointing system. One way this could be tackled in the future is to apply an envelope function to the generated jitter timelines that could model variations in rms with time. In addition, in the assessment of the matured ARIEL designs, we used flat PSD profiles restricted to broad 'bright' and 'dim' target categories. The former aspect, while capturing the overall rms required correctly, may have reduced correlation in the jitter timeline. The effect would probably not change the overall conclusions reached here, but Phase B studies may merit formulating a more accurate PSD profile. While the 'bright' and 'dim' PSD categories adhere to the mission requirements and are adequate for the study performed here, the variation in pointing accuracy will in reality be a continuous function of the source brightness. A future simulation could adjust the overall PSD rms based on the brightness of the source. Other limitations of the Phase A simulations included not accounting for more complex read-out modes (such as up-the-ramp sampling), and the fact that the detector dark currents were not finalised in the design. For the latter we tested pessimistic cases, so we would expect the real instrument to perform better. Incorporating the effects of more complex read-out modes could be considered in a future Phase B study.

The star spot model used here had a limited resolution to permit faster

speed for Monte Carlo simulation, and this may have resulted in some of the discrepancies between the inputted values and the measured values, e.g. in the Q factor, though there were other effects too such as the overlap of spot and faculae areas. The faculae simulation too in terms of Q ratio, temperature and shapes was more speculative than for the cold spots, and so the results where these were included need to be viewed with added caution. The simulations also assumed a uniform random distribution that may be a fair for an initial simulation especially if there is no information about the spot distribution on a specific star, but some stars are known to have clustering at preferred latitudes and this will change the distribution due to the occulted spot effect.

In the TRAPPIST-1 study I made reasonable assumptions about the albedo of the planets and tidal locking such that my equilibrium temperatures differed slightly from those in other studies, however of course the actual temperatures may vary significantly from the equilibrium temperature depending on the exact conditions including the actual albedo, rotation rate and greenhouse effects. Of note many of the masses from Wang et al. (2017) differ significantly from the published masses used here. This could significantly change the analysis and so the study should be repeated once robust mass data has been established.

## 7.5 FUTURE WORK

Possible modifications to the ExoSim code and data reduction pipeline were discussed above and would be the focus of on-going upgrades. The data reduction pipeline, currently external to ExoSim itself, could be packaged for optional use by future users of ExoSim.

In terms of the Hubble WFC IR model, future work can address adding the additional instrumental and observation effects noted above, and perhaps replicating more of the studies listed in Table 3.1, with different scan rates, to see if we can confirm or refute the final uncertainties reported in each study, that may pertain to the scientific conclusions of each.

As mentioned, a future JWST model would be another interesting use of ExoSim. Although many simulators exist for JWST and its instruments, none have the capabilities demonstrated in ExoSim for modeling time domain effects in particular. Scanning mode would be a good simulated experiment to see if this remains a superior mode of operation in JWST. Additionally feasibility studies can be performed with ExoSim, perhaps combining the uncertainties obtained on reconstructed spectra with spectral retrieval studies.

For ARIEL, assuming selection, a Phase B study will be performed in which ExoSim will be key. As discussed above, in Phase B we can further develop the realism of the pointing simulation, accounting for source brightness and incorporating dynamic changes in rms during an observation. More advanced read-out modes could also be included. Combining results with spectral retrieval studies will allow more detailed assessment for key science questions or for specific targets. New discoveries may prompt further feasibility studies as in Chapter 6. The phase curve function can be utilised for simulation of phase curve spectroscopy in tier 2, assessing retrievability of the underlying global atmospheric model.

Future directions for spot simulations could be to improve the SpotSim model by making the faculae simulation more accurate, with more realistic shapes, and taking into account the brightness variation with limb angle; however there is still limited knowledge of the faculae content of other stars which restricts how much weight these simulations should carry. Testing decorrelation methods could be a major use of the SpotSim-ExoSim set up, especially for ARIEL Phase B. This framework can be used to test occulted spot decorrelation methods as well as the existing methods for unocculted spot corrections. The effects of spots on other targets for ARIEL such as the more active K-type star HD 189733b could be simulated as well, and since this is a well-studied system, results could be compared to real data as a way of validating the overall SpotSim-ExoSim simulation. Also the impact for other instruments with increased precision (and thus increased vulnerability to the effects of spot noise) such as JWST could be simulated. In ARIEL Phase B, examining how the spot noise impact varies with spectral resolution in tiers 1 and 2 would be important to establish, as these current results were performed in tier 3 resolution. To generalise results better, a study with a set of archetypal exosystems could be performed with distance changed in the simulation; since distance will affect the photon noise, this will impact the overall spot noise/photon noise ratio for a given instrument. From this, the noise-distance relation could be constructed for a given archetype, giving estimates for the probable spot noise for any given real system. It would also be important to examine the effect of clustering of spots at preferred latitudes as this could result in different distribution patterns for contrast ratio spectra. Finally a future simulation could examine the impact of spectral enhancements due to spot absorption features; this would require a fairly minor modification to the SpotSim code, using model stellar spectra instead of blackbodies.

For feasibility studies of Earth-like planets, a more general study can be performed using ExoSim and a range of different key mirror sizes representing

current and future telescopes, including perhaps 10 and 30 m class ground-based telescopes, with a generic transit spectroscopy instrument designed to study an Earth-like atmosphere. Unlike previous studies looking at the feasibility of transit spectroscopy on such planets, this would incorporate a more detailed noise model with instrumental effects included (not just photon noise) and would produce more general results looking at different mirror sizes and the detectability with distance. Combined with stellar and planetary statistics this could result in possible 'yields' for the detection of Earth-like planet atmospheres for each telescope class.

There are many potential future uses for ExoSim including application to new exoplanets projects and proposals, including the modeling of ground-based instruments, balloon-borne telescopes as well as future space-based telescopes.

---

In this thesis, I showed how simulated exoplanet transit spectroscopy observations with ExoSim could be used to address and find solutions to a range of problems in the field, resolving a specific controversy about instrumental noise, helping to develop a key instrument that will perform transformative exoplanet science, enhancing the understanding of the impact of convection-related stellar noise and spot effects on transmission spectra, and assessing the feasibility of characterising Earth-sized planets. Transit spectroscopy has a bright future in the coming decade, with the possibility of new discoveries that will address truly fundamental questions about the formation and evolution of planets as well as the search for habitable worlds and life itself. ExoSim will be available to the community as a tool to advance our understanding of transit, eclipse and phase-curve spectroscopy and to optimise observations that will address such questions.



# APPENDIX

---

---

## A.1 PROOF FOR 2-D JITTER NOISE EXPRESSION

Consider a symmetrical 2-D Gaussian,  $z(x, y) = f(x)f(y)$ , of height unity and standard deviation  $s$  representing a monochromatic beam. We will find an expression for the jitter noise about a point  $(a, a)$ , where  $a$  is the distance from the peak. The jitter about this point occurs with a random normal distribution of standard deviation  $rms_{jit}$  independently in each axis.

$$z = \exp\left(\frac{-x^2}{2s^2}\right) \exp\left(\frac{-y^2}{2s^2}\right) \quad (\text{A.1})$$

where  $x$  and  $y$  are zero at the peak of the Gaussian. Considering just  $f(x)$ :

$$f(x) = \exp\left(\frac{-x^2}{2s^2}\right) \quad (\text{A.2})$$

We can replace the RHS with a second order Taylor expansion about the point  $a$ .

$$\begin{aligned} f(x) \approx \exp\left(\frac{-a^2}{2s^2}\right) - \left(\frac{a}{s^2}\right) \exp\left(\frac{a^2}{2s^2}\right) (x - a) \\ + \exp\left(\frac{-a^2}{2s^2}\right) \left(\frac{a^2 - s^2}{2s^4}\right) (x - a)^2 \end{aligned} \quad (\text{A.3})$$

Let  $A = \exp\left(\frac{-a^2}{2s^2}\right)$  and  $\beta = \left(\frac{a^2 - s^2}{2s^4}\right)$  and  $\alpha = \exp\left(\frac{-a^2}{s^2}\right)$ . Thus:

$$f(x) \approx A + \alpha A(x - a) + \beta A(x - a)^2 \quad (\text{A.4})$$

and it follows that

$$f(y) \approx A + \alpha A(y - a) + \beta A(y - a)^2 \quad (\text{A.5})$$

Therefore

$$z(x, y) \approx [A + \alpha A(x - a) + \beta A(x - a)^2][A + \alpha A(y - a) + \beta A(y - a)^2] \quad (\text{A.6})$$

We now need to find the variance on  $z$  around the point  $(a, a)$  when subjected to the jitter  $rms_{jit}$  in each axis. The variance of  $z$  is given by:

$$Var(z) = \langle (z - \langle z \rangle)^2 \rangle \quad (\text{A.7})$$

The variance of the jitter,  $rms_{jit}^2$ , in the  $x$  axis is given by:

$$rms_{jit}^2 = \langle (x - a)^2 \rangle \quad (\text{A.8})$$

Therefore (and logically for the  $y$  axis):

$$rms_{jit}^2 + a^2 = \langle x^2 \rangle = \langle y^2 \rangle \quad (\text{A.9})$$

We now find  $\langle z \rangle$ . Expanding the RHS of Equation A.6,

$$\begin{aligned} z(x, y) \approx & A^2 + \alpha A^2(y - a) + \beta A^2(y - a)^2 + \alpha A^2(x - a) \\ & + \alpha^2 A^2(x - a)(y - a) + \alpha\beta A^2(x - a)(y - a)^2 \\ & + \beta A^2(x - a)^2 + \alpha\beta A^2(y - a)(x - a)^2 \\ & + \beta^2 A^2(x - a)^2(y - a)^2 \end{aligned} \quad (\text{A.10})$$

The average position for the jitter will be  $(a, a)$ , therefore  $\langle x \rangle = \langle y \rangle = a$ . It follows that  $\langle (x - a)(y - a) \rangle = 0$ . Also  $\langle (x - a)^2 \rangle = \langle x^2 \rangle - a^2$  and  $\langle (y - a)^2 \rangle = \langle y^2 \rangle - a^2$ . When finding  $\langle z \rangle$  therefore a number of terms will be eliminated, and  $\langle z \rangle$  can be expressed as:

$$\begin{aligned} \langle z \rangle \approx & A^2 \left[ 1 + \beta \langle y^2 \rangle + \beta \langle x^2 \rangle - 2\beta a^2 \right] \\ & + A^2 \beta^2 \left[ \langle y^2 \rangle \langle x^2 \rangle - \langle y^2 \rangle a^2 - \langle x^2 \rangle a^2 + a^4 \right] \end{aligned} \quad (\text{A.11})$$

For  $z$ , in Equation A.6 we can eliminate higher order terms of second order and above, since if  $(x - a) < 1$  and  $(y - a) < 1$  these will be small compared to the first and zeroth order terms. Therefore:

$$z \approx A^2 - \alpha A^2(y - a) + \alpha A^2(x - a) \quad (\text{A.12})$$

Making the substitutions  $\langle x^2 \rangle = \langle y^2 \rangle = rms_{jit}^2 + a^2$  in Equation A.11 and eliminating terms in  $rms_{jit}$  higher than 4th order (since these will be small if  $rms_{jit} < 1$ ), we can find  $z - \langle z \rangle$ .

$$z - \langle z \rangle \approx A^2 \left[ \alpha(x - y) - 2\beta rms_{jit}^2 - \beta^2 rms_{jit}^4 \right] \quad (\text{A.13})$$

Then the variance on  $z$ ,  $Var(z) = \langle (z - \langle z \rangle)^2 \rangle$  is given by:

$$Var(z) \approx A^4 \left[ \alpha^2 \langle x^2 \rangle - 2\alpha^2 \langle x \rangle \langle y \rangle + \alpha^2 \langle y^2 \rangle + 4\beta^2 rms_{jit}^4 \right] \quad (\text{A.14})$$

Using again the above substitution for  $\langle x^2 \rangle$  and  $\langle y^2 \rangle$  and recalling that  $\langle x \rangle = \langle y \rangle = a$ , this becomes:

$$Var(z) \approx A^4 \left[ 2\alpha^2 (rms_{jit}^2 + a^2) - 2\alpha^2 a^2 + 4\beta^2 rms_{jit}^4 \right] \quad (\text{A.15})$$

Simplifying this becomes:

$$Var(z) \approx A^4 \left[ 2\alpha^2 rms_{jit}^2 + 4\beta^2 rms_{jit}^4 \right] \quad (\text{A.16})$$

Substituting back the expressions for  $A$ ,  $\alpha$  and  $\beta$ , we obtain:

$$Var(z) \approx \exp(-a^2/2s^2) \left( 4rms_{jit}^4 \left[ \frac{a^2 - s^2}{s^4} \right]^2 + rms_{jit}^2 \left[ \frac{2a^2}{s^4} \right] \right) \quad (\text{A.17})$$

This gives the variance of  $z$  at the point  $(a, a)$ , thus the noise at  $(a, a)$  is given by:

$$\sigma_{(a,a)} \approx \left[ \exp(-a^2/2s^2) \left( 4rms_{jit}^4 \left[ \frac{a^2 - s^2}{s^4} \right]^2 + rms_{jit}^2 \left[ \frac{2a^2}{s^4} \right] \right) \right]^{1/2} \quad (\text{A.18})$$

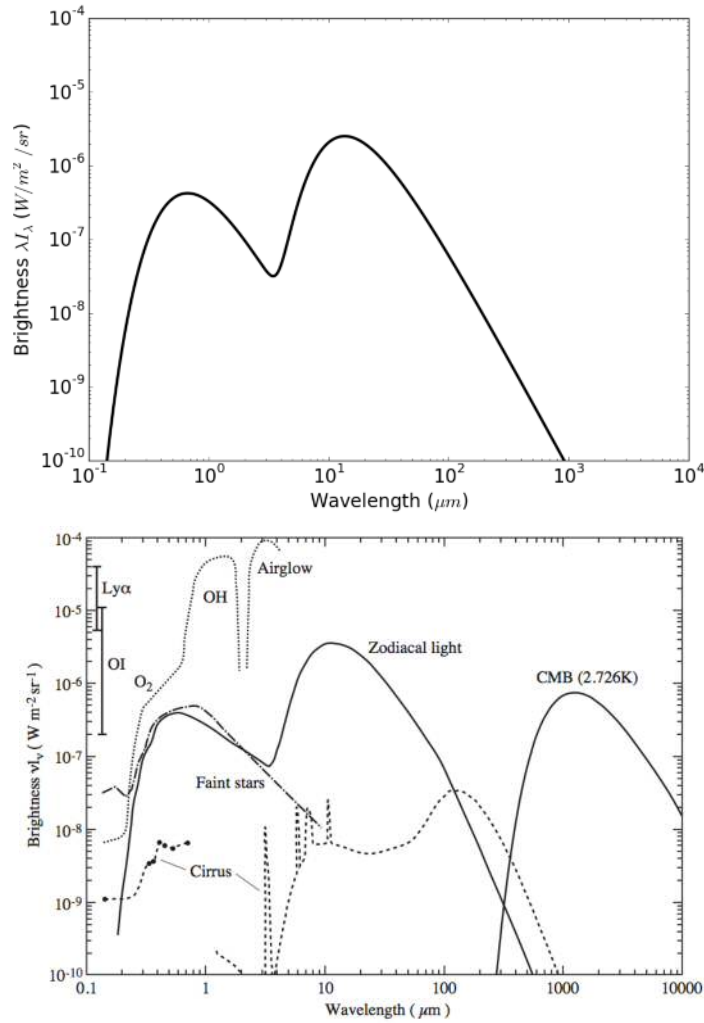


FIGURE A.1 ExoSim Zodiacal light model (top) vs Leinert et al. (1998) (bottom). The latter measured zodiacal light from the South Ecliptic Pole. The ExoSim model closely matches this.

## A.2 ZODIACAL LIGHT ADJUSTMENT

As mentioned in Chapter 2, the baseline zodiacal dust model used in ExoSim closely matches the dust reflection and emission spectrum measured by Leinert et al. (1998) from the South Ecliptic Pole (Figure A.1). Therefore this model can be used without alteration for high ecliptic latitudes.

To estimate how the emission may change at lower latitudes, I resampled (using WebPlotDigitizer (Rohatgi, 2017) charts from Tsumura et al. (2010) and James et al. (1997), that show how the intensity from zodiacal light varies with latitude. Tsumura et al. (2010) used the Low Resolution Spectrometer (LRS) onboard

the Cosmic Infrared Background Experiment (CIBER) observing between 750 and 2100 nm. I sample the LRS points shown in Figure A.2, left, and find the average of the three points above  $40^\circ$ . I assume this average represents intensity consistent with the ExoSim zodi spectrum and Leinert et al. (1998). I then find the relative change in intensity for all 5 points relative to this average, the highest intensity point occurring at about  $6^\circ$  latitude. I then randomly sample, using WebPlotDigitizer, the 6 intensity curves from James et al. (1997), shown in Figure A.2, right, who performed CCD photometry with a 16 mm fish-eye lens in the V and B bands. These curves measure changes down to about  $0.3^\circ$  ecliptic latitude. Note the sampled points do not match exactly in terms of latitude between the different curves. Each sampled point is normalized to the value of its own curve at about  $6^\circ$ , which itself is normalized to the relative intensity of the  $6^\circ$  point of the Tsumura et al. (2010) curve. This generates a set of points showing intensity at different latitudes relative to that at the highest latitudes (Figure A.3). This appears to be a sigmoidal curve in normal-log space, to which a 5th order polynomial was fitted as shown. The equation of the polynomial is:  $y = 1.384 \times 10^{-9}x^5 - 3.119 \times 10^{-7}x^4 + 2.100 \times 10^{-5}x^3 - 7.430 \times 10^{-6}x^2 - 4.675 \times 10^{-2}x + 2.256$ .

The positions of the various exosystems simulated in this thesis are shown on Figure A.3. For the three planets at the highest latitudes, the baseline zodi model is probably an adequate estimate of the first order effect on ARIEL observations. Although reaching 1.43 relative intensity at HD 219134, the low contribution of zodi noise to the overall noise budget (Chapter 4 Figure 4.27) means that this factor will have negligible impact on the results. For 55 Cancri we obtain a relative intensity of 1.79. 55 Cancri was only used early in the ARIEL Phase A study for the relative assessment of the LRS and HRS designs (Chapter 4 Figure 4.7). Since it was a comparison study and in both designs, the zodi noise was extremely low compared to most other noise sources, applying this factor would have no significant impact on the findings. For TRAPPIST-1, being very close to the ecliptic, it was important to account for the increased intensity due to zodiacal dust. The chart indicates a factor of 2.23 relative intensity and thus this was applied to the zodi model spectrum used in the simulations in Chapter 6.

This chart however must be used with some caution since the exact intensity of the zodiacal dust is not uniform at a given latitude. More detailed zodi models could be developed, but in the absence of such a model this chart serves as a reasonable first order guide for scaling the intensity with ecliptic latitude.

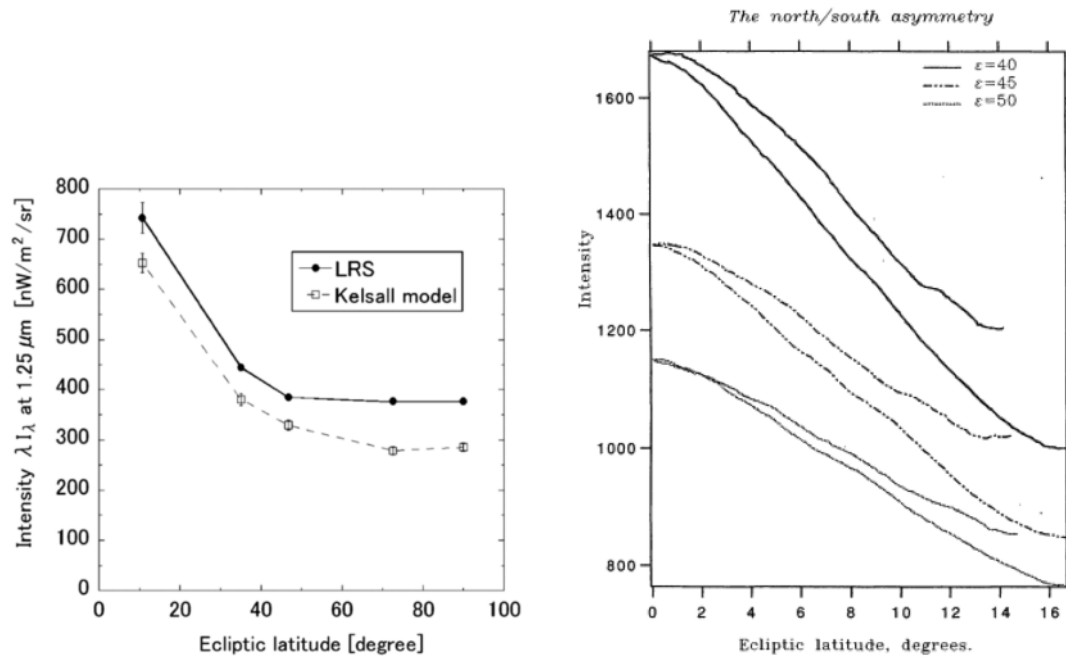


FIGURE A.2 Intensity of zodiacal light as a function of ecliptic latitude from two studies. Left: Tsumura et al. (2010). Right: James et al. (1997).

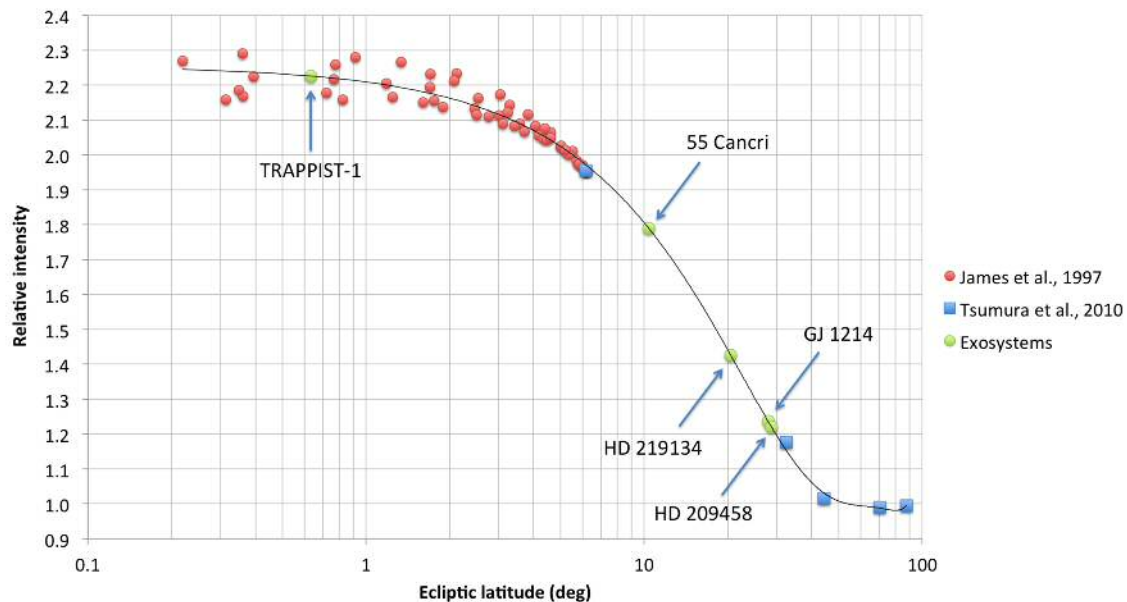


FIGURE A.3 Relative intensity of zodiacal light versus ecliptic latitude. Sampled points from Tsumura et al. (2010) and James et al. (1997) are shown. A 5th order polynomial is fitted and exosystems simulated in this thesis are located on this line.

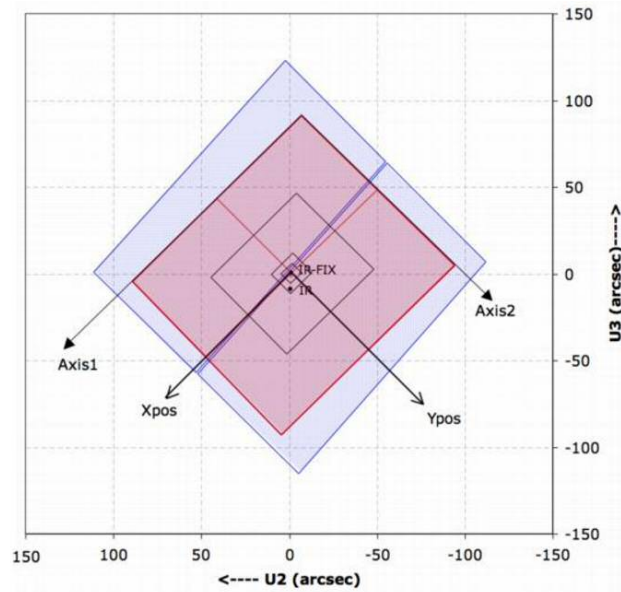


FIGURE A.4 IR-FIX aperture in relation to spacecraft U2 and U3 axes.  $U2 = -V2$  and  $U3 = -V3$ . Figure taken from Dressel (2017).

### A.3 V2,V3-X,Y TRANSFORMATION

The transformation of HST spacecraft V2 and V3 axis coordinate to X and Y detector axis coordinates (all in arcsec) is described here. The X and Y axes are for the IR-FIX aperture (Figure A.4) which is the 'POS TARG' coordinate system used in scanning mode observations (McCullough & MacKenty, 2012). This was required for the analysis of scanning mode and the development of the Hubble pointing jitter PSD in Chapter 3.

From the Hubble WFC3 Aperture File<sup>1</sup>, I obtain the following parameters:

- 1) magnitude of distance along the V2 axis to the X-Y origin,  $a = 1.1794''$
- 2) magnitude of distance along the V3 axis to the X-Y origin,  $b = 0.4119''$
- 3) angle from V3 axis to Y axis in anticlockwise direction,  $\theta = 44.667^\circ$

Then:

$$4) A = b \sin \theta + a \cos \theta$$

$$5) B = b \cos \theta - a \sin \theta$$

Finally:

$$6) X = A + V3 \sin \theta - V2 \cos \theta$$

$$7) Y = B + V3 \cos \theta + V2 \sin \theta$$

<sup>1</sup> <http://www.stsci.edu/hst/observatory/apertures/wfc3.html>



# BIBLIOGRAPHY

---

---

- Akiyama E. et al., 2016, *ApJ*, 818, 158
- Allard F., Homeier D., Freytag B., 2012, *Phil. Trans. R. Soc. A*, 370, 2765
- Alonso R. et al., 2007, *Astron. Soc. Pac. Conf. Ser.*, 366, 13
- Andersen J. M., Korhonen H., 2015, *MNRAS*, 448, 3053
- ARIEL Consortium, 2015, ARIEL Proposal Document
- ARIEL Consortium, 2017, ARIEL Yellow Book, ESA/SCI(2017)2
- Barstow J. K. et al., 2015a, *MNRAS*, 448, 2546
- Barstow J. K. et al., 2015b, *Exp. Astron.*, 40, 545
- Barstow J. K., Irwin P. G. J., 2016, *MNRAS Letters*, 461, L92
- Barstow J. K. et al., 2017, *ApJ*, 834, 50
- Batalha N. E. et al., 2015, arXiv:1507.02655 [astro-ph.EP]
- Batalha N. E. et al., 2017, *PASP*, 129, 064501
- Batalha N. M., 2014, *PNAS*, 111, 12647
- Beichman C. et al., 2014, *PASP*, 126, 1134
- Belu, A. R. et al., 2011, *A&A*, 525, A83
- Berdyugina S. V., 2005, *Living Rev. Sol. Phys.*, 2, 8
- Berta Z. K. et al., 2011, *ApJ*, 736, 12
- Berta Z. K. et al., 2012, *ApJ*, 747, 35
- Bogdan T. J. et al., 1988, , 327, 451

- Bowler B. P. et al., 2010, *ApJ*, 723, 850
- Bradley L. et al., 2016, *astropy/photutils*: v0.3
- Bryson S. T. et al., 2010, *Proc. SPIE* 7738, 773808
- Carter J. A., Winn J. N., 2009, *ApJ*, 704, 51
- Cassan A. et al., 2012, *Nature*, 481, 167
- Chapman G. A., Cookson A. M., Dobias J. J., 1997, *ApJ*, 482, 541
- Chapman G. A. et al., 2001, *ApJ*, 555, 462
- Charbonneau D. et al., 2002, *ApJ*, 568, 377
- Colón K. D. et al., 2012, *MNRAS*, 419, 2233
- Crossfield I. J. M. et al., 2016, *ApJS*, 226, 7
- Crouzet N. et al., 2014, *ApJ*, 795, 166
- Cubillos P. et al., 2017, *AJ*, 153, 3
- Content D. et al., 2013, *Proc. SPIE* 8860, 88600E
- de Mooij E. J. W. et al., 2012, *A&A*, 538, A46
- de Wit J. et al., 2016, *Nature*, 537, 69
- Deming D. et al., 2011, *ApJ*, 740, 33
- Deming D. et al., 2013, *ApJ*, 774, 95
- Deustua S. E., 2016, *WFC3 Data Handbook*, v3.0, Baltimore: STScI
- Diaz R., 2012, *Instrument Science Report CDBS 2012-01*, Baltimore: STScI
- Dressel L., 2017, *WFC3 Instrument Handbook*, v9.0, Baltimore: STScI
- Dressing C. D., Charbonneau D., 2015, *ApJ*, 807, 45
- Eccleston P., 2017, *ESA/ARIEL Technical Note ARIEL-RAL-PL-DD-001*, Iss 2.0
- Ehrenreich, D. et al., 2014, *A&A*, 570, A89
- ESA, 2011, *ESA Pointing Error Engineering Handbook*.

- Evans T. M. et al., 2016, *ApJL*, 822, L4
- Forget F., Leconte J., 2014, *Phil. Trans. R. Soc. A*, 372, 20130084
- Fortier A. et al., 2014, *Proc. SPIE* 9143, 91432J
- Foukal P., 1998, *ApJ*, 500, 958
- Fraine J. et al., 2014, *Nature*, 513, 526
- Fruchter A. et al., 2009, *The Multidrizze Handbook*, v3.0, Baltimore: STScI
- Gibson N. P. et al., 2012, *MNRAS*, 2683
- Gilliland R., 2005, *Instrument Science Report TEL 2005-01*, Baltimore: STScI
- Gillon M. et al., 2007, *A&A*, 471, L51
- Gillon M. et al., 2016, *Nature*, 533, 221
- Gillon M. et al., 2017, *Nature*, 542, 456
- Gondoin P., 2008, *A&A*, 478, 883
- Grillmair C. J. et al., 2008, *Nature*, 456, 767
- Hansen C. J., Schwartz J. C., Cowan N. B., 2014, *MNRAS*, 444, 3632
- Hathaway D. H., 2013, *Sol. Phys.*, 286, 347
- Hathi B. et al., 2008, *Icarus*, 197, 579
- Herrero E., Ribas I., Jordi C., 2015, *Exp. Astron.*, 40, 695
- Horne K., 1986, *PASP*, 609
- Ingalls J., Mighell K., 2014, presented at 224th AAS Meeting, 1-5 June 2014, Boston, MA
- IRAC Instrument and Instrument Support Teams, 2015, *IRAC Instrument Handbook*, v2.1.2, NASA/IPAC
- Irwin J. et al., 2008, *Proc. Int. Astron. Union*, 4(S253), 37
- Irwin P. G. J. et al., 2008, *J. Quant. Spectrosc. Radiat. Transfer*, 109, 1136
- Iverson R. J. et al., 2007, *MNRAS*, 380, 199

- James J. F. et al., 1997, *MNRAS*, 288, 1022
- Jehin E. et al., 2011, *The Messenger*, 145, 2
- Kaltenegger L., 2011, *Proc. Int. Astron. Union*, 7(S280), 302
- Kasting J. F., Whitmire D. P., Reynolds R. T., 1993, , 101, 108
- Knutson H. A. et al., 2007, *Nature*, 447, 183
- Knutson H. A. et al., 2008, *ApJ*, 673, 526
- Knutson H. A. et al., 2014a, *Nature*, 505, 66
- Knutson H. A. et al., 2014b, *ApJ*, 794, 155
- Kopparapu R. K., 2013, *ApJL*, 767, L8
- Kreidberg L. et al., 2014a, *Nature*, 505, 69
- Kreidberg L. et al., 2014b, *ApJ Letters*, 793, L27
- Kreidberg L. et al., 2015, *ApJ*, 814, 66
- Krist J. E., Hook R. N., Stoehr F., 2011, *Proc. SPIE* 8127, 81270J
- Kummel M., Kuntschner H., Walsh J., 2007, *Space Telescope European Coordinating Facility Newsletter*, 43, 8
- Lanza A. F. et al., 2003, *A&A*, 403, 1135
- Lanza A. F., Bonomo A. S., Rodonò M., 2007, *A&A*, 464, 741
- Leger A. et al., 2004, *Icarus*, 169, 499
- Leinert C. et al., 1998, *A&AS*, 127, 1
- Line M. R. et al., 2013, *ApJ*, 778, 183
- Line M. R. et al., 2016, *AJ*, 152, 203
- Luger R. et al., 2017, *Nature Astronomy*, 1, 0129
- Majeau C., Agol E., Cowan N. B., 2012, *ApJL*, 747, L20
- Mandell A. M. et al., 2011, *ApJ*, 728, 18
- Mandell A. M. et al., 2013, *ApJ*, 779, 128

- Mandel K., Agol E., 2002, *ApJL*, 580, L171
- Marcos-Arenal, P. et al., 2014, *A&A*, 566, A92
- Marois C. et al., 2008, *Science*, 322, 1348
- Mayor M., Queloz D., 1995, *Nature*, 378, 355
- McCullough P. R., MacKenty J., 2012, Instrument Science Report WFC3-2012-08, Baltimore: STScI
- McCullough P. R. et al., 2014, *ApJ*, 791, 55
- McMurtry C. et al., 2013, *Optical Engineering*, 52, 091804
- Meunier N., Desort M., Lagrange A.-M., 2010, *A&A*, 512, A39
- Micela G., 2015, *Exp. Astron.*, 40, 723
- Nascimbeni V. et al., 2015, *A&A*, 579, A113
- Oberg K. I., Murray-Clay R., Bergin E. A., 2011, *ApJL*, 743, L16
- Oshagh M. et al., 2014, *A&A*, 568, A99
- Parviainen H., 2015, *MNRAS*, 450, 3233
- Pascale E. et al., 2015, *Exp. Astron.*, 40, 601
- Pavlovsky C., McCullough P., Baggett S., 2011, Instrument Science Report WFC3-2011-19, Baltimore: STScI
- Peale S. J., 1977, in: J. A. Burns (ed.), *Planetary Satellites*, University of Arizona Press, pp 87-111
- Perryman M. et al., 2014, *ApJ*, 797, 14
- Petigura E. A., Howard A. W., Marcy G. W., 2013, *PNAS*, 110, 19273
- Pierrehumbert R., Gaidos E., 2011, *ApJL*, 734, L13
- Pirzkal N. et al., 2011, Instrument Science Report WFC3-2011-11, Baltimore: STScI
- Pont F., Zucker S., Queloz D., 2006, *MNRAS*, 373, 231
- Pont F. et al., 2008, *MNRAS*, 385, 109

- Pont F. et al., 2013, *MNRAS*, 432, 2917
- Poppenhaeger K., Schmitt J. H. M. M., Wolk S. J., 2013, *ApJ*, 773, 62
- Puig L. et al., 2015, *Exp. Astron.*, 40, 393
- Quirrenbach A. et al., 2014, *Proc. SPIE* 9147, 91471F
- Ranjan S. et al., 2014, *ApJ*, 785, 148
- Rauer H. et al., 2011, *A&A*, 529, A8
- Rauer H. et al., 2014, *Exp. Astron.*, 38, 249
- Redfield S. et al., 2008, *ApJL*, 673, L87
- Rein H., 2012, arXiv:1211.7121 [astro-ph.EP]
- Ricker G. R. et al., 2014, *JATIS*, 1, 014003
- Rogers L. A., Seager S., 2010, *ApJ*, 716, 1208
- Rohatgi A., 2017, *WebPlotDigitizer* v3.12
- Sanchis-Ojeda R., Winn J. N., 2011, *ApJ*, 743, 61
- Sarkar S., Papageorgiou A., Pascale E., 2016, *Proc. SPIE* 9904, 99043R
- Sarkar S. et al., 2017a, *ESA/ARIEL Technical Note ARIEL-CRDF-PL-AN-001*, Iss 2.2
- Sarkar S., Papageorgiou A., Pascale E., 2017b, in preparation
- Schaefer L. et al., 2016, *ApJ*, 829, 63
- Seager S., Sasselov D. D., 2000, *ApJ*, 537, 916
- Seager S., Mallén-Ornelas G., 2003, *ApJ*, 585, 1038
- Shapiro A. I. et al., 2014, *A&A*, 569, A38
- Sing D. K. et al., 2011, *MNRAS*, 416, 1443
- Sing D. K. et al., 2015, *MNRAS*, 446, 2428
- Sing D. K. et al., 2016, *Nature*, 529, 59
- Solanki S. K., 1999, *Astron. Soc. Pac. Conf. Ser.*, 158, 109

- Solanki S. K., Unruh Y. C., 2004, *MNRAS*, 348, 307
- Southworth J., 2011, *MNRAS*, 417, 2166
- Stevenson K. B. et al., 2014, *Science*, 346, 838
- Swain M. R., Vasisht G., Tinetti G., 2008, *Nature*, 452, 329
- Swain M. R. et al., 2009a, *ApJ*, 704, 1616
- Swain M. R. et al., 2009b, *ApJL*, 690, L114
- Swain M. R. et al., 2010, *Nature*, 463, 637
- Swain M. R. et al., 2013a, *Icarus*, 225, 432
- Swain M. R., Deroo P., Wagstaff K. L., 2013b, arXiv:1311.3934 [astro-ph.IM]
- Tessenyi M. et al., 2013, *Icarus*, 226, 1654
- Tinetti G. et al., 2007, *Nature*, 448, 169
- Tinetti G., Encrenaz T., Coustenis A., 2013, *Astron. Astrophys. Rev.*, 21, 63
- Tinetti G. et al., 2016, *Proc. SPIE* 9904, 99041X
- Tsiaras A. et al., 2016a, *ApJ*, 820, 99
- Tsiaras A. et al., 2016b, *ApJ*, 832, 202
- Tsumura K. et al., 2010, *ApJ*, 719, 394
- Varley R., 2016, *Comput. Phys. Comm.*, 207, 298
- Varley R., Tsiaras A., Karpouzas K., 2015, *ApJS*, 231, 13
- Vidal-Madjar A. et al., 2003, *Nature*, 422, 143
- Wakeford H. R. et al., 2013, *MNRAS*, 435, 3481
- Wakeford H. R. et al., 2017, *Science*, 356, 628
- Waldmann I., 2013, presented at EChO Open Science Workshop, July 1-3 2013, ESA-ESTEC (the Netherlands)
- Waldmann I. P. et al., 2015, *ApJ*, 802, 107
- Wallace L. et al., 1995, *Science*, 268, 1155

- Wang S. et al., 2017, arXiv:1704.04290 [astro-ph.EP]
- Wheatley P. J. et al., 2017a, MNRAS Letters, 465, L74
- Wheatley P. J. et al., 2017b, MNRAS, stx2836
- Wilkins A. N. et al., 2014, ApJ, 783, 113
- Winn J. N. et al., 2008, ApJ, 683, 1076
- Winn J. N., 2010, arXiv:1001.2010 [astro-ph.EP]
- Winn J. N. et al., 2011, ApJL, 737, L18
- Wolf E. T., 2017, ApJL, 839, L1
- Wolszczan A., Frail D. A., 1992, Nature, 355, 145
- Zellem R. T. et al., 2017, ApJ, 844, 27
- Zingales T. et al., 2017, arXiv:1706.08444 [astro-ph.EP]

*'How many fires are there, how many suns, how many dawns, how many waters? I am not posing an awkward question for you fathers; I ask you, poets, only to find out.'*

---

RIGVEDA, HYMN 10.88, VERSE 18